The interaction of light with WS2 nanostructures

Komen, I.

DOI
10.4233/uuid:63030917-8bbb-45d6-83f2-83fc1cb2bc47

Publication date
2021

Document Version
Final published version

Citation (APA)
Komen, I. (2021). *The interaction of light with WS2 nanostructures*. [Dissertation (TU Delft), Delft University of Technology]. https://doi.org/10.4233/uuid:63030917-8bbb-45d6-83f2-83fc1cb2bc47

THE INTERACTION OF LIGHT WITH WS_2 NANOSTRUCTURES

THE INTERACTION OF LIGHT WITH WS_2 NANOSTRUCTURES

Proefschrift

ter verkrijging van de graad van doctor

aan de Technische Universiteit Delft,

op gezag van de Rector Magnificus prof.dr.ir. T.H.J.J. van der Hagen,

voorzitter van het College voor Promoties,

in het openbaar te verdedigen op maandag 20 december 2021 om 15:00 uur

door

Irina KOMEN

Master of Science in Physics,
Universiteit Leiden, Nederland

geboren te Delft, Nederland.

Dit proefschrift is goedgekeurd door de

promotor: prof.dr. L. Kuipers
copromotor: dr. S. Conesa-Boj

Samenstelling promotiecommissie:

Rector Magnificus,	voorzitter
Prof.dr. L. Kuipers,	Technische Universiteit Delft, promotor
Dr. S. Conesa-Boj,	Technische Universiteit Delft, copromotor

Onafhankelijke leden:

Dr. A.G. Curto	Technische Universiteit Eindhoven
Prof.dr. P. Steeneken	Technische Universiteit Delft
Prof.dr. L. Siebbeles	Technische Universiteit Delft
Dr. A. Caviglia	Technische Universiteit Delft
Dr. T. van der Sar	Technische Universiteit Delft

Keywords: 2D materials, WS_2, light, optics, light-matter interaction, polarization-resolved, photoluminescence, Raman scattering, polaritons

Printed by: Gildeprint

Front & Back: An artist impression of light exciting and subsequently being emitted by a triangular WS_2 flake. Image created using Blender.

Casimir PhD Series, Delft-Leiden 2021-33

ISBN 978-94-6384-271-6

An electronic version of this dissertation is available at
http://repository.tudelft.nl/.

And God said: "Let there be light,"
and there was light.
God saw that the light was good.

Genesis 1:3-4, Bible, NIV (2011)

CONTENTS

SUMMARY

The field of optics studies the properties of light and the interaction between light and matter. This interaction goes two ways: matter can influence light, but light can also influence matter. The experiments described in this thesis are based on a number of interactions between light and the material tungsten disulphide (WS_2). WS_2 consists of layers that are only loosely connected, which means you can peal them off layer by layer. Subsequently, you will end up with a WS_2 flake of only three atoms thick, a so-called monolayer. Because of the negligible height of the material, WS_2 is commonly called a two-dimensional material.

WS_2 exhibits the electronic properties of a semiconductor. The electrons in a semiconductor material do not possess enough energy to conduct a current, but experience a barrier. One of the interactions between light and WS_2 that we describe, is photoluminescence. This process involves two steps: first, the material absorbs the light and uses the energy to let the electrons cross the energy barrier. Second, after some time when the electron relaxes back to its original energy level, the energy is released in the form of a light particle. Some of the energy in this process is lost to heat and friction, so the released light particle has a somewhat lower energy and therefore another color than the original light.

One of the main advantages of WS_2 is related to the polarization of light. Light can be described as a wave, with a propagation direction and a direction in which it oscillates. For instance, the light beam can propagate in the z-direction, while oscillating in the x-direction: it is linearly, horizontally polarized. If the direction in which the light oscillates rotates uniformly, the result is circularly polarized light. The rotation direction determines whether the light is right-handed or left-handed circularly polarized. During the photoluminescence process, in most materials all information about the absorbed light is lost, including information about the polarization. The interesting property of WS_2 is that it has some kind of memory for the polarization direction of circularly polarized light. WS_2 possesses two memory boxes to store information on the polarization direction of the absorbed light, the so-called valleys. One of the valleys interacts exclusively with left-handed, and the other with right-handed circularly polarized light.

Hence, WS_2 could be used for storing and transporting information, where the polarization direction of light forms a computer bit. In Chapter 3 we describe two experiments: one where we store information in the WS_2, and one where we read the information from the WS_2. To this end, we combine the WS_2 with so-called nanowires made of silver or zink oxide. The light flows through the wires like water through a canal or electricity through an electrical wire. By looking at the direction in which the light is propagating through the nanowire and on which side it exits the wire, we can read out from which WS_2 valley the light originated.

Unfortunately, WS_2 does not have a perfect memory for the polarization direction of light: if you shine left-handed circularly polarized light on WS_2, part of the resulting photoluminescence will be right-handed circularly polarized. In Chapter 4 we study how the memory capacity of WS_2 varies over the monolayer, and how it depends on temperature. Furthermore, we study the interaction between the two valleys of WS_2, by shining a combination of left-handed and right-handed circularly polarized light on it. By determining exactly what is the polarization state of the photoluminescence light, we gain access to the so-called coherence between the two valleys.

Next to photoluminescence, WS_2 can also interact with light in other ways. As mentioned before, the energy of a light particle can be used to help an electron cross the energy barrier. When the negatively charged electron crosses the barrier, it leaves a positively charged 'hole'. As the electron and the hole have opposite charges, they are attracted by each other. In WS_2 the strength of the attraction is so large, that a new particle, called an exciton, is formed. In Chapter 5 we describe a special interaction between light and this exciton, where they combine to form a so-called exciton-polariton. This exciton-polariton behaves like a wave, propagating through the monolayer of WS_2. Because this wave is confined in an ultrathin layer, the interaction between light and the WS_2 exciton is extremely strong. We calculate the properties of exciton-polaritons, namely the amplitude, the wavelength and how that depends on the frequency, and how far the wave propagates before it fades out. Combining the monolayer of WS_2 with another two-dimensional material called boron nitride allows for adjusting the mentioned properties as you wish.

In the last two chapters of this thesis we describe the interaction of light with three dimensional structures, fabricated by growing multiple layers of WS_2 on top of each other. To our surprise, these structures barely exhibit any photoluminescence, but only so-called Raman scattering. To understand Raman scattering, it is important to know that the atoms in a material are always slightly vibrating. Different vibrations are possible in a material, for instance atoms that move towards or away from each other. With a Raman interaction, light initiates such a vibration, also called a phonon, but the light looses some of its energy by doing so. By comparing the energy of the light before and after the interaction, you know the amount of energy that the phonon is using to vibrate.

We use Raman scattering to visualise differences in geometry and orientation of WS_2 structures. In Chapter 6 we study the Raman scattering of pyramid-like WS_2 structures. The triangular pyramids consist of steep walls with a crater in the middle. We observe that both the intensity and the energy of the various Raman phonons are different in the middle than at the walls of the hollow pyramids. Finally, in Chapter 7 we study the Raman scattering of flower-like WS_2 structures. The flower structures contain petals with different orientations: some are standing up, some are lying down, and everything in between. By studying the interaction of WS_2 flower sturctures with different kinds of polarized light, we can distinguish between flower petals of different orientations.

SAMENVATTING

Het vakgebied van de optica bestudeert de eigenschappen van licht en de interactie van licht met materie. Deze interactie gaat twee kanten op: materie kan licht beinvloeden, maar licht kan ook materie beinvloeden. De experimenten uit dit proefschrift berusten op verschillende interacties van licht met het materiaal wolfraam disulphide (WS_2). WS_2 bestaat uit laagjes die losjes aan elkaar vast zitten, waardoor het mogelijk is om ze één voor één van elkaar af kan pellen. Uiteindelijk houd je dan een schilfer WS_2 over van maar drie atomen dik, een zogenaamd monolaagje. Omdat het materiaal zo verwaarloosbaar dun is, wordt WS_2 ook wel een twee dimensionaal materiaal genoemd.

WS_2 heeft de elektronische eigenschappen van een halfgeleider. De elektronen in een halfgeleider materiaal hebben niet genoeg energie van zichzelf om vrij stroom te geleiden, maar ondervinden een barrière. Eén van de interacties van licht met WS_2 die wij beschrijven, is fotoluminescentie. Dit proces bestaat uit twee stappen: eerst absorbeert het materiaal het licht en gebruikt die energie om elektronen de energiebarrière te laten oversteken. Als het elektron na enige tijd weer terugvalt naar zijn oorspronkelijke energieniveau, komt de energie weer vrij in de vorm van een lichtdeeltje. Hierbij gaat er wel wat energie verloren aan warmte en wrijving, dus het vrijkomende lichtdeeltje heeft een wat lagere energie en daarmee een andere kleur dan het oorspronkelijke.

Eén van de grote voordelen van WS_2 heeft te maken met de polarisatie van licht. Licht kun je beschrijven als een golf, met een bewegingsrichting en een richting waarin de golf uitwijkt. De lichtbundel kan bijvoorbeeld bewegen in de z-richting, en golven in de x-richting: het is lineair gepolariseerd. Als de richting waarin het licht golft gelijkmatig verandert, noem je dat circulair gepolariseerd licht. De draairichting bepaalt of het licht rechtsom of linksom circulair gepolariseerd is. Nu gaat bij de meeste materialen tijdens het fotoluminescentieproces alle informatie over het geabsorbeerde licht, waaronder de polarisatie, verloren. Het interessante van WS_2 is dat het een soort geheugen heeft voor de polarisatierichting van circulair gepolariseerd licht. WS_2 heeft twee geheugenvakjes om de informatie over de polarisatierichting van het geabsorbeerde licht in op te slaan, zogenaamde valleien. De ene vallei reageert alleen op linksom, de andere alleen op rechtsom circulair gepolariseerd licht.

Je zou WS_2 dus kunnen gebruiken voor het opslaan en transporteren van informatie, waarbij de polarisatierichting van licht een computerbit vormt. In Hoofdstuk 3 beschrijven we twee experimenten: één waarbij je informatie opslaat, en één waarmee je informatie weer uitleest uit het WS_2. Hiervoor combineren we WS_2 met zogenaamde nanodraadjes, gemaakt van zilver of van zinkoxide. Het licht loopt dan door die draadjes zoals water door een gracht of elektriciteit door elektriciteitsdraden loopt. Door te kijken naar de bewegingsrichting van het licht in de nanodraad en aan welke kant het de draad uit komt, kunnen we aflezen uit welke WS_2 vallei het licht afkomstig was.

WS_2 heeft helaas geen perfect geheugen voor de polarisatierichting van licht: beschijn je het WS_2 bijvoorbeeld met linksom circulair gepolariseerd licht, dan komt er ook een beetje rechtsom gepolariseerde fotoluminescentie terug. In Hoofdstuk 4 bestuderen we hoe de geheugencapaciteit van WS_2 varieert in een monolaagje, en hoe het afhangt van de temperatuur. Daarnaast bestuderen we de interactie tussen de twee valleien van WS_2, door er een combinatie van linksom en rechtsom gepolariseerd licht op te schijnen. Door vervolgens te analyseren wat de polarisatie van het fotoluminescentielicht is, leren we iets over de zogenaamde coherentie tussen de twee valleien.

Naast fotoluminescentie kan WS_2 nog meer interacties aangaan met licht. Zoals gezegd, kan de energie van een lichtdeeltje gebruikt worden om een negatief geladen elektron de energiebarrière over te helpen, laat het een positief geladen 'gat' achter. Doordat het elektron en het gat een tegengestelde lading hebben, worden ze tot elkaar aangetrokken. In WS_2 is die aantrekkingskracht zo groot, dat zich een nieuw deeltje vormt, wat exciton heet. Hoofdstuk 5 beschrijft een bijzondere interactie tussen licht en dit exciton, waarbij die samen op hun beurt weer een zogenaamde exciton-polariton vormen. Deze exciton-polariton gedraagt zich als een golf, die door het monolaagje WS_2 heen beweegt. Omdat deze golf opgesloten zit in een ultradun laagje, is de interactie tussen het licht en de excitonen van het WS_2 extreem sterk. Wij berekenen de eigenschappen van exciton-polaritonen, namelijk de golflengte en hoe die afhangt van de frequentie, de amplitude, en hoe ver de golf komt voordat hij uitdooft. Door het monolaagje WS_2 te combineren met een ander tweedimensionaal materiaal, boor nitride, kun je de genoemde eigenschappen optimaal aanpassen.

In de laatste twee hoofdstukken van dit proefschrift beschrijven we de interactie van licht met driedimensionale structuren, ontstaan door meerdere lagen WS_2 op elkaar te laten groeien. Tot onze verbazing blijken deze structuren amper fotoluminescentie te vertonen, maar alleen zogenaamde Raman verstrooiing. Om Raman verstrooiing te begrijpen, is het belangrijk om te weten dat de atomen in een materiaal altijd een beetje trillen. Er zijn veel verschillende trillingen mogelijk in een materiaal, bijvoorbeeld atomen die naar elkaar toe of van elkaar af bewegen. Bij de Raman interactie slaat licht zo'n trilling aan, die ook wel een fonon heet, maar het licht raakt daardoor wel wat energie kwijt. Door de energie van het licht voor en na de interactie met elkaar te vergelijken, weet je met hoeveel energie die fonon staat te trillen.

Wij gebruiken de Raman verstrooiing om de verschillen in geometrie en orientatie van de WS_2 structuren te visualiseren. In Hoofdstuk 6 bestuderen we de Raman verstrooiing van WS_2 piramidestructuren. De driehoekige piramides bestaan uit steile wanden met een krater in het midden. We observeren dat zowel de intensiteit als de energie van de verschillende Raman fononen anders zijn in het midden dan bij de wanden van de holle piramides. Tenslotte bestuderen we in Hoofdstuk 7 de Raman verstrooiing van WS_2 bloemstructuren. De bloemstructuren bestaan uit bloemblaadjes met verschillende orientaties: sommigen staan rechtop en anderen liggen plat. Door de interactie van WS_2 bloemstructuren te bestuderen met gepolariseerd licht, kunnen we de verschillen tussen bloemblaadjes met verschillende orientaties zichtbaar maken.

1

INTRODUCTION

What is WS_2 and how does it interact with light in the processes of photoluminescence, Raman scattering and the formation of hybrid light-matter modes?

1

1.1. LIGHT

Light is essential for life on earth. Light and its interaction with matter is all around us: in the sun, the rainbow and our own ability to see. Where optical phenomena as reflection and refraction were already described by the ancient Greeks and Arabs, it took humanity many ages to fully understand light-matter interaction at the atomic scale [1–3]. Light has also been a driving force for scientific discoveries: bacteria and cells would have never been seen without lenses, and the whole field of quantum mechanics would have never started without the observation of absorption lines in sunlight [2]. Light is also at the basis of various technologies that we use daily: no pictures, no movies, and no internet without light.

In the field of optics, we study both light itself and its interaction with matter [3]. The discovery of light amplification based on stimulated emission of radiation (LASER) [4] has opened the way to new scientific discoveries. And despite its long history, light keeps surprising us. Arguably, no other physical phenomenon can be described in so many ways: as reflecting and refracting rays, as interfering and polarized electromagnetical waves or as absorbing and exciting quantum mechanical particles [3]. In this thesis, we investigate the interaction of light with tungsten disulphide nanostructures.

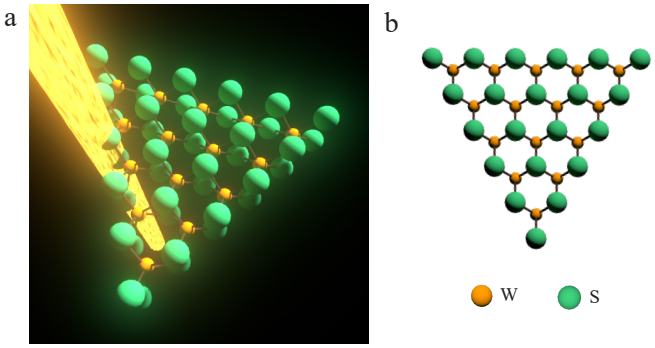

Figure 1.1: Tungsten Disulphide
a. Schematic representation of the interaction of light with a WS_2 flake. **b.** Top view of a WS_2 flake, with the W (orange) and S (green) atoms in a hexagonal lattice called 2H.

1.2. TMD MATERIALS

Tungsten disulphide (WS_2) is a Transition Metal Dichalcogenide (TMD) material, commonly used as a lubricant. TMDs combine a transition metal atom (Mo, W, ...) with two chalcogenides atoms (S, Se, ...). TMDs belong to a larger class of van der Waals materials, the most famous of which is graphene [5], the discovery of which resulted in the Nobel prize for the discoverers Geim and Novoselov in 2004 [6]. Van der Waals materials consist of layers, that are only held together by van der Waals forces and can therefore be easily 'peeled off' until a single atomically thin layer of material (a monolayer) is left (see Section 1.3.1) [5, 7]. For instance, graphene as a monolayer of graphite, can be produced using scotch tape and the lead of a pencil. Therefore, van der Waals materials are called

two dimensional (2D), atomically thin but with in-plane dimensions of micrometers or even millimeters [5, 8].

2D van der Waals materials possess many promising properties: they are extremely elastic [9], they exhibit various interesting electrical properties [5], they can be combined to form electronic devices [8, 10, 11], and they can be stacked together to form new materials with new properties [7]. The electrical properties of 2D materials vary: whereas graphene is metallic, hexagonal boron nitride (hBN) is insulating and TMDs are semiconductors. TMDs materials therefore have an electronic bandgap, which governs the interaction with light [12]. In this work, we focus on the intriguing optical properties of WS_2 nanostructures.

Figure 1.1a depicts a schematical representation of the interaction of a WS_2 flake with light. Figure 1.1b presents a schematic top view of the flake, with the W (orange) and S (green) atoms in a hexagonal lattice. This atomic structure, called 2H, is the structure of naturally occuring TMDs materials. Alternative atomic structures of WS_2 exist, namely 3R and 1T [13, 14].

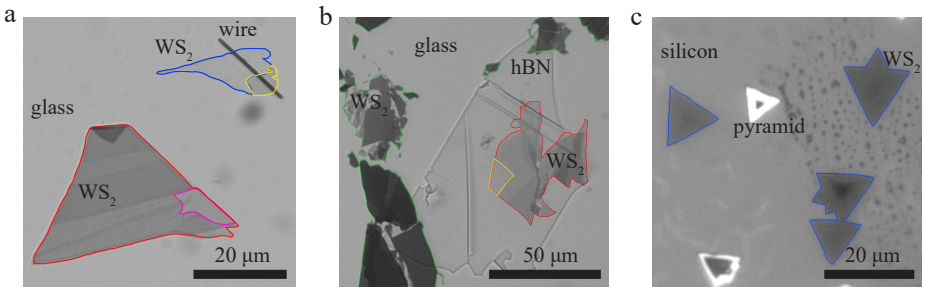

Figure 1.2: Optical microscopy images of WS_2 samples
a. Exfoliated WS_2 flakes on a glass substrate. A silver nanowire is deposited on top of the flake marked in blue/yellow in the upper right corner. As the flake marked in blue is a monolayer of WS_2, it can hardly be distinguished from the glass. The flake marked in yellow is a trilayer. The large, roughly triangular flake marked in red/pink exhibits parts with different thicknesses, as becomes apparent from the variations in contrast. The pink part of the flake contains 5 layers of WS_2, the rest of the flake is thicker. **b.** WS_2 flakes (marked in red/yellow) with an hBN flake of 150 nm stamped on top (transparent) on a glass substrate. The lightest part of the WS_2 flake (marked in yellow) under the hBN is a trilayer, the rest of the flake marked in red is thicker. The other WS_2 flakes present on the substrate are marked in green. **c.** CVD-grown monolayer WS_2 flakes (marked in blue) and pyramid-like structures (white) on a Si/SiN substrate.

1.3. FABRICATING WS_2 STRUCTURES

1.3.1. EXFOLIATION AND STAMPING

As the layers of 2D materials are held together only by van der Waals interactions, one of the ways of creating few-layered samples is mechanical exfoliation from a bulk crystal, *e.g.*, using adhesive tape [7, 15]. The specific exfoliation recipe used, dictates the size and quality of the resulting few-layer sample. Firstly, proper cleaning of the substrate using chemicals and oxygen plasma has an important influence [7, 15]. Secondly, heating the

substrate and tape with 2D flakes while in contact improves the yield of exfoliated flakes [7, 15]. Furthermore, the resulting sample is influenced by the choice of tape, substrate and bulk crystal.

Figure 1.2a depicts exfoliated WS_2 flakes on a glass substrate. The variations in contrast points to the differences in thickness, where thinner flakes have a lighter colour. The large triangular flake in the image (marked in red) contains a region of five layers of WS_2 (marked in pink). The other parts of this flake are thicker than five layers, as becomes apparent from the darker grey colour. The flake in the top right corner, marked in blue, is a monolayer of WS_2 and can hardly be distinguished from the glass. The darker part of this flake, marked in yellow, is a trilayer.

Stacking different 2D materials or placing nanostructures on top is relatively straightforward using a dry-transfer stamping technique [7, 16]. We use this method to place the silver and ZnO nanowires on top of few-layered WS_2 in Chapter 3. To this end, nanowires are deposited on a flat PDMS stamp, that is brought into contact with the WS_2 on a substrate and carefully released [7, 16]. In Fig.1.2a, a nanowire can be observed that is deposited on top of the monolayer flake (marked in blue) .

Alternatively, a pick-up-and-stamp method using semispherical PDMS/PC stamps can be used for stacking of 2D materials or placing nanostructures on top [7, 16]. This offers higher spatial positioning precision than a flat PDMS stamp, but has the disadvantage that the sample needs to be heated, leaving more residuals. Figure 1.2b depicts exfoliated WS_2 flakes with an hBN flake (150 nm thickness) placed on top. Here the darker grey flakes are WS_2 (marked in green). The transparent hBN flake is deposited on top of the thinner WS_2 flake (marked in red/yellow), where the thinnest part is a trilayer (marked in yellow). The lines on the hBN flake are cracks as a result of the transfer process.

1.3.2. CVD GROWN STRUCTURES

An alternative method to create samples of Van der Waals materials is Chemical Vapor Deposition (CVD) [17–22]. Depending on the growth conditions, CVD can both reproduce flat layers as found in naturally occurring TMDs, and enable the growth of nanostructures such as vertical walls, pyramids [23] and flower-like geometries [13]. Fig.1.2c depicts CVD grown WS_2 monolayers (marked in blue) and pyramid-like structures (white).

To grow the WS_2 structures investigated in this work on a microchip, the following procedure is used [13]. For the monolayers and pyramids in Chapter 4 and 6, the microchip is composed of a silicon frame with open windows, covered with a continuous silicon nitride (Si_3N_4) film [23]. For the nanoflowers in Chapter 7, the microchip is composed of a silicon frame with a large window, spanned by a silicon nitride film with an array of holes, penetrating both through the silion frame and the silicon nitride film [13]. Before the CVD growth procedure, WO_3 is deposited on the microchip and the chip is placed in the middle zone of a gradient tube furnace (Carbolite Gero). For the sulfurization process, sulfur is placed in a crucible upstream from the microchip and a constant argon flow of 150 sccm is applied. The zone containing the sulfur is heated to 220°C and the middle zone is heated to 750°C, and kept at this reaction temperature for 1 hour after which the system is naturally cooled down to room temperature [13].

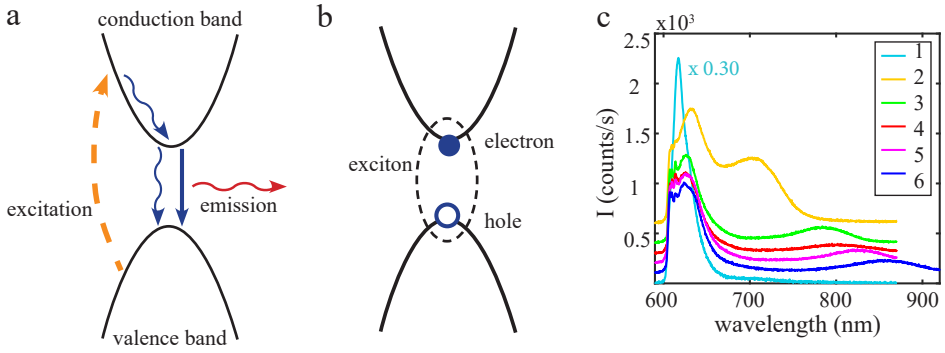

Figure 1.3: WS_2 bandgap and photoluminescence
a. In the photoluminescence process, an electron is excited (orange dashed line) by the absorbed photon. After decaying non-radiatively (blue wavy line) to the bottom of the conduction band, the electron relaxes to the valence band either non-radiatively (blue wave line) or radiatively (blue arrow). In the latter case, the released energy is emitted via a photon (red wavy line). **b.** In WS_2, the negative electron and positive hole exhibit such a strong Coulomb interaction, that they can bind together to form an exciton. Note that the energy of the exciton is slightly lower than the energy of the bandgap transition. **c.** Photoluminescence spectra of exfoliated WS_2 flakes with 1 - 6 layers. The intensity of the monolayer emission (in cyan) is much higher than the few-layer WS_2, therefore rescaled for an easy comparison. The few-layer WS_2 exhibits emission both from the direct and an indirect bandgap. The spectral position of the direct transition is at 630 nm, independent of the number of layers. The spectral position of the indirect transition is 700 nm for a bilayer (in yellow), and between 790 and 850 nm for 3 - 6 layers of WS_2.

1.4. INTERACTION OF WS_2 AND LIGHT

Light interaction with TMDs materials can have a number of appearances. Firstly, part of the light impinging on a TMDs material is reflected and part of the light is transmitted, being refracted while propagating through the material [3, 24]. Furthermore, the light can be absorbed by the material or scattered by the atoms of the material [24]. After absorption, the process of photoluminescence may occur (Section 1.4.1). The scattering can be elastic (Rayleigh scattering) and inelastic (Raman scattering) (Section 1.4.3) [24, 25]. Finally, hybrid light-matter modes, polaritons, can be formed between WS_2 and light.

1.4.1. PHOTOLUMINESCENCE

In Chapter 3 and 4, the light-WS_2 interaction leads to the process of photoluminescence (PL): the absorption and emission of light by a TMDs material. Photoluminescence is schematically depicted in Fig.1.3a, where the energy of absorbed light is used to excite electrons from the valence band to the conduction band (orange dashed line). After relaxation within the conduction band (blue wavy line), the electrons relax back to the valence band either non-radiatively (blue wavy line) or radiatively (blue arrow). In the latter case, the energy resulting from the electron decay is emitted as light via spontaneous emission (red wavy line) [24, 25]. This system will experience a so-called Stokes shift, whereby the emitted photon has a lower energy than the excitation photon. It is important to note that absorption does not always lead to luminescence, as

the electron can also relax back to the valence band via non-radiative decay [24, 25] (see Chapter 4).

An interesting property of TMDs materials is the formation of stable excitons at room-temperature [26–29]. Here, the electrons and holes, created after the absorption of a photon, bind together via Coulomb interaction to form a pair that behaves similarly to a hydrogen atom [24], as depicted schematically in Fig.1.3b. In TMDs materials these stable electron-hole pairs exhibit such a strong Coulomb interaction and possess such a high binding energy that they exist even at room temperature [26–29]. Note that the energy of the exciton is slightly lower than the bandgap energy, because of the attractive Coulomb interaction between the negative electron and positive hole. In TMDs, the conduction band is nearly spin degenerate, but the valence band splits due to a remarkably high spin-orbit coupling [30]. Multiple types of exciton exist, namely the A and the B exciton at the transition between the conduction band and the higher and lower valence band respectively (see Fig.1.7a in Section 1.5.2) [31–33], and charged excitons or so-called trions [34–37]. In this work we focus on the neutral A exciton. The transition of the B exciton has a lower wavelength (530 nm) than that of the A exciton, and therefore falls outside of our experimental detection region. The presence of trions is visible at cryogenic temperatures in the spectra of monolayer WS_2 in Chapter 4, but trions are not studied specifically.

In the few-layer regime, TMDs materials experience a transition from an indirect to a direct bandgap semiconductor [12, 31, 33, 38]. The energy of the exciton associated with the direct bandgap transition typically lies in the (near) visible wavelength range in TMDs materials, making them attractive for optical experiments. Figure 1.3c depicts photoluminescence spectra of WS_2 flakes with 1 - 6 layers. The few-layer WS_2 exhibits emission both from the exciton resonance around 630 nm and from the indirect bandgap transition, whereas the monolayer only emits from the exciton resonance. Note that the observed photoluminescence intensity of the WS_2 monolayer (in cyan in Fig.1.3c) is much higher than that of the few-layer WS_2. The spectral position of the indirect bandgap is around 700 nm for the bilayer (in yellow), and ranges from 790 to 850 nm for 3 - 6 layers of WS_2 (see also [39, 40]).

1.4.2. EXCITON-POLARITONS

In Chapter 5, the interaction between light and WS_2 results in the formation of a hybrid light-matter mode. Here, an exciton in the WS_2 valley and a photon interact strongly and form a so-called exciton-polariton [41, 42]. Like the better known plasmon-polariton, the resulting mode, propagating in the WS_2 plane, decays exponentially away from the plane and therefore spatially exists only close to the material [43–46]. Polaritons are found in different classes of 2D materials: plasmon-polaritons are commonly studied in graphene, phonon-polaritons in hexagonal boron nitride and exciton-polaritons in TMDs materials [45, 46]. The interest in polaritons lies in the confinement of a (hybrid) electromagnetic mode in an atomically thin material, orders of magnitude smaller than the wavelength of the light. The large exciton binding energy creates an enormous interaction strength and enhances the light-matter interaction [46]. Polaritons in 2D materials hold the promise of applications in nanophotonics, as they can be used for lasing [47],

sensing [48] and many ways of light concentration and manipulation [49, 50].

1.4.3. RAMAN SCATTERING

In Chapter 6 and 7, we investigate the Raman response of WS_2 nanostructures. Here, the excitation light is not absorbed like in the case of photoluminescence. Rather, it is scattered inelastically by collective vibrations of the WS_2 atoms, also called phonons. Not all vibrational modes of the atoms are Raman active, this depends on the symmetries of the modes with respect to the symmetries of the crystal [25, 51]. On a single molecule level, the vibrating atoms consist of positively charged cores and mobile negative charge, that can be described as oscillating dipoles that can interact with electromagnetic radiation [51]. Raman scattering is depicted schematically in Fig.1.4a, where the impinging photons cause a transition from the initial to the final state via a virtual state, interacting with phonons in the material, either loosing energy (Stokes process, see Fig.1.4a) or gaining energy (anti-Stokes process, not depicted) [24, 25]. The phonon energy can thus be determined by comparing the frequencies of the incident and scattered light.

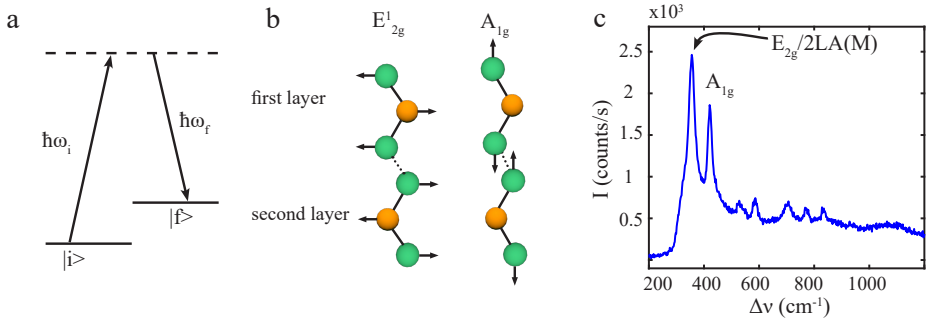

Figure 1.4: Raman scattering of WS_2
a. In Raman scattering a transition occurs from the initial to the final state via a virtual state. The energy difference between the incoming and outgoing light is used to excite a vibration or phonon. **b.** The two Raman active optical modes of WS_2. Both the W (orange) and S (green) atoms participate in the in-plane E_{2g} mode, whereas only the S atoms vibrate in the out-of-plane A_{1g} mode (compare Fig.1.1). **c.** Raman spectrum of a WS_2 nanoflower (see Chapter 7), with the two characteristic modes E^1_{2g} and A_{1g}, and a number of higher order phononic modes involving the LA(M) mode.

The characteristic Raman-active vibrational modes of WS_2 which can be measured in the back-scattering configuration [52–54], are depicted in Fig.1.4b. The E^1_{2g} mode corresponds to the in-plane vibration of both the W and the S atoms, and the A_{1g} mode corresponds to the out-of-plane vibration of the S atom. Relevant is also the longitudinal acoustic mode LA(M), as the spectral position of two times LA(M) (2LA(M)) is very close to the E_{2g} mode of WS_2 [55]. Figure 1.4c depicts the Raman response of a WS_2 nanoflower, where the two characteristic Raman features are marked. The spectral feature at 350-355 cm^{-1} is a combination of the E_{2g} and 2LA(M). The spectral feature at 417 cm^{-1} is the A_{1g} mode. The other spectral features are higher order phononic modes, involving the LA(M) phonon (see Chapter 6 and 7).

1

Raman spectroscopy is commonly used to characterize the structural properties of TMDs materials, because the spectral position of the Raman features can be used to determine the number of layers. The largest spectral differences exist between monolayer, bilayer and trilayer [53, 56, 57]. Furthermore, TMDs Raman features may provide information on defect density [58, 59] and strain [60, 61] in a TMDs flake. The TMDs spectral Raman features are influenced by many factors. Both spectral position and (relative) peak intensity of TMDs Raman features depend on the temperature [57, 62–66] (see Chapter 6 and 7). The TMDs Raman response is influenced by the polarization of the excitation light, as the E_{2g} mode and the A_{1g} respond differently to horizontally or vertically polarized light [32, 55], and to circularly polarized light with opposite handedness [67–69] (see Chapter 7). Important for this work is the influence of the excitation wavelength on the Raman response. Raman features are greatly enhanced when the excitation is in resonance with an excitonic transition [32, 56, 70–74] (see Chapter 6 and 7).

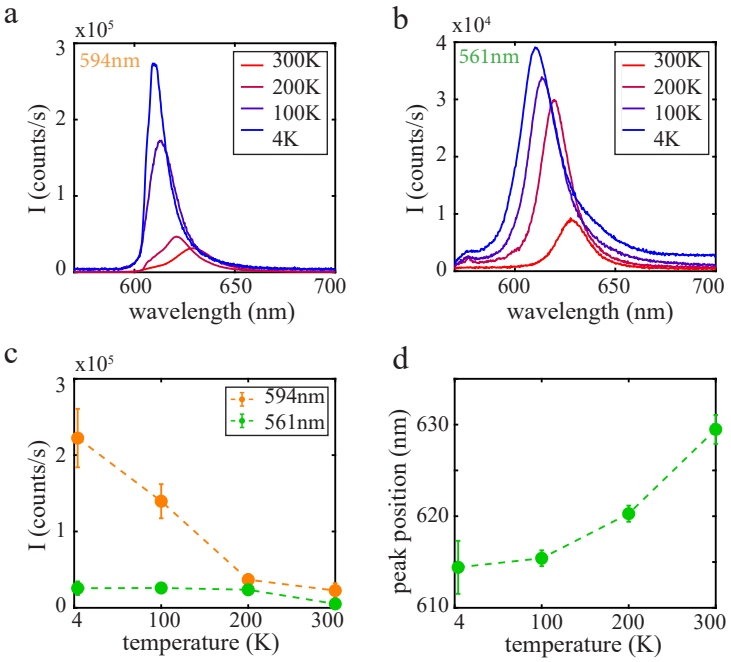

Figure 1.5: Temperature dependence of monolayer WS_2 photoluminescence
a-b. Photoluminescence spectra of the emission of a CVD-grown WS_2 monolayer for **a.** 594 nm excitation and **b.** 561 nm excitation. The photoluminescence intensity for 594 nm excitation is an order of magnitude larger at 4 K than at room temperature. **c.** The photoluminescence intensity as a function of temperature for both excitation energies, where the intensity corresponds to the peak maximum, and the bars indicate the spatial variations over the monolayer flake rather than the error. At lower temperatures, the PL intensity increases by a factor of 4 for 561 nm excitation (in green), and a factor of 9 for 594 nm excitation (in orange). **d.** The spectral position of the exciton shifts to lower wavelengths upon decreasing the temperature. Note in **a.** that the spectrum taken at 4 K is partially cut off by the optical filter.

1.5. INFLUENCING PHOTOLUMINESCENCE

1.5.1. TEMPERATURE DEPENDENCE

Figure 1.5a-b presents temperature-dependent photoluminescence (PL) spectra of a CVD-grown WS_2 monolayer, for two different excitation wavelengths. When decreasing the temperature from room temperature (red spectra) to 4 K (blue spectra), the spectral position of the exciton peak shifts to lower wavelengths and the PL intensity increases. Note that in Fig.1.5a, the spectrum taken at 4 K is partially cut off by optical filters in the set-up (see Chapter 2). Comparing Fig.1.5a and b, it becomes apparent that the PL intensity of a WS_2 monolayer is higher for excitation with 594 nm than with 561 nm excitation. At 4 K (blue spectra), the PL intensity for a 594 nm excitation is an order higher than for a 561 nm excitation. Figure 1.5c depicts the photoluminescence intensity of the WS_2 monolayer for 594 nm (in orange) and 561 nm excitation (in green). The monolayer PL intensity increases with decreasing temperature for both excitation energies. For a 561 nm excitation, the PL intensity at 4 K is four times higher than at room temperature (compare Fig.1.5b), and for a 594 nm excitation, the PL intensity is even an order of magnitude higher at 4 K.

The difference between the PL intensity with different excitation energies can be attributed to the fact that the 594 nm excitation is more in resonance with the transition of the WS_2 A-exciton. Figure 1.5d depicts the spectral position of the measured photoluminescence from the exciton as a function of temperature. Upon decreasing temperature, the exciton peak position shifts to lower wavelengths (see also [34–36]). The shift explains the large increase in intensity upon decreasing the temperature, as using a fixed excitation wavelength will tune the excitation more into resonance with the WS_2 exciton. The more resonant the excitation wavelength to the excitonic resonance of WS_2, the more of the excitation light is absorbed and the more the measured PL intensity increases. The 561 nm excitation is spectrally relatively far away from the exciton resonance both at room temperature and at cryogenic temperatures. The 594 nm excitation is already relatively close to the excitonic resonance at room temperature. When decreasing the temperature, the spectral position of the excitonic resonance shifts to lower wavelengths, tuning the excitation even more into resonance. Therefore the influence of the excitonic resonance on the PL intensity is more apparent for a 594 nm than for a 561 nm excitation.

Figures 1.6a-c depict temperature dependent PL spectra of an exfoliated bilayer, trilayer and five layers of WS_2 for 594 nm excitation. The spectra exhibit two peaks: the high intensity peak in the wavelength range of 614-630 nm corresponds to PL from the exciton associated to the direct bandgap, and the low, broad intensity peak at higher wavelengths corresponds to PL from the indirect bandgap transition (see Fig.1.3c). The sharp features around 610 nm on top of the direct bandgap emission are the result of the Raman response from the WS_2 and from the silicon substrate. When comparing the spectra at room temperature (in red) to the spectra at 4 K (in blue), it becomes apparent that the PL intensity from the exciton increases with decreasing temperature. However, the emission from the indirect bandgap remains constant, thus changing the intensity ratio between light from the direct and indirect bandgap. Figure 1.6d depicts the spectral position of the indirect bandgap emission for WS_2 samples of different layer thickness.

Upon decreasing the temperature, the spectral position shifts to higher wavelengths (see also [39, 75]), whereas the spectral position of PL from the exciton shifted to lower wavelengths. Thus the PL from the exciton and the indirect bandgap are spectrally further away from each other at cryogenic temperatures than at room temperatures.

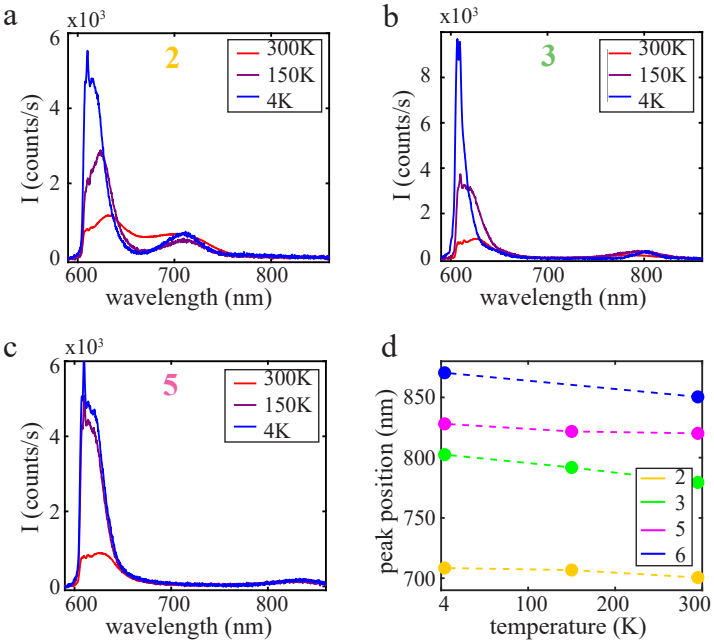

Figure 1.6: Temperature dependence of few-layer WS_2 photoluminescence
a-c. Photoluminescence spectra of the emission of a WS_2 **a.** bilayer, **b.** trilayer and **c.** five layers (for 594 nm excitation). The intensity of the direct bandgap emission increases at cryogenic temperatures, whereas the intensity of the indirect bandgap emission remains constant. **d.** At lower temperatures, the spectral position of the indirect bandgap emission shifts to higher wavelengths. Note that this shift is in the opposite direction to the spectral position of the direct bandgap emission, which shifts to lower wavelengths as the temperature decreases (see Fig.1.5).

1.5.2. VALLEY PSEUDOSPIN

MONOLAYERS

Arguably, the most intriguing aspect of the TMDs photoluminescence is the TMDs interaction with polarized light. Figure 1.7a schematically depicts the TMDs direct bandgap valleys, that are situated at the K and K' points in the Brillouin zone and are energy-degenerate [76–79]. The conduction band is nearly spin degenerate but the valence band splits due to a remarkably high spin-orbit coupling [30]. Because of time-reversal symmetry, the spin splitting in the valence band has opposite signs at the K and K' valley, making them nonequivalent. In TMDs inversion symmetry is broken as a result of the atomic structure (see Section 1.2). This broken inversion symmetry ensures that spin and valley and the associated excitons are strongly coupled at the K and K' valleys (see

Section 1.4.1). The combination of high spin-orbit coupling, time-reversal symmetry and broken inversion symmetry results in a set of optical selection rules for the TMDs semiconductor valleys [76–79]. A pseudospin and a spin can be attributed to the TMDs valleys and the associated excitons, that allows the selective addressing of each valley separately by using circularly polarized light of opposite handedness [80–82]. This selectivity is depicted schematically in Fig. 1.7a, where the K and K' valley can be addressed with σ_- and σ_+ polarized light, respectively.

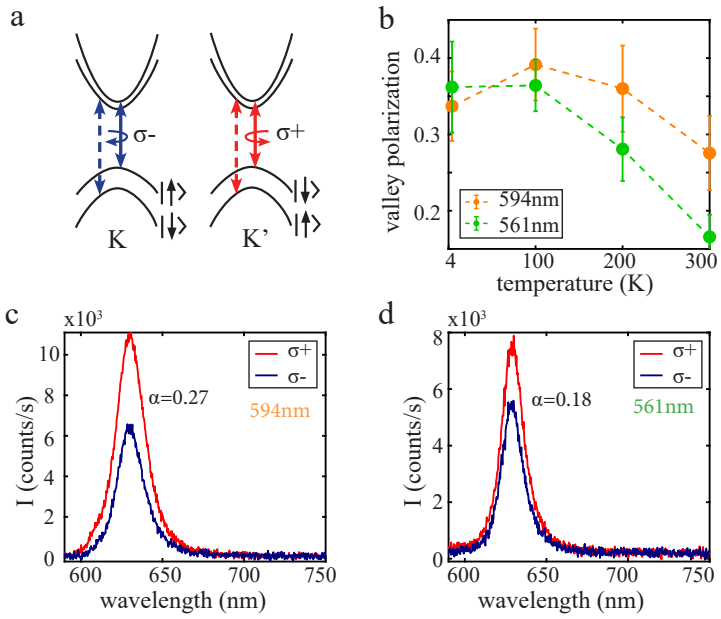

Figure 1.7: Valley polarization of monolayer WS_2
a. The optical selection rules of the WS_2 semiconductor valleys dictate that the K and K' valley can be addressed selectively using circularly polarized light of specific handedness. The transition of the lower valence band (dashed lines) yields the B exciton, while the transition from the upper valence band (solid line) yields the A exciton. **b.** Temperature dependence of the valley polarization for 594 nm (in orange) and 561 nm (in green) excitation. The valley polarization increases with decreasing temperatures for both excitation wavelengths. The valley polarization is position dependent (see Chapter 4): the bars indicate the spread of the valley polarization over the monolayer flake rather than the error. **c,d.** Photoluminescence spectra of a CVD grown WS_2 monolayer for **c.** 594 nm and **d.** 561 nm excitation, acquired at room temperature. The WS_2 is excited with σ_+ polarized light, and from the difference in the σ_+ (in red) and σ_- (in blue) emission, we determine a degree of valley polarization of **c** 0.27 and **d** 0.18.

For potential applications of the valley pseudospin, it is essential to have a large asymmetric occupation of electrons in the two valleys, i.e., a high valley polarization. To determine valley polarization, the WS_2 is excited with circularly polarized light, thus addressing only one specific WS_2 valley, and the handedness of the resulting emission is determined. The value of the valley polarization depends on many factors. The first factor is the kind of TMD: although the valley-dependent optical selection rules apply to all

TMDs materials, WS_2 exhibits a particularly high valley polarization at room temperature [77, 83, 84].

Figure 1.7c presents PL spectra of a CVD grown monolayer, excited with σ_+ light at room temperature. Comparing the emission spectra with different polarization handedness, it becomes apparent that the emission with σ_+ polarization (red in Fig.1.7c-d) has a higher intensity than the σ_- polarization (blue in Fig.1.7c-d). From the PL spectra we determine a valley polarization $\alpha = \frac{I_{LH}-I_{RH}}{I_{LH}+I_{RH}}$, where I_{LH} and I_{RH} are the left-handed and right-handed circularly polarized emission respectively. The determined valley polarization is 0.27 for 594 nm excitation (Fig.1.7c) and 0.18 for 561 nm excitation (Fig.1.7d). Figure 1.7c,d thus demonstrate the second factor influencing the value of the valley polarization, namely the excitation energy: the more the excitation is in resonance with the exciton energy, the higher the valley polarization [28, 81, 85, 86].

Figure 1.7b presents the temperature dependence of valley polarization for an excitation wavelength of 594 nm (in orange) and 561 nm (in green), respectively. Even though at room temperature, the value of the valley polarization for 561 nm is lower than for 594 nm, with decreasing temperature valley polarization increases to around 0.35 for both excitation wavelengths. It is therefore clear that the third factor influencing TMDs valley polarization is temperature: for lower temperatures valley polarization increases [77, 80, 85, 87] (see Chapter 4).

MULTILAYERS

The fourth factor influencing valley polarization is the WS_2 thickness. As mentioned before, the broken spatial inversion symmetry in the TMDs atomic structure is essential for coupling the spin and valley. When increasing the thickness of a TMDs material from a monolayer to a bilayer and thicker, each layer is rotated by 180^o with respect to the previous one [77, 83]. The rotation of each TMDs layer means that the broken inversion symmetry from monolayer TMDs is lifted, so few-layer TMDs do exhibit spatial inversion symmetry. Therefore for most TMDs materials, increasing the thickness from a monolayer to a bilayer or thicker results in a loss (MoS_2, $MoSe_2$) or a lowering (WSe_2) of valley polarization [80, 81, 88–90]. In these TMD materials, high valley polarization in bilayers can only be achieved by electrical gating [88, 91, 92]. Surprisingly, WS_2 bilayers do exhibit an appreciable valley polarization with values even larger than WS_2 monolayers [14, 40, 77, 83, 85, 87]. The proposed explanation of the difference between WS_2 and the other TMDs is the large spin-valley coupling strength with respect to the interlayer hopping energy, allowing a few-layer WS_2 system to be regarded as decoupled layers [77]. Moreover, increasing the thickness beyond a monolayer suppresses some of the valley depolarization mechanisms in WS_2, making valley polarization of few-layer WS_2 more robust than that of monolayers [77, 83, 85]. Therefore, for the coupling of optical spin to the valley pseudospin in Chapter 3, we use few-layer WS_2 [40, 93].

Figure 1.8a-c depicts PL spectra of exfoliated WS_2 flakes of various thickness. The spectra are obtained at room temperature, upon a σ_+ polarized excitation with 594 nm wavelength. Comparing the σ_+ and σ_- emission from the bilayer and trilayer in 1.8b-c, it becomes apparent that the exciton emission is polarized. However, the emission from the indirect bandgap is unpolarized (see also [28, 83, 85]). In the same way as for the mono-

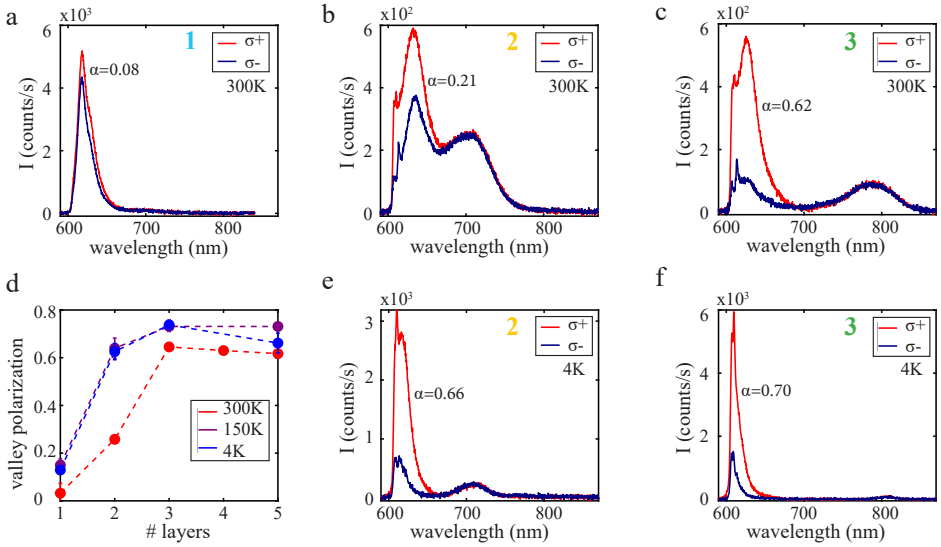

Figure 1.8: Valley polarization of few-layer WS_2
a-c. Photoluminescence spectra of an exfoliated WS_2 **a.** monolayer, **b.** bilayer and **c.** trilayer. The spectra are obtained at room temperature, for 594 nm excitation that is σ_+ polarized. Note that the emission from the direct bandgap is polarized, but the emission from the indirect bandgap is unpolarized. From the difference in σ_+ and σ_- emission we determine the valley polarization. The valley polarization of the exfoliated monolayer (**a**) is around 0.08, much lower than that of the CVD-grown monolayer in Fig.1.7c. The valley polarization of the bilayer (**b**) is 0.21 and of the trilayer (**c**) 0.62. **d.** The valley polarization increases with an increasing number of WS_2 layers. With decreasing temperature, the valley polarization increases to a maximum of approximately 0.75. **e-f.** Photoluminescence taken at 4 K of the WS_2 **e.** bilayer and **f.** trilayer. The valley polarization of the bilayer increases with respect to the room temperature value to approximately 0.66. The valley polarization of the trilayer also increases with respect to room temperature to 0.70.

layers in Fig.1.7, we determine valley polarization of the exciton emission. The valley polarization of the bilayer is 0.20 (Fig.1.8b) and of the trilayer is 0.62 (Fig.1.8c). In other words, valley polarization increases with an increasing number of layers. This increase becomes apparent from Fig.1.8d, that depicts the valley polarization of few-layer WS_2 flakes at room temperature (red) and cryogenic temperatures (purple and blue).

Like for the monolayer, the valley polarization of few-layer WS_2 increases with a decreasing temperature (see also [28, 85, 87]). Figure 1.8e-f depicts photoluminescence spectra taken at 4 K of the WS_2 bilayer and trilayer. The valley polarization of the bilayer increases tremendously with respect to the room temperature value, to 0.66. The valley polarization of the trilayer also increases with respect to room temperature, but only to 0.70. A maximum valley polarization of 0.75 is reached at 4 K for 3-5 layers of WS_2 (see [85]).

Note that the valley polarization of the exfoliated monolayer in Fig.1.8a is much lower (around 0.08) than that of the CVD-grown monolayer (around 0.27) in Fig.1.7c. The last factors influencing the valley polarization are the sample preparation and the substrate. Substrate roughness and sample preparation methods influence the quantum yield of the WS_2, e.g., the radiative and non-radiative decay rates (see also [83, 87]). As discussed in Chapter 4, valley polarization is destroyed due to valley hopping of electrons from one valley to the other. If the (non-)radiative decay rate of the electron in the valley is faster than the valley-hopping rate, effectively, the measured valley polarization is higher. Therefore the measured valley polarization varies for different sample preparations and substrates.

1.6. WS_2 AND LIGHT IN THIS THESIS

To summarize, we have described three results of the interaction between WS_2 and light: photoluminescence, the formation of exciton-polaritons and Raman scattering. The chirality of the photoluminescence interaction between WS_2 and light opens the way for applications in nanophotonics and specifically valleytronics, the field of interacting with and manipulating the valley pseudospin. In Chapter 3 we propose a way to optically address and read out the valley pseudospin using silver and ZnO nanowires. In Chapter 4 we confirm the existence of coherence between the WS_2 valleys. Furthermore, as described in Chapter 5, exciton-polaritons in WS_2 hold the promise of applications in nanophotonics that make use of the enormous light-matter interaction. Raman spectroscopy is commonly used as a characterization tool to confirm the nature of a material and its properties. In Chapter 6 we go one step further, determining how structural and morphological variations in WS_2 pyramids manifest themselves in Raman spectra. In addition, in Chapter 7 we describe how Raman spectroscopy can be used to probe the orientation of WS_2 nanoflowers.

2

EXPERIMENTAL SET-UP

How do we measure the position-dependent intensity and frequency of the photoluminescence and Raman response of WS_2 nanostructures?

2.1. ESSENTIAL COMPONENTS MICROSCOPE

To measure the photoluminescence of WS_2 (Introduction, Chapter 3 and 4) and the Raman response of WS_2 (Chapter 6 and 7) we use a home-built set-up that combines spectroscopy with microscopy. Different versions of this set-up are used for the different investigations described in this thesis, but the basic components are presented in Fig.2.1. We start with the excitation (**I**, in yellow), which is provided by either a continuous-wave laser with a wavelength of 594 nm and a power of 1.6 mW/mm^2 (Coherent OBIS 594 LS), or a continuous-wave laser with a wavelength of 561 nm and a power of 3.6 mW/mm^2 (Cobolt 08-DPL 561). It is essential for the excitation light to be collimated (see Section 2.3). The excitation light is reflected by a beam splitter or a dichroic mirror **(II)**, and enters an objective lens **(III)**, that focuses the light on the sample (see Section 2.2). The sample **(IV)** is mounted on a XYZ translation stage (Thorlabs TDC001 T-cubes at room temperature, see Section 2.5 for cryogenic temperature). Light coming from the sample is collected in reflection using the same objective lens and passes through the same beam splitter or dichroic. Light coming from the sample consists predominantly of the reflected excitation light, with only a small contribution of the photoluminescence and the Raman response. Since the latter have a different wavelength than the excitation, the reflected light can be blocked using a combination of optical filters **(V)** and a dichroic mirror. Finally, the light from the sample is imaged on a spectrometer **(VI)** (Princeton Instruments SP2358) fitted with a CCD (charge-coupled detector) camera **(VII)** (Princeton Instruments ProEM 1024BX3).

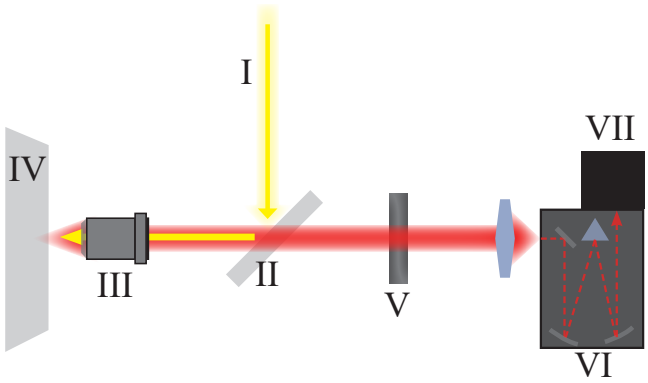

Figure 2.1: Essential components set-up
Schematic representation of our home-built spectroscopy microscope set-up. The collimated excitation beam (**I**, in yellow) is reflected by a beam splitter or a dichroic mirror **(II)** and enters an objective lens **(III)**, where the light is focused on a sample mounted on a XYZ translation stage **(IV)**. As the photoluminescence and Raman response from the sample (in red) have a different wavelength than the reflected excitation light, the reflection can be removed using optical filters **(V)** and the dichroic mirror. The generated light is imaged on a spectrometer **(VI)** and CCD camera **(VII)**. Inside of the spectrometer (see dashed lines for the beam path inside of the spectrometer **VI**), the light is diffracted by a grating (blue triangle) and guided to the CCD camera, where the different wavelength components of the generated light are analyzed.

The combination of spectrometer and CCD camera enables us to study both the spectral properties and the intensity of the generated light. To study the light intensity, we use the zeroth order of the spectrometer grating as a mirror, studying the non-diffracted part of the light with the CCD camera. As this method does result in a loss of intensity, we focus the light directly onto a CCD camera for parts of Chapter 3. The described basic components of the set-up allow us to focus the excitation light on the sample and study the frequency and intensity of the generated light from the WS_2 sample.

2.2. FOCUSSING WITH THE OBJECTIVE LENS

For our experiments, we focus and collect the light of the sample using an objective lens. We use either an oil-immersion objective lens (Nikon Plan Apochromat 100x NA=1.45, Chapter 3), or an air objective (Zeiss 100x NA=0.85, Chapters 4, 6 and 7). Figure 2.2a depicts schematically how the light enters the oil-immersion objective lens **(1)** and is focused **(2)** through the oil **(3)** and the glass substrate **(4)** on the sample **(5)**. As the oil, the glass substrate and the glass lenses have comparable refractive indices, the use of an oil-immersion objective lens ensures the least amount of refraction losses. Figure 2.2b depicts how the light enters the air objective lens **(1')** and is focused **(2')** on the sample **(5')** that is deposited on top of the substrate **(4')**.

There are several differences between collection with the oil-immersion or the air objective. First of all the numerical aperture (NA), defined as $NA = n\sin\theta$, with n the refractive index of the medium and θ the maximum semi-angle of the cone of light, collected from or focused on the sample by the objective lens (see Fig.2.2a,b) [94]. Both objective lenses are used to focus the excitation light on and to collect the sample emission from a diffraction limited spot. The size of this spot is given by the Abbe diffraction limit: $d = \frac{\lambda}{1.22NA}$ [94]. Therefore for a given wavelength, using the oil-immersion objective with a higher NA (1.45) than that of the air objective (0.85) ensures that an area with smaller dimension d is excited, and that emission is collected from this smaller area.

To understand the implications of the NA of the objective lens, it is important to note that both the studied photoluminescence and the Raman scattering from WS_2 can be described by radiating dipoles [24]. When a dipole is located next to a dielectric interface, e.g., on top of a substrate, it does not radiate uniformly into all 4π directions in space [95–97]. In the emission pattern of a dipole at the air-glass interface, the emitted intensity is concentrated at angles corresponding to NA=1.0 on the glass side [96, 97]. As light at these angles can only be collected through the oil-immersion objective, the collected intensity by such an objective is larger than by the air objective: around 4 times for a dipole oriented in the transverse direction [97]. Furthermore, a dipole close to an interface radiates more into the high n (glass) side than into the low n (air) side [95]. In Fig.2.2a and b, it becomes apparent that in our set-ups, the oil-immersion objective collects through the glass substrate, while the air objective the emission on the air side and therefore has a much larger collection efficiency.

The influence of the type of objective on the collected efficiency becomes apparent when comparing the spectra of a bilayer and five layers of WS_2 acquired using the oil-immersion and the air objectives in Fig.2.3. As mentioned in Section 1.4.1 of the Introduction, few-

2

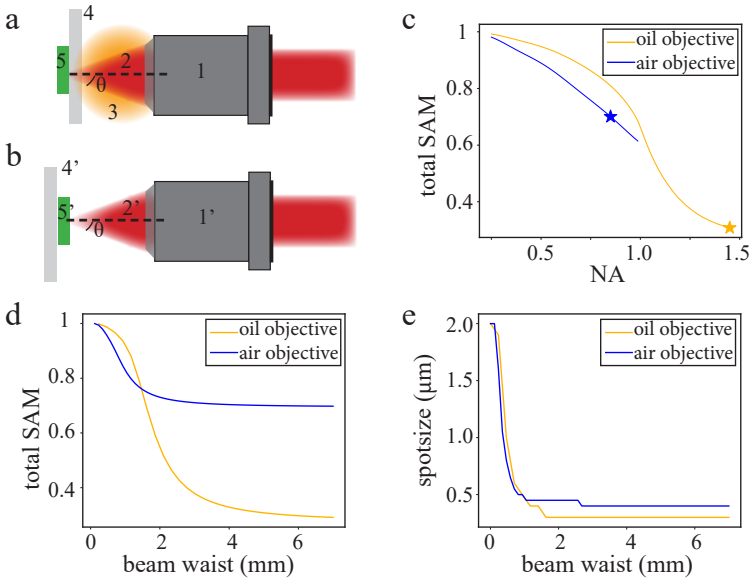

Figure 2.2: Focusing using an objective lens
a. Light enters an oil-immersion objective **(1)** and is focused **(2)** through the oil **(3)** and the glass substrate **(4)** on the sample **(5)**. **b.** Light enters an air objective **(1')** and is focused **(2')** through the air on the sample **(5')** that is lying on the substrate **(4')**. **c.** When tightly focusing circularly polarized light, the total spin angular momentum (SAM) decreases. For an air objective with NA = 0.85 the total SAM decreases to 0.70, for an oil objective with NA = 1.45 it decreases to 0.30. These calculations assume that the full back focal plane of the objective lens is filled. Decreasing the excitation beam size decreases the effective NA. **d.** Total SAM of the air objective and the oil-immersion objective for different beam waists. For a beam waist up to 2 mm, the total SAM is above 0.80. **e.** As the effective NA decreases, the diffraction limited size of the spot on the sample does increase tremendously. Therefore, as a trade-off between spin angular momentum and diffraction limited spot, we use a beam diameter of 1 mm for both objective lenses.

layer WS_2 exhibits photoluminescence emission both from the direct transition around 630 nm, and from the indirect transition around 720 nm for a bilayer and 850 nm for five layers of WS_2. We observe that the measured intensity of emission from the direct transition is 50x larger for the oil-immersion objective (Fig.2.3a,b) than for the air objective (Fig.2.3c,d). Surprisingly, the intensity difference acquired using the two different objectives is even larger (100x) for the emission from the indirect transition. This means that for the bilayer, the emission from the direct vs. indirect transition exhibits the same intensity in the spectrum in Fig.2.3a, acquired using the oil-immersion objective, but the emission from the indirect transition exhibits only half of the intensity of the direct transition in the spectrum in Fig.2.3c, acquired using the air objective. The relatively low intensity of the indirect transition in the spectrum of the five layers of WS_2 in Fig.2.3d makes it less straightforward to distinguish it from the background when acquiring using the air than using the oil-immersion objective. We hypothesise that the intensity differences between light from the direct and indirect transition collected using the two objectives, can be explained by differences in radiation patterns.

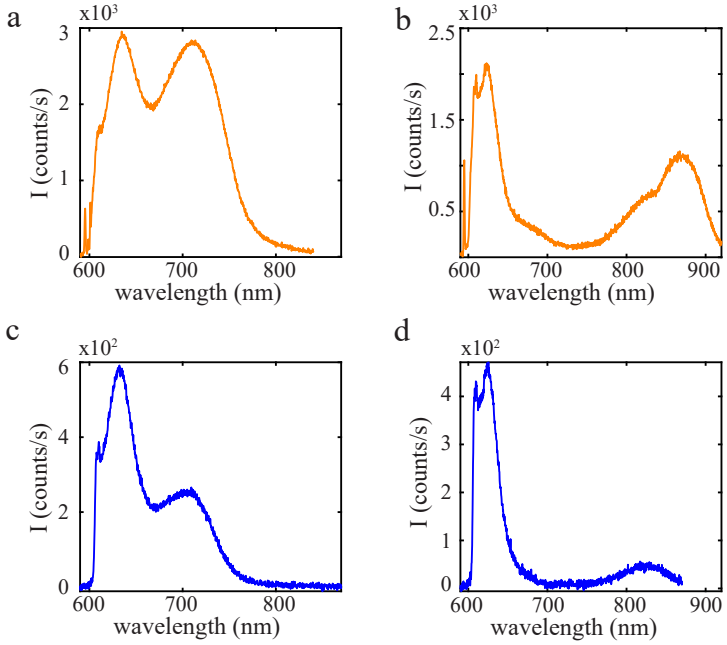

Figure 2.3: Comparing spectra oil and air objective
a-b. Spectrum of **a.** a bilayer and **b.** 6 layers of WS_2, acquired using the oil-immersion objective. **c-d.** Spectrum of **c.** a bilayer and **d.** 5 layers of WS_2, acquired using the air objective. The intensity of the emission from the direct transition is 50x larger for the oil-immersion than for the air objective. The intensity difference acquired using the oil vs. air objective is even larger for the emission from the indirect transition, namely 100x. The relatively low intensity of the indirect transition makes it less straightforward to distinguish from the background.

Even though tight focusing with objective lenses with a large NA has many advantages on the collected radiation intensity, it may have a significant disadvantage related to polarization detection. When tightly focusing circularly polarized light (essential for studying valley polarization and helicity), the spin density vector of the light will not be parallel to the beam axis anymore, and therefore the total spin angular momentum (SAM) decreases [97–99]. Figure 2.2c depicts the total SAM for oil-immersion and air objectives (calculations by T.Bauer [97]). For the air objective lens that we use, the SAM decreases to 0.70. For the oil-immersion objective this is reduced even further to 0.30. Note that for these calculations, the back focal plane of the objective lens is completely filled (the back focal planes of the oil-immersion objective and air objective are 1.9 mm and 1.35 mm respectively). When decreasing the beam size of the excitation entering the objective lens, the effective NA decreases. Figure 2.2d depicts the total SAM for both objective lenses for different beam waists of the excitation light. For incident beam waists up to 2 mm, the total SAM is above 0.80. However, as depicted in Fig.2.2e, for small beam waists the size of the diffraction limited spot on the sample does increase tremendously. Therefore we use an incident beam diameter of 1 mm for both objective lenses, as a trade-off between spin angular momentum and the size of the diffraction limited spot. Note that decreasing the beam diameter only affects the size of the excitation spot. When collecting light from the sample we still make use of the full NA of the objective lens, with the advantages of more collected radiation from a smaller spot.

2.3. TUBE LENSES AND 4F SYSTEM

In practice, we use a more extended microscopy set-up than the basic microscope presented in Fig.2.1. We use two lenses **1a** and **1b** in a telescope-like configuration to adjust the beam size to the desired diameter (see Section 2.2). To image the sample properly on the CCD camera, it is essential that the excitation light is collimated [94], for which lens **1a** and **1b** are used as well. The sample emission is collected using the objective lens at a focal distance f_1 of the sample. The first tube lens **2a** is at a distance $f_1 + f_2$ from the back focal plane of the objective, and the second tube lens **2b** is at a distance $2f_2$ from the first tube lens. The last lens **3** is at a distance $f_2 + f_3$ of lens **2b**, focusing onto the spectrometer slit or the CCD camera at the focal distance f_3.

For optimal imaging of the sample, relevant factors are the field of view, the magnification and aberrations. These factors are not only influenced by the objective lens, but also by the accompanying lenses **2a**, **2b** and **3**. Every objective lens is designed to work with a specific accompanying lens, the so-called tube lens. Using the correct tube lens in combination with the objective lens will ensure the optimal correction for spherical and chromatic aberrations. The focal distance of the tube lens, the tube length, depends on the company. For the Nikon oil-immersion objective it is 200 mm, for the Zeiss air objective it is 165 mm. Both of our objective lenses are specified to magnify the sample image by 100 times. This magnification is achieved when the correct combination of objective and tube lens is used.

Imaging an object with a lens can be described as performing a Fourier transform on the electric field generated by that object [94]. Here a sine wave coming in under normal incidence results in a delta peak in the focal plane on the optical axis, while a tilted sine

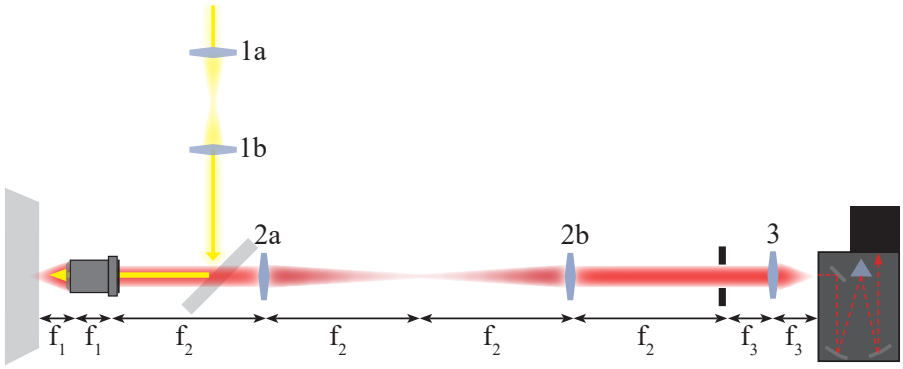

Figure 2.4: 4F system
We use a more extended microscopy set-up than the basic microscope in Fig.2.1. Lenses **1a** and **1b** are used to collimate the excitation beam and control its beam diameter. The sample emission is collected using the objective lens at focal distance f_1. The first tube lens **2a** is at a distance $f_1 + f_2$ from the back focal plane of the objective. The second tube lens **2b** is at a distance $2f_2$ from the first tube lens. In Chapter 3, we perform k-space selection at a distance f_2 after the second tube lens **2b**. The last lens **3** is at a distance $f_2 + f_3$ of lens **2b**, focusing onto the spectrometer slit or the CCD camera at the focal distance f_3.

wave leads to a delta peak slightly shifted away from the optical axis. The plane at the focal distance of the lens, called the Fourier plane, therefore contains all the angular information of the plane waves coming from the image [94]. Using two lenses as in Fig.2.1 can be described as Fourier transforming twice, where the object is imaged on a camera [94]. The camera is placed at the focal distance of the second lens, which is called the image plane. It contains all real-space, e.g., spatial information of the image. In the 4F system in Fig.2.4, the image planes are at the focus in between lens **2a** and lens **2b** and at the entrance of the spectrometer. The Fourier planes in Fig.2.4 are on the back focal plane of the objective lens and between lens **2b** and lens **3**. One of the advantages of using the 4F system is that the real-space and the reciprocal-space information of the image are fully separated and decoupled. We use this property to perform k-space selection at a distance f_2 after the second tube lens **2b** (Chapter 3). Spatial selection could be performed in the image plane between lens **2a** and **2b**. Furthermore, the use of a 4F system is also motivated by practical considerations, as the space between lens **2b** and **3** is suitable for placing optical components such as filters and polarization components.

2.4. POLARIZATION-RESOLVED MEASUREMENTS

To perform polarization-resolved measurements, the correct placement of the polarization optics is essential. Figure 2.5 depicts a more extended version of the set-up. It contains the optical components depicted in Fig.2.1 and in Fig.2.4, with an additional mirror before the lens that focusses the sample emission on the spectrometer. The positions in the set-up where we place polarization components, are marked A,B,C. As our excitation laser is not perfectly linearly polarized, we place a polarizer (Thorlabs LPVIS100-MP2) at position **A**. Throughout this thesis, we place polarization components

for three types of experiments: to control the excitation polarization state, to analyze the (position-dependent) polarization state of the generated emission, or a combination of both.

For the first type of experiment we are not interested in the polarization state of the emission, but in position-dependent intensity information, upon excitation with linearly or circularly polarized light respectively (Chapter 7, Section 7.2.2 and Chapter 3, Section 3.2.2). To excite the sample with linearly or circularly polarized light, we place a half-wave plate (Thorlabs SAHWP05M-700) or a quarter-wave plate (Thorlabs SAQWP05M-700), respectively, after the polarizer at position **A**.

In the second type of experiment we are interested in the polarization state of the emission, and therefore place polarization components in the collection path (in red). To analyze the polarization direction of linearly polarized emission, theoretically the use of a rotating polarization analyzer would be enough. However, as the spectrometer has a different response to vertically vs. horizontally polarized light, we do not use a single polarization analyzer, but a combination of a rotating half-wave plate and a fixed polarization analyzer at position **C** (Chapter 4, Section 4.2.2). In the same way we place a combination of a quarter-wave plate and a fixed polarization analyzer position at **C** to analyze the polarization handedness of circularly polarized WS_2 emission (Chapter 3, Section 3.2.3).

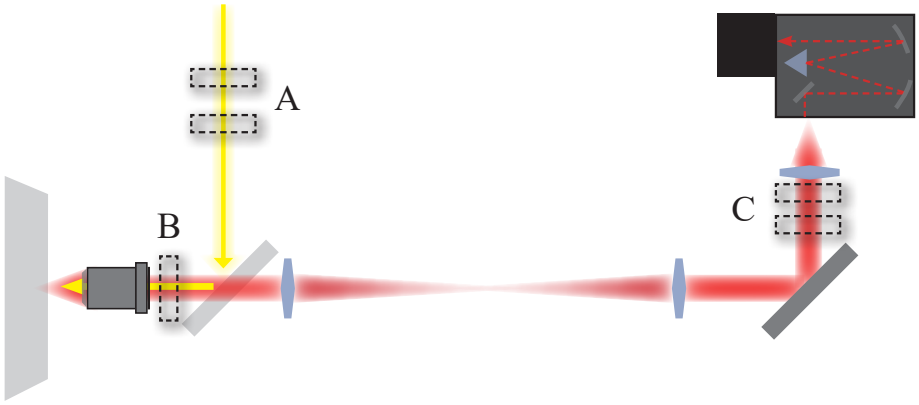

Figure 2.5: Polarization-resolved experiments
To perform polarization-resolved measurements, the placement of the polarization optics is essential. As our excitation laser is not perfectly linearly polarized, we place a polarizer at position **A** to excite our sample with vertically polarized light. To excite our sample with linearly or circularly polarized light of different polarization directions, we place a half-wave plate or a quarter-wave plate respectively after the polarizer at **A**. To analyze the polarization direction of the emission, we place a half-wave plate and analyzer at **C**. To excite the sample with circularly polarized light and analyze the resulting polarization handedness, e.g. to measure valley polarization (Chapter 3, 4) or Raman helicity (Chapter 7) we place a quarter-wave plate at **B** and a half-wave plate and polarization analyzer at **C**. For the rotating quarter-wave plate experiment (Chapter 4), we place a quarter-wave plate at **C**.

The most executed polarization experiment in this thesis is measuring the valley polarization of the WS_2 (Section 3.2.1 in Chapter 3 and Section 4.2.2 in Chapter 4). The helicity of the WS_2 Raman response (Chapter 7) is measured using the same set-up. To this end, we excite the sample with circularly polarized light and analyze the polarization handedness of the emission. Hence we place a quarter-wave plate at position **B** and a combination of a rotating half-wave plate and a fixed polarization analyzer at position **C**. Note that at position **B**, both the excitation and the emission light will pass through the same quarter-wave plate. The advantage of this over placing two quarter-wave plates in the excitation and the emission path respectively, is that the experiment becomes more versatile against misalignment and small variations in retardance between individual waveplates. Moreover, optical components such as (dicroic) mirrors and beam splitters in general respond differently to vertically than to horizontally polarized light, e.g., they reflect or transmit more intensity of one polarization than the other (see *thorlabs.com*). As a consequence, perfectly circularly polarized light will, for example, reflect from a non-perfect mirror as elliptically polarized. Therefore placing the quarter-wave plate at position **B** makes the experiment more robust against experimental imperfections, as the light is linearly and not circularly polarized in the main part of the set-up.

The described experiments to determine the polarization state of the emission provide information about either linear or circular polarization direction and handedness, but not about whether the light is partially unpolarized. To this end we perform the rotating quarter-wave plate experiment, which yields all Stokes parameters that describe the full polarization state of light (see Chapter 4, Section 4.2.3 and Appendix B). Hence, we place a rotating quarter-wave plate (Thorlabs WPQ05M-633) and a fixed polarization analyzer at position **C**.

2.5. THE CRYOSTATION

To investigate the optical response of WS_2 at cryogenic temperatures down to 4 K (Chapter 4, 6 and 7), we place our sample in a Montana cryostation S100. The cryostation contains two parts: the sample space inside of a radiation shield, and the space around it. Both spaces are pumped down to high vacuum. The sample space, containing the sample mounted on piezo positioners, is cooled down to cryogenic temperatures. The objective lens is mounted inside the cryostation, but outside of a radiation shield. This allows for the objective lens to be held at room temperature, while at the same time permitting the use of a high NA objective lens that needs to approach the sample to small working distances. The use of oil and hence an oil-immersion objective lens is not possible at cryogenic temperatures and in vacuum.

To position and focus the sample, we use six piezo positioners in total, as the use of motorized stages is not possible at cryogenic temperatures and in vacuum. The long range (5 mm) stick-slip piezo's (Attocube ANPx101RES/LT and ANPz102RES/LT) are used to position the sample with respect to the focus of the excitation laser. These piezo positioners have the long range, but their step size (50 nm) is non-reproducible. Therefore, we use the short range (60 μm) piezo's (Attocube ANSxyz100) to perform scans and characterize position-dependent optical features of WS_2 (see Chapter 4, 6 and 7). These piezo positioners have a sub-nanometer step size. It is important to note however, that there

is a cross coupling between the y and the x axis of these piezo positioners: when moving in the y direction, the sample also moves partially in the x direction. This can be noted when comparing the microscope and SEM images of the nanostructures with the scans of the photoluminescence and Raman response.

3

COUPLING THE VALLEY PSEUDOSPIN TO THE TRANSVERSE OPTICAL SPIN

How can you use the optical spin of guided modes in a nanowire to address and read out the valley pseudospin state of WS_2?

Parts of this chapter have been published in [93], copyright 2021 American Chemical Society.
Data acquired for this publication can be found at DOI: 10.4121/uuid:b45aadad-6687-40f2-8e60-fc1c2e583fdc
Parts of this chapter are based on [40].

3.1. INTRODUCTION

As described in Section 1.5.2 of the Introduction, the valley-dependent optical selection rules of 2D-TMDs provide easy access to their valley pseudospin using circularly polarized light [76–79]. The chirality of their interaction with light opens the way for applications in for instance photonic transistors [100, 101]. Moreover, analogous to spin in spintronics, the valley pseudospin can be used as a promising qubit candidate to encode and process information in the field of valleytronics [78, 102, 103].

For practical applications, on-chip access to and manipulation of valley pseudospins is paramount. In the context of information storage, it needs to be possible to both read out and to set up the valley pseudospin state. There have been several on-chip experimental demonstrations of such a spin-dependent directional emission [104], using a plasmonic resonator [105] or a metasurface [106, 107]. In this chapter, we describe two experiments involving the manipulation of the valley pseudospin. In the first experiment, we experimentally demonstrate the on-chip optical read out of the valley pseudospin state using the transverse optical spin of a metal nanowire. Note that the method and analysis used in this experiment are the same as previously described in [40], but the data presented in this chapter are original. Reading out the spin state is done by deterministically controlling the TMDs emission of each state in different directions. Thus, the direction of the emitted photons reflects the originating spin/valley state.

For the realization of a chiral spin-photon interface, not only spin read-out but also spin addressing or transport via chiral spin-photon interaction should be demonstrated, but this still remains challenging. In the second experiment, reproduced from [93], we again exploit the valley pseudospins in TMDs layers and the optical spin-orbit coupling near a nanowire waveguide. We demonstrate local propagation-dependent, selective valley addressing with near-field light. Combining addressing and read-out of the valley pseudospin, real on-chip valleytronic devices with 2D TMDs come one step closer.

3.1.1. TRANSVERSE OPTICAL SPIN

In this chapter, we exploit the so-called spin orbit interaction of light. In traditional free-space electromagnetic waves, the spatial and polarization degrees of freedom of light can be treated independently [108]. However, in some cases this treatment does not hold, for instance when a circularly polarized beam is reflected, refracted or focused (see Chapter 2, Section 2.2), or when an optical mode propagates along a surface or in a waveguide. The polarization of light in the described situations, affects its spatial degrees of freedom like intensity and propagation path [108]. Figure 3.1a presents schematically light guided in a wire (in grey). The electric field of the light in the wire (in green) not only possesses a transverse component along y, like a free-space wave, but also a longitudinal component along the propagation direction z. This longitudinal component is evanescent [95], decaying exponentially in the y direction, and typically in quadrature with the transverse component. The combination of the longitudinal and transverse electric fields therefore yield an electric field angular momentum in the plane of propagation (in yellow) [108, 109]. Note that free-space circularly polarized light is also spinning, but around the propagation direction, e.g., it exhibits a longitudinal optical spin, whereas this waveguide mode exhibits a transverse optical spin (in red). From the sketch

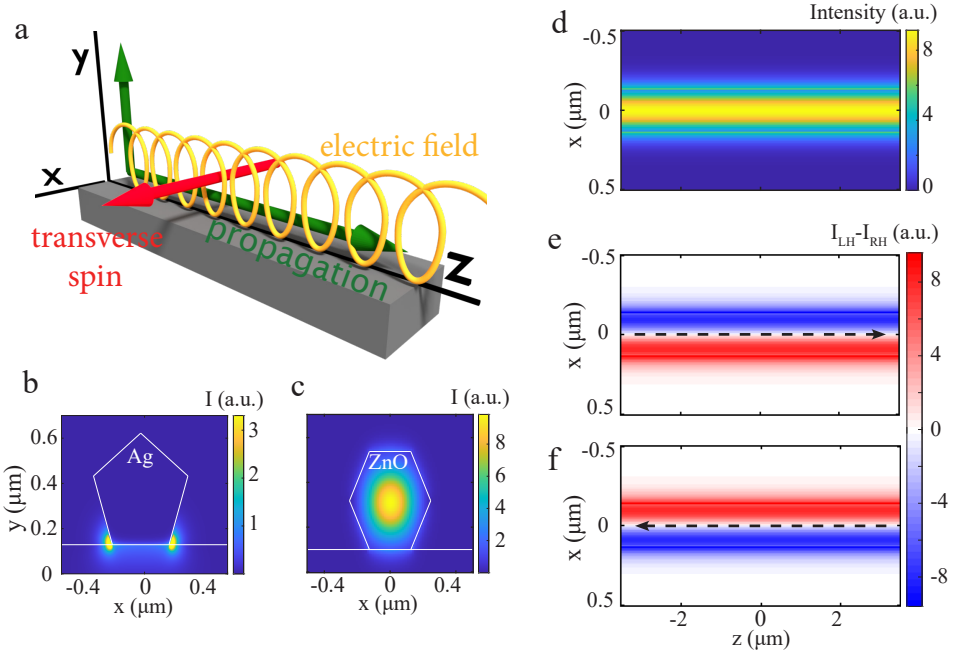

Figure 3.1: Transverse optical spin of a nanowire
a. Schematic representation of light propagating through a wire (in grey). The field in the wire has both a transverse component (in green, along y) and an evanescent and longitudinal component (in green, along z), which is $\pi/2$ out of phase with the transverse component. This leads to a transverse spin angular momentum (in red), making the electric field spin in the plane of propagation (in yellow) (see also [108]). **b.** Calculated highly confined plasmonic guided mode in an Ag nanowire (reproduced with permission from [40]). **c.** Calculated optical guided mode in a ZnO nanowire (see Fig.A.2 in Appendix A). **d.** Calculated intensity distribution of a guided ZnO nanowire mode in the plane of the WS_2 flake, i.e., between the nanowire and the glass substrate. **e-f.** Calculated spin density of this optical mode, propagating in the direction of the arrow. The blue and red colours indicate a clockwise and counter-clockwise rotating electric field, respectively. The spin-orbit interaction in the nanowire results in a one-to-one relation between the local handedness (sign) of the optical spin angular momentum locked with the propagation direction.

in Fig.3.1a it becomes apparent that reversal of the propagation direction of the guided light will flip the sign of the transverse spin. In other words, light with a transverse optical spin exhibits spin-momentum locking. This spin-orbit coupling of light has been used to steer light deterministically [110–113]. Furthermore, when transverse optical spin couples to an emitter with spin angular momentum, the interaction becomes chiral: the local light-matter interaction depends on the propagation direction of the relevant light modes [40, 110, 114–116].

In this chapter, we use a nanowire as a waveguide, silver for the first experiment and ZnO for the second. The advantages for using each kind of nanowire are described in Section 3.2.1. Fig.3.1b depicts the calculated plasmonic guided mode in an Ag nanowire (reproduced with permission from [40]). In this metal nanowire, the guided mode is confined to the lower wire corners at the interface between the nanowire and the glass substrate. Fig.3.1c depicts a calculated optical guided mode in a ZnO nanowire (see also Appendix A, Section A.1.2). Even though the specific guided modes in the Ag and the ZnO nanowires are completely different in terms of electric field distribution, the guided modes in both wires exhibit a transverse spin angular momentum that is locked with the propagation direction of light.

To clarify the situation, Fig.3.1d presents the simulated intensity distribution of the relevant guided optical mode for the plane between a dielectric waveguide and a glass substrate. The intensity is highest in the center of the nanowire, and diminishes to the sides. Fig.3.1e depicts the calculated spin handedness of this optical mode using the non-normalized Stokes parameter $S_3 = I_{LH} - I_{RH}$ (arrow depicts propagation direction), where I_{LH} and I_{RH} are the left-handed and right-handed circularly polarized emission respectively . For x < 0, the handedness of the transverse optical spin is clockwise (blue colour), whereas at the lower part of the picture near the nanowire, for x > 0, the handedness is anti-clockwise (red colour). Because of time-reversal symmetry, changing the propagation direction in the nanowire results in a reversal of all local rotation of electric fields (see Fig.3.1f). In short, the handedness of the local transverse optical spin is locked with the propagation direction of light. The same spin-orbit locking holds true for the modes of the Ag nanowire. The simulated intensity distribution and the spin handedness around the Ag nanowire can be found in [40].

3.1.2. EXPERIMENTAL SCHEME

Figure 3.2 presents an overview of our experimental schemes. In both the experiments of reading out and of initiating the valley pseudospin, we place a nanowire (in grey) on top of few-layer WS_2 (in green). In the first experiment, summarized in Fig.3.2a, we locally excite excitons in a specific WS_2 valley, for instance the K valley (see Fig.1.7a in Section 1.5.2) using circularly polarized excitation. The subsequent circularly polarized WS_2 photoluminescence (PL) is emitted partially into free space and partially into the guided mode of the wire. It is important to note that the excitation light cannot couple directly to the guided nanowire mode due to the large k-vector mismatch. Through the near-field, the WS_2 can however emit into the guided mode of the wire [117]. As the handedness of the local transverse optical spin of the wire mode is locked with the propagation direction of light, the polarized WS_2 emission will propagate through the wire in

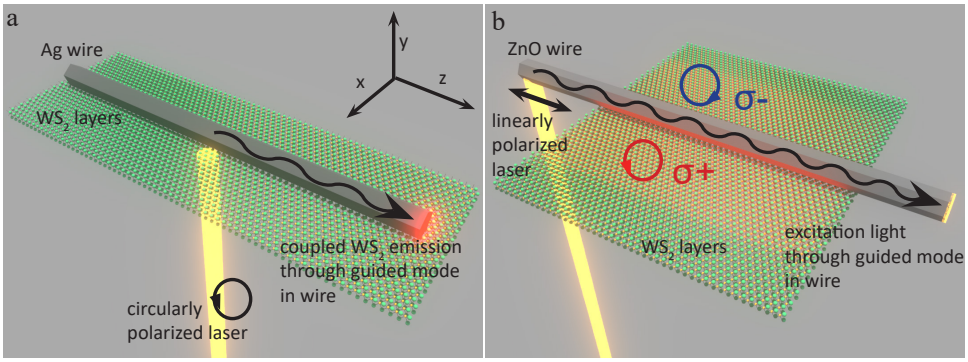

Figure 3.2: Coupling the transverse optical spin of guided modes in a nanowire to local valley pseudospins in WS_2 layers and vice versa
a-b. Sketch of the sample, with a nanowire on top of few-layer WS_2. **a.** Valley-polarized excitons in WS_2 are excited using a circularly polarized laser beam. The light is emitted into the optical nanowire mode, the transverse optical spin of which has the same handedness. Subsequently, the directional emission scatters from the ends of the wire (lighting up in red). **b.** A laser beam launches an optical waveguide mode in the nanowire. Through their transverse optical spin these modes locally excite the WS_2 valley-pseudospins (lighting up in red in the WS_2).

a specific direction (arrow in Fig.3.2a), subsequently scattering from the right end of the wire (lighting up in red in Fig.3.2a).

This system can be used to read out the local valley pseudospin of the WS_2 in the following way. In the case depicted in Fig.3.2a where the WS_2 is excited at $x > 0$, the emission from the right end of the nanowire is caused by the coupling of σ_+ emission from the K valley of the WS_2. Changing the handedness of the excitation light will excite the K' valley of the WS_2, that in turn will emit σ_- light into the guided nanowire mode. As the handedness of the transverse optical spin of the guided mode of the nanowire is locked with the propagation direction of the light in the wire, σ_- emission from the WS_2 will couple to the nanowire mode propagating to the left end. Therefore the directional emission from the nanowire reflects the original spin/valley state of the excited WS_2. Naturally, the system is symmetric around the nanowire (see Fig.3.1d,e). Therefore, addressing the WS_2 on the other side of the nanowire ($x < 0$) will result in σ_+ and σ_- emission to couple to the guided nanowire mode propagating to the left and to the right direction, respectively.

An overview of the experimental scheme for the second experiment is presented in Fig.3.2b, where a laser beam is focused at the nanowire end to launch guided modes in one direction. In this case, the k-vector mismatch between the excitation light and the guided nanowire mode is overcome by the breaking of the translational symmetry at the end of the wire, this allowing light scattering at the end of the wire into the mode. Subsequently, the propagating waveguide mode will have a transverse optical spin in its near-field, which will selectively excite specific valley pseudospins in the WS_2 flake. This local excitation will yield reradiating photons through spontaneous emission, depicted in Fig.3.2b by the red shading of the WS_2 on both sides of the nanowire. Please note that

we collect the emitted light in the far field on the glass side (see Chapter 2 for a description of our experimental set-up.) Exciting the nanowire on the right end will result in the opposite propagation direction of the light in the wire. Due to spin-momentum locking of the transverse optical spin, the opposite propagation direction enables us to flip the valley pseudospins (compare Fig.3.1d,e).

3.2. RESULTS AND DISCUSSION

3.2.1. WS_2 AND WIRE SAMPLES

For the first experiment we use chemically grown metal nanowires with a pentagonal cross-section [40, 118]. The advantage of metal nanowires is the relatively high coupling efficiency between the TMDs' emission and the guided wire mode, due to the high local density of states [117]. In our experiment, a single Ag nanowire is located on top of a WS_2 flake with approximately 5 layers, as depicted in the optical image in Fig.3.4a-c. At room temperature the use of a multilayer WS_2 flake is preferred over a monolayer, since the multilayer exhibits a much higher degree of valley polarization due to spin-layer locking effects (see Introduction, Section 1.5.2). Fig.3.3 depicts photoluminescence spectra from the used WS_2 flake, measured without the Ag nanowire. We use the WS_2 PL from the exciton (at 630 nm) that is associated to the direct bandgap. From the spectral position of the indirect bandgap (at 870 nm) we determine the number of layers of the flake. However, as described in Section 1.4.1 of the Introduction, the spectral differences between WS_2 flakes with four or more layers are smaller than for instance between a monolayer, bilayer and trilayer of WS_2. Therefore the thickness of 5 layers for this WS_2 flake is an estimation. We determine a degree of valley polarization of 0.70 from the difference in the σ_+ (in red) and σ_- (in blue) emission, after exciting the WS_2 with σ_+ light (see Section 1.5.2).

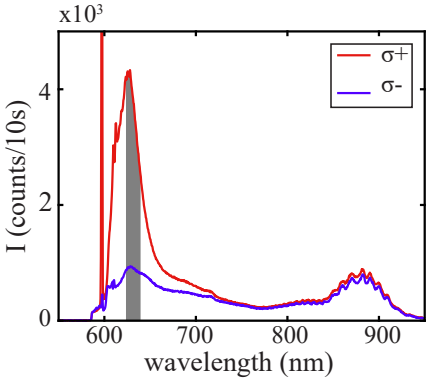

Figure 3.3: WS_2 spectra
Photoluminescence of the WS_2 flake in Fig.3.4a, measured without the Ag nanowire. The grey area depicts the spectral region of the excitonic photoluminescence that is used in our experiment. The spectral position of the indirect bandgap emission indicates the number of WS_2 layers, namely 5 (see Section 1.4.1). The WS_2 is excited with σ_+ light, and from the difference in the σ_+ and σ_- emission, we determine a degree of valley polarization of 0.70 (see Section 1.5.2).

For the second experiment, we use chemically synthesized ZnO nanowires with a hexagonal cross-section, commercially available from the company ACS Materials. A single ZnO nanowire of radius 254 nm is located on top of a WS_2 flake with approximately 5 layers, as depicted in the optical image in Fig.3.5a (for an AFM image of the ZnO nanowire, see Appendix A, Fig.A.6a,b). The spectra of the used WS_2 flake are similar to the one in Fig.3.3a (see [93]). This WS_2 flake also has approximately 5 layers and a valley polarization of 0.70.

There are several reasons to use dielectric waveguides [119] for the second experiment. For the first experiment, the high coupling efficiency of the TMDs' emission to the guided nanowire mode is important. For the second experiment however, the influence of the nanowire on the TMDs' radiation efficiency is more relevant. Both a metal and a dielectric waveguide will modify the radiation properties of excitons, such that much of the exciton emission couples to the waveguide again. This results in a weak free-space radiation signal. In addition, the proximity of a nanowire will affect the polarization properties of the radiated field [120]. In practice, this means that emission from a perfect circular dipole would result in a reduced magnitude of S3 collected in the far field. Our simulations show that dielectric waveguides have less influence than plasmonic waveguides on the intensity and especially on the polarization of the collected light (see Appendix A, Section A.1.1 and Fig.A.1 for details). Therefore, the lower coupling efficiency back to the dielectric waveguide modes as compared to a metal waveguide, will enable us to observe direct radiation from the addressed excitons. Moreover, dielectric waveguides also have a lower propagation loss.

3.2.2. EXPERIMENT 1: READ OUT OF THE VALLEY PSEUDOSPIN

We initiate a valley pseudospin by focusing a circularly polarized 594 nm excitation beam on the WS_2 flake next to the Ag nanowire. The yellow circle in Fig.3.4a-c depicts schematically the position of the excitation spot with respect to the nanowire: $x < 0$, $x=0$ and $x > 0$. Using optical filters, we remove the excitation light in order to investigate only the exciton photoluminescence of the WS_2 (see grey area in Fig.3.3) and its interaction with the nanowire. Fig.3.4d-f,k-m presents microscopy images of the WS_2 exciton PL. The bright region in the middle of the images is the PL that propagates from the WS_2 directly into the far field and our microscope camera. The small dots on either side of the bright middle region are the result of exciton PL that is emitted into the guided mode of the nanowire, propagates through the wire and is scattered from either of its ends (see also [117]).

Figures 3.4e,l present a microscopy image of the exciton emission upon excitation on the very middle of the nanowire, at x=0 and z=0 (compare Fig.3.4b). The WS_2 exciton emission coupled to the guided nanowire mode propagates through the wire until it reaches the wire ends, where it is scattered to the far field and imaged on our microscope camera. From the intensity crosscuts at the position of the nanowire in Fig.3.4h,o it becomes apparent that the intensity of the emission propagating in opposite directions in the nanowire is the same. Figure 3.4d depicts the PL intensity and the intensity crosscut when exciting the WS_2 on the $x < 0$ side of the nanowire with σ_+ polarization. From the crosscut in Fig.3.4g it becomes apparent that the intensity of the emission propagating to

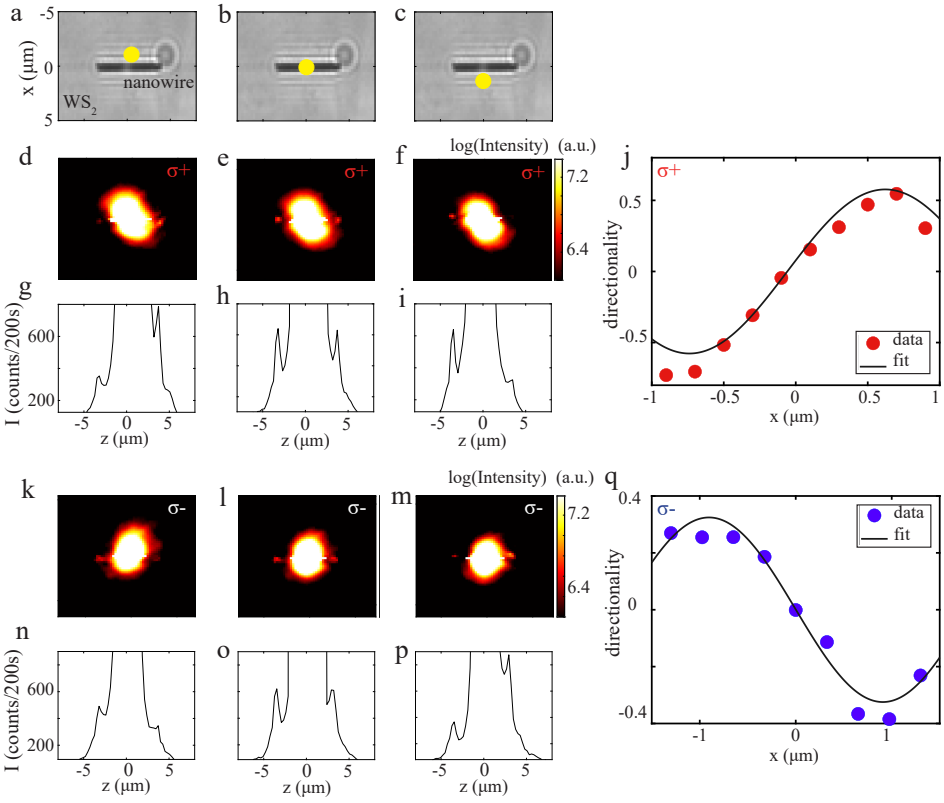

Figure 3.4: Reading out the WS_2 valley pseudospin

Data are acquired and analyzed with permission using the same method as [40].

a-c. Optical microscopy image of the WS_2 sample (light grey) with the Ag nanowire (black). The yellow circle indicates the position of the excitation spot in **d-f.** WS_2 photoluminescence upon σ_+ excitation and **k-m.** upon σ_- excitation. When exciting the WS_2 close to the nanowire, a large part of the PL scatters from the nanowire and couples to the far field directly (high intensity region in the middle), and part of the WS_2 emission is coupled to the guided mode of the nanowire and scatters from both one or the other wire end. **g-i,n-p.** Crosscuts of the PL intensity at the position of the nanowire allow for a comparison of the intensity from the left and the right end of the wire. When exciting in the middle of the nanowire in **e,l**, the intensity of the emission scattering from both ends of the wire is the same (compare the intensity crosscuts in **h,o**). However, when exciting either on the x < 0 or the x > 0 side of the nanowire (see **a,c**) with σ_+ polarization, in **d,g** most of the light scatters from the right end of the wire and in **f,i** most of the light scatters from the left end. The situation is inverse when using σ_- excitation: in **k,n** most of the light scatters from the left end of the wire, and in **m,p**, most of the light scatters from the right end. **j,q.** Experimentally determined directionality $D = \frac{I_{wireL} - I_{wireR}}{I_{wireL} + I_{wireR}}$ as a function of distance from the nanowire, upon **j** σ_+ and **q** σ_- excitation, where the line is a sine fit as a guide to the eye.

the right end of the wire is higher than to the left end. When the excitation spot is moved to the other side of the nanowire, *i.e.*, to x > 0 in Fig.3.4f,i, more emission propagates to the left than to the right end of the wire. Therefore, the directionality of the emission can already be distinguished from the raw PL images. We define the directionality of the emission coupled to the nanowire as $D = \frac{I_{wireL} - I_{wireR}}{I_{wireL} + I_{wireR}}$, with I_{wireL} and I_{wireR} the maximum intensity from the left and right wire ends. Figure 3.4j depicts the directionality of the emission upon σ_+ polarization as a function of distance x from the nanowire. When exciting at the x < 0 side of the nanowire, the directionality is around -0.70, and at the x > 0 side it is around 0.50.

Fig.3.4k,n depicts the PL intensity and the intensity crosscut when exciting the WS_2 at the x < 0 side of the nanowire with σ_- polarization, exciting the K' instead of the K valley of the WS_2. In this case, the intensity is higher on the left than on the right end of the wire, e.g., the opposite of Fig.3.4d,g. When exciting at the x > 0 side of the wire with the same σ_- polarization, the intensity is higher on the right than on the left end of the wire (Fig.3.4m,p). Figure 3.4q depicts the directionality of the emission upon σ_- polarization as a function of distance from the nanowire. Now when exciting at the x < 0 side of the nanowire the directionality is around 0.30, and at the x > 0 side it is around -0.40.

The directionality of the emission leads us to conclude that the valley pseudospin of the WS_2 is coupled to the transverse optical spin of the Ag nanowire, where the direction of the emission guided through the wire reflects the originating spin state. In Fig.3.4j,q, the value of the directionality is not exactly the same for all four cases of exciting at different sides of the wire and coupling different WS_2 valley pseudospins to the wire mode, as would be expected. We attribute this asymmetry in the directionality values to experimental imperfections, such as the experimental challenge of determining the exact middle of the nanowire and (both at x=0 and z=0) and therefore breaking the symmetries of the system. When the nanowire is excited at another position than x=0, the WS_2 emission propagates more the left or the right of the nanowire, as described above. When the nanowires is excited at another position than z=0, light in the guided nanowire mode will have to propagate a smaller distance and therefore will be absorbed less, leading to a higher intensity on one side of the nanowire. As described in [40], there are several reasons for the directionality not to reach the value of 1.0. The first reason is the WS_2 valley polarization of 0.70 that dictates a theoretical maximum on the directionality. A value of 0.70 for the valley polarization means that, even though the WS_2 is excited with circularly polarized light with a specific polarization handedness, only part of the emission originates from the excited valley and exhibits the polarization handedness of the excitation. The part of the emission with opposite handedness, propagates in the opposite direction through the wire and therefore reduces the total directionality. The second reason is the finite size of the diffraction limited excitation spot: the laser beam does not excite a single spot of WS_2, but a small region (see [40]). Therefore the intensity on both nanowire ends is a result of the convolution of the near-field transverse optical spin of the guided nanowire mode, and the size of the excitation spot. The same factors will be relevant in the second experiment of this chapter, and will be discussed in more detail in Section 3.2.4.

3.2.3. EXPERIMENT 2: LOCAL INITIATION OF THE VALLEY PSEUDOSPIN

We launch optical waveguide modes by shining a linearly polarized 594 nm excitation on the ZnO nanowire end. To investigate the WS_2 excitons excited via the transverse optical spin of the ZnO nanowire modes, free-space radiation of the excitons is collected and imaged on a CCD camera (see Chapter 2, Section 2.4). Excitation light and light scattered from the nanowire end is filtered out using optical filters (see Chapter 2), so only photoluminescence is visible on the CCD camera. We want to measure the WS_2 emission, excited using ZnO wire modes that have transverse optical spin, but to avoid measuring light coming from leaky optical modes in the ZnO wire directly. Therefore we place an aperture at the Fourier plane of the optical setup, that reduces the numerical aperture of our detection system to 0.75 (for images with the full NA of 1.45 see Appendix A, Section A.2.3 and Fig.A.6). The degree of circular polarization of the emitted light is measured using standard quarter waveplate projection (see Chapter 2, Section 2.4).

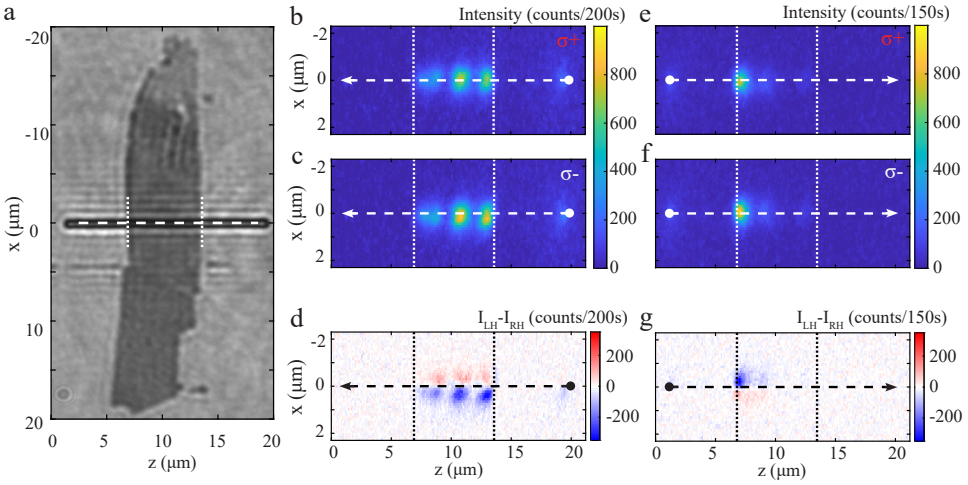

Figure 3.5: Initiation of the local WS_2 valley pseudospin
a. Optical image of the WS_2 sample with the ZnO nanowire. The dotted lines coincide with the lines in **b-g**, indicating the centre of the ZnO nanowire and the position of the WS_2 flake. **b,c,e,f.** Left (right) handed circularly polarized part of WS_2 photoluminescence (the arrow points in the propagation direction of the light in the nanowire). The emission intensity is not uniform along the nanowire, but exhibits maxima and minima indicating mode interference. **d,g.** By subtracting intensities in **c** and **b**, we determine the effective polarization handedness of the luminescence near the nanowire. The degree of circular polarization shows non-zero values at the positions of high intensity. In **d** the upper part of the picture for $x < 0$ has a positive handedness (red colour) and the lower part for $x > 0$ has a negative handedness (blue colour). In **g**, these values are exactly flipped. We conclude that opposite WS_2 valley pseudospins are emitting at opposite sides of the nanowire. The handedness is as expected from the transverse optical spin of the ZnO nanowire modes (see Fig.3.1d,e). Therefore, opposite valley pseudospins are addressed selectively by the near-field of the ZnO nanowire modes.

Figures 3.5b-c,e-f present PL images at the exciton wavelength (620-630 nm, grey region in Fig.3.3) on the WS_2 flake in Fig.3.5a. Focusing laser light at the right end of the nanowire, i.e. launching the waveguide modes propagating in the direction of the arrow, left- and right-handed circularly polarized emission is selectively detected as shown in Fig.3.5b and 3.5c respectively. Bright emission can be clearly seen along the nanowire,

coming only from the region of the WS_2 flake (see the dotted lines in Fig.3.5a), indicating that all emission comes from WS_2. The emission intensity is not constant along the nanowire, exhibiting maxima and minima, indicating mode interference (see below). We conclude that we have excited the WS_2 at both sides along the ZnO nanowire, using the near field of the ZnO nanowire modes. When exciting the nanowire at the left end (Fig.3.5e,f) and thus changing the propagation direction of the light, left- and right-handed circularly polarized emission are again selectively detected as shown in Fig.3.5e and f. Note the strength of the exciton photoluminescence, indicating the cleanliness of the interface between nanowire and WS_2.

To investigate the spatial distribution of the spin density even further, we subtract the intensity of the left-handed photoluminescence from the right-handed. Note that we do not normalize the subtracted intensities, as would be the case for calculating the normalized S3 Stokes parameter. This procedure is chosen to avoid noise to dominate the figure in the low-signal-intensity regions. The normalized S3, experimentally determined close to the nanowire (for $-1.5\mu m < x < 1.5\mu m$) has values between -0.3 and +0.3 (see Appendix A, Section A.2.1 Fig.A.4). Fig.3.5d demonstrates the handedness of the collected light at the three positions of maxima intensity. On the upper (x > 0) and lower (x < 0) side of the wire the handedness has a positive (red colour) and negative value (blue colour), respectively. These opposite handednesses on either side of the waveguide are only visible in the presence of WS_2. Away from the waveguide $I_{LH} - I_{RH}$ is roughly zero. When flipping the propagation direction in Fig.3.5g, we observe a similar effect. Now, however, the handedness at each position has flipped sign: it is negative (blue) and positive (red) above and below the wire, respectively. When comparing this to the calculated transverse optical spin of the ZnO nanowire in Fig.3.1d-e, we note that the sign of the spin density matches for both propagation directions in the nanowire: the WS_2 excitons emit light from the two valleys with a sign corresponding to the local transverse optical spin of the nanowire. Where the transverse spin has a positive handedness, WS_2 excitons from the K valley emit σ_+ light, and at negative handedness excitons from the K' valley emit σ_-. As a control experiment, we collected emission from the indirect bandgap (see Appendix A, Fig.A.5), which did not exhibit any non-zero spin density, as expected since this bandgap is not spin polarized. Therefore we conclude that we have selectively and controllably addressed WS_2 excitons in their K and K' valleys through the transverse spin of the ZnO nanowire modes.

3.2.4. SIMULATION RESULTS

To estimate the efficiency of the valley-selective excitation of our system of the second experiment, we theoretically modelled the experimental situation. The first thing that catches the eye when comparing Fig.3.1c and our measured PL images Fig.3.5, is an interference pattern in the detected PL. ZnO nanowires with a radius 594 nm support several guided modes, in addition to a number of leaky modes[121]. Using the finite element method (FEM), we identified two modes, whose combination of propagation constants explains the observed beat length (see Section A.1.4). The interference pattern in the mode intensity is reflected in the spatial distribution of the exciton population.

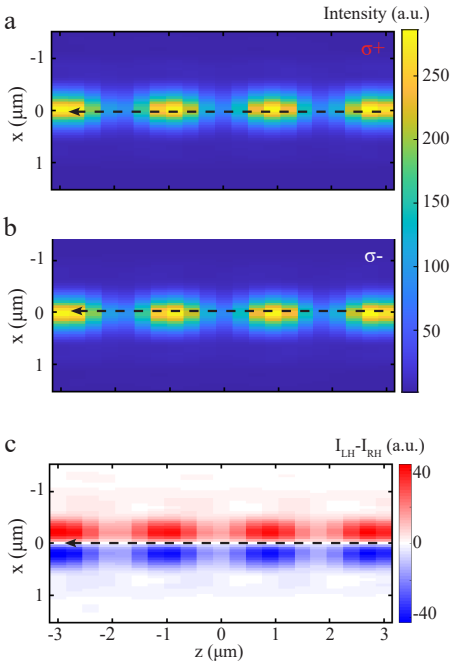

Figure 3.6: Simulation results of the polarization-dependent exciton emission near a ZnO nanowire. **a,b.** Simulation of the photoluminescence of excitons with left (right) handed circular polarization near a 254nm radius ZnO nanowire. Exploiting the reciprocity of light, we model in FDTD simulation the collection through a diffraction-limited system with an effective NA of 0.75, by focusing a circularly polarized Gaussian light source on a ZnO nanowire. The results are convoluted with the calculated near-field intensity distribution of the mode beating pattern. **c.** Degree of circular polarization, $I_{LH} - I_{RH}$, the non-normalized S3 of the exciton emission of the modes in the nanowire. For x < 0, the upper part of the nanowire, the handedness has positive values (red colour), and in the lower part it has negative values (blue colour). The local sign of the handedness is the same as in the measurements in Fig.3.5d.

In our model, we take into account both the finite numerical aperture (NA) of the detection optics and the 0.70 valley polarization of WS_2. Detailed information of the modelling is discussed in Appendix A, Section A.1.5. Fig.3.6a and 3.6b depict the modelled right-handed and left-handed circularly polarized emission distributions near a ZnO nanowire with radius 254 nm at the position of the WS_2 on the glass substrate, where the arrows indicate the propagation direction in the nanowire. The emission intensity is maximum around the center of the nanowire and is beating along the nanowire. Figure 3.6c represents the calculated spin density around the nanowire, demonstrating how the beating phenomena affects the transverse optical spin. It is important to note that all different waveguide modes propagating in the same direction contribute to the same handedness of the optical spin in the region of evanescent fields as a result of the nature of optical spin-orbit coupling (see Appendix A, Section A.1.2 and A.1.3, Fig.A.2 and Fig.A.3). The mode beating results in a different intensity distribution along the nanowire, while having the same handedness and thus exciting the same WS_2 valleys regardless of their position. The normalized S3 close to the nanowire has values between -0.30 and +0.30.

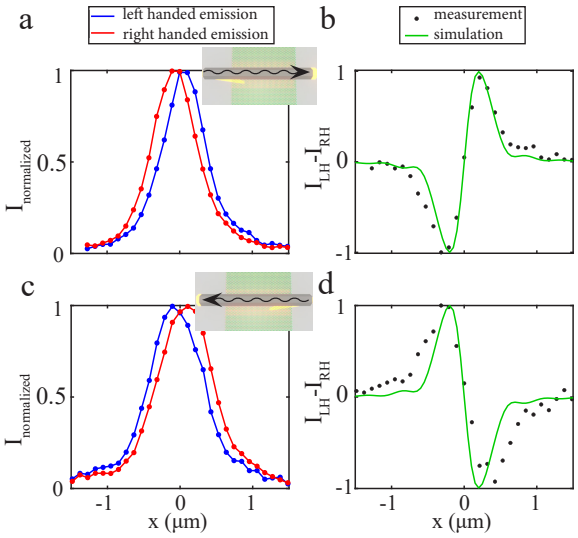

Figure 3.7: Normalized crosscuts of left- and right-handed WS_2 emission and the resulting spin density $I_{LH} - I_{RH}$ in both experiment and simulation.
a,c. Crosscuts of the experimentally measured left (in blue) and right (in red) handed part of the WS_2 emission shown in Fig.3.5b-c (e-f). The position of the emission is not perfectly in the middle of the ZnO nanowire (at x = 0), but is slightly shifted from the axis of symmetry. In **a** the right-handed emission (red colour) is shifted to the left of the ZnO nanowire and the left-handed emission (blue colour) is shifted to the right. Changing the propagation direction, indicated by the insets, flips the handedness of the emission in **c**. **b,d.** Crosscuts of $I_{LH} - I_{RH}$ from Fig.3.5d,g (black dots) compared with the calculated $I_{LH} - I_{RH}$ from Fig.3.6c (in red). The plots are normalized for easy comparison. The simulation results reproduce the experimental results very well qualitatively (for a quantitative comparison of the normalized S3, see Section A.2.1 Fig.A.4).

It is clear that our simulation results presented in Fig.3.6 qualitatively reproduce our experimental results in Fig.3.5. To take a closer look while accounting for the beating pattern, crosscut profiles of Fig.3.5b-c and 3.5e-f at the position of highest intensity are shown in Fig.3.7a and 3.7c. The position of the right-handed and the left-handed parts of the WS_2 emission is not perfectly on the middle of the ZnO nanowire, but is slightly shifted from the axis of symmetry. The same can be observed qualitatively in simulation. In Fig.3.7b and 3.7d crosscuts of the handedness are presented from Fig.3.5d and 3.5g and 3.6c. The plots are normalized for easy comparison. The normalized S3 in both experiment and simulation has values ranging from -0.3 to +0.3 close to the waveguide, which is enough to distinguish the different polarization handedness at both sides of the nanowire already in the raw experimental data (see Section A.2.1 in Fig.A.4). No free parameters are required to achieve good quantitative agreement with the experiment for both propagation directions, but parameters such as degree of valley polarization, size of the nanowire and relevant nanowire modes are confirmed by independent measurements. The modes that are most likely to cause the experimental measured beating pattern are selected based on the beating features in the data (see Section A.1.4). Taking into account the valley polarization and the effect of diffraction-limited collection, we conclude that the ZnO nanowire guided modes excited the valley pseudospins in WS_2 with a near-unity selectivity. The lower measured value of S3 is caused mainly by the diffraction limit of our detection system (see Chapter 2, Section 2.2) and the presence of the nanowire.

3.3. CONCLUSION

We demonstrated the on-chip read out and local initiation of specific valley pseudospins in multilayer WS_2 with near-unity selectivity by exploiting the chiral photon-valley interaction mediated by the transverse optical spin of propagating waveguide modes. The created valley polarization was quantified from the optical spin of the emission of the excitons collected in the far-field. As transverse optical spin and spin-momentum locking is a universal property of guided light other waveguide materials can be chosen in the future to tailor the amount of far-field radiations to the desired device characteristics. This proof-of-concept combines addressability of valley pseudospin with the previously established on-chip optical read-out. Together they can form the basis for on-chip integration of valleytronics and photonics.

4

VALLEY POLARIZATION AND VALLEY COHERENCE OF WS_2 MONOLAYER FLAKES

What does the polarization of the WS_2 photoluminescence emission reveal about the interaction, hopping and coherence of electrons and excitons in its valleys?

Data acquired for this chapter can be found at DOI: 10.4121/14406938

4.1. INTRODUCTION

Section 1.3.2 of the Introduction describes how 2D TMD layers can be fabricated by chemical vapor deposition (CVD). Interestingly, the photoluminescence (PL) intensity of CVD grown single layered TMDs (monolayers) is non-uniform across the flakes [122–129]. Many explanations have been proposed to explain the non-uniformity in the PL intensity, including growth conditions [123, 124], differences in defect density [123, 129, 130], variations in chemical composition [122, 126], grain boundaries [125], variations in strain [127] and variations in electron doping [131]. The chiral optical selection rules and the resulting valley pseudospin are a fundamental aspect of the electronic bandstructure of TMDs materials, and a key feature for potential applications. Therefore, investigating the interaction of the TMDs valleys with polarized light will clarify the processes that result in the inhomogeneous PL intensity.

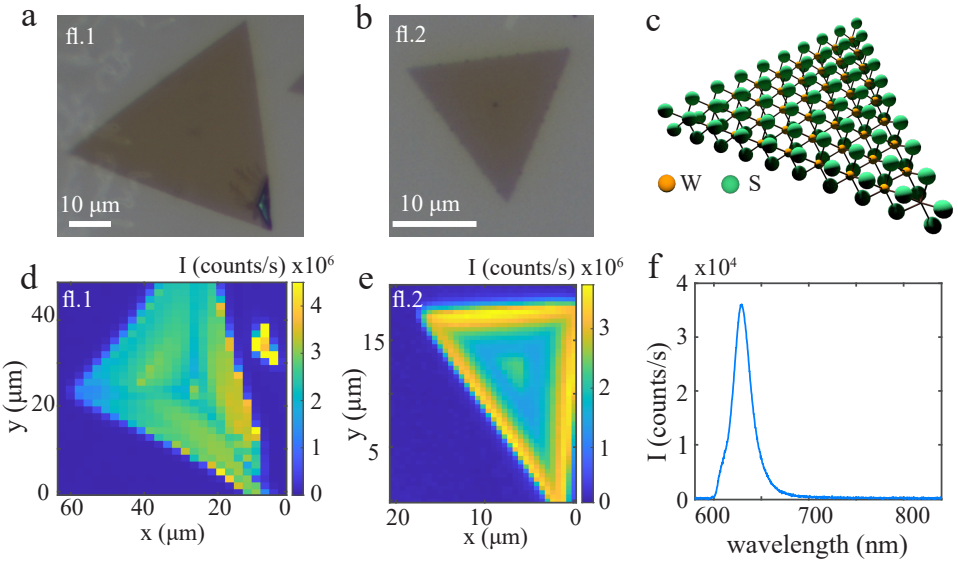

Figure 4.1: WS_2 monolayer flakes
a-b. Optical (wide-field) images of CVD grown WS_2 monolayer flakes. The scans have pixel sizes of 2 and 0.5 μm, and the flake sizes are 55 and 20μm (see the scalebar). **c.** Schematic representation of a triangular WS_2 monolayer flake, depicting the atomic hexagonal structure that induces the growth in a triangular geometry. **d-e.** Raster scan of the non-uniform photoluminescence (PL) intensity over two monolayer flakes. Flake 1 exhibits lower intensity along the triangle medians, dividing the flakes into three regions with higher intensity. Flake 2 exhibit higher intensity along the edges. Note that the x and y axis in the raster scan are slightly skewed due to experimental constraints (see Appendix B, Section B.3) **f.** Representative PL spectrum from WS_2 monolayer flake 1, acquired at room temperature. The high intensity and absence of indirect bandgap emission demonstrates that this is a monolayer and not a multilayer.

Two relevant keywords in the polarization behaviour of the TMDs' photoluminescence are valley polarization and valley coherence. For valleytronics applications, it is paramount to generate a large asymmetric occupation of electrons in the two inequivalent valleys, i.e., a high valley polarization [132] (see Section 1.5.2 in the Introduction). Moreover,

any presence of coherence between the TMDs valleys holds the intriguing promise of quantum manipulation of the valley index [77, 79, 133–135]. To date valley quantum coherence was probed either via a cross-polarization analysis of the TMDs emission [77, 79, 132, 135], or via time-dependent pump-probe measurement schemes [133, 134, 136–138]. Zhu et al measured a 4% linear polarization contrast on a monolayer WS_2 at 10K [77], suggesting the presence of a quantum coherence between the two WS_2 valleys. However, a linear polarization contrast measurement does not allow to distinguish between unpolarized and circularly polarized components, while pump-probe protocols in general rely on uniform samples and do not yield nanoscale information. Here, a position-dependent full Stokes polarization analysis will add the missing information, e.g., it yields the spatially resolved full polarization state of the emitted light on the Poincaré sphere [139]. Therefore, a full Stokes polarization analysis of the TMDs emission would conclusively prove the existence of valley coherence.

Here, we investigate the position-dependent photoluminescence intensity, valley polarization and valley coherence of CVD-grown, triangular WS_2 monolayer flakes. By performing a full Stokes polarization analysis on the WS_2 emission, we confirm the existence of coherence between the two WS_2 valleys and the formation of a superposition of the excitons in the different valleys. Surprisingly, we observe that high valley-polarization regions exhibit lower PL intensity. This anti-correlation between on the one hand intensity and on the other valley-polarization is confirmed in multiple monolayer flakes, both at room temperature and cryogenic temperatures. Moreover, valley coherence also exhibits a trend towards anti-correlation with the PL intensity. The temperature-dependence reveals that phonons are the main source of valley depolarization and valley decoherence. The polarization behaviour of the emission of WS_2 monolayer flakes provides a tool to understand the interaction, hopping and coherence of electrons in the WS_2 valleys and the interaction between the WS_2 excitons.

4.2. RESULTS AND DISCUSSION

4.2.1. PHOTOLUMINESCENCE INTENSITY

In Figure 4.1a-b we present optical microscopy images of WS_2 monolayer flakes with lateral dimensions of 55 μm and 20 μm, numbered fl.1 and fl.2. The triangular growth morphology of the WS_2 flakes is induced by the underlying hexagonal atomic structure, which is schematically represented in Fig.4.1c. Figure 4.1f depicts a typical photoluminescence spectrum of a WS_2 flake. Spectra of monolayer WS_2 flakes exhibit photoluminescence both from the radiative recombination of the electron-hole pair that form the neutral so-called A exciton, and from charged excitons or trions. Spectra of multilayer WS_2, in addition to PL from the exciton in the direct bandgap transition, exhibit PL from an indirect bandgap transition at 700-900 nm that depends on the amount of layers [40]. The high intensity of the PL spectra from fl.1 and fl.2 and the absence of indirect bandgap emission at longer wavelengths indicate that these are monolayer rather than multilayer flakes. The height of the flakes is determined to be 0.80-1.0 nm using atomic force microscopy (AFM) measurements (see Fig.S2 of the Supplementary Materials), which corresponds to a monolayer thickness [17, 18, 22].

In Figure 4.1d-e we present the position-dependent PL intensity of the monolayer flakes (determined by integrating the area under every PL spectrum). Clearly, the photoluminescence intensity is non-uniform, exhibiting regions of higher and lower intensity. The pattern of the PL intensity seems to divide fl.1 into three smaller triangles with a higher intensity in the centre, and a low PL intensity along the flake medians (Fig.4.1d). Fl.2 exhibits higher PL intensity at the edges (Fig.4.1e). The position-dependent PL of other monolayer flakes exhibits similar intensity patterns, e.g., either a lower intensity along the flake medians or a higher intensity at the edges (see Appendix B Fig.B.1 for other examples). Local field effects may affect the PL intensity from the edges of a monolayer flake [122], which would explain the PL intensity pattern of fl.2. However, neither the Scanning Electron Microscopy (SEM) images nor the AFM height measurements of the monolayer flakes reveal any grain boundaries, height variations or other structural reasons that would explain the spatial non-uniformity in the PL intensity of fl.1 (see Appendix B Fig.B.1 for the SEM images and Fig.S2 for the AFM measurements).

Comparing the PL spectra originating from the very middle to spectra from the rest of the flake, we find significant spectral differences (see Appendix B, Fig.B.1). All other spectra, both obtained from higher and lower intensity regions, do not exhibit differences in shape or spectral position, but only in intensity. The spectra from the very middle of fl.1 and fl.2 however are significantly red shifted. Based on the spectral position of this shifted peak, we attribute it to the presence of local structural defects. Not all the monolayer flakes exhibit these defect-related spectra (see Appendix B Fig.B.1 for examples). Structural characterization on the atomic level cannot be performed on the investigated monolayer flakes, as the relatively thick silicon substrate is not transparent to Transmission Electron Microscopy.

Similar position-dependent variations in the PL intensity of CVD grown TMDs monolayer flakes have been reported before [122–131]. A correlation was observed between the size of the monolayer flakes and PL intensity pattern [126]. The intensity pattern of fl.1, with the low intensity triangle medians, indeed matches the reported patterns for monolayer flakes of size 55 μm, and the intensity pattern of fl.2, with the high intensity along the edges, matches the reported pattern for monolayer flakes of size 20 μm.

4.2.2. VALLEY POLARIZATION

The observed spatial heterogeneities in the PL intensity in Fig.4.1d,e raise the question about the potential spatial variations in the valley polarization. A correlation was previously reported between the PL intensity of monolayer flakes and the valley polarization [128]. We therefore determine the valley polarization as a function of position for the triangular WS_2 monolayers at both room- and cryogenic temperatures. The WS_2 valleys with their valley-dependent optical selection rules are schematically depicted in Fig.1.7a in the Introduction. As described in Section 1.5.2, valley polarization is measured by addressing one of the TMDs valleys with circularly polarized incident light and determining the degree of circular polarization of the resulting PL. This quarter-wave plate projection method is a common and straightforward technique, used both for measuring valley polarization with linear [77, 80–82] and nonlinear approaches [140, 141]. The employed experimental set-up is described in Section 2.4 of Chapter 2.

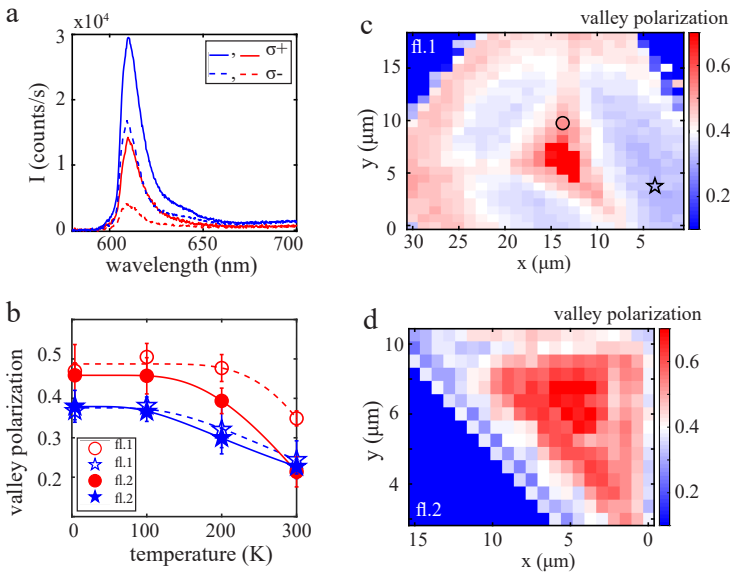

Figure 4.2: Position-dependent valley polarization
a. PL spectra on fl.1 taken at a temperature of 4 K, on a high intensity region (blue) and a low intensity region (red) (star and circle in **c**). The WS_2 is excited with σ_+ light, and from the difference in the σ_+ and σ_- emission we determine the degree of valley polarization. **b.** Temperature dependence of the average valley polarization of the low and high valley polarization regions (blue stars vs. red circles) of fl.1 and fl.2 (open vs. filled markers). Note that the bars do not indicate errors, but rather the standard deviation of the distribution of the measured valley polarization obtained over the specific region of the flake. The temperature dependence is fitted with a Boltzmann distribution, assuming valley depolarization is caused mainly by phonons. **c,d.** Degree of valley polarization of fl.1 and fl.2, where the scans have a pixel size of 1.5 μm. A clear distinction can be seen between regions with high valley polarization (in red) and low valley polarization (in blue). Note that the regions with lower intensity exhibit higher valley polarization than the lower intensity regions on these flakes (compare with Fig.4.1d,e).

Figure 4.2a depicts photoluminescence spectra from the high-intensity regions (blue spectra) and low-intensity regions (red spectra) of fl.1 (obtained at 4 K). We excite the WS_2 with $\sigma+$ light, and from the difference in the $\sigma+$ (solid line) and $\sigma-$ (dashed line) emission, we determine the degree of valley polarization $\alpha = \frac{I_+ - I_-}{I_+ + I_-}$ (with I_+ and I_- determined by integrating the area under the neutral exciton contribution in the $\sigma+$ and $\sigma-$ PL spectra) (see Section 1.5.2). For fl.1 (see Fig.4.1d) the low-intensity spectra on the medians (in red) yield a valley polarization of 0.46±0.02, whereas on the high-intensity spectra of the monolayer (in blue) the valley polarization is significantly lower, α = 0.37±0.02. The measured valley polarization in the monolayer flakes is relatively high, compared to previously reported values (see Fig.1.8a in the Introduction) [77, 128]. Note that the measured valley polarization values are influenced by the sample preparation methods and the used substrate [87, 142, 143]. We conclude that the used preparation method for our samples (see Section 1.3.2 of the Introduction) results in high valley polarization values of the monolayer flakes.

Figures 4.2c-d present the valley polarization of (the central region of) fl.1 and fl.2 at 4 K. The valley polarization of fl.1 follows a similar pattern as the PL intensity, dividing the flake into three smaller triangles with lower valley polarization (blue in the Fig.4.2c), and exhibiting a higher valley polarization along the flake medians (red in Fig.4.2c). When comparing the valley polarization in Fig.4.2c with the PL intensity in Fig.4.1d, it becomes apparent that the WS_2 flake exhibits high valley polarization in the regions of low PL intensity (along the flake medians), and low valley polarization in the regions of high PL intensity. The same inverse relationship between intensity and valley polarization is observed in fl.2 (compare Fig.4.1e), where the lower intensity region in the middle of the monolayer flake exhibits a higher valley polarization (red in Fig.4.2d) than the high intensity edges (blue in Fig.4.2d). We conclude that the valley polarization and the PL intensity are inverse proportional. It is interesting to note that the valley polarization of fl.3 and fl.4, which do not exhibit defect-related spectra, is more homogeneous across these flakes (see Appendix B Fig.B.7). Nevertheless, fl.3 and 4 between them exhibit the same inverse relationship between intensity and valley polarization as fl.1 and 2, where the correlation was observed within a single flake.

In order to understand the processes that determine the degree of valley polarization better, we investigate its temperature dependence. The spatial variations and the specific patterns of high and low valley polarization, as presented in Fig.4.2c-d, are present both at room- and at cryogenic temperatures (see Appendix B Fig.B.5 for valley polarization maps at different temperatures). Figure 4.2b depicts the temperature dependence of the average valley polarization of the high valley polarization (red circles) and low valley polarization (blue stars) regions of fl.1 and fl.2 (open vs. filled markers, compare blue and red regions in Fig.4.2c-d). In all cases, the valley polarization decreases with increasing temperature. As a guide to the eye, we fit the temperature-dependent valley polarization by a Boltzmann distribution following Zhu et al [77], assuming that phonons are the main source for valley depolarization. From the good quality of fit we qualitatively conclude that temperature-dependent valley depolarization is mainly caused by phonons. As only four temperature points are used, we refrain from quantitative conclusions.

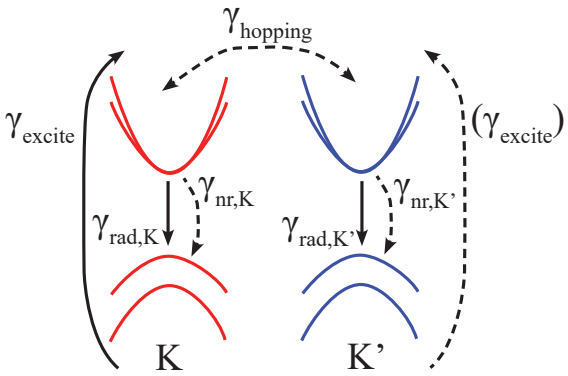

Figure 4.3: Excitation and decay processes in WS_2 valleys
Schematic of the processes in the WS_2 valleys with their different rates. The radiative vs. non-radiative decay rates (γ_{rad} and γ_{nr}) influence the photoluminescence intensity, and the valley hopping $\gamma_{hopping}$ reduces the degree of valley polarization and valley coherence.

Figure 4.3 schematically presents all the relevant processes in the WS_2 valleys. After the selective excitation of one of the WS_2 valleys (γ_{excite} in Fig.4.3) and the creation of an exciton, there are several possible scenarios: the electron can hop to the other valley ($\gamma_{hopping}$), the electron can decay radiatively ($\gamma_{rad,K}$) or non-radiatively ($\gamma_{nr,K}$). On the one hand, a fast radiative decay and a slow non-radiative decay results in a higher PL intensity. On the other hand, the valley hopping rate reduces the valley polarization. Differences in intensity and valley polarization on CVD grown flakes have been attributed before to differences in radiative and non-radiative lifetime components [128]. We observe an inverse relationship between PL intensity and valley polarization, which implies a correlation between the valley hopping rate and the (non-)radiative decay rate, or in other words, it implies a correlation between the exciton lifetime and the valley lifetime [128, 132]. More specifically, we observe a high valley polarization at regions of low PL intensity. We conclude that in these regions, the valley hopping rate is relatively slow with respect to the rest of the flake and the non-radiative decay rate is relatively fast. At regions of high PL intensity we observe a low valley polarization. In these regions therefore the valley hopping rate is relatively fast and the non-radiative decay rate is relatively slow.

4.2.3. VALLEY COHERENCE

The valley coherence reflects the interaction and phase relation of both valleys. Valley coherence is measured by exciting both valleys equally using linearly polarized light, which is a coherent superposition of left-handed and right-handed circularly polarized light. If we suppose the presence of valley coherence in a TMDs material, the coherence of the excitation photons is transferred to the valleys and the related excitons, so that the pseudospins associated to the two TMDs valleys will form a superposition state. In most semiconductors, phase information is lost in the photoluminescence process [25], therefore the random phase of the emission of different valleys or atoms always results

in unpolarized light. However, if the pseudospins associated with the two TMDs valleys and the related excitons retain their coherence perfectly, the emitted photons exhibit a coherent superposition of left-handed and right-handed circularly polarized light again, e.g. the emission will be linearly polarized.

By performing a full Stokes analysis [144–146] on the steady-state emission of the flakes, we determine the exact polarization state of the emitted light and therefore gain access to the valley coherence without having to rely on time-resolved measurements [133, 134, 136–138]. With this method, we measure the PL intensity as a function of the angle of a rotating quarter-wave plate and retrive the Stokes parameters using Fourier analysis [144–146] (see Appendix B Section B.2). In contrast to cross-polarization polarimetry in a linear or circular basis [77, 79, 132, 135], the full Stokes vector both provides information on the polarization state of the PL, e.g., whether the PL has components that are circularly or linearly polarized, as well as on the amount of unpolarized vs. polarized light.

Figure 4.4a presents a schematic of our set-up, where linearly polarized excitation light (594 nm wavelength) is focused on the sample, after which the emission is collected and directed towards the spectrometer (see Section 2.4 of Chapter 2). The emission passes through a quarter-wave plate, that is rotated from 0 to π in steps of $\pi/8$, and a fixed analyzer (oriented along θ=0). Figure 4.4b presents PL spectra of fl.1 acquired using the rotating quarter-wave plate method. The spectra are from a low-intensity region (in yellow) and a high-intensity region (in red) (circle vs star in Fig.4.4d). The spectra with a 0 waveplate angle (solid line) have a higher intensity than the ones with a $\pi/4$ angle (dashed line). Spectra as a function of quarter-wave plate angle and position on the flake are measured on both fl.1 and fl.2. Figure 4.4c depicts the derived PL intensity of the neutral WS_2 exciton on different regions of fl.2 as a function of the quarter-wave plate angle (see circles/stars in Fig.4.4e). The derived PL intensity exhibits minima at $\pi/4$ and $3\pi/4$ of around 0.75 at high PL intensity (blue and yellow curves) and around 0.60 at low PL intensity (red and green curves). We attribute the small intensity differences between $\pi/4$ and $3\pi/4$ to slight imperfections in the optical alignment and polarization elements (see Appendix B Section B.3 for details). The depth of the intensity minima at $\pi/4$ and $3\pi/4$ provides information about the polarization state of the WS_2 emission. If the phase of the WS_2 emission would be fully incoherent, the emission intensity would be constant for all quarter-wave plate angles, whereas for linearly polarized emission we would expect a dip of 0.50 at $\pi/4$ and $3\pi/4$. The measured 0.60-0.75 dips in the PL intensity therefore confirm that the WS_2 emission exhibits partial phase coherence.

To derive the value of the position-dependent valley coherence, we perform a Fourier analysis of the measured intensity curves as depicted in Fig.4.4c, and first derive the Stokes parameters of the WS_2 monolayer emission (see Appendix B Section B.2). The coherence of the WS_2 emission $\Delta = \sqrt{S_1^2 + S_2^2 + S_3^2}/S_0^2$ is used as the valley coherence. We find that of the measured Stokes parameters, S_2 and S_3 are negligible (< 0.05, see Appendix B Fig.B.3), so the WS_2 emission does not have components that are circularly polarized or linearly polarized along the diagonal axis with respect to the excitation polarization direction. We calculate the valley coherence Δ at every position on the mono-

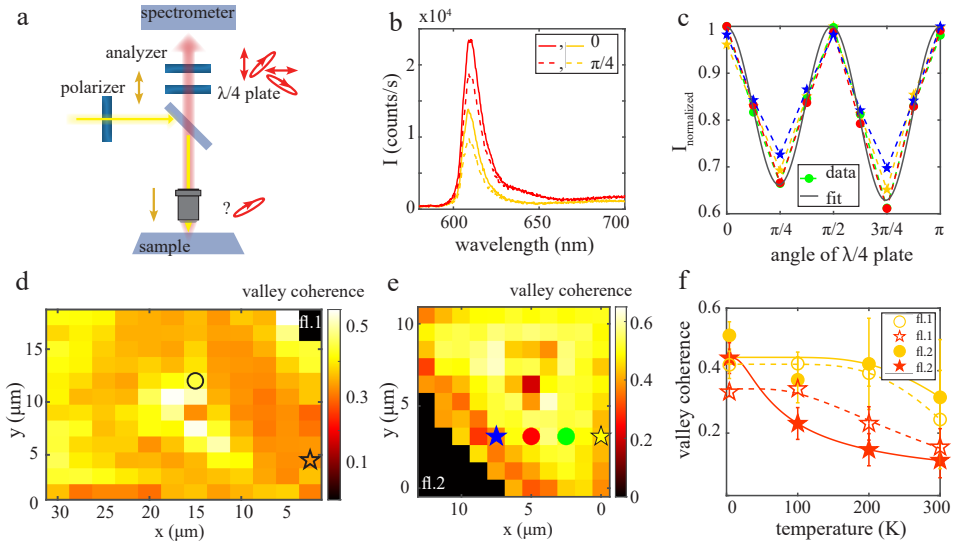

Figure 4.4: Position-dependent valley coherence
a. Schematic of the set-up, where linearly polarized excitation light is focused on the sample (see section 2.4 of Chapter 2). The emission is directed to a spectrometer, passing through a quarter-wave plate (rotated from 0 to π in steps of $\pi/8$) and analyzing polarizer (fixed along 0). **b.** PL spectra on fl.1 at 4 K, on a high intensity region (red spectra), and a low intensity region (yellow spectra) (star/circle in **d**). **c.** Normalized intensity as a function of quarter-wave plate angle, at high and low intensity regions on fl.2 (stars/circles in **e**). The curves at high intensity (blue and yellow) exhibit a dip of only 0.75 at an angle of $\pi/4$ and at low intensity (red and green) a dip of 0.65. The Stokes parameters and thus the polarization coherence can be extracted via Fourier analysis of these curves. **d,e** Valley coherence of the middle regions of fl.1 and fl.2, where the scans have pixel sizes of 2.5 and 1 μm. Note that the regions with lower intensity have a higher valley coherence than the high intensity regions. **f.** Temperature dependence of the average valley coherence of the low and high valley coherence regions (red stars vs. yellow circles) of fl.1 and fl.2 (open vs. filled markers). (Note that the bars do not indicate errors, but rather the standard deviation of the distribution of the measured valley polarization obtained over the specific region of the flake). The temperature dependence of the valley coherence can be fitted with a Boltzmann distribution, assuming valley decoherence is caused mainly by phonons.

layer flakes. As S_2 and S_3 are negligible, the main contribution to the valley coherence is S_1. We confirm a non-zero WS_2 valley coherence, ranging from 0.1 to 0.5 depending on position and temperature. As a comparison, we perform linear polarization measurements on fl.1 and confirm that the extracted S_1 parameter and valley coherence are in good agreement for both measurement methods (see Appendix B Fig.B.3). The presence of phase coherence of the WS_2 emission conclusively proves that the WS_2 valleys indeed emit while still in a partial superposition state.

Figure 4.4f depicts the temperature dependence of the average valley coherence of fl.1 (open circles/stars) and fl.2 (filled circles/stars), where the values from the high and low valley coherence regions are yellow circles and red stars respectively. As was the case for the degree of valley polarization, the spatial variation in high valley coherence (yellow in Fig.4.4d,e) and low valley coherence (red in Fig.4.4d,e) is present at all temperatures for the same regions on the flakes: the medians on fl.1 and the central region on fl.2 (see Appendix B Fig.B.6 for valley coherence maps at different temperatures). As a guide to the eye, we fit the temperature-dependent valley coherence by a Boltzmann distribution following Zhu et al [77], attributing valley decoherence to the excitation by phonons. If both the valley decoherence and the valley depolarization are phonon-related, this raises the question how the two processes are related.

4.2.4. DISCUSSION

There are various processes that lead to valley decoherence. After the excitation of both the WS_2 valleys (γ_{excite} in Fig.4.3) and the formation of two excitons, a number of processes may occur: either one of the electrons can hop to the other valley ($\gamma_{hopping}$), or one of the electrons can decay radiatively ($\gamma_{rad,K}$) or non-radiatevely ($\gamma_{nr,K}$). The only way for the emitted photons to be in a coherent superposition, e.g. the emitted polarization to be linearly polarized, is when both electrons emit radiatively at the same time with a fixed phase relation between them. With the observed negligible S_2 parameter, we can further conclude that the phase relation between the valleys is preserved, leading to the same linear polarization as the emitted light. The coherent superposition of the excitons and the electrons in the two valleys will both be destroyed by valley hopping of either one of the electrons, the non-radiative decay of either one of the electrons, or when the phase relation between the two electrons is broken by further decoherence mechanisms. Thus, there are more potential processes to reduce the valley coherence than the valley polarization.

As valley hopping is both a source of valley decoherence and of valley polarization, a finite valley polarization gives an upper limit for the valley coherence. There are two ways to reduce the valley coherence: valley hopping, e.g., the same mechanism that reduces valley polarization, or the breaking of the phase relation between the electrons in the two WS_2 valleys. Furthermore, many mechanisms have been proposed to explain valley depolarization. From their temperature dependence we have deduced that both valley depolarization and valley decoherence have a phononic nature (see [77, 147]). Naturally, the exciton dynamics in the WS_2 valleys have a large impact on the valley polarization and valley coherence. Both the intra- and the intervalley Coulomb interactions between excitons in the WS_2 can cause valley depolarization [84, 148–150]. The observed

position-dependent variations in PL intensity, valley polarization and valley coherence point at a position dependence of the exciton vs. the valley lifetimes [128, 132]. We observe an inverse relationship between PL intensity and valley coherence. At regions with low PL intensity we detect a high valley coherence. Therefore, in these regions, the non-radiative decay rate is relatively fast with respect to the rest of the flake and the exciton lifetime is short, and either the valley hopping rate is relatively slow and the valley lifetime is long, or the valleys are very well protected against phase jumps. At regions with high PL intensity we observe a low valley coherence. We conclude that these regions exhibit the opposite trend: slow non-radiative decay rates and long exciton lifetimes, with a fast valley hopping rate and a short valley lifetime.

Thus we reported both inter-flake and intra-flake correlations between intensity, degree of valley polarization and valley coherence. It is interesting to note that the flakes that exhibited a more homogeneously distributed valley polarization and valley coherence over their surface area, do not possess a defect region (see Appendix B Fig.B.1). This hints at the physical importance of this defect region. A higher amount of phonons, causing valley hopping and breaking the phase relation between the WS_2 valleys, can come from the presence of strain, for instance caused by defects. We hypothesize that a defect in the middle of an ultrathin triangular flake would lead to spatially varying strain, *e.g.*, along the flake medians. Attributing the position-dependent variations of the PL intensity of CVD grown monolayer flakes to differences in defect density and strain is in line with previous work [122–131]. Nevertheless, the explanation of the inverse relationship between PL intensity and valley polarization and valley coherence and the position-dependent variations in exciton vs. valley lifetime are not straightforward. We have attributed valley depolarization and valley decoherence to phonon-induced valley hopping and phase jumps as well as Coulomb-induced intra- and intervalley interactions. However, variations in the non-radiative decay are also phononic in nature and influenced by the exciton dynamics in the WS_2 valleys. If phonons or Coulomb interactions both induce valley hopping lowering the valley polarization, and induce non-radiative decay that lower the intensity, both can explain the correlation between high valley polarization and low intensity. This makes the observed high valley polarization and valley coherence at regions of low PL intensity surprising. As defects and strain not only result in a larger amount of available phonons, but strain also slightly modifies the bandgap, this naturally affects the photoluminescence intensity [151]. Moreover, strain can also induce an imbalance in the amount of electrons in the two valleys and therefore in the measured valley polarization [152]. Therefore the observed inverse correlation between PL intensity and valley polarization and valley coherence might be related to strain.

4.3. CONCLUSION

We have characterized the position-dependent polarization properties of the light emission of CVD grown WS_2 monolayer flakes, where the measured valley polarization sheds light on the processes within one WS_2 valley, and the measured valley coherence on the interaction and phase relation between both valleys and the related excitons. Using a rotating quarter-wave plate method to derive the Stokes parameters of the emitted light,

we have characterized the full polarization state of the WS_2 emission and proven unambiguously the existence of coherence between the two WS_2 valleys. Hereby we have confirmed that the attribution of linear polarization contrast to valley quantum coherence is valid [77, 79, 132]. Moreover, we observe that both the intensity, the valley coherence and the valley polarization is non-uniform along the WS_2 monolayer flakes. A clear correlation exists between intensity and valley polarization, and a trend towards a correlation between intensity and valley coherence, implying a correlation between radiative and non-radiative decay rates and the exciton lifetime on one hand, and valley hopping and valley phase jumps and the valley lifetime on the other hand. As the temperature dependence of the valley coherence and valley polarization can be fitted with a Boltzmann distribution, we conclude that the source of valley depolarization and decoherence is phonon-related. We observe that the central regions of some of the WS_2 monolayer flakes exhibit a defect-related spectral behaviour. We conclude that the presence of defects, in 2D materials naturally causing strain, influences the amount of available phonons and reduces the valley polarization and the valley coherence. By investigating the full polarization-resolved emission of WS_2 monolayer flakes, we take the first steps in unraveling the interaction of the WS_2 valleys and confirming the existence of valley coherence, and thereby open the way for applications involving quantum valley manipulation and valleytronics.

5

EXCITON-POLARITONS IN MONOLAYER WS_2

Under which circumstances does light hybridize with the WS_2 exciton, and what are the properties of the resulting exciton-polariton mode?

5.1. INTRODUCTION

The previous chapters (Chapter 3 and 4) investigated phenomena related to the process of photoluminescence, *e.g.*, the absorption and re-emission of light by the WS_2 (see Introduction, Section 1.4.1). However, as described in Section 1.4.2 of the Introduction, strong interaction between the light and a WS_2 exciton [26–28], may also lead to the formation of a hybrid light-matter mode that is called exciton-polariton [41, 42]. The exciton-polaritonic mode has an evanescent field in the out-of-plane direction [45].

As mentioned in the Introduction, the interest in polaritons lies in the large confinement of the (hybrid) electromagnetic mode in an atomically thin material, that enhances the light-matter interaction and creates an enormous interaction strength [46]. The same name is used to refer to different kinds of exciton-polaritons. Most commonly polaritons studied in the field of TMDs are the so-called cavity-polaritons, where the electromagnetic field is confined in a two-dimensional cavity and exhibits strong coupling to the excitonic mode of the TMDs material [153–155]. A promising alternative for applications in information transport would be a propagating polariton [156], where the electromagnetic field in an optical waveguide interacting with the TMDs exciton, for instance combining the TMDs material with a photonic crystal [157, 158]. Recent work reports propagating exciton-polaritons in bulk TMDs materials, detected using scanning near-field techniques [159–161].

While in the case of the cavity-polaritons energy is exchanged between the TMDs exciton and a single confined electromagnetic mode, exciton-polaritons described by Alpeggiani *et al* originate from the interaction of the exciton with the continuum of electromagnetic modes in 3D [43, 44]. The existence of these polaritons has been predicted by Khurgin *et al* [43], and the dispersion and decay rate of these modes have been described theoretically by Alpeggiani *et al* [44]. These modes are analogues to exciton-polaritons in semiconductor quantum wells and have been studied both theoretically and also experimentally [41, 42]. However, the absence of confinement of the electromagnetic field makes these exciton-polaritons highly vulnerable to an imbalance of the dielectric constant of the medium surrounding the TMDs material [44]. This vulnerability may be addressed by the fine control over the optical properties of the embedding medium, achievable by encapsulating the TMDs material into a stack of another two-dimensional atomic crystal, namely hexagonal boron nitride (hBN). Note that the polaritons in hBN-WS_2 in [156] originate in a local negative permittivity, associated with the imaginary part of the electric permittivity of the exciton, and therefore have a different physical nature and exhibit different polarization properties than the exciton-polaritons of interest in the current chapter.

For the use of exciton-polaritons in opto-electronic applications, understanding their propagation properties is paramount. Here, we use simulations (following the methodology of [44]) to study the influence of encapsulating with hBN on the exciton-polaritons formed in WS_2 monolayers, and to investigate the influence of the thickness of the various layers on the polariton properties. To this end, we compare the dispersion curves of the exciton-polaritons, their out-of-plane mode profile and their in-plane propagation length. This approach enables us to define the experimentally optimal sample,

having a dispersion relation with wavevectors that are easily distinguishable from free-space light, a mode profile with a high intensity at the interface and a large in-plane propagation length. We focus on two experimental excitation and detection schemes for the exciton-polaritons: phase-resolved near-field microscopy and non-linear four-wave-mixing. For the latter, we calculate the specific excitation wavelengths and angles of incidence needed to excite the exciton-polariton. The calculations described in this chapter bridge the gap between the theoretical predictions of exciton-polaritons in monolayer WS_2 and their experimental detection for potential applications.

5.2. RESULTS AND DISCUSSION

5.2.1. CONDITIONS FOR THE FORMATION OF EXCITON-POLARITONS IN WS_2

The properties and formation of exciton-polaritons in 2D materials are highly influenced by the dielectric constants of the medium surrounding the material, as described in [44]. Figure 5.1a schematically presents a monolayer of WS_2 (in green), embedded in a dielectric medium (for instance air). To calculate the dispersion relation of the modes of this system, we use the same method described in [44]. We assume a layered system. Within each layer, the standard wave equation for the electric field **E** holds:

$$\nabla \times \nabla \times \mathbf{E}(\mathbf{r},\omega) - \bar{\bar{\epsilon}}(z,\omega)\frac{\omega^2}{c^2}\mathbf{E}(\mathbf{r},\omega) = 0, \tag{5.1}$$

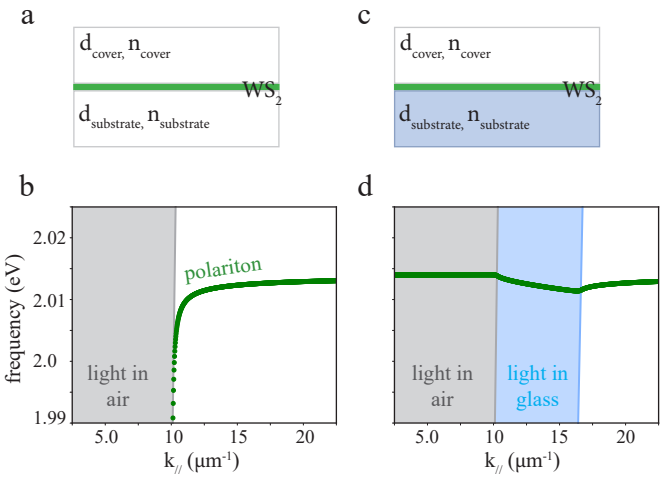

Figure 5.1: Conditions for exciton-polaritons to form
This figure summarizes the conclusions of [44]. **a.** A sample with a WS_2 monolayer, embedded in a dielectric medium (such as air), where $n_{substrate} = n_{cover}$. **b.** The dispersion relation of the exciton-polariton (in green), that starts around the bandgap energy of WS_2 and bends to continue along the light cone (in grey). **c.** A sample with a WS_2 monolayer deposited on a glass substrate (blue). Here $n_{substrate} \neq n_{cover}$. **d.** The dispersion curve (in green) is essentially flat, except for a slight perturbation when it crosses the light-line of glass. Thus the interaction with light only generates a weak perturbation on the original exciton dispersion.

with c the speed and ω the frequency of light in vacuum, and $\bar{\bar{\epsilon}}$ the permittivity tensor. Since the system is translationally invariant in two dimensions, we look for electromagnetic modes for a fixed in-plane wavevector $k_{//}$. The electromagnetic modes are defined as the solutions of the system of wave equations for all the layers (including the boundary conditions at the interfaces) as a function of the complex eigenfrequency $\tilde{\omega} = \mathrm{Re}(\tilde{\omega}) + i\,\mathrm{Im}(\tilde{\omega})$. In practice, the system is solved using a transfer matrix method, to match the analytical solutions of the wave equation from one layer to the other. There are various solutions to the characteristic system of equations. A first family of solutions consist of radiative modes. They are responsible for the direct light scattering from the exciton and exist within the lightcone, *i.e.*, $|k_{//}| < |\tilde{\omega}|/c$. However, in this chapter we focus on a non-trivial family of modes, the so-called exciton-polaritons, exhibiting the intriguing properties of enhanced light-matter interaction. These exciton-polaritons are TE-polarized modes, which means the out-of-plane component of the electric field is zero. The real part of the dispersion relation of the exciton-polariton is presented in Fig.5.1b. Here and in all dispersion curves in this chapter, the real part of the frequency is displayed as a function of the in-plane wavevector $k_{//}$. The imaginary part of the frequency is neglible (see [44]). For high wavevectors, the polariton mode in Fig.5.1b follows the horizontal excitonic dispersion, where the exciton energy of WS_2 around 2.01 eV. For lower wavevectors, the mode bends and continues parallel to the line of free-space light in air (in grey). This mode exists outside of the light-cone, as expected from a polaritonic mode [42].

The existence of an exciton-polariton mode is theoretically predicted by this dispersion relation for the ideal case of a suspended monolayer. From a practical point of view, a configuration where the monolayer is positioned on a substrate would be favorable (see Fig.5.1c). However, as originally pointed out in [43], balancing of the dielectric constant in the upper and lower claddings is a critical condition for the existence of the exciton-polariton. Figure 5.1d presents the dispersion curve of the mode for the sample of Fig.5.1c. This dispersion curve is essentially flat, except for a slight perturbation when it crosses the line of light in glass. The slope of this perturbation is opposite to the dispersion of a standard electromagnetic mode in vacuum, implying a slightly negative group velocity. As the dispersion is essentially flat, it strongly resembles the original excitonic mode. This means that the interaction of the exciton with light only generates a weak perturbation of the exciton dispersion, and no strong coupling effects are visible (see [162] for a rigorous definition of the strong coupling threshold in this kind of systems). Exciton-polaritons are only formed when $n_{substrate} = n_{cover}$ (see Fig.5.1a) [44]. Therefore the geometry of a WS_2 monolayer on a substrate is unsuitable to support the existence of the polariton mode.

Embedding the WS_2 in a material with fully homogeneous optical properties is experimentally challenging. Moreover, the highest field strength will typically be found close to the WS_2, whereas the thickness of this embedding material will prevent the detection and practical use of the polaritonic mode. We take one step beyond what was previously described [44] and propose an alternative geometry, which allows us to preserve the polaritonic state of the mode, while at the same time guaranteeing experimental detectability and usability. If a layer of hexagonal boron nitride (hBN) is deposited on

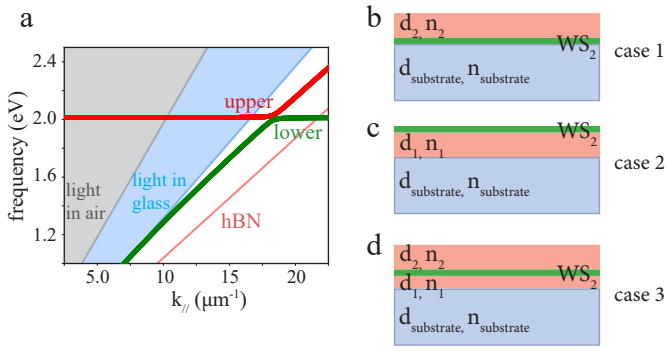

Figure 5.2: Exciton-polaritons in WS_2 - hBN samples
a. The dispersion relation of a hybrid exciton-polariton mode between the waveguide mode in a slab of hBN and the WS_2 exciton. A clear avoided crossing is observed between the upper (in red) and lower (in green) polariton branches. **b-d.** The dielectric constants of the materials surrounding the WS_2 layer can be controlled by adding a slab for instance hBN, **b.** on top of the WS_2 (case 1), **c.** between the WS_2 and the substrate (case 2) or **d.** encapsulating the WS_2 monolayer (case 3).

the WS_2 layer, a waveguide mode will be available under suitable conditions that are explored below. The exciton will hybridize with such a waveguide mode, generating a polariton. This hybridization becomes apparent in the dispersion relation of the resulting exciton-polariton depicted in Fig.5.2a, which exhibits an avoided crossing between the lower (in green) and the upper polariton branch (in red). The splitting between the two branches is around 25 meV, which is a measure of the coupling strength between the exciton and light. Although the nature of the exciton-polaritons in these WS_2 - hBN samples is different than the ones analyzed in [43, 44], such hybrid polaritons will therefore still allow us to obtain a high coupling between the excitons and a light-like waveguide mode.

In this chapter, we will focus on the lower polariton branch. Like the polariton mode of WS_2 suspended in air (see Fig.5.1b), the lower branch of this exciton-polariton starts in Fig.5.2a at a frequency just below that of the WS_2 bandgap (2.0 eV / 620 nm), and bends away to assymptotically approach the light-line of light in glass (in blue). In the frequency region where the dispersion is linear and approaches the light-line, the exciton-polariton will behave almost like light. The point of maximum curvature in the dispersion is the most interesting part to study, because here the exciton-polariton exhibits a distinctly different behaviour than light, as the dispersion bends away from the light-line and is not linear.

The overall shape of the dispersion curve, including the slope of the different parts of the dispersion and the maximum curvature, depends on the specific sample configuration and the thickness of the used layers. Hybrid exciton-polariton modes require coupling with a waveguide mode in the hBN. In order for such waveguide mode to be formed, a minimum thickness of the hBN slab of about 80 nm is required. There are three possible

sample configurations, presented in Fig.5.1b-d: a slab of hBN on top of the WS_2, hBN between the substrate and the WS_2, and encapsulating the WS_2 with hBN (from now on these configurations will be referred to as case 1, 2 and 3). The differences in the dispersion and spatial properties of the exciton-polaritons formed in these three sample configurations will be discussed in the following part of this chapter.

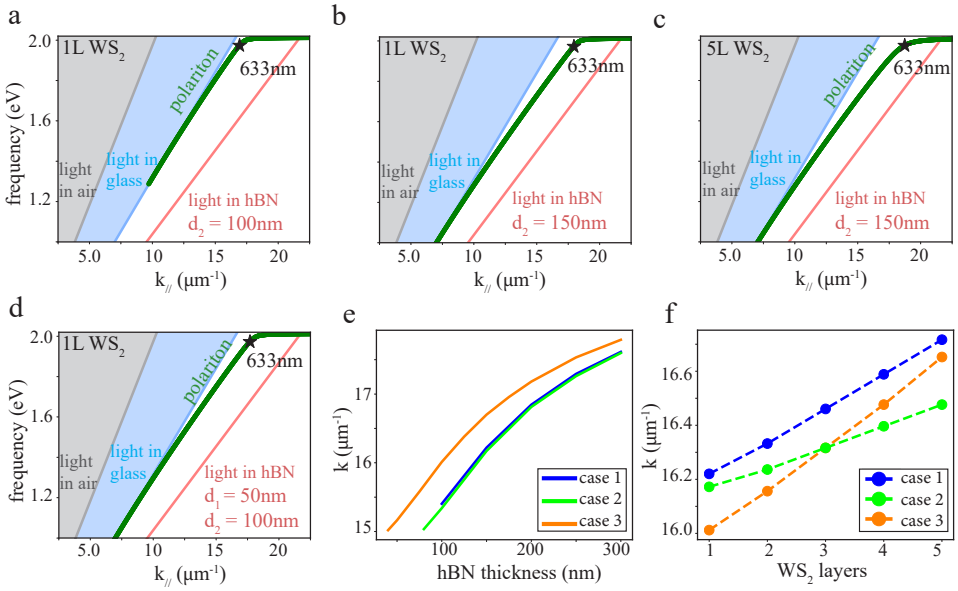

Figure 5.3: Dispersion relations of exciton-polariton in different WS_2 samples
a-d. Dispersion relation of an exciton-polariton in WS_2 - hBN samples (see Fig.5.2b-d), with a glass substrate (n=1.5), an air cover (n=1.0). **a-c.** Dispersion relation of an exciton-polariton in a sample of case 1 (see Fig.5.2b), with in **a.** 100 nm of hBN and in **b.** 150 nm hBN and a monolayer of WS_2, and in **c.**, the sample contains five layers of WS_2. **d.** Dispersion relation of an exciton-polariton in a sample of case 3 (see Fig.5.2d), with d_1 = 50 nm and d_2 = 100 nm. **e.** The dependence of the exciton-polariton dispersion on the hBN thickness becomes clear when comparing the polariton wavevector at a frequency of 633 nm (indicated by a star in **a-d**). Note that in the case 3 sample (in orange), d_1 is taken 50 nm and d_2 is varied. **f.** The wavevector at a 633 nm frequency also decreases when the number of WS_2 layers increases (the dotted lines through the data points are added as a guide to the eye).

5.2.2. THE DISPERSION RELATION OF THE EXCITON-POLARITONS

Figure 5.3a-d presents the dispersion relation of exciton-polariton modes in various WS_2 - hBN layer stacks, with in Fig.5.3a-c samples with hBN on top of WS_2 (case 1) and Fig.5.3d the WS_2 encapsulated in hBN (case 3, see Fig.5.2b-d). To compare the different dispersion curves with each other, we have indicated the point at a frequency of 633 nm (indicated by a star in Fig.5.3a-d). As this frequency lies around the point of maximum curvature of the dispersion of the polariton mode, it is always in the interesting frequency range where the polariton behaves clearly differently than light. When the thickness of the hBN slab increases, from 100 nm in Fig.5.3a to 150 nm in Fig.5.3b, the point of 633 nm moves

to higher wavevectores. When the amount of WS_2 layers increases, from a monolayer in Fig.5.3b to five layers in Fig.5.3c, the curvature of the polariton mode becomes less and the point of maximum curvature moves even further away from the line of light in glass. Note that our calculations for multilayer WS_2 samples only take into account the change in thickness, and no changes in the optical response, *i.e.*, in the electric permittivity. The impact of the decreasing excitonic strength due to the transition of few-layer WS_2 from a direct to an indirect bandgap semiconductor is therefore not taken into account. Hence the observed change in the polariton dispersion is caused solely by the increase in WS_2 thickness.

It is interesting to compare the dispersion curves in Fig.5.3b (sample case 1, hBN on top of WS_2) and Fig.5.3d (sample case 3, hBN encapsulating WS_2) (see Fig.5.2b,d). Although the sample configuration is different, we observe no differences in the slope of the dispersion curves, no differences in curvature and no shifts in the point of maximum curvature. As long as the total hBN thickness in a sample configuration is conserved, we observe no qualitative differences in the dispersion curves of the polariton modes in all three cases of Fig.5.2b-d.

To determine potential subtle differences in the dispersion of different sample configurations, and to study the influence of the thickness of hBN and WS_2 on the exciton-polariton dispersion in a more quantitative way, we compare the polariton wavevector at a frequency of 633 nm (indicated by a star in Fig.5.3a-d). Note that for the case 3 sample (in orange), d_1 is fixed at 50 nm and d_2 is varied. With increasing number of WS_2 layers, the polariton wavevector at the frequency of 633 nm increases in all sample configuration cases. However, there are subtle differences between the different samples: the slope of the curve in case 3 (orange) is larger than the in case 1 (blue) or case 2 (green). This could indicate subtle differences between the shape of the mode profiles of the polaritons in different samples.

5.2.3. THE POLARITON MODE PROFILES

To characterize the exciton-polaritons in WS_2 - hBN samples beyond the dispersion relation, we also study other relevant properties for potential applications, *e.g.*, the spatial extent of the polariton modes. Figure 5.4a-d presents the out-of-plane mode profile (in black) of the normalized intensity of the exciton-polariton. In all cases, the maximum of the mode profile lies in the hBN slab (in pink), and not in the glass (in blue), nor is it overlapping with the WS_2 (in green). We attribute this to the hybrid nature of the exciton-polariton mode with the optical waveguide mode in the hBN slab. With increasing hBN thickness, from 100 nm in Fig.5.4a to 150 nm in Fig.5.4b, a larger part of the mode lies in the material and becomes inaccessible for practical purposes such as sensing, as one cannot physically enter the material to interact with the mode. As depicted in Fig.5.4e, the intensity of the mode at the air interface decreases as the thickness of the hBN slab increases. This decrease becomes apparent in the mode profile in Fig.5.4d, with a case 3 sample of d_1 = 50 nm and d_2 = 100 nm, where only 60 % of the maximum mode intensity reaches the surface. Figure 5.4f depicts the mode intensity at the air interface for the three sample configuration cases. Interestingly, the intensity at the air interface of the mode in samples of case 1 (Fig.5.2b) increases with increasing number of WS_2 layers,

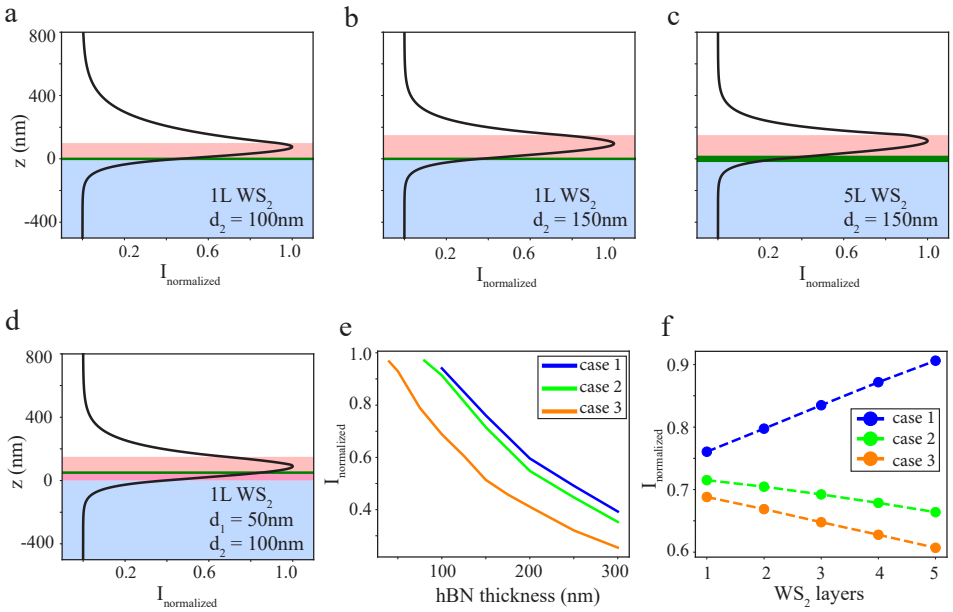

Figure 5.4: Out-of-plane mode profile
a-d. Mode profile (in black) of the exciton-polariton intensity at a frequency of 633 nm (compare stars in Fig.5.3) in a sample of WS_2 (in green) on a glass substrate (in blue) with a hBN slab (in pink). **a-c.** Mode profile of an exciton-polariton in a sample of case 1, with in **a.** 100 nm of hBN and in **b.** 150 nm hBN and a monolayer of WS_2, and in **c.**, the sample contains five layers of WS_2. **d.** Mode profile of a polariton in a case 3 sample with d_1 = 50 nm and d_2 = 100 nm. **e.** The normalized intensity of the mode at the air interface as a function of hBN thickness. **f.** The normalized intensity of the mode at the air interface as a function of the amount of WS_2 layers (the dotted lines through the data points are added as a guide to the eye).

but decreases for samples in case 2 and 3 (Fig.5.2c,d). This might be related to the fact that case 1 is the situation where the WS_2 monolayer is located furthest away from the air-interface. This effect can be observed in the mode profile in 5.4c (five layers of WS_2), that exhibits a slightly higher intensity at the interface with air than the profile in 5.4b (monolayer WS_2).

5.2.4. THE POLARITON PROPAGATION LENGTH

Another aspect of the spatial extent of the exciton-polariton modes is given by the in-plane propagation length ($\delta_{propagation}$):

$$\delta_{propagation} = -\frac{d\omega}{dk} \Big/ Im(\omega(k)) \,, \tag{5.2}$$

where $\frac{d\omega}{dk}$ is the group velocity and $Im(\omega(k))$ the imaginary part of the dispersion relation. Figure 5.5a-d presents the propagation length of the polariton as a function of the wavevector. The wavevector corresponding to the frequency of 633 nm is indicated by a star. With increasing hBN thickness, from 100 nm in Fig.5.5a to 150 nm in Fig.5.5b, the curve shifts to higher wavevectors resulting in a larger propagation length at the 633 nm frequency. The influence of the hBN thickness on the propagation length at this frequency is depicted in Fig.5.5e, with a minimum at 100 nm hBN thickness in all cases. When comparing the propagation length of case 1 in Fig.5.5b and case 2 in Fig.5.5c, it becomes apparent that the shape of the curve changes. This leads to a considerable increase of the propagation length at a 633 nm frequency for case 2 (see Fig.5.2c) with respect to the propagation length in the other two sample configurations.

We observe a decrease of the propagation length with an increasing number of WS_2 layers. This becomes apparent when comparing the shape of the curve in Fig.5.5d, that depicts the propagation length in a sample with five layers of WS_2, to the curves obtained for a monolayer. The curvature and the slope of the different parts of the curve change drastically, resulting in a propagation length of only 4 μm at a 633 nm frequency. Fig.5.5f depicts the propagation length at a 633 nm frequency for all sample configurations. When the thickness of the WS_2 is increased from one to five layers, we observe a decrease in propagation length.

5.2.5. EXPERIMENTAL DETECTION SCHEMES

The application potential of exciton-polaritons in WS_2 - hBN samples depends greatly on the choice of sample. On the one hand, the challenge in a practical context would be to distinguish the dispersion of the exciton-polariton from free-space light in air, glass or hBN. Given that the polariton dispersion follows the line of light in glass, the experimental optimum would be for the polariton that have a large coupling strength and/or a dispersive waveguide mode. Both conditions will result in a higher wavevector for a given frequency. Based on Fig.5.3e,f we conclude that samples with thick layers of hBN and multiple layers of WS_2 meet this requirement. On the other hand, it is important to detect as much of the potentially weak mode intensity as possible, typically at the sample-air interface. Given that the polariton mode lies mainly in the hBN, the exper-

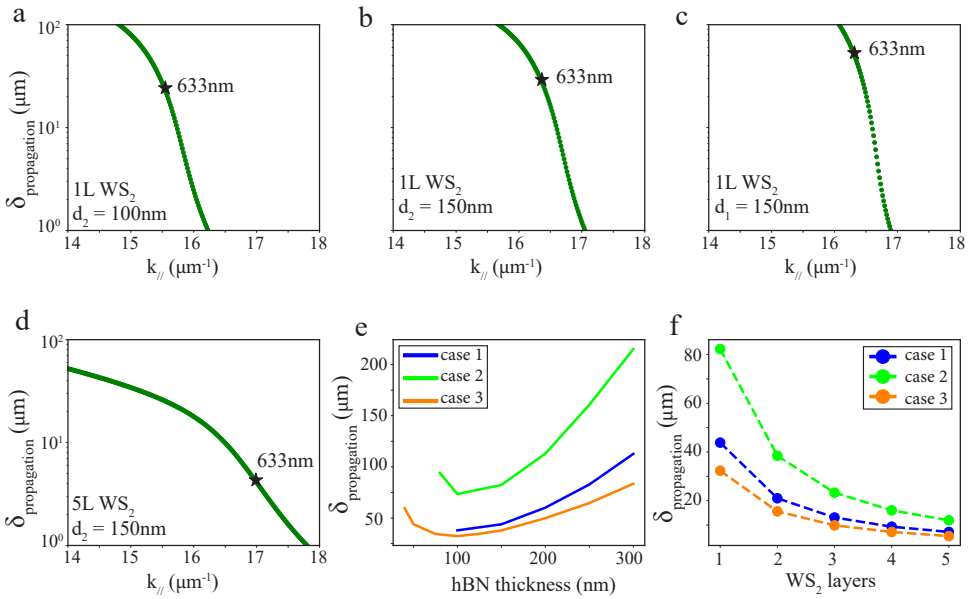

Figure 5.5: In-plane propagation length
a-d. The in-plane propagation length of the exciton-polariton. **a-b.** Propagation length of the exciton-polariton in a sample of case 1, with in **a.** 100 nm of hBN and in **b.** 150 nm hBN and a monolayer of WS_2. **c.** Mode profile of a polariton in a case 2 sample with 150 nm hBN. **d.** Mode profile of a polariton in a case 1 sample with five layers of WS_2. **e.** Propagation length at a frequency of 633 nm as a function of the hBN thickness. **f.** Propagation length at a frequency of 633 nm as a function of the hBN thickness (the dotted lines through the data points are added as a guide to the eye).

imental optimum would mean samples with thinner slabs of hBN and monolayers of WS_2, *e.g.*, requirements opposite to an optimal dispersion curve as mentioned above. Moreover, a large in-plane propagation length at least above 10 μm is essential for the detection and identification of a polariton. The optimum in this respect would be to use samples with monolayer or bilayer WS_2 and a hBN thickness larger than 100 nm. As a trade off between the different requirements we therefore suggest a case 2 sample (hBN between the WS_2 and the glass, see Fig.5.2c) with a monolayer or bilayer of WS_2 and a hBN thickness around 150 - 200 nm.

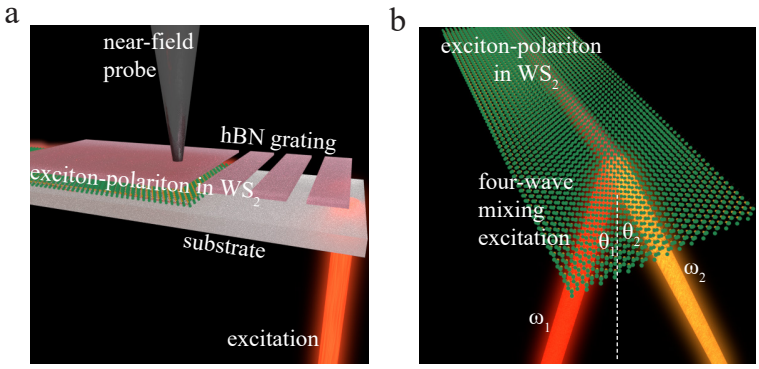

Figure 5.6: Measuring the exciton-polaritons
a. Method to measure the exciton-polaritons in WS_2 using a near-field microscope, with the WS_2 (in green) on a glass substrate (in grey) and with hBN on top (in pink). The excitation light (in red) initiates an exciton-polariton in the WS_2, after which the evanescent polariton mode is detected using a scanning aperture near-field probe (dark grey). **b.** Method to excite the exciton-polaritons in WS_2 using the non-linear optics of four-wave mixing. Here two excitation beams with different frequencies ω_1 and ω_2 (red and yellow) are combined on the WS_2 sample under different angles θ_1 and θ_2, to excite the exciton-polariton (red wave) in WS_2 (green).

Different experimental ways exist to initiate and detect polaritons [46], which is not entirely straightforward given their dispersion lying outside of the lightcone. This results in a wavevector mismatch between the maximal in-plane wavevector of the excitation light and the wavevector of the polariton. In this chapter, we propose two different initial experiments to excite and detect the exciton-polaritons in WS_2. As mentioned before, polaritons can and have been detected using near-field microscopy techniques [159–161]. Alternatively, nonlinear optical methods like four-wave mixing also allow addressing modes outside of the lightcone [163, 164]. Gratings can be added in both cases as a common aid for converting modes outside of the lightcone into free-space light or *vice versa* [165].

Figure 5.6a schematically presents the way of exciting and detecting polaritons in WS_2 using an aperture near-field microscope. The wavevector of the excitation light (in red) is matched to the wavevector of the polariton using a grating in the hBN slab (pink), exciting the exciton-polariton in WS_2 (green) on a glass substrate (grey). An alternative for solving the wavevector mismatch between excitation and polariton would be the use of a plasmonic nanoparticle. After excitation, the evanescent polariton mode is detected

by scanning an aperture near-field probe over the sample (dark grey). In order to measure the dispersion relation of the polariton mode, it would be essential for the near-field microscope to have phase sensitivity, in order not to rely on the presence of reflections of the mode [166]. Thus the dispersion can be deduced by the Fourier-transforming the measured electromagnetic field and determining the polariton wavevector at different excitation frequencies [166]. To distinguish the exciton-polariton from the contributions of light in air, glass, hBN in the Fourier transformed fields, a large WS_2 flake and therefore a large microscope scan length is needed.

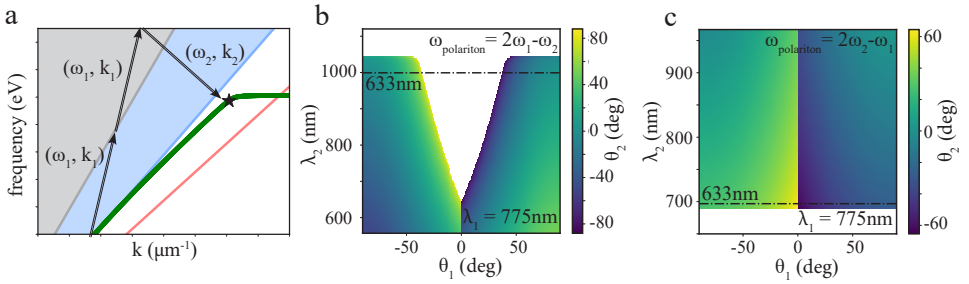

Figure 5.7: Four-wave mixing to excite the polaritons
a. Using four-wave mixing, the correct combination of the frequencies ω_1 and ω_2 and wavevectors k_1 and k_2 of the used excitation sources (depicted with arrows) is able to excite the polariton mode at different positions of its dispersion. **b,c.** all possible combinations of incident angles θ_1 and θ_2 and wavelengths λ_2 that will excite the exciton-polariton, taking a fixed wavelength $\lambda_1 = 775$ nm. The position of $\omega_{polariton} = 633$ nm is indicated by the dotted line in **b.** with $\omega_{4wm} = 2\omega_1 - \omega_2$ and in **c.** with $\omega_{4wm} = 2\omega_2 - \omega_1$.

Figure 5.6b schematically presents the method of exciting the exciton-polaritons using the non linear optical method four-wave mixing. Here two excitation beams with different frequencies ω_1 and ω_2 (red and yellow) are combined on the WS_2 sample under different angles θ_1 and θ_2, to excite the exciton-polariton (red wave) in WS_2 (green). In four-wave mixing, the frequencies of two beams are combined as $\omega_{4wm} = 2\omega_1 - \omega_2$ or $\omega_{4wm} = 2\omega_2 - \omega_1$ [164, 167]. Figure 5.7a depicts how the correct combination of the frequencies ω_1 and ω_2 and wavevectors k_1 and k_2 of the used excitation sources is able to excite the polaritonic mode that lies outside the light-cone. Here, we follow the method as proposed for exciting surface plasmon-polaritons using four-wave mixing [164]. The relevant equations are given by

$$\begin{aligned} \mp Re\{k_{polariton}(\omega_{polariton_1})\} &= 2k_1 \sin\theta_1 - k_2 \sin\theta_2 \text{ and} \\ \pm Re\{k_{polariton}(\omega_{polariton_2})\} &= 2k_2 \sin\theta_2 - k_1 \sin\theta_1, \end{aligned} \tag{5.3}$$

where the upper sign of $k_{polariton}$ corresponds to solutions $\theta_2 > \theta_1$, and the lower sign to $\theta_1 > \theta_2$. The solutions to these equations, *e.g.*, all possible combinations of incident angles θ_1 and θ_2 and wavelengths λ_2 with a fixed wavelength λ_1 that will excite the exciton-polariton mode in Fig.5.7a, are given in Fig.5.7b,c. For practical purposes, we

give the solutions in terms of the wavelength $\lambda = \frac{2\pi}{k}$ and not in terms of the frequency $\omega = \frac{ck}{n}$ (see [3]). Fig.5.7b corresponds to solutions with $\omega_{4wm} = 2\omega_1 - \omega_2$ and Fig.5.7c to $\omega_{4wm} = 2\omega_2 - \omega_1$. The dotted line indicates the position where $\lambda_{polariton} = 633\,\text{nm}$. In Fig.5.7b, the dotted line is at $\lambda_2 = 999\,\text{nm}$, and the horizontal cut-off around 1040 nm is caused by the horizontal part of the polariton dispersion at the bandgap energy of 2.0 eV. In Fig.5.7c, the dotted line is at $\lambda_2 = 697\,\text{nm}$, and the cut-off around 690 nm is caused by the horizontal part of the polariton dispersion. Therefore, the incident angles needed to excite the more interesting non-linear part of the polariton dispersion are in the upper part of Fig.5.7b and the lower part of Fig.5.7c. Given the larger range between the dotted line and the horizontal cut-off in Fig.5.7b, we conclude that it is experimentally feasible to use the four-wave mixing $\omega_{4wm} = 2\omega_1 - \omega_2$.

5.3. CONCLUSION

We have demonstrated the existence and studied the properties of hybrid exciton-polaritons in WS_2 - hBN samples. The shape of the polariton dispersion, the intensity of the polariton mode at the air interface and its in-plane propagation length are all affected by the thickness of both the hBN and the WS_2 in the used sample. For an experimental optimum, a trade-off needs to be found between a polariton dispersion that can be distinguished from free-space light, a high mode intensity at the air interface and a large in-plane propagation length. We therefore advice to use a sample with a monolayer of WS_2 and a hBN slab of 150 - 200 nm between the WS_2 and the glass substrate. The exciton-polaritons can be studied using a phase-sensitive near-field microscope, or using the non-linear method of four-wave mixing. For the latter, we calculate that a combination of 775 nm and roughly 1000 nm will excite the exciton-polariton in the more interesting and non-linear part of its dispersion relationship. With these calculations, we have bridged the gap between the theoretical prediction of exciton-polaritons and their practical realization. Thereby we open the way to applications based on the enhanced light-matter interaction so fundamental to exciton-polaritons.

6

MORPHOLOGY-INDUCED SPECTRAL MODIFICATION OF WS_2 PYRAMIDS

How do hollow WS_2 pyramids interact with light, and how are the intensity and the frequency of the optical response influenced by the nanogeometry of the pyramids?

Parts of this chapter have been published in [23], copyright 2021 Royal Society of Chemistry.
Data acquired for this publication can be found at DOI: 10.4121/13246751

6.1. INTRODUCTION

As mentioned in Section 1.3.2 of the Introduction, chemical vapor deposition (CVD) can both reproduce horizontal layers as found in naturally occurring TMDs, as well as produce nanostructures with diverse geometries. Under certain CVD growth parameters TMDs materials form pyramid-like structures [168, 169], having many active adsorption site useful for applications in hydrogen sensors [170] and water disinfection [171], at the same time possessing interesting electronic properties like ferromagnetism [172] and high mobility [173, 174]. Moreover, pyramid-like TMDs structures have applications in non-linear optics [173, 175, 176], as they exhibit higher non-linear optical conversion efficiency than monolayers due to the thickness increase, while demonstrating a much larger non-linear optical response than multilayer TMDs.

It is interesting to note that only in a limited number of studies in the literature photoluminescence of these spiral or pyramid like structures is reported [168, 169, 171, 173]. In some, the non linear optical response is studied [173, 175, 176]. In most, the TMDs spirals and pyramids are studied using Raman spectroscopy [168–175]. However, comparing the measured optical response of pyramid-like structures of different studies needs to be done with caution, as the terms spiral flake or pyramid are used for nanostructures that have different thicknesses, geometry and sizes. As described in Section 1.4.3 of the Introduction, Raman spectroscopy is a powerful tool to study 2D TMDs, as knowledge on the vibrational modes of the layers provides insights in their structure. Studying the Raman response as a function of temperature [62–66], excitation polarization [32, 55, 67] and excitation wavelength [71–73], provides information on structural properties like number of layers, strain and defect density. The existence of exciton resonances in 2D TMDs has large implications for its Raman response. Raman features are greatly enhanced when the excitation is in resonance with an excitonic transition [32, 56, 70–73]. Resonance Raman spectroscopy on 2D TMDs materials results in the excitation of higher-order phononic resonances [74], which yields rich Raman spectra with many more modes than the two mentioned characteristic modes.

Many questions arise about the nature of the optical response from complex CVD-grown TMDs pyramid like nanostructures. It is unknown how the nanogeometry of TMDs pyramids influences its photoluminescence and Raman response and how it depends on temperature and polarization. For potential applications, this knowledge is paramount. Here, we study the Raman and photoluminesence response of CVD-grown hollow WS_2 pyramids, comparing it to the optical response of WS_2 monolayers. Even though the WS_2 monolayers and pyramids are grown on the same substrate and under the same conditions, their measured optical response is completely different. We find, surprisingly, that the pyramids exhibit a strongly reduced photoluminescence (PL) with respect to horizontal layers. The reduced PL enables us to study the Raman signal of the hollow WS_2 pyramids, that contains both the characteristic Raman peaks of flat layers and a great number of higher-order phononic resonances. In contrast with the monolayers, the measured optical response of the hollow WS_2 pyramids is non-uniform over the nanostructures. Annular dark-field (ADF) scanning transmission electron microscopy (STEM) measurements confirm position-dependent variations in atomic arrangement.

6.2. RESULTS AND DISCUSSION

6.2.1. HOLLOW WS_2 PYRAMIDS

Figure 6.1a presents an SEM image of a CVD-grown hollow WS_2 pyramid (the substrate is a SiN film on Si, see Section 1.3.2 of the Introduction). The WS_2 is crystallized in a 3R-phase (see Fig.C.2c-d and Section C.1 in Appendix C.) The clear lines along the pyramid sides indicate single steps (see Fig.C.1c and Fig.C.2a,b in Appendix C). The geometry of the darker middle becomes more clear when examining the AFM image in Fig.6.1b. The height profile measured with the AFM along the blue line is presented in Fig.6.1c. The bottom of the crater in the middle is roughly 5.6 nm high with respect to the substrate, whereas the pyramid sides reach a height of 44 nm. The inset of Fig.6.1a displays a schematic representation of the hollow pyramid, depicting the stair-like sides in white and the crater with a bottom of finite thickness in the middle.

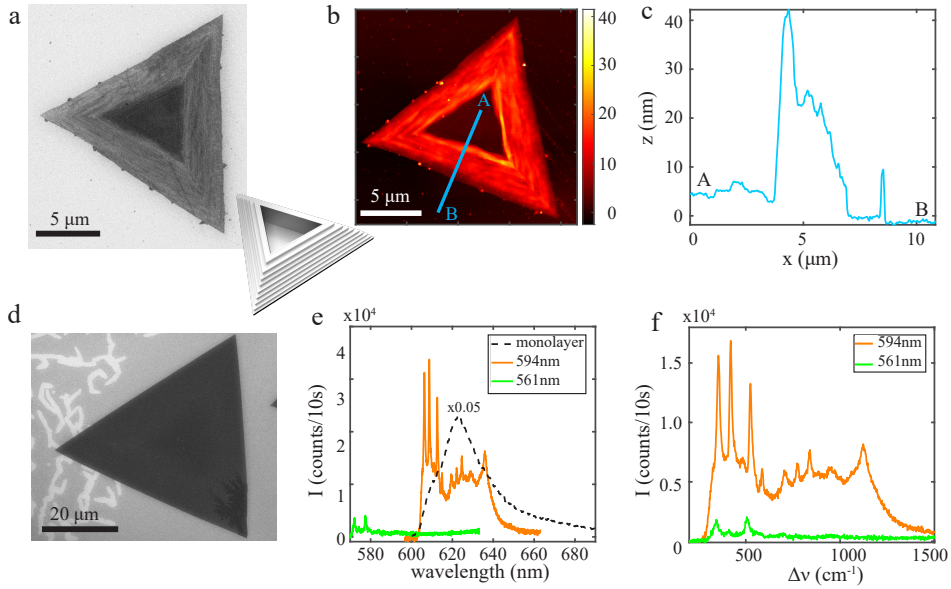

Figure 6.1: Hollow WS_2 pyramids
a. SEM image of the hollow WS_2 pyramid. The lines along the sides indicate the single stair steps, whereas the darker region in the middle is the crater. *inset.* Schematic representation of the hollow pyramid. **b.** AFM image of the hollow WS_2 pyramid. The blue line indicates the position of the AFM crosscut depicted in **c**, ranging from **A** the pyramid crater to **B** the substrate. **d.** SEM image of a WS_2 monolayer on the same substrate. **e.** Photoluminescence spectrum of the WS_2 monolayer (black dotted line), and spectra of a pyramid obtained with a 594 nm excitation (orange) and a 561 nm excitation (green). When converting the x-axis to wavenumber $\Delta\nu$ in **f**, the spectral response on the two different lasers overlaps nicely, indicating that the collected light originates from Raman processes rather than photoluminescence.

Figure 6.1e presents optical spectra obtained by exciting a WS_2 pyramid at the stair-like side with either a 594 nm laser (orange) or a 561 nm laser (green). The spectra contain a similar sequence of peaks, but their spectral position does not overlap in wavelength. However, these peaks are located at the same relative frequency distance to the excita-

tion laser, as depicted in Fig.6.1f. The clear overlap of the larger peak positions in the spectra from the two different lasers indicates that the collected light originates from an inelastic Raman process rather than from photoluminescence.

Figure 6.1d presents an SEM image of a single horizontal layer (monolayer) WS_2 grown on the same substrate (next to hollow pyramids and monolayers, also fully grown pyramids are present on this substrate, see Appendix C, Fig.C.1a, Fig.C.5 and Fig.C.6). Comparing in Fig.6.1e the optical response of the monolayer (black dotted line) with that of the pyramid, it becomes apparent that the pyramid exhibits a strongly reduced photoluminescence with respect to monolayer WS_2. A small background under the Raman modes is visible in the spectrum of the pyramid around the PL wavelength of 630 nm. If this is remnant PL emerging from the hollow WS_2 pyramid, it has an intensity of at most 1% of the WS_2 monolayer (see Appendix C Fig.C.3). The immense reduction of the photoluminescence intensity from the hollow pyramids is unexpected. Even though the pyramid crater is only a few nanometers thin, the pyramid spectra do not resemble spectra of standard few-layered horizontal WS_2 (see Appendix C Fig.C.3f). When the WS_2 thickness increases from monolayer to bulk, it transitions from a direct to an indirect bandgap semiconductor [12] (see Section 1.4.1). It is important to note that, in contrast to the hollow pyramids, the reduced PL from the direct bandgap can be easily measured for few-layered WS_2 [12, 93]. Moreover, the hollow WS_2 pyramids do not exhibit any luminescence at the known wavelength of the indirect bandgap, as would have been expected from both bulk and few-layer WS_2 (see Appendix C Fig.C.3f). Therefore we conclude that the increase of the layer number from monolayer WS_2 to the pyramid crater cannot explain the reduction of the PL intensity. CVD-grown horizontal 2D TMDs flakes exhibit a similar amount of photoluminescence as exfoliated samples. Hence, the PL intensity reduction by at least two orders of magnitude of the hollow pyramids cannot merely be explained as being intrinsic to the CVD growth process, *e.g.* through an increase in defect density. Furthermore, the 3R-WS_2 nanostructure cannot explain the PL intensity reductions, as 3R-WS_2 exhibits the same photoluminescence as the naturally occurring 2H-WS_2 [177, 178].

We conclude that our hollow WS_2 pyramids have a lower quantum efficiency than WS_2 flakes: assuming that the optical absorption of a WS_2 monolayer and a pyramid is the same, the quantum efficiency of these pyramids is at least two orders of magnitude lower than that of a monolayer WS_2. Given the fact that the pyramids have a thickness of 5 nm - 44 nm, it is safe to assume that a pyramid actually absorbs more than a monolayer, therefore the quantum efficiency is likely to be at least another order of magnitude lower. We attribute the decrease in the quantum efficiency to the increase in possible non-radiative loss channels due to the presence of all the edges in the structure of these pyramids. The increase in non-radiative loss channels due to the edges in the pyramid structure is therefore the main factor that leads to a severe quenching of the exciton photoluminescence, without influencing the Raman modes.

The reduction of the PL enables us to study the Raman response of the hollow WS_2 pyramids in more detail, as many Raman features are usually obscured by the PL spectrum. The pyramid spectra obtained with the 594 nm excitation exhibit roughly 10-12 Raman features, three of which have not been reported before for neither horizontal WS_2 layers

nor WS_2 nanostructures (see Fig.6.3). For the 561 nm excitation, fewer Raman features are visible in the spectra, and these features have a lower intensity. This can be attributed to the fact that the 594 nm excitation light is close to the A-exciton resonance, whereas the 561 nm is out-of-resonance with both the A- and B-excitons. Raman modes of TMDs can be greatly enhanced when they are excited in resonance with an excitonic transition [32, 56, 70, 72, 73].

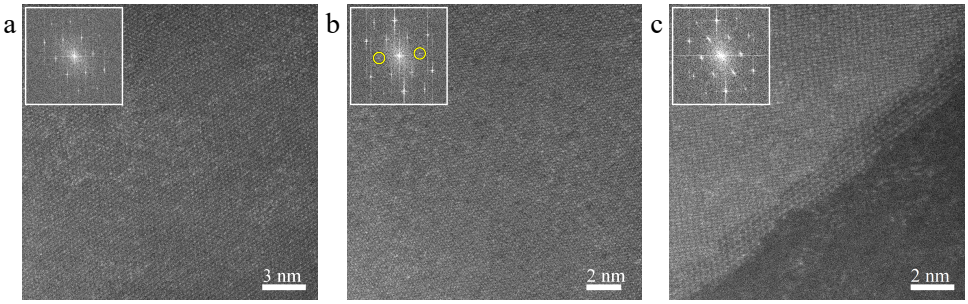

Figure 6.2: ADF-STEM of a hollow WS_2 pyramid
Atomic resolution annular dark-field scanning transmission electron microscopy images taken in **a-b** the middle region, and **c.** the side of a hollow WS_2 pyramid. Subtle variations in the atomic arrangement can be observed. The corresponding FFTs, as given as insets in each of the panels, highlight this feature further. Changes in the Bragg reflections occur between them. One of which is a reduction of the intensity of one of the Bragg reflections in the middle region of the hollow pyramid, as marked by the yellow circles in **b**.

6.2.2. STRUCTURAL CHARACTERIZATION

In order to help interpret the studied optical response, we perform a detailed structural characterization of the hollow WS_2 pyramids by means of Transmission Electron Microscopy measurements. Figure 6.2 displays annular dark-field (ADF) scanning transmission electron microscopy (STEM) images taken in different regions of these WS_2 nanostructures. Figures 6.2a and 6.2b display atomic resolution ADF-STEM images of two different locations corresponding to the middle region of the hollow pyramid, while Fig.6.2c corresponds to the pyramid side. By comparing these three images, we can clearly observe differences in the atomic arrangement. In Figure 6.2a, the atomic distribution displays a well defined hexagonal shape, and this symmetry is also highlighted by the corresponding fast Fourier transform (see inset in Fig.6.2a). As we can observe from Fig.6.2b, the atomic arrangements at this location are somewhat different from those observed in Fig.6.2a. This structural variation is also reflected in the corresponding FFT (inset in Fig.6.2b), where one of the Bragg reflections exhibits a reduced intensity (marked with a yellow circles to facilitate its visualization). Structural variation is also observed in the side region of the hollow pyramid. The difference in contrast in Fig.6.2c corresponds to two stair-like steps in the pyramid side. By comparing their relative atomic arrangement, we can determine that, while the external step exhibits a clear hexagonal honeycomb structure, this arrangement is lost in the subsequent layer. Note also that, as observed from the results obtained in the middle region of the nanostructures, even across its sides the atomic arrangement can vary slightly (see also Fig.C.7 in Appendix C).

These subtle variations of the atomic arrangement might be induced by the local pres-

ence of strain, which in turn results into a slight change of the orientation of the flake. Importantly, the level of structural disorder is more marked in the middle of the pyramids as compared to the sides (see Fig.C.7) due to the additional presence of free-standing WS_2 flakes arising from the walls of the hollow pyramid.

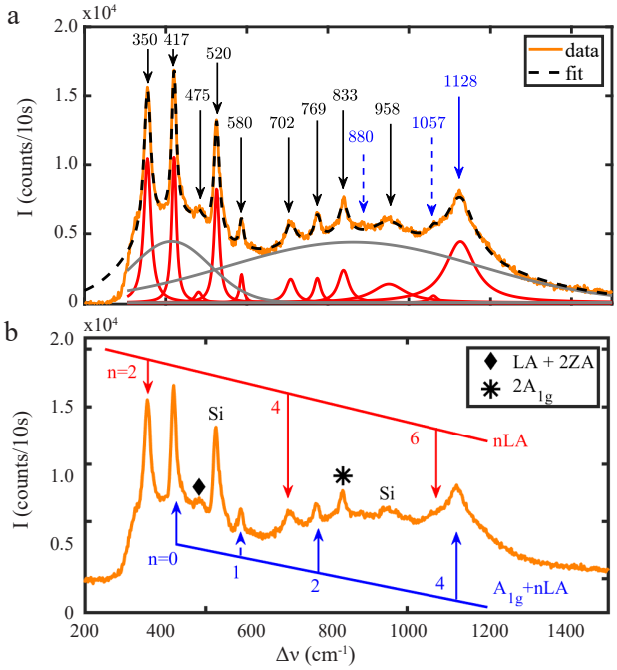

Figure 6.3: Characterization of Raman peaks
a. The optical response of the hollow pyramids (orange) can be fitted by eleven Lorentzian lineshapes (red) and two Gaussians (grey). The Raman features are indicated by arrows with their spectral position in cm^{-1}. The last three features (in blue) have not been reported before. **b.** Part of the features can be explained as being multiphonon resonances involving the LA(M) phonon. The blue line depicts the higher order resonances of A_{1g}+n*LA(M). The red line depicts the higher order resonances of n*LA(M).

6.2.3. CHARACTERIZATION OF VIBRATIONAL MODES

In Figure 6.3a we present a WS_2 pyramid spectrum, acquired at the pyramid side, in which all Raman features are indicated with arrows. Commonly, only three Raman modes are measured on both horizontal TMDs layers or nanostructures. We measure 10-12 Raman features, three of which have not been reported previously (indicated in blue in Fig.6.3a). The other modes can be attributed following a limited amount of previous investigations (see also Table 6.1). In order to analyze the spectra in more detail, we fit the overall spectrum with a collection of eleven Lorentzian lineshapes (red) and a background consisting of two Gaussians (grey) (see Appendix C, Section C.2 for a discussion on the background). This way we are able to attribute the new Raman modes from hollow WS_2 pyramids to being multiphonon resonances involving the LA(M) phonon, adopting the methodology for high frequency Raman features in MoS_2 [74]. The blue

line in Fig.6.3b depicts the higher order resonances of A_{1g}+n*LA(M). The peak 580 cm^{-1} is commonly attributed to A_{1g}+LA(M) [56, 62, 63, 179], and the peak at 769 cm^{-1} is attributed to A_{1g}+2LA(M) by Molas *et al* [179]. Thus we attribute the newly observed peak at 1128 cm^{-1} (n=4) to A_{1g}+4LA(M). The red line in Fig.6.3b depicts the higher order resonances of n*LA(M). The peak at 702 cm^{-1} is commonly attributed to 4LA(M) [56, 62], which is twice the first 2LA(M) Raman peak at 350 cm^{-1}. Therefore we attribute the newly observed small shoulder of the last peak around 1057 cm^{-1} to 6LA(M). The expected resonance at 3LA(M) (red line in Fig.6.3b) would spectrally overlap with the first silicon peak at 520 cm^{-1}, as well as the expected resonance at n=3 (blue line in Fig.6.3b) would overlap with the second silicon peak 955 cm^{-1}, so these possible features cannot be distinguished from the substrate response. The expected 5LA(M) (red line in Fig.6.3b) would be around 880 cm^{-1}, but is too dim to distinguish very clearly from the background. The peak at 833 cm^{-1} is 2*A_{1g}, and the peak at 475 cm^{-1} is commonly attributed to LA(M)+2ZA(M) (see Table 6.1). We conclude that the observed high-frequency Raman modes are multiphonon resonances involving the LA(M) phonon, excited because the 594 nm laser is in resonance with the A-exciton.

The highest frequency Raman modes have not been reported before on horizontal WS_2 layers (indicated in blue in Fig.6.3a). A possible explanation for not observing them on monolayers is that investigating Raman modes on horizontal WS_2 layers is experimentally challenging because of the presence of photoluminescence, that is much brighter than any Raman feature. An intriguing alternative hypothesis is that the nanogeometry of the hollow pyramid plays a role in exciting the higher order Raman modes more resonantly, *e.g.* through a higher phonon density of states.

6.2.4. POSITION DEPENDENCE OF SPECTRAL FEATURES

The hollow WS_2 pyramids contain two distinct regions: the crater in the middle and the stair-like sides. We find that these regions exhibit a different spectral response. This is in contrast from the more homogeneous spectral response for horizontal WS_2 flakes (see Appendix C, Fig.C.5 and Fig.C.6). Figure 6.4a presents an intensity map of the first Raman peak (E_{2g},2LA). To create this map, the maximum value of the fitted peak is used (see Fig.6.3a). The peak intensity is higher and the peaks are more pronounced at the pyramid crater than at the stair-like sides. For the other WS_2 Raman peaks, as well as at different temperatures and using different excitation wavelengths, this intensity distribution looks similar (see Appendix C Fig.C.4).

Figure 6.4b presents an intensity map for the silicon peak at 520 cm^{-1}. As expected, there is a constant intensity for the substrate next to the pyramid. It is interesting to note that the intensity of this substrate peak also decreases on the pyramid edges. We hypothesise that light scatters a lot from the stair-like pyramid sides, as seen from the bright white colour of the sides in the optical image (Fig.6.4c). This both reduces the available excitation light to excite Raman modes, and scattering of the resulting Raman response reduces the detected light, including the Raman response of the silicon substrate. Figures 6.4d-e depict spectra on three different positions: on the hollow pyramid middle (red), on the substrate (green) and on the pyramid side (black) (indicated by stars in Fig.6.4a,b). In both the room temperature spectra in Fig.6.4d and 4 K spec-

position	std (cm^{-1})	brightness	attributed to	possibly	literature
350 cm^{-1}	1.6	++	E^1_{2g} / 2LA(M)		[32, 55, 56, 62] [72, 179, 180]
417 cm^{-1}	1.5	++	A_{1g}		[32, 56, 62] [72, 179, 180]
475 cm^{-1}	4.7	- -	LA + 2ZA or E"(M) + TA(M)		[179] [73]
520 cm^{-1}	0.8	++	Si	3LA(M)	[181–183]
580 cm^{-1}	1.0	+-	A_{1g} + LA(M)		[56, 62, 63] [179, 180]
702 cm^{-1}	1.4	+	4LA(M)	$2E^1_{2g}$	[56, 62, 180] ([179])
769 cm^{-1}	1.0	+	A_{1g} + E^1_{2g}	A_{1g} + 2LA(M)	[179]
833 cm^{-1}	1.2	+	$2A_{1g}$		[179]
880 cm^{-1}		- -		5LA(M)	
958 cm^{-1}	3.3	+-	Si	A_{1g} + 3LA(M)	[181–183]
1057 cm^{-1}	1.0	- -		6LA(M)	
1128 cm^{-1}	4.0	+		A_{1g} + 4LA(M)	

Table 6.1: Overview of the measured Raman features on the hollow pyramid (see Fig.6.3) at room-temperature. The first column gives the peak position determined by fitting, with the statistical standard deviation in the second column and the brightness in the third. The fourth column indicates known Raman modes, where the last column gives a few references. The fifth columns indicates possible explanations, either taken from only one article or being our hypothesis.

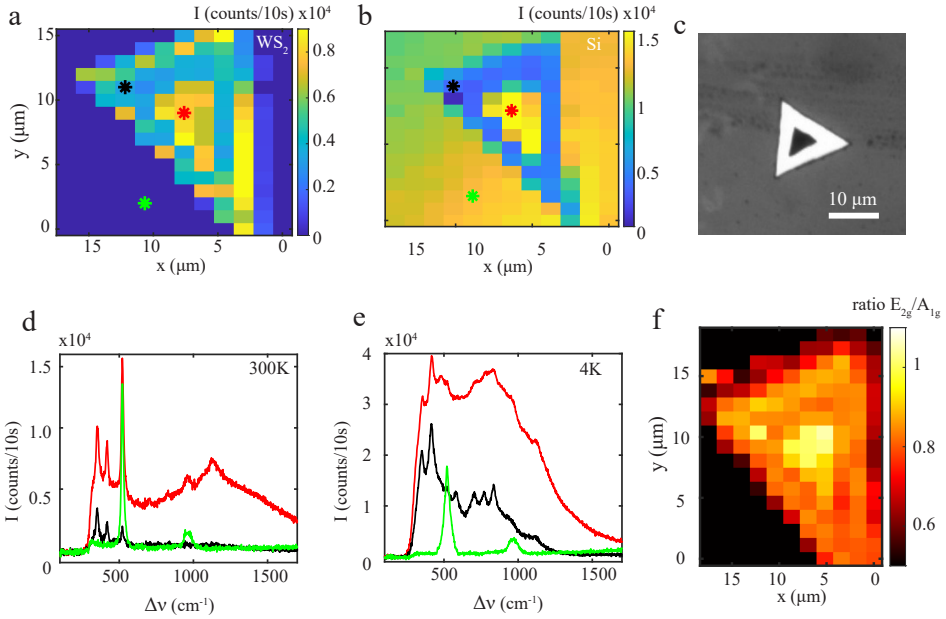

Figure 6.4: Position dependence of intensity and shape of spectra
a. Intensity map of the first WS_2 Raman feature around 350 cm^{-1}, with a step size of around 1.5 μm. The stars indicate the positions of the spectra in **d-e**. Note that the x and y axis in the map are slightly skewed due to experimental constraints (see Experimental Section). **b.** Intensity map of the Si Raman peak at 520 cm^{-1}. **c.** Optical image of a hollow WS_2 pyramid. Note the white colour at the sides, indicating a clear increase in scattering from the sides with respect to the top. **d,e.** Pyramid spectra at 300 K and 4 K. The substrate spectrum (green) shows the two Si peaks at 520 and 955 cm^{-1}. The spectrum at the hollow part of the pyramid (red) has an overall higher intensity than at the side (black). **f.** Map of the ratio between the first two Raman features in the spectra (E_{2g}/A_{1g}).

tra in Fig.6.4e (temperature dependence will be discussed later), the two silicon peaks at 520 and 955 cm^{-1} can be clearly distinguished (in green). The spectrum at the pyramid crater (red) has clearly a higher overall intensity. In addition to the Raman peaks, there is also a background visible. Especially at 4 K, this background signal becomes extremely high, turning the signal from all the higher frequency Raman modes into mere shoulders. Based on its spectral position, we attribute this background to intermediate gap states or defect states (see Appendix C Fig.C.3). It is interesting to note that this background is significantly higher in the pyramid crater than on the sides, which might be originated by the presence of crystallographic defects.

Figure 6.4f presents a map of the intensity ratio between the first two Raman peaks (E_{2g}/A_{1g}). Just like the intensity of the individual peaks, this intensity ratio is also non-uniform over the WS_2 pyramid. In the pyramid crater, the peak ratio is approximately 1.0, whereas on the stair-like sides, the A_{1g} peak is higher. The difference in peak ratio between the pyramid crater and sides is also present and much higher for the 561 nm excitation (see Appendix C Fig.C.5). Note that the spectral features of a fully grown pyramid are very similar to the spectral response from the hollow pyramid sides (see Appendix C Fig.C.5). We conclude that both the peak intensity and the overall shape of the spectra are non-uniform along the WS_2 pyramid, behaving differently at the hollow pyramid crater and the stair-like sides. This indicates a difference in the atomic arrangement between the two parts of the pyramid.

We also find a spatial non-uniformity in the spectral position of the peaks. Figure 6.5a depicts the spectral position of the first WS_2 Raman peak (E_{2g},2LA) as a function of position. This spectral position is fairly uniform over most of the nanostructure, except for the right edge, where the spectral position is red shifted significantly up to 320 cm^{-1}. Moreover, a small blue shift of the peak is seen on the left pyramid edge. The second WS_2 Raman peak exhibits a similar spectral shift (not shown), as do spectra obtained for a 561 nm excitation. This spectral shift of peaks becomes more evident when comparing the spectra at the positions of the blue stars (Fig.6.5b). The second line indicates the position of the silicon peak at 520 cm^{-1}, which is clearly constant in all three spectra. However, when comparing the line at 355 cm^{-1} with the position of the first Raman peak, it is clear that the WS_2 peaks in the spectrum are blue shifted.

The spectral position of Raman modes in TMD materials is known to depend on the number of layers [32, 53, 56, 172, 173]. One might therefore have expected a gradual spectral shift along the stair-like sides of the pyramid, because of their gradual increase in WS_2 layer thickness. Unfortunately, the diffraction-limited laser spot of size 500 nm (see Section 2.2 of Chapter 2) is much larger than the width of the individual terraces. Therefore, if the size of the steps is one or even a few layers, we do not have the resolution to distinguish thickness-dependent changes in the Raman response of individual steps. The changes in the Raman response are smallest for low N, where N is the number of layers. The reported difference in spectral position for different layer thicknesses is at most 5 cm^{-1} (between a monolayer and a bilayer), much less than the shift of 30 cm^{-1} that we observe at the edge of this pyramid. Therefore this spectral shift cannot be explained by a thickness increase alone.

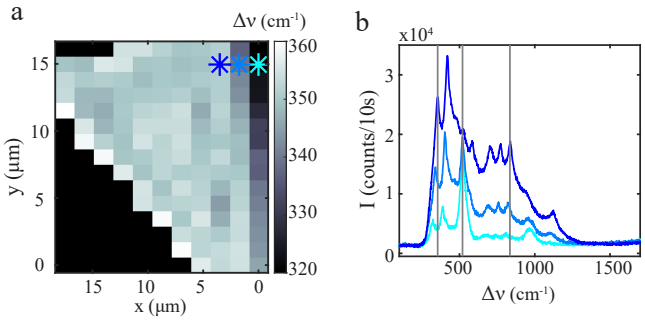

Figure 6.5: Position dependence of spectral position
a. Map at 4 K of the spectral position of the first WS_2 Raman feature (2LA(M),E_{2g}), with a step size of around 1.5 μm. The spectral position is fairly homogeneous over most of the pyramid, except for the edge, where it is blue shifted up to 320 cm^{-1}. The stars indicate the position of the spectra in **b.** Three gray lines are drawn as guides to the eye. Comparing the position of the Si peak of the three spectra with the line at 520 cm^{-1} indicates that the spectral position of this peak does not shift. Comparing the position of the first WS_2 peak with the line at 355 cm^{-1} does indicate the large shift of the spectrum on the pyramid edge (light blue) with respect to the rest of the nanostructure.

The spectral position of Raman modes in TMD materials does not only depend on the number of layers, it is also known to be influenced by the defect density [58, 59], strain [60, 61] and pressure [64]. The reported shift due to strain is 2-3 cm^{-1} [60, 61] and due to an increased defect density is 5-10 cm^{-1} [58, 59]. For both strain and defects, the A_{1g} peak is much less affected than the E_{2g} peak. The reported shift due to pressure is up to 40 cm^{-1} for pressures up to 20 GPa [64]. Since our measurements were performed in either ambient (room temperature) or vacuum (low temperature) conditions, we do not expect a spectral shift due to pressure. It is not unlikely that a large defect density and/or the presence of strain are present in the hollow pyramids. Interestingly, spectra taken on fully grown WS_2 pyramids with curved edges do exhibit small shifts in the spectral peak position along the edges with highest curvature, where a higher stress or strain is expected (see Appendix C Fig.C.6). Therefore we assume that the origin of the large spectral shift in the hollow WS_2 pyramid in Fig.6.5 lies in a combination of the mentioned effects of defect density and strain or stress. Having said that, the previously reported shifts, even when added, are much lower than the 30 cm^{-1} that we observe on the edge of the hollow pyramid, so we cannot exclude unknown other causes related to the specific nanogeometry of the hollow pyramid.

In this context, it is interesting to note that we measure an average spectral position of the first Raman peak on a WS_2 monolayer of 357 cm^{-1}, which is higher than the average of 350 cm^{-1} of this and other WS_2 pyramids (see Appendix C Fig.C.6). Given that the first WS_2 Raman feature is a combination of the E_{2g} and 2LA(M) phonon, we hypothesise that the first Raman feature in the monolayer has a larger contribution from the E_{2g} than the same first feature in the hollow pyramid spectra.

We conclude that the spectral features of the hollow pyramids, namely intensity, peak ratio and spectral peak position, vary in space over the nanostructures. This in con-

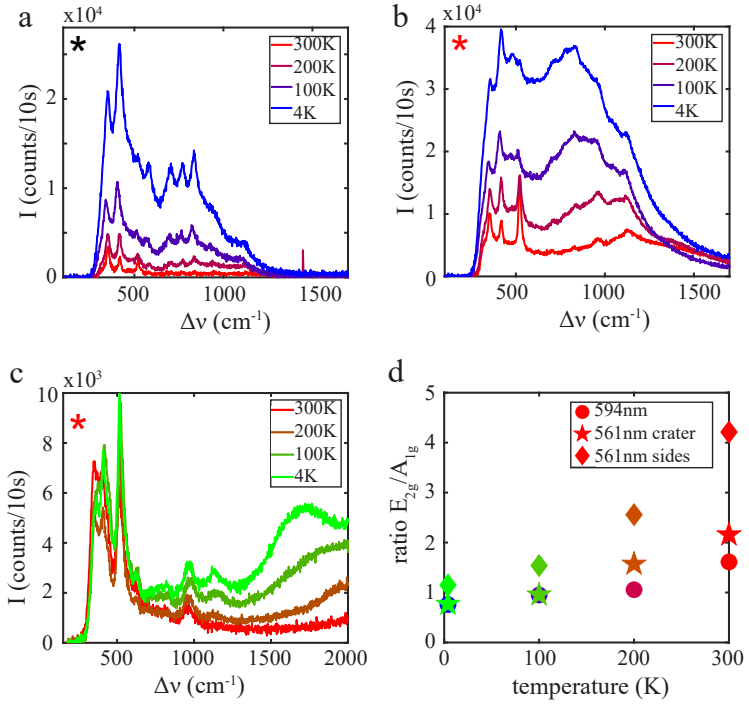

Figure 6.6: Temperature dependence of spectral features
a. Spectra obtained with a 594 nm excitation on the stair-like pyramid sides (black star in Fig.6.4) as a function of temperature. **b.** Spectra (with a 594 nm excitation) of the hollow pyramid middle (red star in Fig.6.4) as a function of temperature. **c.** Spectra obtained with a 561 nm excitation of the hollow pyramid middle as a function of temperature. The background visible at higher frequencies overlaps in wavelength with the background under the 594 nm spectra in Fig.6.4b (see Supplementary Materials Fig.S3) **d.** Temperature dependence of the intensity ratio of the first two Raman features, the fingerprint of WS_2 material. The intensity ratio is presented for spectra upon 594 nm excitation (circles), spectra at the pyramid crater (stars) and pyramid sides (diamonds) upon 561 nm excitation.

trast with the homogeneous distributions of these spectral features on a WS_2 monolayer. Moreover, the spectral position of the first WS_2 Raman feature is different for a WS_2 monolayer than for a hollow WS_2 pyramid, indicating a larger contribution from the E_{2g} than the 2LA(M) phonon.

6.2.5. TEMPERATURE DEPENDENCE OF SPECTRAL FEATURES

Studying the temperature dependence of spectral features provides insights on the structural properties of the WS_2 pyramids. Figure 6.6a presents spectra at four temperatures at the pyramid side (black star in Fig.6.4a), obtained with a 594 nm excitation. With decreasing temperature, the Raman modes become more pronounced. Note for instance the three features at 702, 769 and 833 cm^{-1}. The intensity of both the Raman features and the background increases with decreasing temperature. This intensity increase of the background is even more clear in Fig.6.6b-c, that presents the spectra from the hollow pyramid middle (red star in Fig.6.4a) obtained upon either 594 nm or 561 nm excitation. The background also seems to exhibit a spectral blue shift as a function of temperature, with its maximum moving from 635 nm at room temperature to 620 nm at 4 K. Based on the temperature dependence of its spectral position, we attribute this background to intermediate gap states or defect states rather than excitons, trions or an indirect bandgap response (see Section C.2 of Appendix C).

Figure 6.6d presents the temperature dependence of the average intensity ratio of the first two Raman peaks (E_{2g}/A_{1g}). As shown in Fig.6.4f, this ratio is not uniform over the pyramid, but is higher at the hollow pyramid middle than at the stair-like sides. This non-uniformity is most evident in the spectra obtained by 561 nm excitation (diamonds in Fig.6.6d), as the A_{1g} peak in the spectra from the pyramid sides almost completely disappears at room temperature (see Appendix C Fig.C.5). For a 594 nm excitation, at room temperature the first Raman peak (E_{2g},2LA(M)) is 1.5x higher than the second Raman peak (A_{1g}) and at 4 K this ratio is exactly inverted (circles in Fig.6.6d). The peak ratio upon 561 nm excitation of spectra taken at the pyramid middle follow a similar temperature-dependent behaviour (stars in Fig.6.6d).

The temperature-dependent intensity increase of TMDs Raman peaks has been reported previously for horizontal TMDs layers, and is attributed to an increase in phonon thermal population [62, 63, 66]. The difference in intensity ratio between the E_{2g} and A_{1g} for the different excitation frequencies can be explained by the more resonant 594 nm laser exciting the Raman peaks differently than the out-of-resonance 561 nm laser [71, 72]. The strength of the exciton-phonon interaction, and therefore the resonance condition, is different for the in-plane E_{2g} than the out-of-plane A_{1g} Raman modes [72, 184]. This explains why the ratio E_{2g}/A_{1g} is higher for a 561 nm excitation, *e.g.*, out-of-resonance with the excitonic transition, than for the resonant 594 nm excitation. The Raman intensity ratio also depends on the layer thickness of the material [32]. However, the main difference in intensity ratio is reported between a monolayer and a bilayer, whereas we observe different relative Raman intensities between the few-layer pyramid crater and the thick pyramid edge. Moreover, the temperature-dependent behaviour of the Raman intensity also depends on the defect density in the sample [65]. These factors are not mutually independent, *e.g.*, the WS_2 thickness influences the exciton-phonon interaction,

the resonance of the excitation affects the influence of phonons and defects on the Raman intensity. The temperature dependence of the Raman peak intensities, excited with two different frequencies, is therefore an interplay between the phonon thermal population, the resonance conditions for the different phonon peaks and the defect density in the structure.

It is interesting to note in this context the intensity ratio of the first two Raman peaks on a WS_2 monolayer, excited at 561 nm. This ratio is 1.4 at room temperature, much lower than both the intensity ratio at the hollow pyramid middle and at the stair-like sides, excited at 561 nm (see Appendix C Fig.C.5). Unexpectedly, this indicates a clear difference in structure and/or thickness between the WS_2 monolayer and hollow pyramid. The large difference in intensity ratio on the hollow pyramid middle and the stair-like sides suggests a difference in atomic arrangement, pointing out that nanogeometrical differences induce spectral modifications.

6.3. CONCLUSION

We have studied the optical response of hollow WS_2 pyramids, comparing them with WS_2 monolayers grown on the same substrate. The optical response of these nanostructures is completely different, as hollow WS_2 exhibit a strongly reduced photoluminescence with respect to WS_2 monolayers. This enables us to study the rich variety of Raman peaks that the pyramids exhibit as a result of the resonant excitation. Following the hypothesis of a multiphonon excitation involving the longitudinal acoustic phonon LA(M), we are able to explain the origin of all 10-12 observed Raman resonances. In contrast with monolayers, the measured optical response of the pyramids is non-uniform in both intensity, intensity ratio between peaks, spectral shape and spectral position. We attribute the spectral differences between the hollow pyramid middle and the stair-like sides to differences in both nanogeometry and atomic arrangement. ADF-STEM measurements confirm variations in the atomic arrangement, where the level of disorder is more marked in the pyramid crater than on the sides. Next to a positional dependence, we measure the temperature dependent behaviour of the spectral response of the hollow WS_2 pyramids. With decreasing temperature, the spectra change in intensity and shape. We see clear differences between spectra obtained with a resonant and out-of-resonance excitation laser. As the optical response of WS_2 monolayers, exhibiting photoluminescence, is completely different, we therefore deduce to have fabricated a platform of structures with tunable optical properties. Both nanostructures offer exciting possibilities, with applications ranging from opto-electronics to non-linear optics.

6.4. EXPERIMENTAL SECTION

The transmission electron microscopy (TEM) measurements were carried out using an ARM200F Mono-JEOL microscope with Cs probed corrected. The microscope was operated at 200 kV both in TEM and STEM modes, with the monochromator on and a slit of 2 μm inserted. For the atomic resolution ADF-STEM measurements, an objective aperture of 30 μm and a camera length of 12 cm were used. The convergence semi-angle was 23 mrad.

7

OPTICAL STUDY OF CVD GROWN WS_2 NANOFLOWERS

How can we use polarization-resolved Raman spectroscopy to probe differences in the orientation of WS_2 nanoflowers?

Data acquired for this chapter can be found at DOI: 10.4121/16628488

7.1. INTRODUCTION

As described in Section 1.3.2 of the Introduction, chemical vapor deposition (CVD) offers the possibility of fabricating vertical TMDs walls [185], pyramids [23] (see Chapter 6) and flower-like nanostructures [13, 186–188]. Potential applications of flower-like TMDs structures range from catalysis [13, 188] to using their large field emission as a potential electron source [186, 187]. However, so far TMDs nanoflowers have mainly been studied using electron microscopy tools [13], and little is known about their interaction with light. It is interesting to note that, in contrast to flat layers, no PL but only a Raman response is reported from vertical TMDs walls [185, 189], TMDs pyramids [23] (see Chapter 6) or flower-like TMDs structures [186–188].

As mentioned in Section 1.4.3 of the Introduction, Raman spectroscopy offers a powerful and non-invasive tool for the investigation of TMDs materials [32, 53, 56, 179]. Interestingly, the TMDs' Raman response is highly enhanced when the excitation is on resonance with an excitonic transition [56, 72–74]. Since this resonance effect can be observed in the Raman response even in the absence of photoluminescence, resonance Raman spectroscopy offers a way to study the TMDs exciton indirectly (see Chapter 6). As the TMDs bandgap energy depends on temperature, varying the temperature of a TMD material enables the tuning of the resonance condition for a fixed excitation frequency. Therefore, studying TMDs at various cryogenic temperatures provides insights on the influence of the excitonic transition on the Raman response. Moreover, temperature-dependent Raman spectroscopy can shed light on the structural properties of TMDs materials [63, 66].

The Raman response of TMDs is influenced by the polarization of the excitation light, where the in-plane and the out-of-plane vibrations of the atoms respond differently to either orthogonal, in-plane polarization [32]. Furthermore, given the chirality of the TMDs valleys and the resonant influence of the excitons on the Raman response, studying the interaction of TMDs phonons with circularly polarized light is important [67–69]. As the Raman effect depends on the polarizability of the material, the interaction of TMDs with polarized light is described by a Raman polarizability tensor [68, 190, 191]. It is important to note that these tensors are defined with respect to the atomic axes, *e.g.*, typically assuming flat-layered TMDs with the excitation light perpendicular to it. Thus, the polarization-resolved Raman response of for instance a vertical TMDs wall will be completely different than that of a flat layer, *e.g.* modes that are usually allowed/forbidden in cross-polarization will now be absent/observed [189–192]. Therefore, polarization-resolved Raman studies will provide insight in the flowers' nanogeometry and orientation.

In this work, we study the polarization- and temperature-dependent optical response of WS_2 nanoflowers. The nanoflowers exhibit a highly reduced PL enabling the study of the thereby unobscured Raman response. At first glance, no spectral differences are observed between WS_2 flowers of different geometry, except for differences in Raman intensity. However, polarization- and helicity-resolved Raman spectroscopy reveals underlying structural differences between flowers. We find that petals of the flowers oriented vertically exhibit a different response to circularly polarized light than more flat

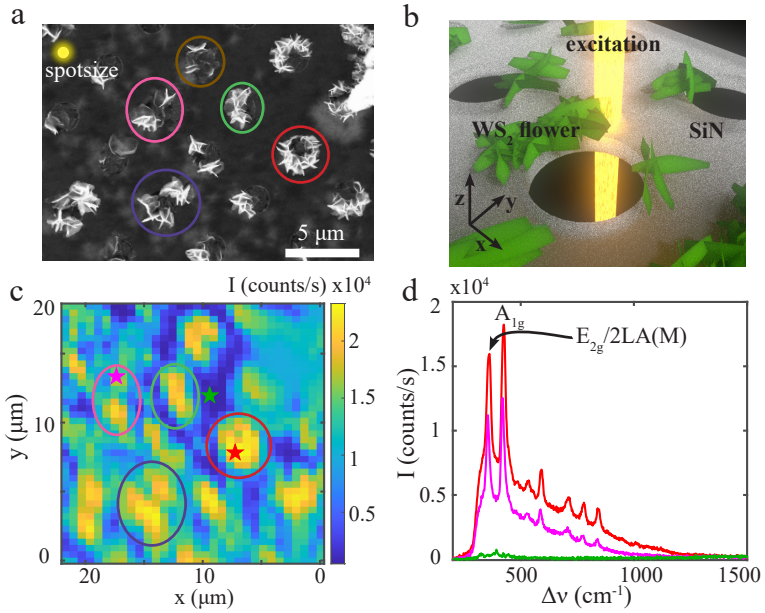

Figure 7.1: Optical response of WS_2 nanoflowers
a. SEM image of the WS_2 nanoflowers on a SiN membrane with circular holes. The flowers grow mainly around the holes, forming diverse flower-like shapes ranging from circles (red) and half-circles (green) to vertical walls (brown, pink) and more chaotic structures (purple, pink). In yellow the size of the excitation laser spot (500 μm). **b.** A schematic representation of the SiN substrate (grey) with holes (black), WS_2 nanoflowers (green) and the excitation laser (yellow). **c.** Map of the peak intensity of the first Raman feature (denoted with an arrow in **d**), where the shape of the flowers can be clearly correlated with the SEM image in **a** (see colored circles as guide to the eye). **d.** Spectra at different positions indicated with stars in **c** on flowers (red and pink) and on the substrate (green). Note that, even though the flowers have a diversity in shapes, the only difference between spectra of flowers is the intensity the Raman features.

flower petals. Moreover, we find that the relative in-plane orientation of the flower petals with respect to the polarization direction of linearly polarized light, affects the optical response. Surprisingly, the polarization- and helicity-dependent behaviour of the characteristic in-plane and out-of-plane WS_2 Raman modes is similar, indicating the similarity of the underlying Raman tensors. Studying the temperature-dependent spectral response of WS_2 nanoflowers, we observe the influence of the excitonic resonance on the Raman intensity, helicity and the ratio between the two characteristic WS_2 Raman features.

7.2. RESULTS AND DISCUSSION

7.2.1. OPTICAL RESPONSE OF WS_2 NANOFLOWERS

Figure 7.1a depicts a Scanning Electron Microscopy (SEM) image of the WS_2 nanoflowers. The flowers are fabricated using CVD on a Si_3N_4 membrane (200 nm thickness) with an array of holes (2 μm radius and 4 μm pitch, see Figure D.3a in Appendix D). Details about the fabrication and an in-depth study of the electronic and crystallographic properties of these nanoflowers are given by Van Heijst *et al* [13]. Just as natural flowers, these WS_2 nanostructures consist of randomly oriented flakes (the petals) expanding from a common point. The WS_2 nanoflowers arise mainly around the holes in the substrate (see Fig.7.1a), forming diverse shapes ranging from circles (red) and half-circles (green) to vertical walls (brown, pink) and more chaotic structures (purple, pink). The larger structure to the right of Fig.7.1a is probably a conglomeration of WS_2 grown around a dust particle. Figure 7.1b schematically presents the nanoflowers (green) around the holes (black) in the substrate (grey). The excitation light is along the z-axis, and the orientation of the flower petals ranges from completely flat (in x-y plane) to standing up (x-z or y-z plane). The petal thickness is estimated to be between 2 and 30 nm [13]. The previously performed scanning transmission electron microscopy (STEM) study reveals that the nanoflowers exhibit a crystallographic polytypism 2H/3R [13] (see Section D.2.2 of Appendix D).

We investigate the optical response of the WS_2 nanoflowers, which consists mainly of a Raman response. Figure 7.1c presents the intensity of the first Raman feature (see arrow in Fig.7.1d) of the flowers depicted in Fig.7.1a. The Raman map can be correlated with the SEM image by comparing the shape and relative position of the flowers (*e.g.*, compare the coloured circles in Fig.7.1a and Fig.7.1c). Not surprisingly, the more dense flowers, for instance the circular flower (red) and the half-circle (green), exhibit a larger Raman intensity than the structures with mainly upstanding walls (brown, upper part of pink). It is important to note in this context that the size of our diffraction limited excitation spot (500 nm, see Section 2.2 of Chapter 2) is much larger than the size of an individual flower petal. For an easy comparison, the size of the excitation spot is indicated on scale in yellow in Fig.7.1a. The Raman signal of the flowers in the Raman map is 'smeared out', and the area of plain substrate is actually much larger than it seems on the Raman maps (compare Fig.7.1c with the SEM image in Fig.7.1a). The reason for the 'smearing out' is that we measure a convolution of the excitation and detection volume with the spatial distribution of the optical response of the flowers. It is to be expected that the spatial distribution of the optical response of the nanoflower response is re-

lated to the size of the flower features. Figure 7.1d presents optical spectra of the WS_2 nanoflowers. Like the spectra of the pyramids (see Chapter 6), the spectra of the flowers contain of 8-10 Raman features, where the first two features are the characteristic vibrational modes of WS_2 (see Figure D.2 in Appendix D). The first feature is a combination of the in-plane vibrational mode E_{2g} and the longitudinal acoustic phonon 2LA(M) (in WS_2, the frequency of these modes is almost the same), and the second feature is the out-of-plane vibrational mode A_{1g}. We attribute the higher frequency Raman features to multiphonon resonances involving the LA(M) phonon, excited because the 594 nm laser is in resonance with the A-exciton, in accordance with the attribution for WS_2 pyramids (see Chapter 6 and Section D.2.1 of Appendix D for details).

The spectra in Fig.7.1d are collected from different positions of the sample: on the Si_3N_4 substrate (green), on a dense nanoflower (red) and on a vertical-wall nanoflower (pink) (indicated with stars in Fig.7.1c). It is interesting to note that the only difference between the red spectrum of the more dense flower and the pink spectrum of the vertical-wall flower is in the overall Raman intensity and not in the spectral position of the Raman peaks. There are no Raman features more or less pronounced for flowers with different nanogeometries.

Like the WS_2 pyramids (see Chapter 6), the WS_2 nanoflowers exhibit a strongly reduced photoluminescence (PL) with respect to horizontally layered WS_2. On some flowers, no PL can be observed from the nanoflowers within our detection efficiency. Specific parts of some nanoflowers do exhibit a low PL, which becomes apparent especially at cryogenic temperatures (see Fig.D.1 in Appendix D). At 4 K, this is at most 2 % of the PL of a monolayer WS_2. Assuming that the absorption and the effective collection efficiency remain constant, we conclude that the CVD grown WS_2 nanoflowers have a lower quantum efficiency than horizontal WS_2 flakes. Here the assumption of a constant absorption is reasonable given the petal thickness, whereas the assumption of a constant effective collection efficiency is related to the unknown emission pattern from the nanoflower petals and therefore less strong. We attribute the decrease in the quantum efficiency to the increase in possible non-radiative loss channels due to the presence of all the edges of the nanoflower petals. This leads to a severe quenching of the exciton photoluminescence, without influencing the Raman response.

7.2.2. POLARIZATION-RESOLVED RAMAN RESPONSE

To investigate the optical differences between different flowers in more detail, we study the interaction of the flower Raman response with linearly polarized light. Here we excite the WS_2 nanoflowers with linearly polarized light, rotating the polarization direction from vertical to horizontal, and analyze the resulting emission intensity (see Section 2.4 in Chapter 2 for a schematic of our set-up). Figure 7.2a depicts an SEM image of a flower-like WS_2 structure (indicated in brown in Fig.7.1a) with mainly wall-like petals, oriented in the x-z plane (see coordinate system in Fig.7.1b). Figure 7.2b-d depicts the intensity of the first Raman feature upon vertical polarization excitation, excitation polarization at 45 degrees and horizontal polarization excitation. The Raman intensity is highest when the excitation polarization direction is parallel to the orientation of the nanoflower petals, in this case upon horizontal excitation (Fig.7.2d). This becomes even

more apparent in Fig.7.2e, where the normalized Raman intensity of different parts of the nanoflower (positions are indicated in Fig.7.2b-d) is plotted as a function of polarization angle (depicted by the arrows). The Raman intensity upon vertical polarization is 60 - 80 % of the Raman intensity upon horizontal polarization. Note in Fig.7.2b that the small flower petal to the right of the flower, oriented vertically in the y-z plane, can only be distinguished upon vertical polarization: it is not visible anymore in Fig.7.2c,d.

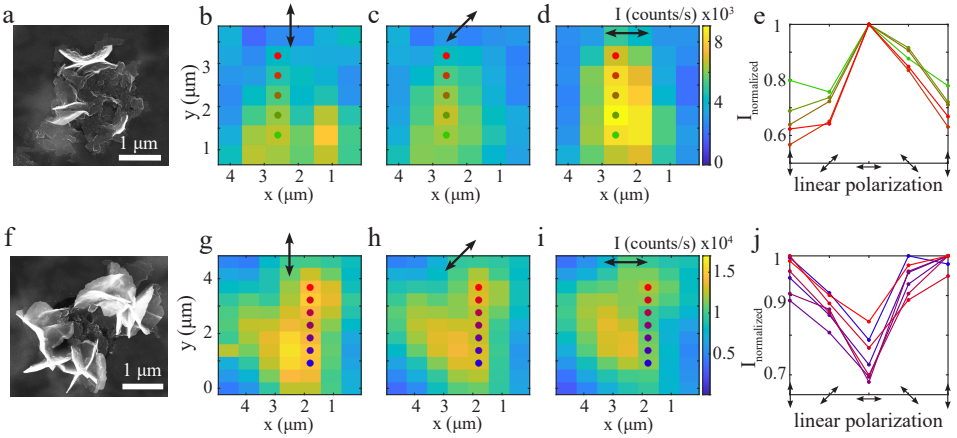

Figure 7.2: Excitation polarization
a. SEM image of a WS_2 flower-like structure (brown circle in Fig.7.1a) with mainly petals oriented in the x-z plane. **b-d,g-h** Map of the intensity of the first Raman feature of the flower-like structure upon **b,g.** vertically polarized, **c,h.** diagonally polarized and **d,i.** horizontally polarized excitation. **e.** Raman intensity of the flower in **a** (used pixels are marked with stars in **b-d**) as a function of excitation polarization angle. Note that the intensity increases drastically when the polarization direction is parallel to the WS_2 flower petals. **f.** SEM image of a WS_2 flower (purple circle in Fig.7.1a) with mainly petals oriented in the y-z plane. **j.** Raman intensity of the flower in **f** (used pixels are marked with stars in **g-i**) as a function of excitation polarization angle. Note that the intensity decreases drastically when the polarization direction is perpendicular to the WS_2 flower petals.

To illustrate the correlation between the Raman intensity of differently oriented flower-like structures and the excitation polarization even more, Fig.7.2f depicts a nanoflower (indicated in purple in Fig.7.1a) which exhibits petals oriented in the y-z plane (see the coordinate system in Fig.7.1b). Here, the Raman intensity upon vertical y polarization excitation (Fig.7.2g) is higher than upon horizontal x polarization excitation (Fig.7.2i). Figure 7.2j depicts the normalized Raman intensity of different parts of the nanoflower (positions are indicated in Fig.7.2g-i) as a function of polarization angle (depicted by the arrows). For this flower, the Raman intensity upon horizontal excitation is now 70 - 90 % of the Raman intensity upon horizontal polarization. The lower contrast can be explained by the fact that this nanoflower is more dense, also containing petals oriented differently than strictly in the y-z plane, which demonstrates the sensitivity of this method. Flowers with petals oriented in random different directions do not exhibit a polarization dependence (see Fig.D.4 of Appendix D).

The response of Raman modes to polarized light is described by Raman polarizability

tensors, based on the crystal symmetries in the material [189–192]. It is interesting to point out that the measured E_{2g} and A_{1g} Raman features exhibit the same polarization response (see Fig.D.5 of Appendix D). This indicates that the Raman polarization tensor for both the in-plane (E_{2g}) and the out-of-plane (A_{1g}) Raman modes are the same. The polarization dependence of the Raman intensity does not depend on temperature and is also observed upon 561 nm excitation (see Fig.D.5 in Appendix D). We conclude that linear-polarization-resolved Raman measurements provide a way to distinguish between differently oriented WS_2 petals and to identify the dominant orientation.

7.2.3. HELICITY OF RAMAN FEATURES

Another tool to investigate potential optical differences between nanoflowers with diverse geometries, is helicity-resolved Raman measurements. Figure 7.3a depicts a schematic representation of our set-up. The excitation light (594 nm wavelength) passes through a quarter-wave plate and is focused on the sample through an objective lens (see Section 2.4 for details on the set-up). The emission is collected through the same objective lens and quarter-wave plate, and directed to a spectrometer through a polarization analyzer. Figure 7.3b,c depicts helicity-resolved nanoflower spectra. Here, the flowers are excited with σ_+ light and the helicity of the Raman features is determined from the difference in σ_+ and σ_- Raman signals. In Fig.7.3b, the blue spectrum with the same polarization as the excitation light, has a higher intensity (σ_+, helicity is conserved) than the red spectrum with the opposite polarization (σ_-, helicity is reversed). We calculate the helicity of the first Raman feature $H = \frac{I_{conserved} - I_{reversed}}{I_{conserved} + I_{reversed}}$ to be 0.172. In Fig.7.3c, the helicity-reversed spectrum (red) has a higher intensity than the helicity-conserved spectrum (blue), with H = -0.083.

The helicity of the Raman response of the WS_2 nanoflowers is position dependent. Figure 7.3d presents a map of the nanoflower intensity of the first Raman feature (compare Fig.7.1c). Figure 7.3e presents a map of the experimentally determined helicity of the first Raman feature (stars indicate the position of spectra in Fig.7.3b,c). Note again that the measured position-dependent Raman intensity and helicity are a convolution of the excitation and detection volume with the spatial distribution of the optical response of the flowers, related to the size of the flower features. The Raman helicity of the WS_2 nanoflowers is negative: the intensity is higher for the helicity-reversed spectrum. Note however that the locations where the most negative Raman helicity is located, is not in the middle of the nanoflower, but towards the edge (*e.g.*, compare the green star in Fig.7.3e and Fig.7.3d). We therefore conclude that we detect a negative Raman helicity at locations where the excitation spot interacts with the side of a nanoflower. The helicity is most positive on locations in between the WS_2 nanoflowers, for instance at the position of the pink star: here the intensity is higher for the helicity-conserved spectrum. The Raman response from these regions confirms the presence of WS_2, e.g., this is not the bare substrate. Comparing the position of the pink star in Fig.7.3d with the SEM image in Fig.7.1a, it seems that the region of positive helicity is actually related to the WS_2 structure to the left of the flower indicated in purple in Fig.7.1a. As this structure looks more flat than the wall-like petals in other flowers, we conclude that the sign of the Raman helicity becomes positive when the WS_2 is oriented in the x-y plane, horizontally

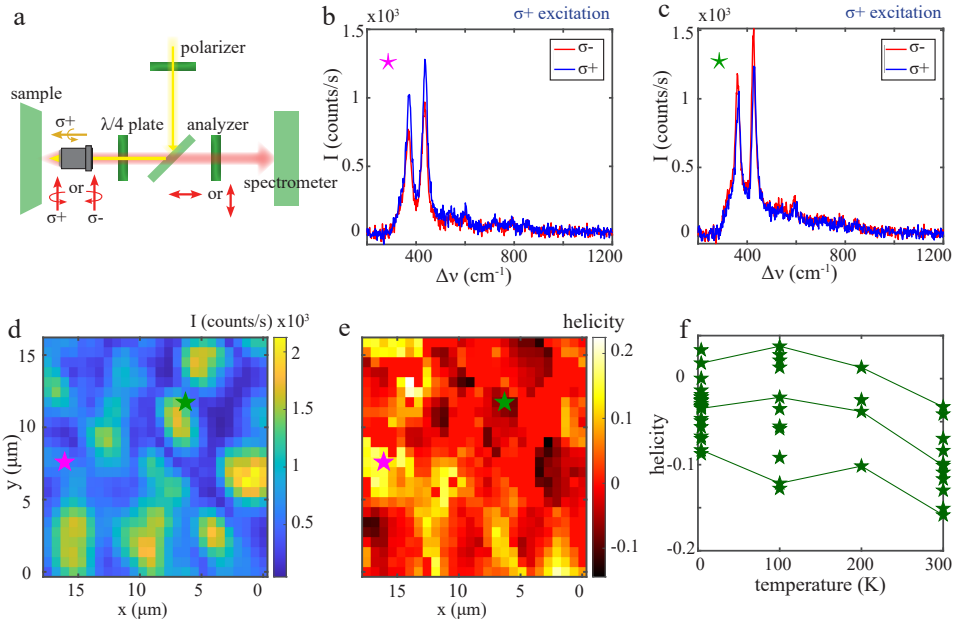

Figure 7.3: Helicity of Raman features
a. Schematic of our set-up, where the excitation light (594 nm wavelength) passes through a quarter-wave plate and is focused on the sample. The emission is collected through the same quarter-wave plate, and directed to a spectrometer through a polarization analyzer. **b,c** Helicity-resolved nanoflower spectra, where the flowers are excited with σ_+ light and the helicity is determined from the difference in σ_+ and σ_- emission. In **b**, the spectrum with the same polarization as the excitation light (blue) has a higher intensity (helicity is conserved). In **c**, the spectrum with opposite polarization to the excitation light (red) has a higher intensity (helicity is reversed). **d.** Map of the intensity of the first Raman feature of the nanoflower spectra. **e.** Map of the same region of the helicity of the first Raman feature. Note that the helicity of the Raman features around the WS_2 nanoflowers is negative (green star), whereas the Raman helicity is positive in regions next to the larger nanoflowers (pink star). **f.** Temperature-dependent helicity of the WS_2 nanoflower marked in green in Fig.7.1a (taking into account all pixels associated with this flower). The lines present the temperature dependence of three locations on the flower marked in green (see Fig.D.6a,b of Appendix D for the taken pixels). The helicity decreases slightly at room-temperature.

with respect to the surface (see Fig.7.1b for a coordinate system).

The Raman helicity response of the WS_2 nanoflowers is completely different than that of flat layers of WS_2. As alluded to before, the response of Raman modes to polarized light is described by Raman tensors [68, 190, 191] (see Section D.5 of Appendix D). In case of TMDs materials, the Raman tensor dictates that the A_{1g} mode is helicity-conserved [67, 68]. This means that the second Raman feature in 7.3b,c should only have had contributions with the same polarization as the excitation (σ_+), leading to H = 1.0. However, we observe a large contribution of light with the reversed helicity, in Fig.7.3c the helicity even becomes negative in places (see Fig.D.6 in Appendix D for a helicity map of the A_{1g} mode). Interpreting the helicity behaviour of the first Raman feature is less straightforward, as this feature contains both the 2LA(M) phonon and the E_{2g}, and the Raman tensor of the E_{2g} depends on the resonance of the excitation. The tensor dictates that the E_{2g} mode is helicity-reversed under non-resonant excitation [67] and helicity-conserved under resonant excitation [68, 69] (see Section D.5.2 of Appendix D). Since the nanoflowers are excited at resonance with the excitonic energy, the first Raman feature in 7.3b,c should have had mainly contributions with the same polarization as the excitation. Therefore the resonance of the excitation explains why the E_{2g} and the A_{1g} features have a similar helicity [68]. However, the observation of negative helicity is surprising for both Raman features, as the response is completely different than that of flat WS_2 layers.

It is important to note that the Raman polarization tensors are typically defined with respect to the crystal axes of flat TMDs layers, which for flat layers are readily connected to a suitable frame of reference of the incident light. The petals of the WS_2 nanoflowers exhibit a variety of orientations with respect to the incident light. Mathematically, a change of WS_2 flake orientation corresponds to a base transformation changing the Raman tensor, which may lead to allowed modes becoming forbidden and forbidden modes becoming allowed (see Fig.D.8 in Section D.5.3 of Appendix D). From Fig.7.3e it is apparent that the Raman helicity of the WS_2 nanoflowers is in general slightly negative, with a larger helicity-reversed than helicity-conserved contribution. This corresponds to the nanoflowers on average having more wall-like petals (oriented in x-z or y-z plane, see Fig.7.1b for a coordinate system), which is in agreement with the SEM images of the flowers. However, the fact that the helicity is at most -0.2 indicates that the contribution of both flat and vertically oriented flower petals within the diffraction-limited excitation spot is relatively large.

Based on the Raman tensor, flat flower petals (oriented in the x-y plane) should exhibit a positive helicity (see Section D.5 of Appendix D). Comparing the helicity map with the SEM image in Fig.7.1a, it is not always straightforward to correlate the regions of positive helicity with the orientation and nanogeometry of flower petals. We hypothesise that there might be flat flakes present that cannot be clearly distinguished from the Si_3N_4 substrate, but that do contribute to the positive Raman helicity. We conclude that the surprising helicity values for the nanoflower Raman response can be explained by the different orientations of the flower petals.

We determine the position-dependent helicity of the Raman features at different tem-

peratures (see Fig.D.7 in Appendix D for a map at room temperature). Figure 7.3f depicts the temperature dependence of the Raman helicity of the flower marked in green in Fig.7.1a,c. At all temperatures, the intensity is depicted of the first Raman feature of all spectra associated to this flower. The lines present the temperature dependence of three specific places on the flower marked in green (see Fig.D.6a,b in Appendix D for the taken pixels). The helicity at room temperature seems to be slightly lower than the helicity at cryogenic temperatures, but the trend is not very clear. The helicity of the A_{1g} mode and of the first Raman feature of spectra of other flowers also decreases at room temperature (see Fig.D.6d,e in Appendix D). The lower helicity at room temperature can be explained by the excitation energy being more out-of-resonance with the excitonic bandgap energy (see further on, Fig.7.4). We conclude that the main mechanism that determines the Raman helicity is the flower petal orientation and therefore independent of temperature. Therefore helicity-dependent Raman spectroscopy can be used to determine the orientation of WS_2 flakes and the contribution of flat vs. wall-like petals in WS_2 nanoflowers.

7.2.4. TEMPERATURE-DEPENDENT RAMAN SPECTROSCOPY

Given the phononic nature of Raman scattering, studying the temperature dependence of the Raman spectra of the WS_2 nanoflowers provides valuable information. Figure 7.4a,b presents the spectral response of the flower indicated in red in Fig.7.1a (see Fig.D.4 of Appendix D for an SEM image), upon a 594 nm and a 561 nm excitation at different temperatures. Like in the spectral response of the pyramids (see Chapter 6), there are 8-10 Raman features distinguishable at room temperature and at cryogenic temperatures (see Fig.D.2 of Appendix D), but the intensity of the features increases drastically with decreasing temperature. At 4 K there is a broad background visible under the Raman features (at 200 - 700 cm^{-1} in Fig.7.4a and at 1200 - 1500 cm^{-2} in Fig.7.4b). We attribute this background to highly reduced WS_2 photoluminescence (see Section D.2.1 of Appendix D). The intensity of the Raman features is much lower for the 561 nm excitation than for the 594 nm excitation. This is attributed to the fact that the 594 nm excitation light is close to the A-exciton resonance of WS_2, whereas the 561 nm is out-of-resonance with the A-exciton. Raman modes of TMDs can be greatly enhanced when they are excited in resonance with an excitonic transition [32, 56, 72, 73].

The inset of Fig.7.4c depicts the temperature-dependent intensity of the first Raman feature (E_{2g},2LA(M)) upon 594 nm excitation (orange) and 561 nm excitation (green). Here, for every temperature the Raman intensity of all the spectra associated to the nanoflower are taken (flower indicated in red in Fig.7.1c). The lines present the temperature dependence of three specific places on the flower. For an excitation at 594 nm, the Raman intensity decreases with increasing temperature, but for an excitation at 561 nm, the Raman intensity is independent of temperature. Figure 7.4c depicts the intensity of the first Raman feature as a function of the difference between the WS_2 exciton and the excitation wavelength. The WS_2 bandgap energy and therefore the exciton energy is temperature dependent, experiencing a blue shift with decreasing temperature (see Fig.1.5 of the Introduction). Therefore varying the temperature of the WS_2 nanoflowers enables the tuning of the exciton resonance condition for a fixed excitation frequency. Since the exciton energy is experiencing a blue shift with decreasing temperatures, cooling down the WS_2

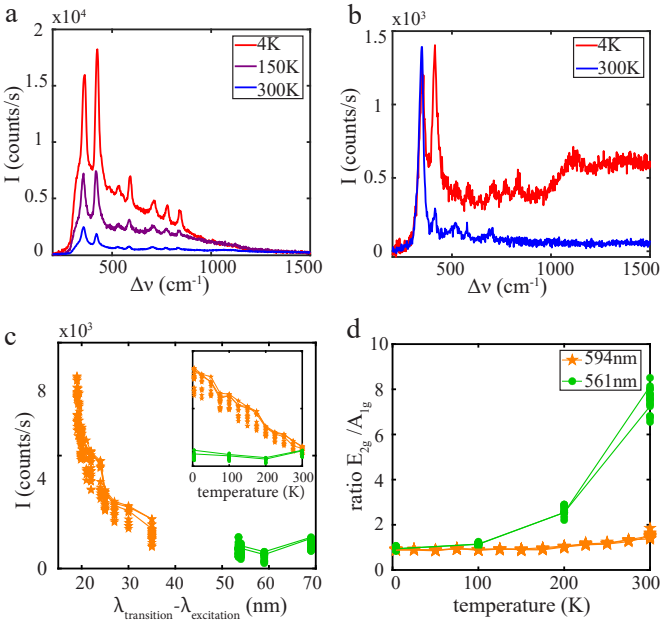

Figure 7.4: Temperature dependence Raman intensity
a. Nanoflower spectra (flower indicated in red in Fig.7.1a) upon a 594 nm excitation at temperatures ranging from 4 K to room-temperature. Note that the intensity of all Raman features increases. **b.** Nanoflower spectra (flower indicated in red in Fig.7.1a) upon a 561 nm excitation at room-temperature and 4 K. Note that the A_{1g} mode is almost absent at room temperature. **c.** *inset* Temperature-dependent intensity of the first Raman feature (E_{2g},2LA(M)) of the nanoflower spectra upon 594 nm excitation (orange) and 561 nm excitation (green). Here at every temperature the intensity is taken from all pixels associated with the flower (indicated in red in Fig.7.1d). *main* The Raman intensity is plotted as a function of the wavelength difference between the WS_2 bandgap and the excitation. Upon cooling down, the WS_2 bandgap energy blue shifts. With a constant excitation energy, the difference between excitation and WS_2 bandgap energy will become smaller at lower temperatures, bringing the excitation more in resonance with the excitonic transition. **d.** Temperature-dependent ratio of the first two Raman features of the nanoflower spectra. Upon a 594 nm excitation, the ratio changes from 0.8 at 4K to 1.6 at room-temperature, as can already seen by comparing the intensity of the first two Raman features in **a**. Upon a 561 nm excitation, the A_{1g} is almost absent at room-temperature. Therefore, the ratio between the two WS_2 flower Raman features increases drastically from 1.0 at 4K to 7.5 at room-temperature.

nanostructures will bring the excitation more in resonance with the excitonic transition. It is clear in Fig.7.4c that the Raman intensity exhibits a resonant-like enhancement as the excitation wavelength approaches the excitonic transition. Since the 561 nm excitation is relatively far away from the WS_2 bandgap, the resonance effect on the Raman intensity upon cool down is much less visible.

When comparing the spectra upon a 594 nm excitation in Fig.7.4a, it becomes apparent that the ratio between the two characteristic WS_2 Raman features (E_{2g}/A_{1g}), is temperature dependent. At room-temperature, the E_{2g} mode is 1.5 times as intense as the A_{1g} mode, and at 4 K, the A_{1g} mode is 1.5 times as intense as the E_{2g} mode. It has been reported before, that the different TMDs Raman modes respond differently to the excitonic resonance [71–73]. When comparing the nanoflower spectra upon 561 nm excitation in Fig.7.4b, the low intensity of the second Raman feature (A_{1g}) at room-temperature draws immediate attention. Figure 7.4d depicts the temperature dependence of the E_{2g}/A_{1g} ratio. At room temperature, the ratio between the characteristic WS_2 Raman features is around 7.0, for an excitation at 561 nm. From Fig.7.4d we deduce that the A_{1g} Raman feature is more sensitive to the resonance conditions than the E_{2g},2LA(M) feature. Even if the 561 nm excitation is relatively far away from the exciton wavelength, the A_{1g} Raman mode is enhanced greatly at cryogenic temperatures, as the excitation is closer to the excitonic resonance. Therefore we conclude that the absence of photoluminescence does not prevent an indirect study of the exciton, the presence of which is revealed by resonant Raman spectroscopy.

7.3. CONCLUSION

We have studied the optical response of CVD grown WS_2 nanoflowers. In contrast to flat WS_2 flakes, the nanoflowers exhibit a highly reduced photoluminescence enabling the study of their clear Raman response. Even though the WS_2 exciton emission is reduced in the nanoflowers, the presence of the excitons is still notable in the Raman response upon resonance excitation. We study the temperature-dependent Raman intensity and observe an enhancement for cryogenic temperatures, where the intensity of the out-of-plane Raman mode A_{1g} is enhanced more than the intensity of the in-plane Raman mode E_{2g}. We conclude that, due to the temperature-dependent bandgap and thus exciton energy shift, the WS_2 nanoflowers are excited more in resonance with the excitonic transition at cryogenic temperatures, leading to a resonant effect on the Raman intensity.

Furthermore, we study the interplay between flower geometry and spectral response. Even though the WS_2 nanoflowers have completely different geometries, at first sight the only spectral differences between them seem to be the Raman intensity. However, helicity-resolved and polarization-resolved Raman spectroscopy reveals underlying structural and geometrical differences between flowers. Studying the Raman response upon excitation with circularly polarized light reveals a completely different behaviour of the Raman helicity of the flowers with respect to flat WS_2 flakes. The Raman helicity of nanoflowers with many vertical walls is slightly negative, and the Raman response of flat lying WS_2 flower petals is slightly positive. We attribute the differences between the nanoflowers and the flat WS_2 to a difference in the Raman polarization tensor, induced

by the differently oriented flower petals. Studying the Raman response upon excitation with linearly polarized light we observe that we can selectively address nanoflower petals oriented parallel to the used polarization. We conclude that there is a interplay between the orientation of the flower petals, the atomic vibrational modes and the polarization direction of the excitation light.

Therefore we envision that temperature-dependent Raman spectroscopy will open the way to study excitonic resonance effects, and polarization-resolved Raman spectroscopy will open the way to determine the nanogeometry and orientation of WS_2 flakes.

8

Conclusion and Outlook

How are the different parts in this thesis connected to each other, and what are the next steps to take?

THIS thesis describes different outcomes of the interaction of light with various WS_2 nanostructures. The studied structures vary from horizontal monolayer and few-layer WS_2 flakes, to pyramid-like and flower-like WS_2 nanostructures. The light-matter interactions under investigation include photoluminescence, Raman scattering and the formation of polaritons. The geometry of the WS_2 structures plays an important role in this thesis: whereas two-dimensional WS_2 layers exhibit photoluminescence (Chapter 3 and 4), three-dimensional WS_2 nanostructures mainly exhibit Raman scattering (Chapter 6 and 7). Thickness plays an important role in the interaction of light with two-dimensional WS_2: the amount of layers influences the photoluminescence spectral response and valley polarization (Introduction), and the amount of layers influences the properties of the formed exciton-polaritons (Chapter 5). The interplay between geometry on the one hand, and the optical interaction on the other hand, is a recurring theme in this work. Chapters 6 and 7 focus specifically on the influence of nanogeometry and orientation of the WS_2 structures on the optical response.

A common denominator in all studied light-matter interactions is the presence of the WS_2 exciton. The observed photoluminescence originates from the recombination of the electron-hole pair forming the exciton in the WS_2 valley. Coupling valley pseudospin to transverse optical spin (Chapter 3) aims at using the WS_2 valley in information storage and processing, which can be extended to using the WS_2 excitons for the same purpose. In addition, the temperature- and position-dependence of valley polarization and valley coherence (Chapter 4) is explained by interactions with and between WS_2 excitons. As the name suggests, the influence of the exciton is most explicitly apparent when the exciton hybridizes with light to form an exciton-polariton (Chapter 5). Because of the strong light-matter interaction, the dispersion relation of the created exciton-polariton exhibits an avoided crossing between the dispersion of the exciton and of the light. Moreover, the exciton even plays a role in the WS_2 structures that exhibit a highly reduced photoluminescence, as the excitonic resonance can be probed in temperature-resolved Raman spectroscopy (Chapter 7).

All the chapters describe manifestations of light-matter interactions, and specifically polarization-dependent optical response of WS_2. The control of the polarization state of the excitation light and the ability to resolve the polarization state of the emission is paramount for all described experiments involving the read-out and addressing of valley pseudospins (Chapter 2). Circularly polarized light is essential to create valley polarization and to set up the valley pseudospin state (Chapter 3), and linearly polarized light initiates valley coherence (Chapter 4). Furthermore, measuring the polarization-resolved Raman response allows probing the orientation of various WS_2 nanoflower petals (Chapter 7).

An unexpected result in this thesis is reduction of the photoluminescence from the studied 3D WS_2 nanostructures. Although parts of the hollow WS_2 pyramids (Chapter 6) and WS_2 nanoflowers (Chapter 7) have a thickness of only a few layers, these nanostructures exhibit strongly reduced photoluminescence with respect to monolayer and few-layer horizontal WS_2. Both kinds of nanostructure are fabricated using CVD, but they are highly different from each other: the pyramids have a size of 15 um, whereas the petals of the nanoflowers are smaller than 1 μm. Furthermore, whereas the pyramids consist

out of horizontal steps or layers, the nanoflowers contain mainly wall-like petals. Interestingly, the pyramid sample both contains pyramids and WS_2 monolayers, but no few-layer WS_2. This points at the influence of the growth mechanism on the presence or absence of PL from the WS_2 structures. Investigating the specific growth mechanism of both nanoflowers and hollow pyramids, and understanding how the growth leads to a reduced PL, is a key for fabricating WS_2 nanostructures that can be used in photonics applications.

For potential applications, the valley pseudospin of WS_2 and the spin-orbit coupling experiments described in Chapter 3 are probably the most promising. An intriguing thought is combining the observed valley coherence (Chapter 4) with nanowires (Chapter 3). Instead of inducing valley coherence at a specific position in a WS_2 flake, it would be interesting to induce coherence between WS_2 valleys that are spatially separated by a nanowire. Achieving spatially separated valley coherence would be a first step towards using WS_2 for (quantum) information storage.

Furthermore, the pseudospin of the WS_2 valley associated with the exciton raises the question of how chirality influences the exciton-polariton mode in WS_2. In other words: if the exciton is chiral and the light is chiral, then perhaps the hybrid light-matter mode is also chiral. The implications of the potential chirality of exciton-polaritons are exciting, but so far unexplored. Polaritons with their strong light-matter interaction hold the promise of applications in light concentration and manipulation, whereas the valley pseudospin is suggested as a good quantum number to encode information. If the initializing and read out of the valley pseudospin (Chapter 3) is combined with the hybridization of light and WS_2 excitons (Chapter 5), a WS_2 based photonics device lies more within reach.

A

SUPPLEMENTARY MATERIALS TO CHAPTER 3

Parts of this chapter have been published as the Supplementary Materials of [93].
Data acquired for this publication can be found at DOI: 10.4121/uuid:b45aadad-6687-40f2-8e60-fc1c2e583fdc

A

A.1. SIMULATIONS

A.1.1. INFLUENCE OF NANOWIRE ON FAR-FIELD DIPOLE RADIATION

To predict the influence of the nanowire on both radiation intensity and polarization, we investigate the far-field radiation of a circular dipole near a wire in a finite-difference-time-domain (FDTD) simulation. Fig.A.1a depicts the collected intensity of the dipole radiation as a function of distance between the emitter and either a silver nanowire or a ZnO nanowire of the same size. In both cases, the intensity decreases drastically close to the wire. Fig.A.1b depicts the degree of circular polarization, quantified through the third Stoke parameter (S3), collected in the far field originating from a circular dipole emitting perfect circularly polarized (σ_-) light. In the presence of the glass substrate, the S3 is already decreased to roughly 0.60. Near the ZnO nanowire, the maximum decrease of the S3 is to 0.45, whereas near the silver nanowire, the S3 decreases to 0.15.

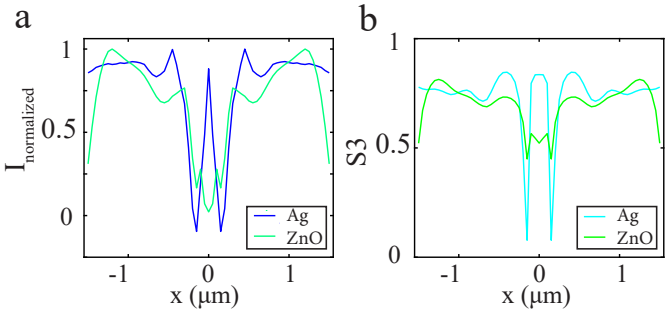

Figure A.1: Dipole radiation near a nanowire
a. The radiation intensity of a dipole in the presence of a nanowire with radius 254 nm at x=0. The intensity decreases slightly more for the silver nanowire (in blue) than for the ZnO nanowire (in green). **b.** The S3 of a dipole that would emit circularly polarized light with an S3 of 1 in free space. This S3 is suppressed to 0.6 in the presence of the glass substrate. Near the ZnO nanowire the S3 decreases further to 0.45, whereas for the silver nanowire the S3 decreases to 0.15.

It is clear that the effect of the nanowires on the far-field dipole radiation is not negligible. In the case of the silver nanowire, the effect is even so high that in the far-field, the S3 of light collected in the far field from a perfect circularly polarized dipole would be almost reduced to zero. Therefore we conclude that dielectric wires are more suitable for the second experiment than metal wires.

A.1.2. ZNO NANOWIRE MODES

Dielectric nanowires like the ZnO nanowire of radius 254nm that we used, may support several optical guided modes [121]. We calculate the electric field distribution of all possible modes in a ZnO nanowire on a glass substrate with a Finite Element Method (FEM) for the emission frequency relevant to the experiment ($\lambda_{free-space}$ = 594 nm). Fig.A.2a-f depicts the intensities of the six guided modes that the nanowire supports with their effective wavenumber. The first mode (Fig.A.2a) is TM-like, the second one (Fig.A.2b) is TE-like, which is relevant for Section A.1.4 further on.

Fig.A.2g-l depicts the calculated S3 pattern of the modes in our ZnO wire on the cross section of the nanowire. The plane where in the experimental situation the WS_2 will be, i.e., at the substrate close to the wire, is indicated with bold lines. At this position the S3 has always a negative value on the left of the wire (blue colour) and a positive on the right (red colour) for the guided mode propagating in negative z-direction, i.e. into the plane of Fig.A.2. At other positions the S3 pattern is more complex.

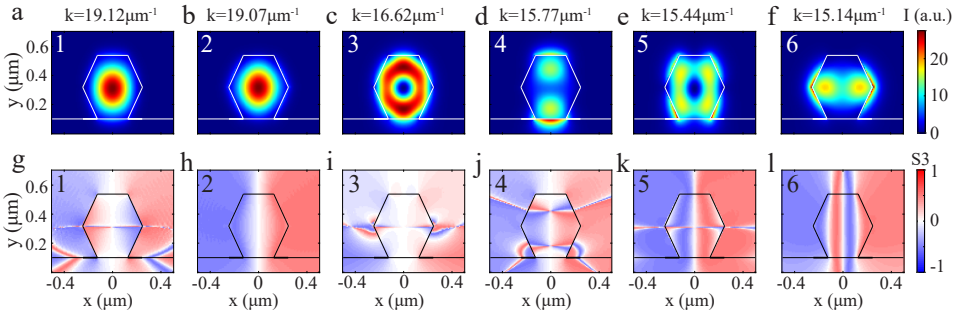

Figure A.2: The guided modes in the ZnO wire
The ZnO nanowire with a radius of 254 nm supports six guided modes at the wavelength used in the experiments, 594 nm. **a-f.** The intensity of all the guided modes with their effective k values in μm^{-1}, where the modes are numbered 1 to 6. Here the fundamental modes in **a-b** have a dominant E-field along the y- and x-direction, respectively. The lines indicate the hexagonal outlines of the wire and the position of the glass substrate. **g-l.** The projected S3 on the (x,y)-plane of the corresponding modes. The experimentally relevant plane is where the WS_2 is located, i.e., the (x,z)-plane at wire-surface interface, here indicated with bold lines. At these positions, the S3 has always a negative value left of the wire (blue colour) and a positive right (red colour).

A.1.3. MODE INTERFERENCE

The measured photoluminescence image near the wire exhibits an interference pattern (see Fig.3.5 in Section 3.2.3). Since the ZnO nanowire supports many modes, this provides a number of possibilities for interference between them. We calculated the expected spacing of the resulting beating pattern of pairs of modes, based on the simulated effective wave numbers. Table A.1 shows the resulting spacings $\frac{2\pi}{k_i - k_j}$ in μm, where the modes are numbered as in Fig.A.2.

	k_1	k_2	k_3	k_4	k_5	k_6
k_1	0.164					
k_2	108.3	0.165				
k_3	2.504	2.564	0.189			
k_4	1.876	1.909	7.480	0.199		
k_5	1.705	1.732	5.338	18.645	0.204	
k_6	1.577	1.600	4.257	9.879	21.014	0.208

Table A.1: The beating spacing in μm between the different ZnO wire modes shown in Fig.A.2, based on their effective wave numbers. The beating spacing is calculated both for the cases the modes interfere with each other, or with their own reflection.

The diagonal of this table shows the spacing as a result of a mode interfering with its reflection. This is of the order of 160 - 200 nm, which is below the diffraction limit and can safely be neglected.

Fig.A.3 depicts the intensity of the interference pattern of mode 1 (see Fig.A.2a) interfering with either mode 3, 4 or 5 (see Fig.A.2c,d,e), and of mode 2 (see Fig.A.2b) interfering with those same modes. There are two types of possible interference patterns, depending on the dominant E-field direction of the mode. In Fig.A.3a,e,i, the interfering modes exhibit a 'wiggly' pattern, an oscillating pattern that is anti-symmetric along the x-direction. In Fig.A.3c,g,k, the modes exhibit an oscillating pattern that is symmetric along the x-direction. This second pattern corresponds to what we observe experimentally, where the maxima in the WS_2 emission are symmetric along the x-direction. Fig.A.3b,d,f,h,j,l, depicts the S3 pattern for the two interfering modes. It is important to note that since all the individual modes always have a negative S3 value on their left side (blue colour) and a positive on their right (red colour), this dominant S3 pattern will also present when they interfere with each other.

For comparison, we calculated the S3 for a range of nanowire radii (150-250 nm). For this full range of radii, the near-field S3 distribution reaches maximally 1. The change of radius only causes different number of modes and beating between these modes.

A.1.4. SELECTING THE EXPERIMENTALLY RELEVANT MODES

To select the modes that are relevant in our experiment, we compared the measured beating spacing in experiment and simulation. We determined the peak positions by fitting triple Gaussians to crosscuts along the wire of the left-handed and right-handed measured exciton emission (Fig.3.5b,c in Section 3.2.3). The spacing between the two high maxima is 2.2 - 2.5 μm, whereas the distance to the lower maximum of the three is 1.8 - 2.1 μm. The data exciting at the left end are not as clear (Fig.3.5f,g), but the data of the indirect bandgap can also be used, since they do show a similar interference pattern (see Fig.A.5). The spacing between the two clear maxima in the indirect bandgap data, is 1.8 - 2.0 μm.

Comparing the experimentally observed mode beating length with the distances given in Table A.1, and ruling out any mode combinations that lead to 'wiggly' interference patterns from Fig.A.3, we conclude that in our experiment it is either mode 1 interfering with mode 4 (Fig.A.3c,d) or mode 2 interfering with mode 3 (Fig.A.3g,h).

To determine which of the two mode pairings is actually observed in experiment, we use the dominant E-field direction of the modes. When exciting the wire at the end, we used a laser propagating in the y-direction and with linear polarization along the wire in z (see the experimental scheme in Fig.3.2a). Mode 1 of this ZnO wire has a dominant E-field along the y-direction and mode 2 along the x-direction. There is a k-vector mismatch between the incoming laser light and the propagation in the wire, which is overcome by to the symmetry breaking of exciting at the end of the wire. It may be expected that when the laser excites the propagation in the wire, it is much easier to excite the modes with dominant E-field in the y-direction than in the x-direction. This leads an argument for the excitation of mode 1 rather than mode 2.

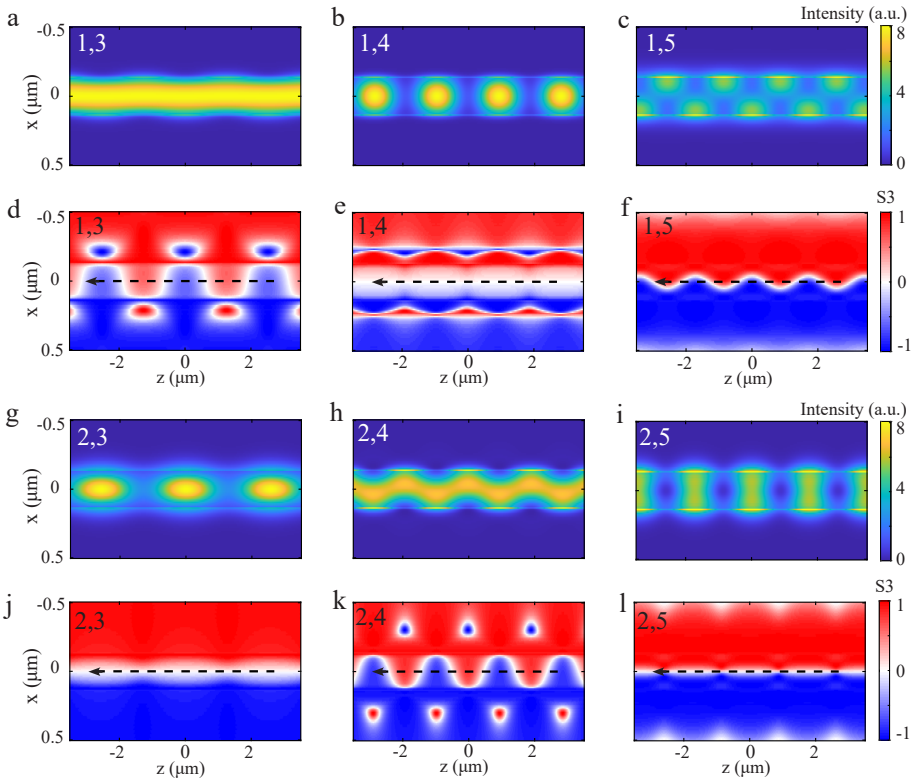

Figure A.3: Possible near-field interference patterns of the modes in the ZnO nanowire
a,c,e,g,i,k. Resulting near-field intensity pattern of the two modes interference, in which the numbers indicate the modes (see Fig.A.2). **a,e,i.** show an oscillating pattern, where there is either a maximum intensity at one or the other side of the wire. **c,g,k,** show a more regular pattern of maxima and minima along the wire. This pattern is more similar to the patterns observed in the experiment than the 'wiggly' interference pattern.
b,d,f,h,j,l. near-field S3 of the two interfering modes. Even though the patterns look complicated, the transverse optical spin does always have a value +1 at one side of the wire and -1 on the other side, independent of the interfering modes.

A

Finally, there is another difference between the two candidates mode 1 and 4 (Fig.A.3c,d) and mode 2 and 3 (Fig.A.3g,h). When comparing the maxima and minima of the interference pattern, we can calculate the extinction ratio. In our experimental data, the extinction ratio is high and the intensity at the minima of the interference pattern goes down by 77%. When interfering mode 1 and 4, the extinction ratio is 70%, but with mode 2 and 3 it is much lower, only 56%.

Therefore we conclude that mode 1 and 4 are the most probable to be relevant to our experiment (see Fig.A.3c,d).

A.1.5. THE SIMULATION APPROACH EXPLAINED

In this section, we provide more details on the simulation results presented in Section 3.2.4. Our simulation approach consists of two main steps: (i) we determine the local excitonic density resulting from the coupling with the guided modes of the nanowire, and (ii) we calculate the circular polarization state of the resulting exciton luminescence as it is collected in the far field.

The local excitonic density is associated with the local intensity of the nanowire guided modes. We numerically compute the electric field in proximity of the nanowire as $\vec{E}(\vec{r}) = \sum_m \vec{E}_m^{(\text{guided})}(\vec{r})$. Here, the sum is over all of the nanowire modes of interest. The corresponding mode profiles are calculated as mentioned in Section A.1.2. Assuming x and z the coordinates along the two-dimensional material (with z being also oriented along the nanowire axis, see Fig.3.2), the local intensity of the electromagnetic guided modes can be split into the two components with opposite transverse spin

$$\begin{aligned} K_+(x,z) &= \tfrac{1}{2}|\vec{E}_z(x,z) - i\vec{E}_x(x,z)|^2, \\ K_-(x,z) &= \tfrac{1}{2}|\vec{E}_z(x,z) + i\vec{E}_x(x,z)|^2. \end{aligned} \tag{A.1}$$

Ideally, the two different transverse spin components should couple exclusively with excitons in the corresponding valley, according to the principle of valley-spin coupling. [30, 80–82, 103] In practice, this effect is partially reduced by the presence of inter-valley electron hopping,[30, 80–82, 103] which we take into account in terms of a phenomenological parameter, the degree of valley polarization, P_V. The ideal case of perfect valley-spin coupling corresponds to $P_V = 1$; in our system we experimentally observed $P_V \simeq 0.7$. Thus, the local excitonic density in the two valleys, J_+ and J_-, can be written as

$$\begin{aligned} J_+(x,z) &= \frac{1}{2}K_+(1.0+P_V) + \frac{1}{2}K_-(1.0-P_V), \\ J_-(x,z) &= \frac{1}{2}K_-(1.0+P_V) + \frac{1}{2}K_+(1.0-P_V). \end{aligned} \tag{A.2}$$

We model the electromagnetic response of the excitons by assuming an infinitely thin layer of dipolar emitters on the surface of the two-dimensional material. The emission from each dipole is incoherent with all the other dipoles in the layer. The dipole moment

of each emitter is circularly polarized with a valley-dependent handedness, i.e.,

$$\vec{P}_+(x,z) \propto \frac{1}{\sqrt{2}}(\hat{z} + i\hat{x}),$$
$$\vec{P}_-(x,z) \propto \frac{1}{\sqrt{2}}(\hat{z} - i\hat{x}). \tag{A.3}$$

Moreover, we assume that the intensity of the emission is proportional to the local excitation density, $|\vec{P}_\pm|^2 \propto J_\pm$.

In the experiment, we measure the far-field polarization incoherently emitted by the excitons. The far-field properties of the emitted light are affected by the presence of the nanowire and the NA of the detection optics. In order to properly model these effects, we exploit the principle of Lorentz reciprocity. We use a finite-difference-time-domain commercial solver (FDTD Solutions by Lumerical, Inc.) to simulate a circularly polarized Gaussian beam focused on the system consisting of the substrate and the nanowire. We set the $NA = 0.75$, as determined from our k-space images. We consider the electric field of the beam on the plane at the position of the two-dimensional material ($y = y_0$), i.e., $\vec{\mathcal{E}}_{L,R}(x,z) = \vec{E}_{R,L}(x,y_0,z)$. The subscripts R and L refer to the right- or left-handed circular polarization of the beam.

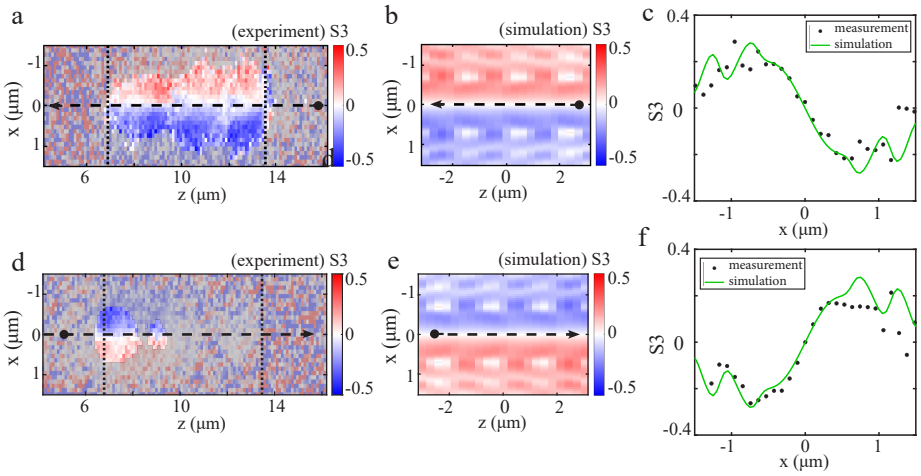

Figure A.4: Normalized S3 in both experiment and simulation
a,d. Calculated normalized third Stokes parameter from the experimental data as shown in Fig.3.5. The parts of the figure where noise dominates and the calculated S3 has a high uncertainty, are covered with a grey mask for clarity. **b,e.** Calculated normalized S3 from the simulation data as shown in Fig.3.6. Since the S3 is now normalized, both the part close to the nanowire where the emission intensity will be high and the part far away appear with similar S3 values, resulting in a complex pattern. **c,f.** Crosscuts of **a-b,d-e.** at a point of high intensity. The measured and simulated S3 values range from -0.3 to +0.3.

A

Due to the principle of reciprocity, the intensity of light emitted by the excitons into the left- and right-handed beams is then given by

$$\begin{aligned} I_L &= \int dxdz \left[J_+(x,z)|\vec{\mathcal{E}}_{L,+}(x,z)|^2 + J_-(x,z)|\vec{\mathcal{E}}_{L,-}(x,z)|^2 \right], \\ I_R &= \int dxdz \left[J_+(x,z)|\vec{\mathcal{E}}_{R,+}(x,z)|^2 + J_-(x,z)|\vec{\mathcal{E}}_{R,-}(x,z)|^2 \right], \end{aligned} \tag{A.4}$$

where $\vec{\mathcal{E}}_{L,+} = (\vec{\mathcal{E}}_{L,z} - i\vec{\mathcal{E}}_{L,x})/\sqrt{2}$ and $\vec{\mathcal{E}}_{L,-} = (\vec{\mathcal{E}}_{L,z} + i\vec{\mathcal{E}}_{L,x})/\sqrt{2}$ are the local components of the electric field of the left-handed circularly polarized beam with opposite transverse spin (compare Eq. A.1). Similarly, $\vec{\mathcal{E}}_{R,+}$ and $\vec{\mathcal{E}}_{R,-}$ are the transverse-spin components of the right-handed beam. Note that, since the beam is not an ideal plane wave, but a structured electromagnetic field (due to the finite NA and the presence of the nanowire), the local near-field polarization in proximity to the nanowire can be different from the global circular far-field polarization of the beam. The intensities are integrated (as opposed to the fields) in view of the incoherent character of the excitonic emission. The handedness discussed in Section 3.2.4 is proportional to the difference between the detected intensities, i.e., handedness $\propto I_L - I_R$.

In order to reproduce the experimental results, we run a set of FDTD simulations by changing the center position of the Gaussian beam relative to the nanowire position. For each different beam, we calculate the corresponding handedness of the far-field emission according to Eqs. (A.4). The resulting map, showing $I_L - I_R$ as a function of the beam center position (x,z), is displayed in Fig.3.6 in Section 3.2.4 and directly compared to the experimental results.

A.2. EXPERIMENTAL

A.2.1. NORMALIZED S3

In Fig.3.5, the effective polarization handedness of the luminescence near the nanowire is depicted. Normalizing the $I_L - I_R$ to the local $I_L + I_R$ would give the normalized third Stokes parameter S3. This however results into the images being dominated by noise when $I_L + I_R$ becomes very small. Fig.A.4a,d depicts the calculated S3 from Fig.3.5 in Chapter 3. Here the part of the image where the noise dominates and the uncertainty in the S3 is large are masked for clarity.

Fig.A.4b,e depicts the calculated S3 from the simulations as shown in Fig.3.6 in Chapter 3. Since the S3 is normalized, both the part close to the nanowire where the emission intensity will be high and the part far away with a lower intensity, appear with a similar S3 value. This results in a complex looking pattern. However, the experimentally most relevant part is the part where there is actual exciton emission, which is close to the wire.

Fig.A.4c,f depicts the crosscuts of the experimental and simulation S3 values depicted in Fig.A.4a-d at points of high intensity. The measured and simulated S3 values range from -0.3 to +0.3.

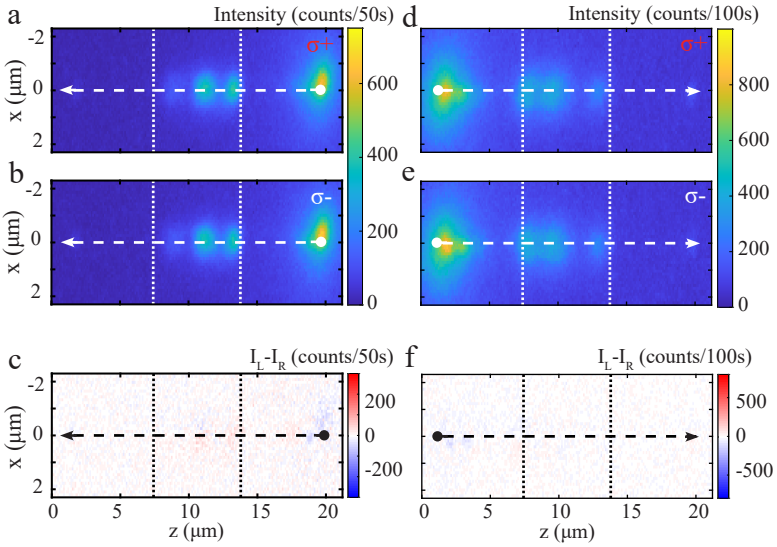

Figure A.5: The right and left-handed parts of the photoluminescence of the WS_2 at the indirect bandgap wavelength and the resulting S3.
a. Optical image of the same sample as used in Chapter 3, with the WS_2 flake of 5 layers and the ZnO wire of radius 254nm. **b.** Photoluminescence of the WS_2 flake measured without the ZnO wire. In **c-h** now only the emission at the wavelengths of the indirect bandgap is measured, indicated here by the gray shaded region. **c-d,(f-g)** Left (right) handed circularly polarized part of WS_2 photoluminescence, where dotted lines indicate position of the wire and WS_2, the arrow points in the propagation direction of the light in the wire. Emission is observed only at the position of the WS_2 along the wire exciting it. Exciting the wire on the left or right ends, the propagation direction of the guided mode is flipped, which is indicated by the arrows. **e,h** Since the photoluminescence from the indirect bandgap is not polarized, we expect to see no structure in the S3, as we were seeing in Fig.3.5 of Chapter 3. Except for noise, the S3 is indeed 0 at the indirect bandgap wavelengths, which gives us confidence in our experimental data.

A.2.2. INDIRECT BANDGAP

Since we are using multilayer WS_2, we measure both photoluminescence from the direct bandgap, e.g. the excitons, and from the indirect bandgap (see Introduction, Section 1.4.1). Since the valleys of the direct bandgap have valley polarization, they can be addressed using the transverse spin of the ZnO wire. The indirect bandgap however is not spin polarized (see Introduction, Section 1.5.2). This means that even though near-field light from the ZnO wire can couple to it, we do not expect to observe any net amount of circular polarization on either side of the wire. Fig.A.5a-b,d-e presents the photoluminescence from the indirect transition, when exciting the wire either at the right or left end. Fig.A.5c,f shows the resulting S3, which is flat and 0 as expected. Thus, we can conclude that the polarized excitons can be addressed selectively, but the unpolarized indirect bandgap cannot.

A.2.3. COLLECTION WITH FULL NA

ZnO wires support many optical modes, both real and leaky. Fig.A.6a-b presents an AFM image and a crosscut of the used ZnO wire. What we want to measure is the WS_2 emission, that has been excited by using ZnO wire modes that have transverse optical spin. However, we do not want to measure light that comes from a ZnO mode directly. This risk is highest with the leaky modes. Therefore we filter them out using k-space selection, since we know the leaky modes exhibit higher in-plane k-values than the exciton luminescence. The full NA of our objective is 1.45, from which we selected an effective NA of 0.75 to obtain Fig.3.5 (see Fig.2.4 in Chapter 2 for an overview of our optical set-up, where the aperture is used for k-space selection).) According to our simulations, no leaky modes exist in a ZnO nanowire for this small in-plane momentum range. Fig.A.6 presents photoluminescence and the calculated S3 values, collected using the full NA of our imaging system. Fig.A.6c-d,f-g exhibit a similar beating pattern as presented in Fig.3.5, since the measurements are done on the same wire. The S3 pattern in Fig.A.6e and h is however not as clear as in Section 3.2.3, but the blue and red colors are more distorted. We assume that the collected emission presented in Section 3.2.3 originated mostly from the free-space radiation of valley-polarized excitons, where in the data shown here, part of the emission comes from the leaky modes in the ZnO wire exciting the WS_2.

A.2.4. SHIFTS DUE TO WAVEPLATES

When rotating the quarter waveplate to distinguish right-handed and left-handed circularly polarized light, the position of the laser beam on the camera can shift by a small amount. This shift is of the order of one pixel, and is corrected for by correlating the images of the WS_2 flake with the ZnO wire like Fig.3.5a. It is important to mention that even without correcting for the shift, the uncompensated S3 pattern along the wire still demonstrates the same local addressing of valley excitons as in Fig.3.5, albeit with a slightly reduced magnitude.

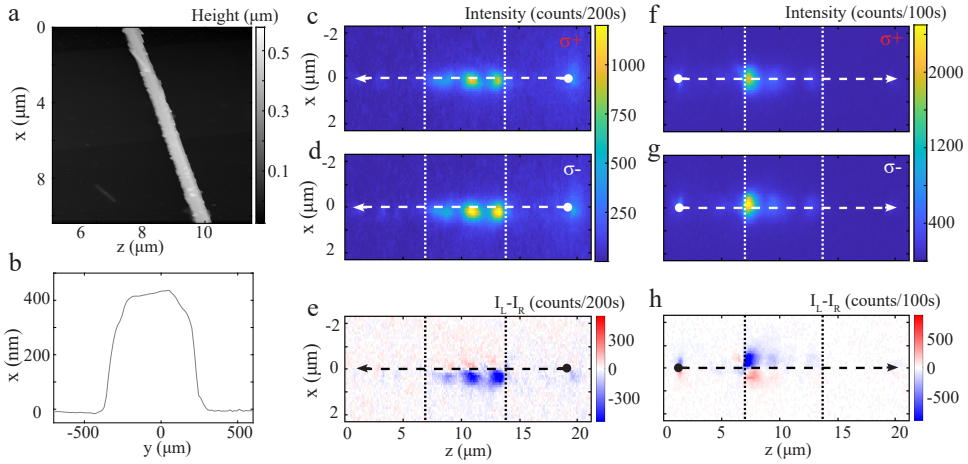

Figure A.6: AFM images, and data collected with full objective NA
a (b) AFM image (crosscut) of the used ZnO nanowire with radius 254 nm **c(d),f(g)** Left (right) handed circularly polarized part of WS_2 photoluminescence, where dotted lines indicate position of the wire and WS_2, the arrow points in the propagation direction of the light in the wire (see Fig.A.5. Emission is observed only at the position of the WS_2 along the wire exciting it. Exciting the wire on the left or right ends, the propagation direction of the guided mode is flipped, which is indicated by the arrows. However, in this case we use the full NA of the objective, without selecting in k-space. **e,h.** Without this k-space selection, we not only measure emission from WS_2 that was excited by the ZnO wire modes, but also direct light from especially the leaky modes of the ZnO wire. The S3 pattern in these images is not as clear as in Fig.3.5, but the blue and red colors are more distorted.

B

SUPPLEMENTARY MATERIALS TO CHAPTER 4

Data acquired for this chapter can be found at DOI: 10.4121/14406938

B.1. SPECTRAL BEHAVIOUR OF MONOLAYER FLAKES

The WS_2 monolayer flakes fl.1 and fl.2 exhibit a significant spectral difference when excited in the central region with respect to the rest of the flakes. Figures B.1a-b depict the PL intensity of fl.1 and fl.2 at room temperature. Figures B.1e,l present spectra (of fl.1) at the flake medians (green and brown), the middle (red) and on the rest of the monolayer (purple and blue) (positions are indicated by stars in Fig.B.1a). The spectra at the medians and on the rest of the monolayer are not fundamentally different, except for the overall photoluminescence intensity. The spectral response in the middle of the monolayer fl.1 is red shifted towards 650 nm at room temperature (red spectrum in Fig.B.1e) and consists of at least three peaks at 4 K, one at the exciton position and two with lower energies (red spectrum in Fig.B.1l). The spectra of fl.2 in Fig.B.1f exhibit a similar behaviour as of fl.1. The spectra on the bright edges of the flake (blue and green) and in the low intensity region (purple and brown) only differ in intensity, but the spectrum in the middle (in red) is red shifted.

Figure B.1c-d presents the PL intensity of fl.3 and fl.4 at room temperature (fl.3 is 35 μm and fl.4 is 15 μm large). The PL intensity is not homogeneous over these two flakes, but is lower at the triangle medians (like fl.1). The PL intensity of the edges of fl.3 is higher (like fl.2). However, the PL spectra of fl.3 and fl.4 in Fig.B.1g,h all have the same shape and only differ in intensity. Even the spectra in the very middle of these flakes (in red) do not exhibit a red-shifted peak as the spectra of fl.1 and fl.2.

Possible explanations for the red shifted spectral response in the middle of the monolayer flakes are either trion or defect related. The trion peak is expected to be close to the spectral position of the exciton (within 10 nm) [35–37, 193, 194], whereas some reported WS_2 defect peaks are further red-shifted from the exciton (to around 650 nm) [36, 195]. Spectra measured in different studies vary greatly, indicating large and possibly unknown sample differences. Based on the spectral position we conclude that the red-shifted spectral response in the very middle of fl.1 and fl.2 might be induced by the presence of local structural defects rather than being the trion.

Scanning electron microscopy (SEM) images of fl.1 - fl.3, presented in Fig.B.1i-k, do not reveal any grain boundaries or other structural reasons that would explain the non-uniformity in the PL intensity. Structural characterization on the atomic level cannot be performed on the investigated flakes, as the relatively thick silicon substrate is not transparent to Transmission Electron Microscopy.

Figures B.2a,b present atomic force microscopy (AFM) height measurements of fl.1 and fl.2. From Fig.B.2b it becomes apparent that there are no height variations that would explain the non-uniformity in the PL intensity. Figures B.2c,d depict AFM crosscuts at the positions indicated by the red lines in Fig.B.2a,b. We measure a height of 0.8 nm for fl.1 and a height of 1.0 nm for fl.2. The measured height confirms that the studied flakes consist of a single layer of WS_2 [17, 18, 22].

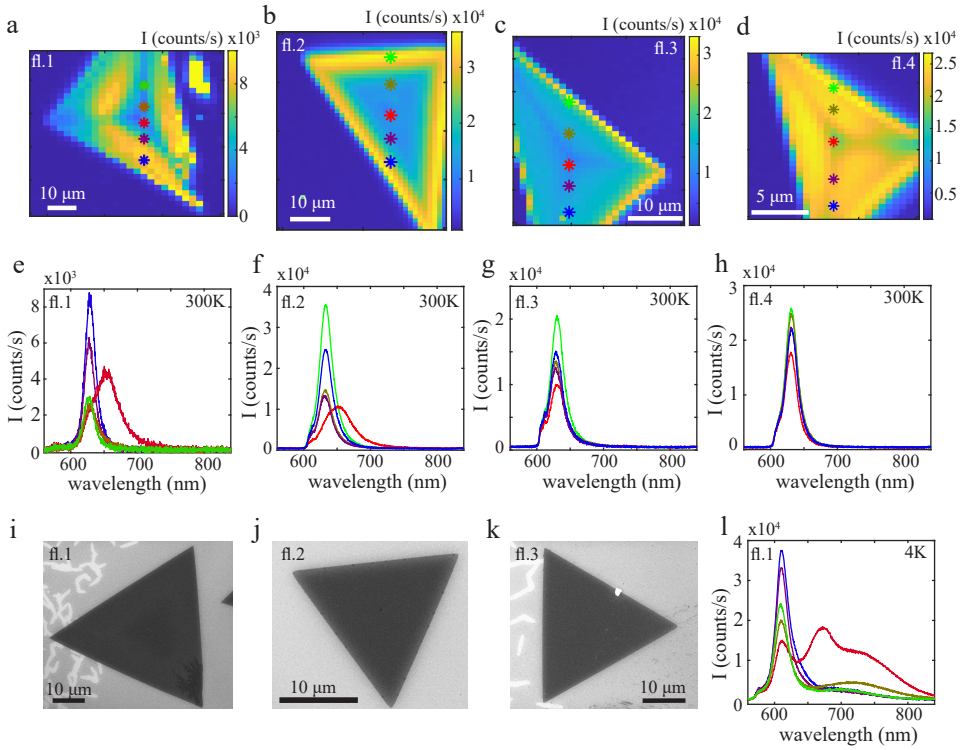

Figure B.1: Defect peak on monolayer flakes
a-d. Raster scan of the PL intensity over fl.1 - fl.4, acquired at room temperature. Note that the x and y axis in the raster scan are slightly skewed due to experimental constraints (see Section B.3) The stars indicate the positions of **e-h.** the PL spectral response taken around the flake centre. For fl.1 (**e.**), the spectral peaks on the medians (green and brown) have a lower intensity but the same shape as the spectra on the flake (purple and blue). The same holds true for fl.2 (**f.**), where the spectral response on the edge (green and blue) has a higher intensity as the spectral response in the middle (brown and purple). The spectral peaks in the middle of fl.1 and fl.2 (in red) are significantly red shifted. **g-h.** The spectra of fl.3 and fl.4 do not reveal defect-like behaviour. The only difference between spectra on different position of these flakes, is the intensity. **i-k.** SEM images of fl.1 - fl.3 do not reveal any grain boundaries or other structural reasons that would explain the non-uniformity in the PL intensity. **l.** PL spectra of fl.1 taken at 4 K. The spectrum in the very middle of the flake (in red) consists of at least three peaks, one at the exciton position and two red shifted to higher wavelengths.

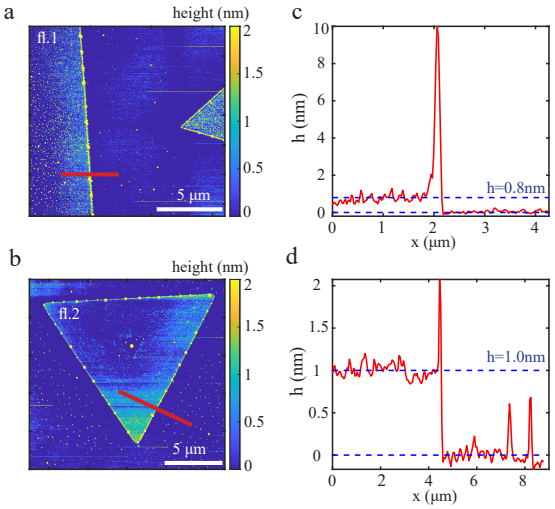

Figure B.2: AFM height measurements
a-b. AFM height measurement of **a** fl.1 and **b** fl.2 reveal a constant height of the flakes over their whole area, without variations or structural defects that would explain the non-uniformity in the PL intensity. The red lines depict the position of the **c-d.** AFM crosscuts. The measured height of 0.8 nm for fl.1 and of 1.0 nm for fl.2, which confirms the monolayer nature of these flakes as was already observed spectrally.

B.2. STOKES ANALYSIS

As mentioned in Chapter 4, we determine the valley coherence using the rotating quarter-wave plate method (see Fig.4.4a in Chapter 4). Given a quarter-wave plate (QWP) with perfect retardance, the measured intensity can be written as a function of the Stokes parameters and the QWP angle using Mueller matrix multiplication as [144–146]:

$$I(\theta) = \frac{1}{2}(S_0 + S_1 cos^2 2\theta + S_2 cos2\theta sin2\theta + S_3 sin2\theta), \tag{B.1}$$

with θ the angle of the QWP and S_0 to S_3 the Stokes parameters. This can be rewritten to a truncated Fourier series, after which the Stokes parameters can be found using Fourier analysis [144–146]. Unfortunately, the experimentally more likely situation of a QWP with non-perfect retardance, as we use in our experiment, is less straightforward (see Section 2.4 of Chapter 2 for more details about the used QWP). In that case, the measured intensity is:

$$I(\theta,\delta) = \frac{1}{2}(S_0 + S_1(cos^2 2\theta + sin^2 2\theta cos\delta) + S_2(cos2\theta sin2\theta)(1 - cos\delta) + S_3 sin2\theta sin\delta, \tag{B.2}$$

with δ the retardance of the QWP. Fig.4.4c in Chapter 4 depicts the measured PL intensity for different angles of the QWP, where the fit of the curve is based on Eq.B.2. Figure

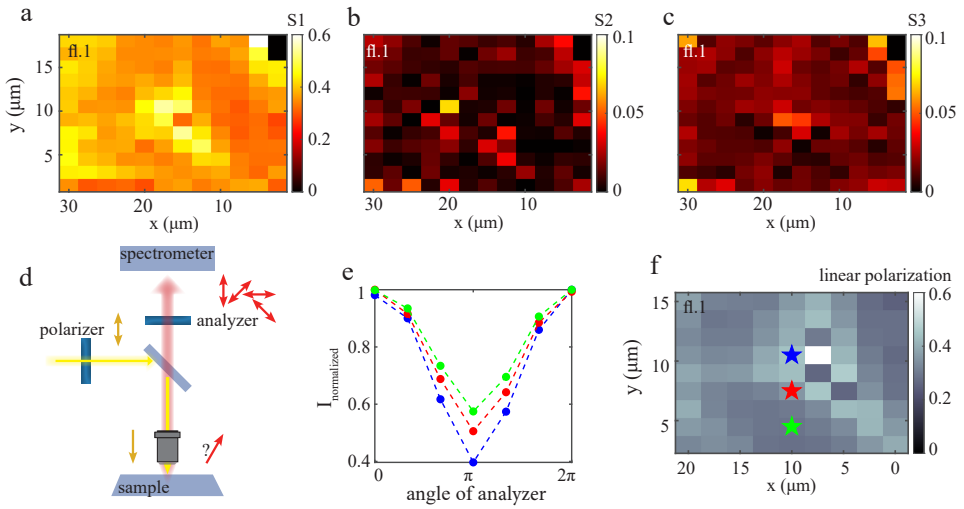

Figure B.3: Stokes analysis and linear polarization contrast
a-c Maps of the Stokes parameters of the PL of fl.1, derived using the rotating quarter-wave plate method (see Chapter 4). It is clear in **b,c** that S_2 and S_3 are negligible and independent of position. Therefore the main contribution to the valley coherence of the emission from the WS_2 valleys is S_1. In **a**, the S_1 parameter of the WS_2 emission has higher values at low intensity regions of fl.1, e.g. the triangle medians, and lower values at the other flake regions. The S_1 values are comparable to the valley coherence (compare with Fig.4.4d in Chapter 4). **d** We also perform linear polarization contrast measurements as performed by other groups [77, 137, 138]. Here we excite with linearly polarized light, but now we analyze the emission polarization using a rotating analyzer (see section 2.4 of Chapter 2). **e** Normalized intensity of the PL emission from fl.1 at different positions, as a function of the analyzer angle. From these curves, we determine the degree of linear polarization by $\frac{I_0 - I_\pi}{I_0 + I_\pi}$. **f** Map of the derived degree of linear polarization of the PL of fl.1 at 4 K (stars indicate the position of the curves in **e**). Note that the degree of linear polarization is very similar to the S_1 and to the valley coherence, which confirms that measuring the degree of linear polarization of WS_2 emission is a valid method for determining the valley coherence.

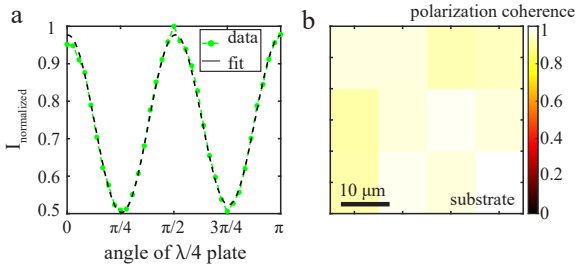

Figure B.4: Polarization coherence of laser reflection
a. Normalized intensity of the reflection of the linearly polarized 594 nm laser on the substrate, as a function of quarter-wave plate angle. The data (in green) are fitted (black dotted line) to extract the Stokes parameters and thus the polarization coherence via Fourier analysis. **b.** The polarization coherence of the linearly polarized laser reflection on the substrate has values between 0.90 and 1.0.

B.3a-c depicts the Stokes parameters as a result of the fitted PL intensity of fl.1 at 4 K. When inspecting Fig.B.3b and c, it becomes apparent that the S_2 and S_3 parameters of the WS_2 emission (upon excitation with linearly polarized light) are negligible and independent of position. The only relevant Stokes parameter is S_1. Therefore, comparing the calculated valley coherence $\Delta = \sqrt{S_1^2 + S_2^2 + S_3^2}/S_0$ of fl.1 in Fig.4.4d in Chapter 4 to the S_1 in Fig.B.3a, it is clear that the value and the position dependence is very similar: S_1 is also higher along the flake medians than on the rest of fl.1, with values between 0.4 and 0.6. This indicates that the previous measurements of linear polarization contrast [77, 137, 138] did indeed point at valley coherence.

To confirm these conclusions and compare the results to the rotating QWP experiment, we perform a linear polarization measurement on fl.1. Figure B.3d depicts the used set-up, where the sample is excited with linearly polarized light, and the resulting emission is analyzed by a polarization analyzer. Figure B.3e depicts the WS_2 PL intensity as a function of the angle of the polarization analyzer, for different positions on the flake. The dip at π is at most 0.40. We calculate the linear polarization contrast $\frac{I_0 - I_\pi}{I_0 + I_\pi}$ and plot this for fl.1 in Fig.B.3f (the stars indicate the position of the curves in Fig.B.3e). Comparing S_1 in Fig.B.3a, determined using the rotating QWP method, and the linear polarization contrast in Fig.B.3f, we conclude that the values and the pattern of high S_1 at the flake medians and low S_1 at the rest of the flake, is present in both experimental methods. Therefore we confirm that the WS_2 emission does indeed exhibit a coherence, indicating a partial quantum entanglement of the WS_2 valleys.

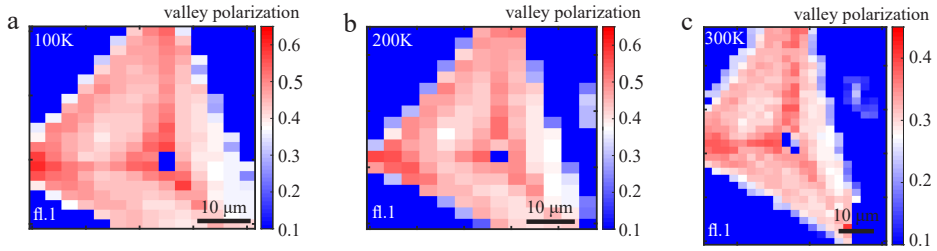

Figure B.5: Temperature-dependent valley polarization
a-c Valley polarization of fl.1 at 100 - 300 K. Just like the valley polarization at 4 K (compare Fig.4.2d in Chapter 4), the regions of the flake with lower PL intensity, e.g. the triangle medians, exhibit higher valley polarization than the higher intensity regions on this monolayer flake. This valley-polarization pattern persists from 4 K to room temperature. Note that we do not calculate the valley polarization of spectra of the defect region, in the middle of the flake.

B.3. EXPERIMENTAL METHODS

As mentioned in Section 2.5 in Chapter 2, the sample is placed on a piezo stage in a Montana cryostation S100 and the raster scans are performed using Attocube ANPxy101/RES piezo scanners. The chosen step sizes in the raster scans range from 500 nm in Fig.4.1e to 2.5 μm in Fig.4.4d in Chapter 4. The step size is not limited by the piezo positioners, which allow for sub-nanometer steps, but by experimental limitations such as the

total integration time and the size of the diffraction-limited excitation spot. There is a small cross-coupling between the in-plane and out-of-plane piezo scanners, causing a skewing between the x and y axis of the raster scans depicted in this work. Comparing the raster scans with the optical and SEM images of the monolayer flakes, we can nevertheless correlate the position of certain spectral features with the position on the flake.

As described in Section 2.4 of Chapter 2, the optical measurements are performed using a home-built spectroscopy set-up. For the rotating quarter-wave plate (QWP) experiments we use a zero-order QWP for 633 nm (Thorlabs WPQ05M-633). The retardance of this waveplate depends on the wavelength of the incident light, and ranges from δ=0.25 for 633 nm to δ=0.265 for 600 nm. For cryogenic temperatures, the bandgap energy of WS_2 red shifts to 605 nm. Therefore, this zero-order QWP works less well for WS_2 emission at cryogenic temperatures then at room temperature. We have taken this wavelength-dependence into account when fitting the angle-dependent PL intensity in Fig.4.4c in Chapter 4.

Even though a superachromatic waveplate would have had a retardance close to 0.25 for the range of the emission wavelengths, it has an experimentally much larger disadvantage. Most superachromatic waveplates cause a beam deviation up to 3 arcmin due to the necessary composition of at least three separate birefringent plates, whereas the beam deviation caused by a zero-order waveplate is an order of magnitude lower, up to 10 arcsec. That means that even with a perfect alignment, light that passed through the superachromatic waveplate will travel under a different angle, depending on the waveplate rotation. As the emission travels to the CCD camera through a spectrometer, angle differences in the incident light will propagate and cause an unwanted dependence of the measured intensity on the waveplate angle. Therefore we have chosen to use the zero-order QWP, taking into account its wavelength-dependent retardance. We attribute the remaining difference in intensity at $\pi/4$ and $3\pi/4$ in Fig.4.4c of the main text with respect to the fitted curve, to small angular deviations caused by the alignment of the zero-order waveplate and the emission path.

To underline the validity of our experimental set-up, we have used the rotating quarter-wave plate method to measure a known polarization state. We have measured the polarization of the linearly polarized 594 nm excitation light reflected off the substrate. Figure B.4a presents the normalized intensity of the collected light as a function of quarter-wave plate angle. The intensity exhibits minima at $\pi/4$ and $3\pi/4$ of 0.50. The depth of the intensity minima already suggests that the light is indeed linearly polarized.

To fully characterize the polarization state of the light, we perform a Fourier analysis of the intensity curve and derive the Stokes parameters of the reflected excitation light. The retardance of the used quarter-wave plate is specified to be δ=0.268 for 594 nm. However, based on the analysis of the known linear polarization state of the excitation laser, we derive that a value of δ=0.245 describes the retardance of our specific zero-order QWP. With this, we find values of 0.9-1.0 for S_1, whereas S_2 and S_3 are negligible, namely $<$ 0.05. Therefore, we calculate the polarization coherence of the laser light Δ to be 0.9-1.0. The difference between experimentally determined and specified retardance yields an

error on the derived valley coherence values in Fig.4.4 in Chapter 4. If the retardance of the used QWP is in reality slightly lower than specified by the supplier, as was the case at the 594 nm wavelength, this would lead to derived valley coherence values that are even larger than presented in Fig.4.4. For fl.2, the derived valley coherence at 4 K as depicted in Fig.4.4e,f in Chapter 4, is on average 0.42 at low valley coherence regions and 0.48 at high valley coherence regions. If the retardance of the used QWP would be δ=0.24 for a 614 nm exciton wavelength, the average valley coherence would be 0.49 at low valley coherence regions and 0.58 at high valley coherence regions.

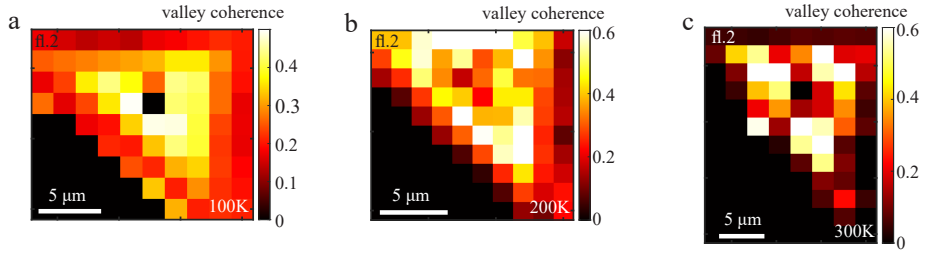

Figure B.6: Temperature-dependent valley coherence
a-c Valley coherence of fl.2 at 100 - 300 K. Just like the valley coherence at 4 K (compare Fig.4.4e in Chapter 4), the middle region of the flake with lower PL intensity exhibits higher valley coherence than the higher intensity edges on this monolayer flake. The difference in higher and lower valley coherence is present even at room temperature, although not as clear as at cryogenic temperatures. Note that we do not calculate the valley coherence of the defect-related spectral response in the middle of the flake.

B.4. TEMPERATURE DEPENDENCE

As mentioned in Chapter 4, the valley polarization on the monolayer flakes follows the same distribution as the intensity. Figure B.5a-c presents the valley polarization of fl.1 at 100 K, 200 K and room temperature. The resulting pattern of high valley polarization at the flake medians and lower valley polarization at the rest of the flake is the same as the pattern at 4 K in Fig.4.2d in Chapter 4. The pattern in the PL intensity also exists at all temperatures, compare Fig.B.1c,d and Fig.B.7a,d. We conclude that the inverse correlation between valley polarization and PL intensity exists at all temperatures.

The same holds for the valley coherence. Figure B.6a-c presents the valley coherence of fl.2 at 100 K, 200 K and room temperature. The pattern of high valley coherence in the middle region and low valley coherence on the edges is the same as the pattern at 4 K in Fig.4.4e in Chapter 4, although the pattern is not as clear at room temperature. We conclude that the inverse correlation between valley coherence and PL intensity also exists at all temperature.

B.5. POLARIZATION BEHAVIOUR OF FLAKE 3 AND FLAKE 4

Figure B.7a,d presents the PL intensity of fl.3 and fl.4 at 4 K. Where fl.1 and fl.2 exhibited a defect-related region in the middle, fl.3 and fl.4 do not (see Fig.B.1). The PL intensity of fl.3 is lower than that of fl.4 (the scale bars are chosen the same for direct comparison).

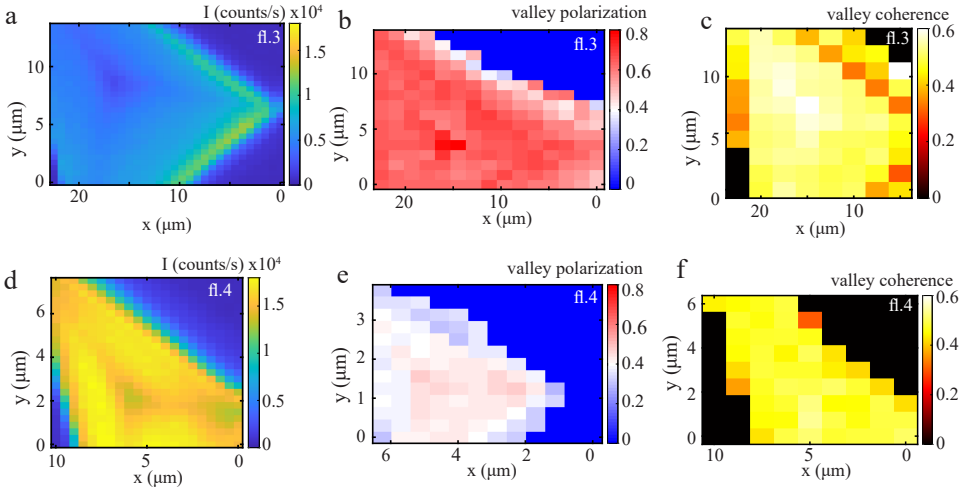

Figure B.7: PL intensity, valley polarization and valley coherence of fl.3 and fl.4
a,d PL intensity of fl.3 and fl.4 at 4 K, representing the monolayer flakes that do not exhibit a defect region in the middle. The extent of the colormaps is chosen the same for easy comparison. As could be seen in Fig.B.1c-d, the intensity of fl.3 is lower than fl.4. **b,e** Valley polarization of fl.3 and fl.4 at 4 K. Note that the valley polarization of these flakes is much more homogeneous than of fl.1 and fl.2. Fl.3 has a lower PL intensity, and a higher valley polarization, when compared to fl.4. This inter-flake inverse relationship between intensity and valley polarization follows the same trend as the intra-flake relationship seen in fl.1 and fl.2. **c,f** Valley coherence of fl.3 and fl.4 at 4 K. Note that now the valley coherence of these flakes is comparable, although fl.3 has slightly higher values. This means that the inverse relationship between PL intensity and valley coherence for regions in fl.1 and fl.2, cannot be confirmed within the experimental margins of error for fl.3 and fl.4.

Figure B.7b,e presents the valley polarization of fl.3 and fl.4 at 4 K. The valley polarization of these monolayer flakes is more homogeneous over the flakes. We hypothesise that this is related to the absence of the defect region in these flakes. The valley polarization of fl.3 is clearly larger than that of fl.4, therefore following the same inverse correlation between PL intensity and valley polarization as the different regions on fl.1 and fl.2.

However, the inverse correlation between PL intensity and valley coherence is not as clear for these flakes. Figure B.7c,f presents the valley coherence of fl.3 and fl.4. The valley coherence of fl.3 is only slightly higher than that of fl.4 (0.55 vs. 0.45), but the values are of the same order of magnitude.

C

Supplementary Materials to Chapter 6

Parts of this chapter have been published as the Supplementary Materials of [23], copyright 2021 Royal Society of Chemistry.
Data acquired for this publication can be found at DOI: 10.4121/13246751

C.1. WS_2 HOLLOW PYRAMID SAMPLE

Figure C.1a presents a wide-field optical image of a part of the sample. Under these growth conditions both hollow pyramids (red), monolayer flakes (green) and full pyramids (blue) are created. Note that there are many hollow pyramids with a comparable size to the one studied in this work (15 μm). Using the same CVD growing conditions (see Methods) yields similar samples with the same distribution of pyramid-like structures.

To provide better insight in the morphology of the hollow WS_2 pyramids, Fig.C.1b,c depicts higher magnification SEM images of the hollow pyramid depicted in Fig.6.1a in Chapter 6. The black triangle in the middle of Fig.C.1b is the bottom of the pyramid crater. The top rim can also be distinguished around the crater triangle. The steps of the stair-like sides can clearly be recognized in Fig.C.1c.

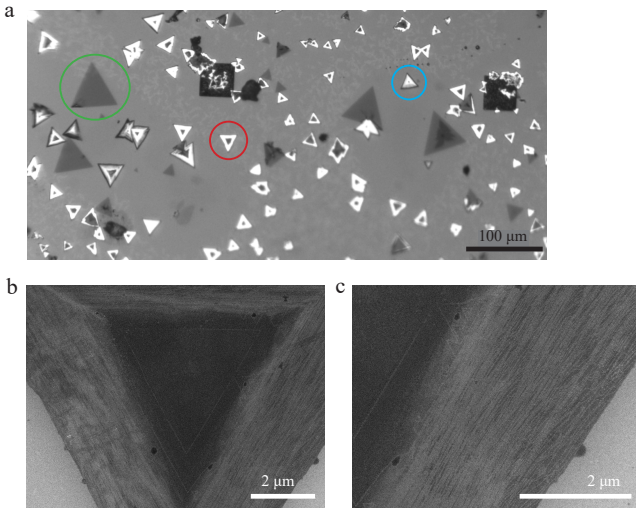

Figure C.1: Hollow WS_2 pyramid sample
a. Wide-field optical image of a part of the sample, with hollow pyramids (red), WS_2 monolayer flakes (green) and full pyramids (blue). The black squares are windows in the silicon frame over which a silicon nitride film is spanned (see Section 1.3.2 of the Introduction). Under these growth conditions, many hollow pyramids arise size 10 - 25 μm, comparable to the one presented in this work. **b,c.** SEM images of the hollow WS_2 pyramid studied in Chapter 6. In **b**, the black triangle in the middle is the bottom of the pyramid crater. The top rim of the pyramid can also be distinguished around the triangle of the pyramid crater. The steps in the stair-like sides can be easily recognized in **c**.

In addition, Transmission Electron Microscopy (TEM) measurements are performed to gain access to the atomic structure of the hollow pyramids. Figure C.2a and C.2b display low-magnification annular dark-field (ADF) scanning transmission electron microscopy (STEM) images of the side of a hollow WS_2 pyramid. The variations in the contrast visualise clearly the step-like nature of the hollow pyramid side. Figure C.2c presents an atomic-resolution ADF-STEM image corresponding to the side of the pyramid. Each bright spot corresponds to an atomic column that is composed of alternating tungsten

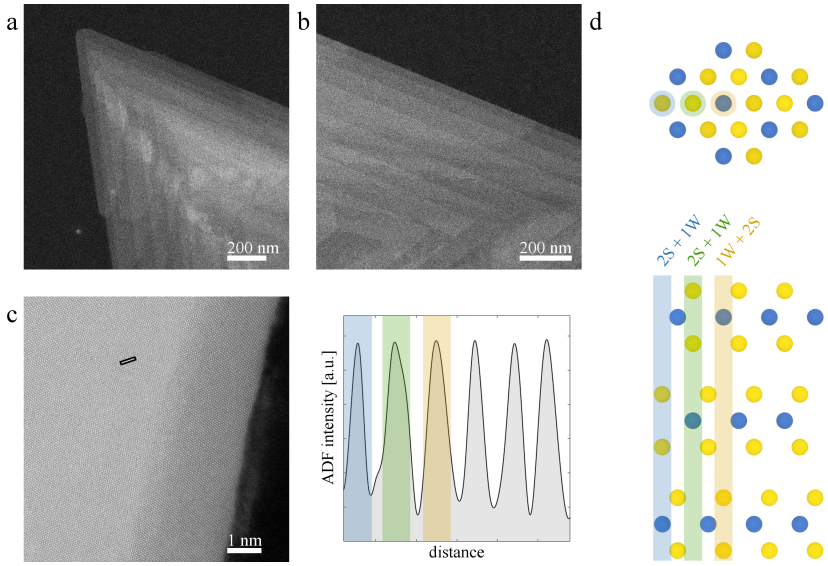

Figure C.2: Morphology and crystal structure of the hollow WS_2 pyramids
a-b. Low-magnification ADF-STEM images of a hollow WS_2 pyramid. The step-like nature of the pyramid side is clearly visible by the changes in contrast with every step. **c.** Atomic resolution image corresponding to the side of the hollow pyramid (left panel) and the ADF intensity profile (right panel) acquired along the black outlines region in the atomic resolution image. **d.** Schematic atomic model of the top-view (upper panel) and side-view (lower) of the crystalline structure associated to the 3R-WS_2 phase.

(W) and sulfur (S) atoms. Using an ADF linescan, extracted from the atomic resolution image across six lattice points, we confirm that the WS_2 within the hollow pyramid crystallizes in a 3R crystal phase (see Fig.C.2d).

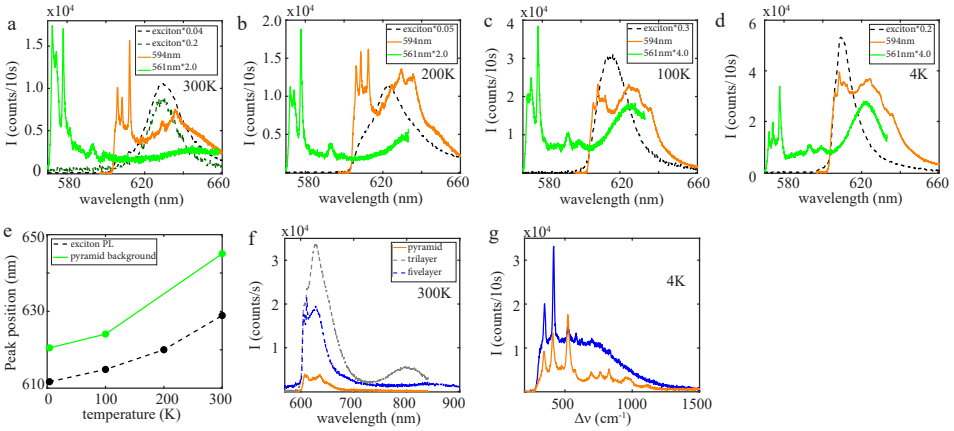

Figure C.3: Comparison pyramid, monolayer and few-layer spectra
a-d. Spectral response of a pyramid upon a 594 nm excitation (orange) or a 561 nm excitation (green), and the spectral response of a monolayer upon 594 nm excitation (black dotted line), at temperatures between room temperature and 4 K (the spectra are re-scaled for easier comparison, see legends). The spectral response of the monolayer upon a 561 nm excitation (green dotted line in **a**) has a lower intensity than to the 594 nm excitation, but is at the same wavelength. **e.** The background under the higher order Raman features in the spectra of the 594 nm excitation, and the spectral position of the exciton PL are both blue-shifting with decreasing temperature. **f.** In contrast to the spectra of a WS_2 trilayer (in grey) and five layers of WS_2 (in blue) (exfoliated on a Si substrate), the spectrum of the WS_2 pyramid (in orange) does not exhibit light from an indirect bandgap at 800 - 850 nm wavelength. Moreover, although reduced with respect to the monolayer, the PL from the direct bandgap of the few-layers of WS_2 is clearly distinguishable from the background. **g.** Comparison of the spectral response of the hollow pyramid (in orange) and of five layers of WS_2 (in blue), acquired at 4 K with a 594 excitation.

C.2. SPECTRAL BACKGROUND

The hollow pyramid spectra exhibit a number of Raman modes plus a background (see Fig.6.3 in Chapter 6). Using the temperature-dependent spectral position of this background, we can explain its origin. Figure C.3 depicts the spectral response of the hollow pyramid upon a 594 nm excitation (orange) and a 561 nm excitation (green), comparing this with the photoluminescence of a monolayer exciton (black dotted line). The spectral response of the hollow pyramid to a 594 nm excitation exhibits a background under the higher order Raman modes, whereas the spectral response of a 561 nm excitation exhibits a background separated from the Raman modes, that overlap spectrally (see Fig.C.3c-d). The spectral position of the photoluminescence peak is completely different (610 - 630 nm in the temperature range 4 K - 300 K). Figure C.3e depicts the spectral position of the pyramid background, determined from the spectra of 561 nm excitation (in green), and the spectral position of the exciton PL (black dotted line). Both the pyramid background and the exciton PL peak are blue-shifting with decreasing temperature, however their spectral position is different from each other. At room tempera-

ture (Fig.C.3a), the spectral position of the PL peak (at 630 nm) is very close to the background of the pyramid spectra acquired with a 594 nm excitation (around 645 nm). At 4 K (Fig.C.3d), the PL peak (at 615 nm) overlaps roughly with the first few Raman features of the pyramid spectra acquired with a 594 nm excitation (around 620 nm). However, at 200 K and especially 100 K (Fig.C.3b,c), the PL peak overlaps neither with the first Raman features nor the background of the pyramid spectra acquired with a 594 nm excitation. Therefore we conclude that the background of the hollow pyramid spectra is not photoluminescence from the direct bandgap of WS_2.

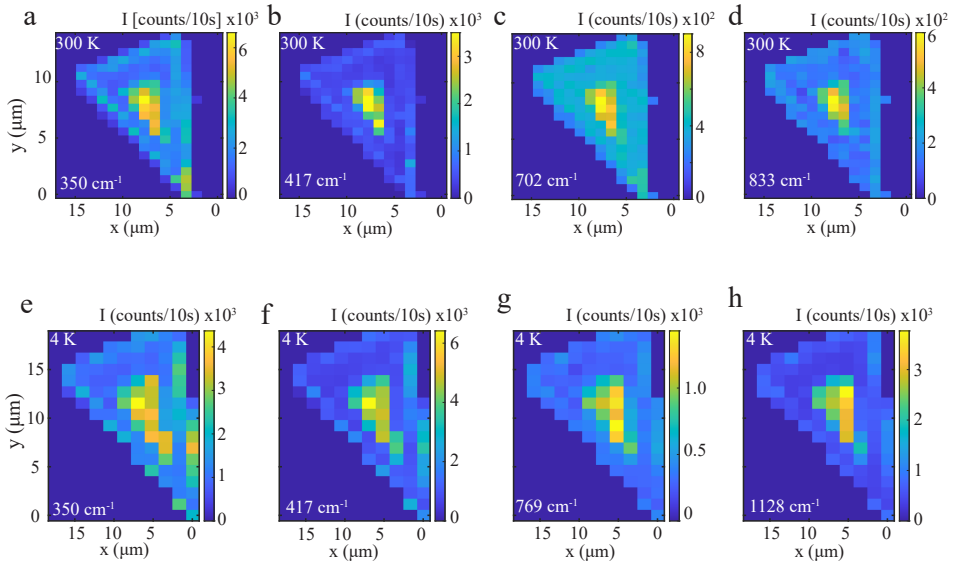

Figure C.4: Position dependence of Raman intensity
a-d Intensity map of the Raman features of the hollow WS_2 pyramid **a.** around 350 cm^{-1} (2LA,E_{2g}), **b.** around 417 cm^{-1} (A_{1g}), **c.** around 702 cm^{-1} (4LA) and **d.** around 833 cm^{-1} ($2A_{1g}$), taken at room temperature upon a 561 nm excitation. **e-h** Intensity map of the Raman features of the hollow WS_2 pyramid **e.** around 350 cm^{-1} (2LA,E_{2g}), **f.** around 417 cm^{-1} (A_{1g}), **g.** around 770 cm^{-1} (A_{1g}+2LA) and **h.** around 1120 cm^{-1} (6LA), taken at 4 K upon a 561 nm excitation. Note that in all cases (compare with Fig.6.4a,b in Chapter 6) the intensity of the Raman features from the pyramid crater is significantly higher than the Raman intensity from the stair-like sides.

Another potential explanation for the background in the pyramid spectra is emission from the indirect bandgap. Few-layer WS_2 samples exhibit a combination of direct and indirect bandgap emission [12]. Figure C.3f compares the room-temperature spectra of a WS_2 trilayer (grey) and five WS_2 layers (blue) (exfoliated on a Si substrate) with a spectrum from the hollow WS_2 pyramid. The room-temperature spectral position of the indirect bandgap ranges from 700 nm for a bilayer to 850 nm for multilayers [40]. This constitutes a large spectral separation with the measured spectrum (compare Fig.C.3a). Moreover, with decreasing temperature, the indirect bandgap is reported to exhibit a

red shift, *i.e.*, away from the exciton position [39, 75], whereas the pyramid background exhibits a similar blue shift to the exciton PL (see Fig.C.3e).

An alternative explanation would be emission from a charged exciton or trion. However, the reported spectral position of the trion lies closer to the exciton than the background in the hollow pyramid spectra [35, 37]. We conclude that this background originates in intermediate gap states or defect states, that are reported to be in a range of spectral positions further away from the exciton PL than the trion [37, 194, 195], but closer than the indirect bandgap [39, 40, 75].

It is interesting to note that the spectral background from these intermediate gap states is more present in the pyramid crater than on the pyramid sides. We propose this might be originated in the higher density of crystallographic defects.

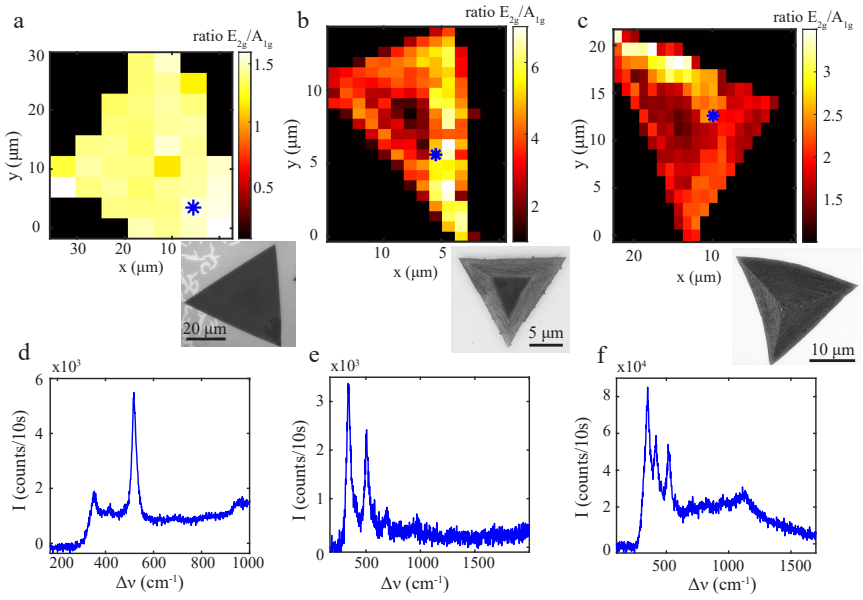

Figure C.5: Position dependence of peak ratio
a-c Room-temperature map of the ratio between the first two Raman features in the spectra (E_{2g}/A_{1g}) of **a** the monolayer, **b** the hollow pyramid and **c** a full WS_2 pyramid (compare SEM images) (blue stars indicate the positions of the spectra in **d-f**). **a.** The peak ratio on the monolayer is homogeneous along the full flake, 1.4 on average (upon a 561 nm excitation). **b.** The peak ratio on the hollow pyramid (upon a 561 nm excitation) is much higher along the stair-like pyramid sides (namely 4-7) than on the pyramid crater (roughly 1.0). **c.** The peak ratio on the full pyramid is significantly higher along the upper side. Note in the presented SEM image that this side of this full WS_2 pyramid is curved, potentially inducing strain. **d.** Raman spectrum of the WS_2 monolayer. **e.** Spectrum of the side of the WS_2 hollow pyramid upon 561 nm excitation. Note that the A_{1g} feature is merely a shoulder on the E_{2g},2LA(M) feature, which explains the high peak ratio in **b**. **f.** Spectrum of the full WS_2 pyramid (594 nm excitation), which is comparable to the spectra of the hollow WS_2 pyramid presented in Chapter 6.

C.3. SPECTRAL FEATURES OF PYRAMIDS, MONOLAYER AND FEW-LAYER WS_2

Figure C.4 presents maps of the intensity of different Raman features in spectra from the hollow WS_2 pyramid, taken at room temperature (Fig.C.4a-d) and at 4 K (Fig.C.4e-h) upon a 561 nm excitation. Note that for all the Raman features the intensity from the pyramid crater is higher than from the pyramid sides, as was the case for the Raman features depicted in Fig.6.4a,b in Chapter 6 (594 nm excitation, 200 K). We conclude that the intensity distribution of the Raman features is independent of temperature or excitation frequency. As alluded to in Chapter 6, we hypothesise that light scatters from the stair-like pyramid sides and thus reduces the available excitation light to excite any Raman modes, or that scattering of the resulting Raman response reduces the amount of light detected.

Figure C.3g depicts a comparison between the spectral response of the pyramid (in orange) and five layers of exfoliated WS_2 (in blue) at 4 K and upon a 594 nm excitation. The spectral response of the few-layer WS_2 exhibits a combination of Raman modes and PL from the excitonic resonance. Due to the PL, the higher-order Raman modes are much less clear in the few-layer WS_2 than in the pyramid spectrum. In both spectra, the A_{1g} mode has a higher intensity than the E_{2g} mode. The ratio of E_{2g}/A_{1g} is 0.60 for few-layer WS_2, whereas it is on average 0.79 for the pyramid spectra (see Fig.6.6b in Chapter 6).

Figure C.5a-c presents room-temperature maps of the ratio between the first two Raman peaks in the spectra (E_{2g}/A_{1g}) of respectively the WS_2 monolayer, the hollow pyramid and a full WS_2 pyramid (compare the presented SEM images). In contrast with the position dependent peak ratio of the hollow pyramids, the peak ratio on the monolayer is homogeneous along the full flake (see Fig.C.5a). This ratio is around 1.4, as can be observed in the Raman spectrum in Fig.C.5d. The Raman peak ratio of the hollow pyramids upon 561 nm excitation is much higher on the pyramid sides than in the pyramid crater (see Fig.C.5b). This difference in ratio was already apparent upon 594 nm excitation, as presented in Fig.6.4f in Chapter 6, but the contrast between the pyramid sides and crater is much larger upon 561 nm excitation. The Raman peak ratio at the pyramid sides is as high as 4-7 times, as the A_{1g} feature is reduced to merely a shoulder on the E_{2g},2LA(M) feature. This becomes apparent in the spectrum in Fig.C.5e. The SEM image under Fig.C.5c depicts a full WS_2 pyramid grown on the same substrate. This pyramid exhibits a clear curvature. Interestingly, the Raman peak ratio of the spectra from this pyramid (upon a 594 nm excitation) exhibit a difference on the side with the largest curvature, potentially induced by strain. Figure C.5f presents a spectrum of the full WS_2 pyramid, which is similar to the spectra of the hollow WS_2 pyramid in Chapter 6. We conclude that the Raman peak ratio provides information on differences in the atomic structure between different nanostructures, as well information on differences in both atomic structure and strain or stress within the same nanostructure.

Another position-dependent spectral feature alluded to in Chapter 6 is the spectral position of the Raman peaks. Figure C.6 presents a map of the spectral position of the first Raman peak on the WS_2 monolayer and the full WS_2 pyramid respectively. The peak po-

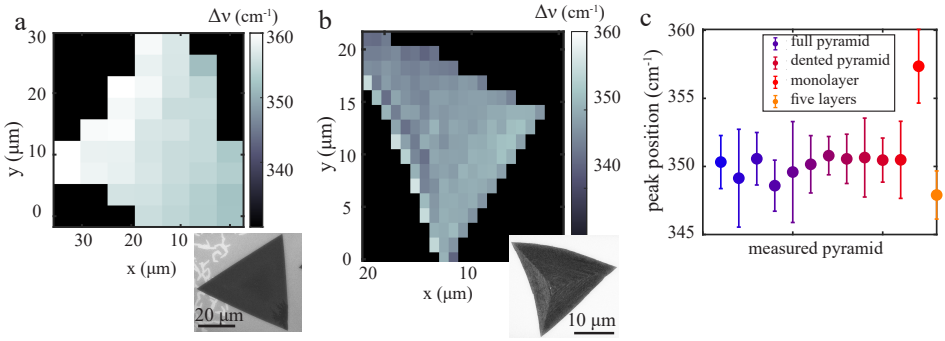

Figure C.6: Position dependence of spectral position
a-b Room temperature map of the first WS_2 Raman feature around 350cm^{-1} on **a** the monolayer and **b** a full WS_2 pyramid (compare SEM images). Comparing **a** and **b** and Fig.6.5 in Chapter 6, it becomes apparent that the Raman peak position on the monolayer is significantly different than on the pyramids. **c** depicts the average spectral position of the first Raman peak on all measured pyramids and the monolayer. Note that the bar does not indicate errors, but rather the spread of the peak position along the pyramids. The first Raman feature on the monolayer is around 357 cm^{-1}, whereas on all measured pyramids, it is around 350 cm^{-1}, and around 348 cm^{-1} on five layers of WS_2. Possibly this Raman peak has a larger contribution from the E_{2g} than the 2LA(M) phonon in the monolayer than in the pyramid spectra.

sition is fairly homogeneous along both nanostructures compared to the hollow pyramid (Fig.6.5a in Chapter 6). Figure C.6c depicts the average spectral position of the first Raman peak, as measured on different WS_2 pyramids and the monolayer (the bar does not indicate errors, but rather the spread of the peak position along the pyramids). The peak position on the monolayer is around 357 cm^{-1}, which is significantly different than the peak position of around 350 cm^{-1} on all the pyramid structures and 348 cm^{-1} for five layers of exfoliated WS_2. We hypothesise that this first Raman peak has a larger contribution from the E_{2g} than the 2LA(M) phonon in the monolayer than in the pyramid spectra. In conclusion, the different nanogeometry of the WS_2 pyramids induces spectral changes with respect to monolayer WS_2.

C.4. STRUCTURAL CHARACTERISATION

Figure C.7 displays additional results obtained in the structural characterization measurements by means of Transmission Electron Microscopy (TEM). Figure C.7a presents a high-resolution ADF-STEM image taken at the side of a hollow WS_2 pyramid. Within Fig.6.2 of Chapter 6 it could already be observed that the atomic arrangements present in the sides of the WS_2 pyramid and the middle are not the same. Figure C.7a depicts how even within a given region the atomic arrangement can vary. This is highlighted by the differences in the FFTs taken in the lower left corner (marked by the green rectangle in Fig.C.7a) and the top right corner (marked by the blue rectangle in Fig.C.7b) of this given region. Where the FFT in the blue area shows two nicely arranged hexagonal patterns, *e.g.*, an inner and an outer hexagon, the green area presents one hexagon. These subtle variations of the atomic arrangement might be induced by the local presence of strain, which in turn results into a slight change of the orientation of the flake.

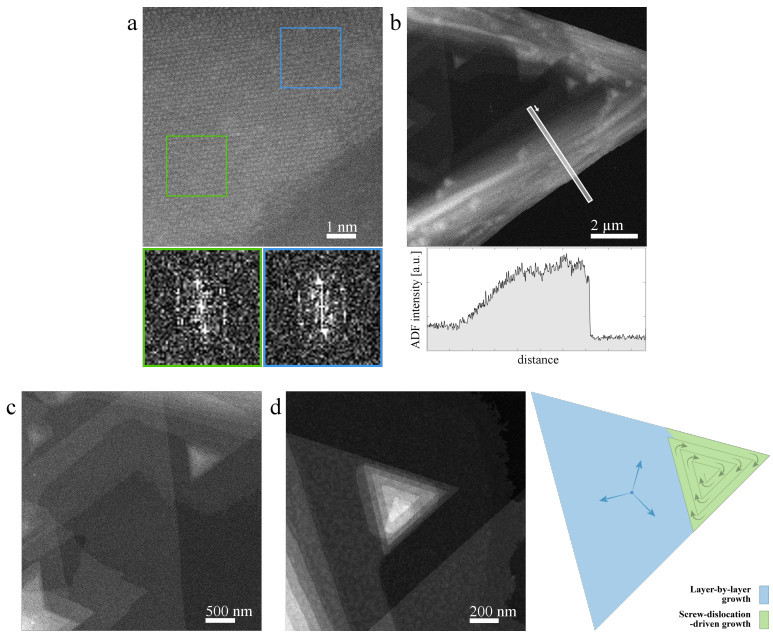

Figure C.7: ADF-STEM of a hollow WS_2 pyramid
a. Atomic resolution ADF-STEM image taken at the side of a hollow WS_2 pyramid. **inset** FFTs are taken within two visual different areas of this given region, highlighting a clear difference between the two areas. **b-d.** Low-magnification ADF images of the same hollow pyramid. The characteristic morphology of the hollow pyramids can clearly be observed, and is also extracted from the line profile over the white line given within **b** (see inset). Each of these images show free-standing flakes which arise from the walls of the hollow pyramid. The free-standing flake shown in **d** suggest a growth mechanism where layer-by-layer stacking and screw-dislocation-driven growth mechanisms co-exist. **inset** A schematic visualises this co-existence. Here a free-standing flake initiates its growing from a central nucleation point via layer-by-layer growth (blue), after which a separate nucleation event occurs leading to a screw-dislocation-driven growth (green) on top.

Figures C.7b and C.7c depict low-magnification ADF images of the hollow WS_2 pyramid. Within Fig.C.7b the hollow nature of the pyramid can clearly be observed, and illustrated even clearer in the line profile taken along the white line given in Fig.C.7b. In addition, both Fig.C.7b and C.7c depict how free-standing WS_2 flakes seem to arise from the walls of the hollow pyramid. These free-standing flakes increase the level of structural disorder in the middle of the pyramids as compared to the sides. The standing flake depicted in Fig.C.7d highlights the possible growth mechanism leading to the hollow WS_2 pyramids. In this figure it can be observed that both layer-by-layer stacking and screw-dislocation-driven growth mechanisms contribute to the overall growth mechanism of the hollow WS_2 pyramids.

D

Supplementary Materials to Chapter 7

Data acquired for this chapter can be found at DOI: 10.4121/16628488

D.1. REMNANT PHOTOLUMINESCENCE

As mentioned in Chapter 7, the spectral response of the WS_2 nanoflowers exhibits 8-10 Raman features, in combination with a broad background. Figure D.1a-d presents temperature-dependent spectra of a nanoflower upon 594 nm excitation (in orange) and 561 nm excitation (in light green). From Fig.D.1c,d it becomes apparent that for the spectra upon 594 nm excitation, the maximum of the broad background is found at approximately 615 nm and overlaps spectrally with the sharp Raman features. For the spectra upon 561 nm excitation, the broad background is well separated from the Raman features. The spectral position of the broad background is the same for both excitations.

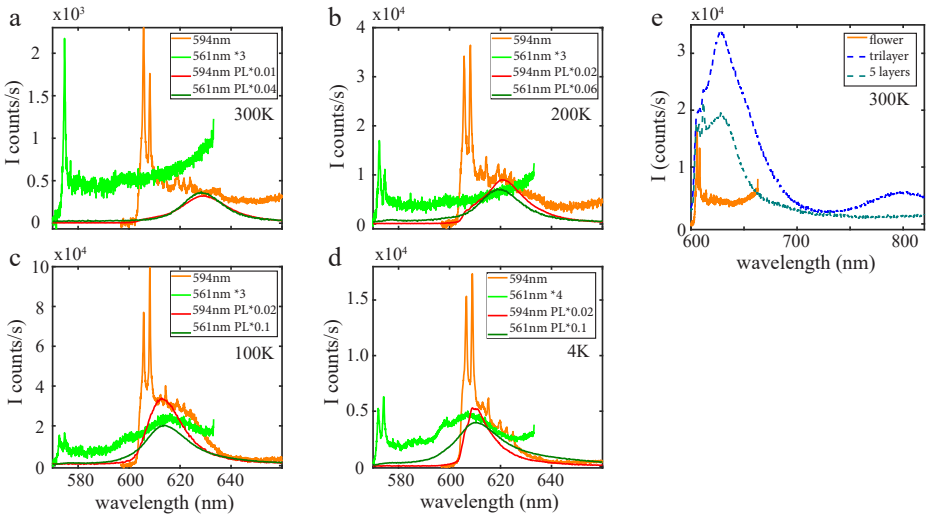

Figure D.1: Comparison spectral response flower and monolayer WS_2
a-d. Temperature-dependent spectral response of a WS_2 nanoflower upon 594 nm excitation (orange) and 561 nm excitation (light green), compared with the photoluminescence (PL) response of a monolayer WS_2 upon 594 nm excitation (in red) and 561 nm excitation (dark green), rescaled for an easy comparison (see legends). The spectral response of the nanoflowers contains both sharp Raman features and a broad background. In **c-d**, this broad background around 615 nm overlaps spectrally with the sharp Raman features upon 594 nm excitation (in orange), but is well separated from the Raman features upon 561 nm excitation (light green). Especially in the spectra at 4 K and 100 K (**c-d**), the spectral background under the Raman features of the nanoflowers is at the same spectral position as the monolayer PL. At all temperatures, the remnant PL in the nanoflower spectra is at most 2% of the monolayer PL. **e.** (Room-temperature) spectra of a WS_2 trilayer (in blue) and five layers of WS_2 (in blue-green) (exfoliated on a Si substrate), compared with a spectrum of a WS_2 nanoflower (in orange). For few-layer WS_2, the PL intensity from the direct transition is reduced by an order of magnitude with respect to a monolayer, but is still clearly distinguishable from the background. The intensity of the remnant PL from the nanoflower is however another order of magnitude lower than the PL of few-layer WS_2.

As a comparison, Fig.D.1a-d also presents temperature-dependent PL spectra of a WS_2 monolayer upon 594 nm excitation (in red) and 561 nm excitation (dark green). The spectral position of the PL shifts from 630 nm at room temperature to 615 nm at cryo-

genic temperatures. At 100 K and 4 K it is clearly visible, that the broad background under the Raman features of the nanoflowers is at the same spectral position as the monolayer PL spectra. The maximum peak intensity of the broad background is around 2% of the PL intensity. At room temperature and 200 K, the background under the Raman features is broader than the monolayer PL spectra. At these temperatures, the intensity of the background is not higher than 2% of the monolayer photoluminescence. As the depicted spectra are taken from nanoflowers with the highest visible background, we conclude that the upper limit for the remnant PL in the nanoflower spectra is 2%.

When comparing the spectra of the WS_2 nanoflowers with the spectra of the hollow pyramids in Fig.C.3 of Appendix C, we observe many differences. The spectra of the hollow pyramids exhibit a spectral background with a different temperature-dependent spectral position than the exciton. Based on the spectral position of this background, we attribute this to intermediate gap states or defect states (see Section C.2 of Appendix C). The spectra of the flowers do not exhibit this defect-related background. This allows a qualitative determination of the amount of remnant PL under the nanoflower spectra, which was not possible for the spectra of the pyramids.

As mentioned in Chapter 7, the thickness of the nanoflower petal is estimated to be between 2 and 30 nm. Therefore we compare the response of the nanoflowers to that of few-layer WS_2 in Fig.D.1e. The spectra of a trilayer (in blue) and five layers of WS_2 (in blue-green) (exfoliated on a Si substrate) exhibit PL both from the direct transition and the indirect transition (around 800 - 850 nm). The intensity of the PL from the direct transition is an order of magnitude lower than the PL of the WS_2 monolayer, but it is still clearly distinguishable from the background. The intensity of the remnant PL of the nanoflower is however another order of magnitude lower than the PL of few-layer WS_2.

D.2. CHARACTERIZATION OF RAMAN MODES

D.2.1. HIGHER ORDER WS_2 RAMAN MODES

The spectral position of the sharp features in the spectra of the WS_2 nanoflower, taken with a different excitation wavelengths in Fig.D.1, does not overlap in wavelength. These features are located at the same relative frequency distance to the excitation laser, as depicted in Fig.D.2a, indicating that the collected light originates from Raman processes, as described for the spectra of the pyramids (see Chapter 6). In the same way as for the pyramids, we attribute the higher frequency Raman modes to multiphonon resonances involving the LA(M) phonon, adopting the methodology for high frequency Raman features in MoS_2 [74]. The dark grey line in Fig.D.2b depicts the higher order resonances of n*LA(M), and the light grey line depicts the higher order resonances of A_{1g}+n*LA(M).

The features around 880 cm^{-1}, 1057 cm^{-1} and 1128 cm^{-1} (marked with dotted arrows in Fig.D.2b) are less pronounced in the spectral response of the flowers than of the pyramids (see Fig.6.3 in Chapter 6). Although one would also expect a feature at 3*LA(M), this is usually not reported. Most experiments are performed with TMDs on a silicon substrate, and the Si resonance at 520 cm^{-1} is around the same position as the mentioned

D

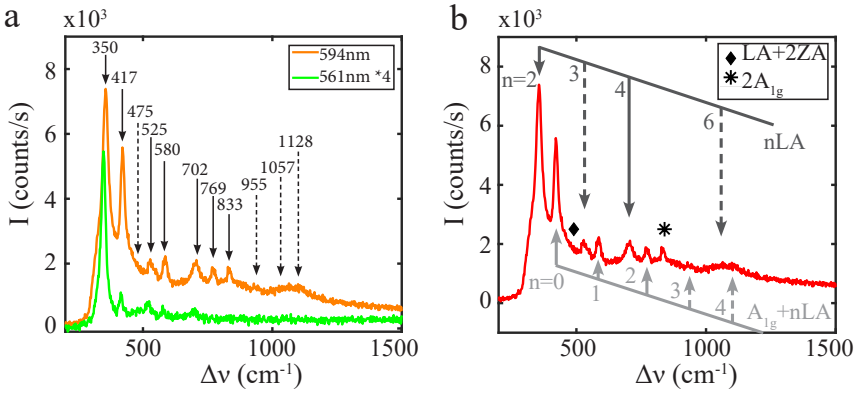

Figure D.2: Characterization of Raman peaks for nanoflowers
a. The optical response of the WS_2 nanoflowers upon 594 nm excitation (in orange) and 561 nm excitation (in green, multiplied by 4 for an easy comparison). The spectral response on the two different lasers overlaps well, indicating that the collected light originates from Raman processes. Many more modes are observed using the more resonant 594 nm excitation (orange), than using the 561 nm excitation (green). The optical response of the WS_2 nanoflowers contains the same 8-10 Raman features as the pyramids (see Fig.6.3 in Chapter 6). **b.** In the same way as for the pyramids, we explain the higher frequency features as being multiphonon resonances involving the LA(M) phonon. The dark grey line depicts the higher order resonances of n*LA(M), and the light grey line depicts the higher order resonances of A_{1g}+n*LA(M). Note the absence of the Raman features associated to silicon (at 520 cm^{-1} and 955 cm^{-1}) in the spectral response of the nanoflowers. We associate the feature around 525 cm^{-1} in the spectral response of the flower to 3LA(M) rather than to the Si Raman resonance. The features around 880 cm^{-1}, 1057 cm^{-1} and 1128 cm^{-1} (marked with dotted arrows) are less pronounced in the spectral response of the flowers than of the pyramids (see Fig.6.3 in Chapter 6).

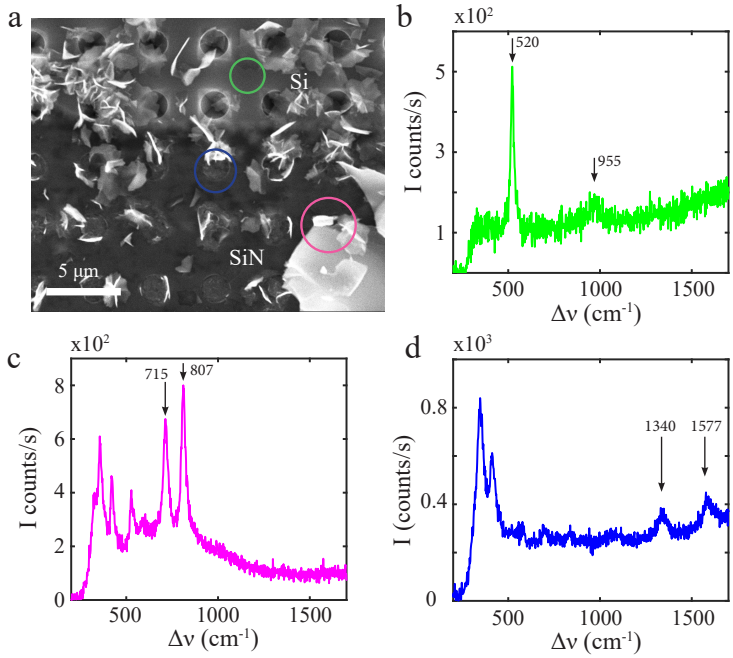

Figure D.3: Non-WS_2 Raman response
a. SEM image of the WS_2 nanoflowers. The substrate is composed of a silicon frame (upper half of image) with a Si_3N_4 window in the middle (lower half of image). The array of holes can be distinguished more clearly in the silicon region of the sample, but the holes are also present in the Si_3N_4 membrane. **b.** Spectrum on the Si substrate (see green circle in **a**), where the characteristic 520 cm^{-1} and 955 cm^{-1} Raman features can be clearly distinguished. These Raman features are not present on the Si_3N_4 membrane. **c.** Spectrum of a WO_3 particle (see pink circle in **a**), where the characteristic 715 cm^{-1} and 807 cm^{-1} Raman features can be clearly distinguished. In most regions of the sample, the only measured Raman features are from WS_2 and not WO_3. **d.** Spectrum with the characteristic Raman features of carbon at 1340 cm^{-1} and 1577 cm^{-1}. We attribute this to the carbon paste that is used to attach the microchip to the sample holder, as the Raman features are only visible at the holes in the Si_3N_4 membrane (see blue circle in **a**).

WS_2 feature (see Fig.6.3 in Chapter 6). For this experiment the flowers are positioned on a Si_3N_4 film far away from the silicon frame, therefore it is safe to assume that the measured feature is not related to Si, but can be attributed to 3LA(M).

D.2.2. ATOMIC STRUCTURE 2H VS 3R

Naturally occurring WS_2 exhibits a hexagonal atomic structure called 2H. However, the scanning transmission electron microscopy (STEM) study reveals that the nanoflowers exhibit a crystallographic polytypism 2H/3R [13]. The 2H and 3R atomic structures can be distinguished comparing the Raman signal of shear- and breathing modes [196, 197]. These Raman resonances have frequencies of 10-60 cm^{-1} and therefore lie outside of our experimental spectral region. Differences have been reported in the layer dependent spectral position of the A_{1g} and E^1_{2g} Raman peaks as well as the spectral position of the photoluminescence [177, 198], but the reported differences are too subtle to allow drawing any conclusions based on our measurements.

D.2.3. NON-WS_2 RAMAN FEATURES

At some positions, the measured spectra exhibit Raman features from other materials than WS_2. As mentioned in Section 1.3.2 of Chapter 1, the studied WS_2 nanoflowers are fabricated on a Si_3N_4 membrane with an array of holes. This membrane spans a window in the middle of a silicon frame. Figure D.3a depicts an SEM image of a part of the sample, where the WS_2 nanoflowers are grown both on the Si frame (upper part of image) and on the Si_3N_4 membrane (lower part of the image). The holes cross present in both the Si and the Si_3N_4. Figure D.3b depicts a spectrum of the Si substrate (see green circle in Fig.D.3a), where the characteristic Raman features of Si are clearly present. These Raman features are not present in any other spectra presented in this work, as all the spectra are acquired from nanoflowers on the Si_3N_4 membrane.

Preceding the CVD growth procedure of the nanoflowers, WO_3 is deposited on the microchip [13]. Signature Raman features of WO_3 can be distinguished in the spectrum in Fig.D.3c, acquired from the large white structure in the right corner of Fig.D.3a (see pink circle). We conclude that this white structure is a WO_3 crystal that has not reacted with sulfur. We do not measure any Raman signatures of WO_3 in other regions of the sample.

Next to Si and WO_3, signature Raman features of C can be distinguished in Fig.D.3d. We attribute this to the carbon paste that is used to attach the microchip to the sample holder. The carbon Raman features are only visible at the holes in the Si_3N_4 membrane (see blue circle in Fig.D.3a).

D.3. POLARIZATION-RESOLVED RAMAN RESPONSE

As mentioned in Chapter 7, we study the interaction of the WS_2 nanoflower Raman response with linearly polarized light. Figure D.4a,f depicts SEM images of flower-like WS_2 structures (indicated in pink and red respectively in Fig.7.1a in Chapter 7). The right upper corner of the flower-like structure in Fig.D.4a contains mainly petals oriented in the y-z plane (see coordinate system in Fig.7.1b in Chapter 7), the petals of the flower

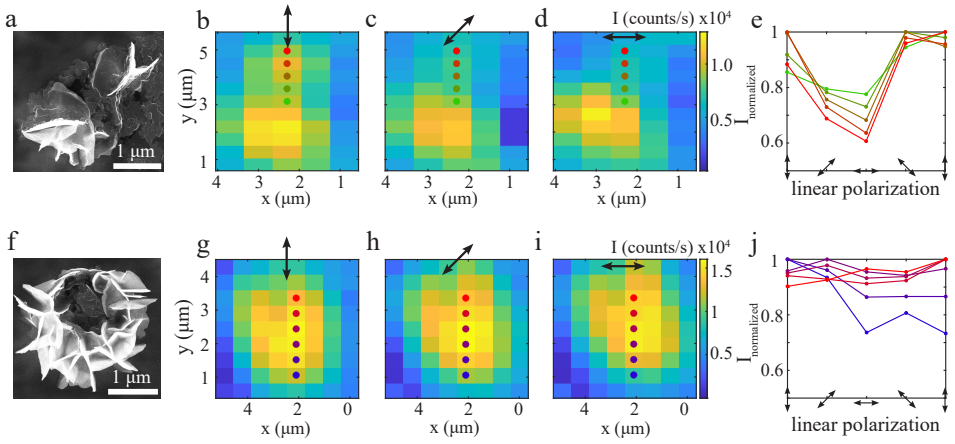

Figure D.4: Excitation polarization
a. SEM image of a WS_2 flower-like structure (pink circle in Fig.7.1a in Chapter 7). The right upper corner of this flower-like structure contains mainly petals oriented in the y-z plane. **b-d,g-h** Map of the intensity of the first Raman feature of the flower-like structure upon **b,g.** vertically polarized, **c,h.** diagonally polarized and **d,i.** horizontally polarized excitation. **e.** Raman intensity of the flower in **a** (used pixels are marked with stars in **b-d**) as a function of excitation polarization angle. Note that the intensity increases drastically when the polarization direction is parallel to the WS_2 flower petals. **f.** SEM image of a WS_2 flower (red circle in Fig.7.1a in Chapter 7), with petals oriented in all directions. **j.** Raman intensity of the flower in **f** (used pixels are marked with stars in **g-i**) as a function of excitation polarization angle. No polarization dependence can be observed in the Raman intensity of this flower.

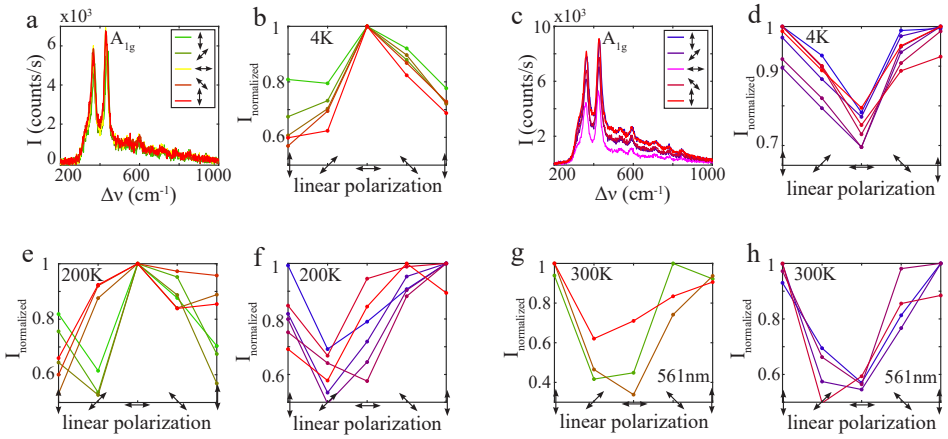

Figure D.5: Excitation polarization dependence of A_{1g} mode and at room temperature
a,c. Polarization-dependent spectra of the WS_2 nanoflowers presented in Fig.7.2a,f in Chapter 7. The intensity of the different Raman features has the same polarization dependence. **b,d.** Raman intensity of the A_{1g} mode of the flower in Fig.7.2a,f in Chapter 7 as a function of excitation polarization angle. As was the case for the Raman intensity of the first WS_2 mode E_{2g},2LA(M), the intensity of the A_{1g} mode increases drastically when the polarization direction is parallel to the WS_2 flower petals, e.g., for a horizontal polarization in **b** (compare Fig.7.2e in Chapter 7) and a vertical polarization in **d** (compare Fig.7.2j in Chapter 7). **e-h.** Intensity of the first Raman mode as a function of polarization angle of **e,f.** the flowers in Fig.7.2a,f in Chapter 7 at a temperature of 200 K and upon 594 nm excitation, and **g,h** of the flower in Fig.D.4a and **h.** in Fig.7.2f in Chapter 7, at room temperature upon 561 nm excitation. As was the case for the Raman intensity at 4 K upon 594 nm presented in Chapter 7, the Raman intensity increases when the polarization direction is parallel to the flower petals. Although the noise on the current data is higher, the contrast between parallel and perpendicular polarization is **e,f** the same for both temperatures upon 594 nm excitation: around 0.60 for the flower in Fig.7.2a and 0.70 for the flower in Fig.7.2f, and the contrast is **g,h** slightly larger upon 561 nm excitation: around 0.40 in **g.** and 0.60 in **h**.

in Fig.D.4f are oriented in all directions. Figure D.4b-d and g-i depicts the intensity of the first Raman feature upon vertical polarization excitation, excitation polarization at 45 degrees and horizontal polarization excitation. For the upper part of the flower in Fig.D.4a, the Raman intensity is highest when the excitation polarization direction is parallel to the orientation of the petals, namely vertically polarized. The Raman intensity of the lower part of this flower, and of the flower in Fig.D.4f, does not depend on the excitation polarization direction. Fig.D.4e,j depicts the normalized Raman intensity of different parts of the nanoflower (positions are indicated in Fig.D.4b-d) as a function of polarization angle (depicted by the arrows). In Fig.D.4e, the Raman intensity upon horizontal excitation is 60 - 80 % of the Raman intensity upon vertical polarization. No polarization dependence can be distinguished in Fig.D.4j.

Fig.7.2 in Chapter 7 displays the polarization dependence of the intensity of the first Raman feature, the combination of the E_{2g},2LA(M) modes. Figure D.5a,c depicts polarization dependent spectra of the nanoflowers presented in Fig.7.2 in Chapter 7. The polarization response of the intensity of the first two Raman features is highly similar. This similarity becomes apparent when comparing the polarization-dependent normalized intensity of the second Raman feature, the A_{1g} mode, in Fig.D.5b,d to the polarization-dependent response of the first Raman feature in Fig.7.2e,j in Chapter 7. As the flower in Fig.7.2a contains mainly petals oriented in the x-z plane, the intensity of both the first and the second Raman feature is highest upon horizontal excitation polarization (Fig.D.5b). As the flower in Fig.7.2f contains mainly petals oriented in the y-z plane, the intensity of two first two Raman modes is highest upon vertical excitation polarization (Fig.D.5d).

Where Fig.7.2 in Chapter 7 displayed the polarization dependence of the Raman intensity at 4 K, Fig.D.5e,f depicts the polarization dependence of the first Raman feature at 200 K. Comparing Fig.D.5e,f with Fig.7.2e,j, it becomes apparent that the Raman intensity at both temperatures increases when the polarization direction is parallel to the flower petals. Although the noise on the data at 200 K is higher, the contrast between parallel and perpendicular polarization is the same for both temperatures, namely 0.60 for the flower in Fig.7.2a and 0.70 for the flower in Fig.7.2f. We conclude that the polarization-dependence of the Raman intensity does not depend on temperature.

So far, all mentioned polarization dependences have been using a 594 nm excitation. Fig.D.5g,h depicts the polarization-dependent Raman intensity of the first Raman feature at room temperature upon a 561 nm excitation, for the flower in Fig.D.4a and in Fig.7.2j in Chapter 7 respectively. As the petals in both cases are mainly oriented in the y-z plane, the Raman intensity is lowest upon horizontal excitation polarization. Although the noise on the data for a 561 nm excitation is higher, the contrast between parallel and perpendicular polarization is slightly larger than for a 594 nm excitation.

D.4. HELICITY OF RAMAN FEATURES

Fig.7.3d-f in Chapter 7 displayed the intensity and helicity of the first WS_2 Raman feature, the combination of the E_{2g} and 2LA(M) modes. Figure D.6a presents a map of the

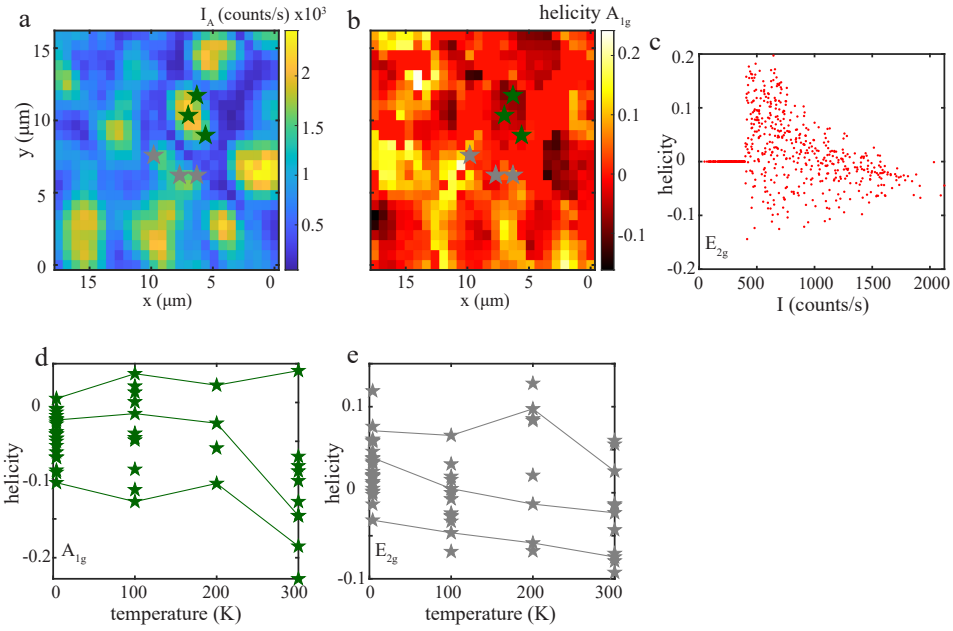

Figure D.6: Raman helicity of A_{1g} mode
a. Map of the intensity of the second Raman feature, the A_{1g}, of the nanoflower spectra presented in Fig.7.3b,c in Chapter 7. **b.** Map of the same region of the helicity of the A_{1g} mode. The helicity of this Raman feature has a similar value as the first Raman feature presented in Chapter 7, being negative around the WS_2 nanoflowers and positive in regions next to the larger nanoflowers (see Fig.7.3e in Chapter 7). **c.** Distribution of the Raman helicity (of the first Raman feature, presented in Chapter 7), as a function of Raman intensity. At low intensity, the helicity can take a broad range of values between -0.1 and +0.2. At high intensity, the helicity goes to a value of around -0.05. **d,e.** Temperature-dependent helicity **d.** of the A_{1g} mode and **e.** of the first Raman feature of the WS_2 nanoflower marked in **d.** green and **e.** grey in **a,b.** (taking into account all pixels associated with this flower). The lines present the temperature dependence of three specific places on the flowers, denoted with stars in **a,b**. Like in Fig.7.3f in Chapter 7, the helicity decreases slightly at room-temperature.

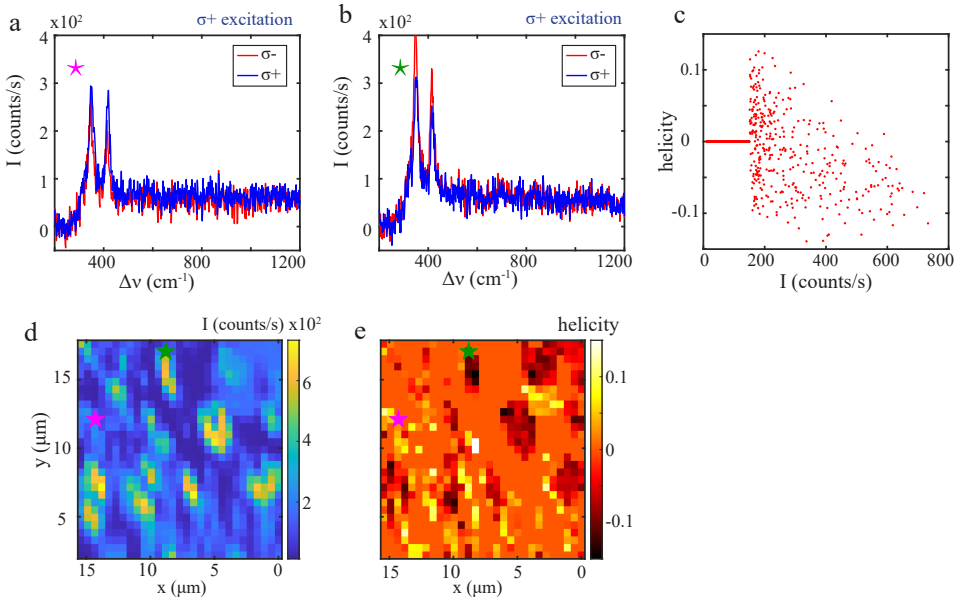

Figure D.7: Raman helicity at room temperature
a,b Helicity-resolved nanoflower spectra, where the flowers are excited with σ_+ light and the helicity is determined from the difference in σ_+ and σ_- emission. The spectra are taken at room temperature at the same positions as in Fig.7.3 in Chapter 7. In **a**, the spectrum with the same polarization as the excitation light (blue) has a higher intensity (helicity is conserved). In **b**, the spectrum with opposite polarization to the excitation light (red) has a higher intensity (helicity is reversed). **c.** Distribution of the helicity of the first Raman feature as a function of Raman intensity. At low intensity, the helicity can take a broad range of values between -0.15 and +0.1. At high intensity, the helicity goes to a value of around -0.1. **d.** Map of the intensity of the first Raman feature, taken at room temperature. **e.** Map of the same region of the Raman helicity. As in Fig.7.3, the helicity of the Raman features around the WS_2 nanoflowers is negative (green star), whereas the Raman helicity is positive in regions next to the larger nanoflowers (pink star).

nanoflower intensity of the second Raman feature, the A_{1g} mode. Figure D.6b presents a map of the experimentally determined helicity of the A_{1g} mode. When comparing Fig.D.6b with Fig.7.3e in Chapter 7, note that the helicity of the two Raman features has very similar position-dependent values. Comparing the position of the (bright) nanoflowers on the intensity map with the helicity map, it becomes apparent that the Raman helicity of the nanoflowers is slightly negative. Figure D.6c depicts the helicity of the first Raman feature as a function of intensity. At low intensity, the helicity values are spread in a range from -0.10 and +0.20. At high intensity, the spread in the helicity becomes smaller and converges to a value around -0.05.

Figure D.6d depicts the temperature dependence of the helicity of the A_{1g} mode for the flower marked in green in Fig.7.1a. At all temperatures, the intensity is depicted of the first Raman feature of all spectra associated to this flower. The lines present the temperature dependence of three specific places on the flower, marked by green stars in Fig.D.6a,b. Figure D.6e depicts the temperature dependence of the helicity of the first Raman mode of another flower. The lines present the temperature dependence of three places on the flower, marked by grey stars in Fig.D.6a,b. As for the flower and the Raman feature in Chapter 7, the helicity of these flowers slightly decreases from 4 K to room temperature.

For comparison, we determine the position-dependent helicity of the Raman features at different temperatures. Figure D.7a,b depicts helicity-resolved nanoflower spectra, taken at room temperature. Here, the flowers are excited with σ_+ light and the helicity of the Raman features is determined from the difference in σ_+ and σ_- emission (see Fig.7.3a in Chapter 7). In Fig.D.7a, the blue spectrum with the same polarization as the excitation light, has a higher intensity (helicity is conserved) than the red spectrum with the opposite polarization (helicity is reversed). In Fig.D.7b, the helicity-reversed spectrum (in red) has a higher intensity than the helicity-conserved spectrum (in blue).

Figure D.7d,e presents a map of the nanoflower intensity and helicity of the first Raman feature, taken at room temperature. The stars indicate the position of the spectra in Fig.D.7a,b (compare Fig.7.3d,e in Chapter 7). As was the case at 4 K (see Fig.7.3 in Chapter 7), at room temperature the Raman helicity is also negative at the position of the WS_2 nanoflowers, and positive on locations in between the flowers (compare position of green and pink star in Fig.D.7d,e). As depicted in Fig.7.3f in Chapter 7, the Raman helicity is on average more negative at room temperature than at cryogenic temperatures. Figure D.7c depicts the helicity of the first Raman feature as a function of intensity. As was the case at 4 K, the spread in the helicity values is large for low intensities, but the spread becomes smaller at high intensity. Comparing Fig.D.6c and Fig.D.7c, it becomes apparent that the helicity at room temperature has lower values: the maximum helicity is only 0.12 instead of 0.20, and the value at high intensity is -0.10 instead of -0.05.

D.5. RAMAN POLARIZABILITY TENSORS

D.5.1. TENSORS AND JONES CALCULUS

As mentioned in Chapter 7, the interaction of TMDs materials with polarized light can be described by Raman polarizability tensors. The Jones vectors for circularly polarized

light are [68]:

$$\sigma_+ = 1/\sqrt{2}\begin{bmatrix}1\\ i\\ 0\end{bmatrix} \text{ and } \sigma_- = 1/\sqrt{2}\begin{bmatrix}1\\ -i\\ 0\end{bmatrix}. \tag{D.1}$$

The first two Raman features of WS_2 are the combination of the E_{2g} and 2LA(M) mode, and the A_{1g} mode. We start with the Raman tensor of the second feature, the A_{1g} mode [67]:

$$R_A = \begin{bmatrix}a & 0 & 0\\ 0 & a & 0\\ 0 & 0 & b\end{bmatrix}. \tag{D.2}$$

If the incident and outgoing light have the same polarization handedness, the calculation yields a non-zero matrix element [67]: $\sigma_+^\dagger R_A \sigma_+ = a$. If the incident and outgoing light have different polarization handedness, the matrix element is zero [67]: $\sigma_+^\dagger R_A \sigma_- = 0$.

Calculating the polarization response of the E_{2g} mode is less straighforward, as the Raman tensors depend on the resonance conditions of the excitation light with the excitonic transition [68]. If the excitation is out-of-resonance, the Raman tensor is [67]:

$$R_E = \begin{bmatrix}0 & d & 0\\ d & 0 & 0\\ 0 & 0 & 0\end{bmatrix}. \tag{D.3}$$

In this case, if the incident and outgoing light have the same polarization handednes, the matrix element is zero [67]: $\sigma_+^\dagger R_E \sigma_+ = 0$. If the incident and outgoing light have different polarization handedness, the matrix element is non-zero: $\sigma_+^\dagger R_E \sigma_- = d$.

In Chapter 7, we calculate the helicity of the measured Raman features: $H = \frac{I_{conserved} - I_{reversed}}{I_{conserved} + I_{reversed}}$, where $I_{conserved}$ had a σ_+ and $I_{reversed}$ a σ_- polarization. Note that the helicity is calculated based on intensities, therefore the matrix elements need to be squared. We calculate the helicity as:

$$H = \frac{I_{\sigma+\sigma+} - I_{\sigma+\sigma-}}{I_{\sigma+\sigma+} + I_{\sigma+\sigma-}}. \tag{D.4}$$

The helicity of the A_{1g} mode is $H = \frac{a^2-0}{a^2+0} = +1$, the helicity is conserved. The helicity of the E_{2g} mode is $H = \frac{-d^2}{d^2} = -1$, the helicity is reversed. In summary: when the excitation light is out of resonance with the excitonic transition of a TMDs material, the first two Raman features respond to circular polarization in an opposite way: the helicity is reversed for the first feature, and conserved for the second.

D.5.2. RESONANT EXCITATION

The measured helicity-resolved Raman of the WS_2 nanoflowers exhibits a different type of behaviour. We experimentally observe that the two first Raman features exhibit the same response to circularly polarized light, either both being helicity conserved or helicity reversed. Part of this difference between theory and experiment can be explained by the fact that the incident light on the nanoflowers is in resonance with the excitonic transition.

In this case, the Raman tensor for the A_{1g} mode remains the same, but the polarization response of the E_{2g} mode has two contributions [68, 69]. The interaction between electrons, photons and excitons is governed by the so called deformation potential (DP) and Frohlich interaction (FI) [68], leading to the following Raman tensors:

$$R_{LO} = \begin{bmatrix} a_F & a_{DP} & 0 \\ a_{DP} & a_F & 0 \\ 0 & 0 & a_F \end{bmatrix}, R_{TO} = \begin{bmatrix} a_{DP} & 0 & 0 \\ 0 & -a_{DP} & 0 \\ 0 & 0 & 0 \end{bmatrix}. \tag{D.5}$$

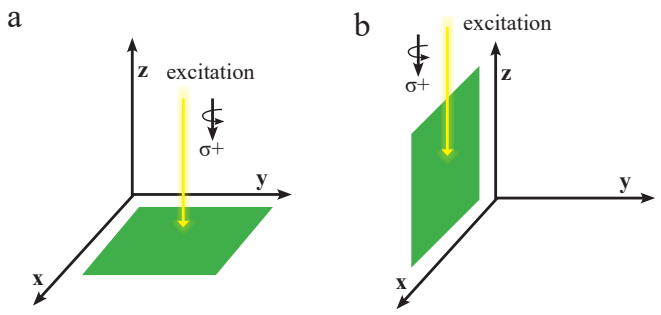

Figure D.8: Coordinate systems
a. Coordination system with a flat WS_2 layer in the x-y plane, and circularly polarized excitation propagating along z. **b.** Exciting a wall-like WS_2 flower petal is like performing a base transform. Here the new base vectors are: $\hat{x}' = \hat{x}$, $\hat{y}' = -\hat{z}$ and $\hat{z}' = \hat{y}$.

If the incident and outgoing light have the same polarization handedness, $\sigma_+^\dagger R_{LO}\sigma_+ = a_F$ and $\sigma_+^\dagger R_{TO}\sigma_+ = 0$. If the incident and outgoing light have different polarization handedness, $\sigma_+^\dagger R_{LO}\sigma_- = -ia_{DP}$ and $\sigma_+^\dagger R_{TO}\sigma_- = a_{DP}$. Therefore, independent on the polarization handedness, the interaction will always contain a non-zero matrix element. The helicity of the E_{2g} mode is $H = \frac{a_F^2 - 2a_{DP}^2}{a_F^2 + 2a_{DP}^2}$. Depending on the contribution of the DP and FI interactions, the helicity of the E_{2g} mode can be either conserved or reversed [68].

In summary: when the excitation light is in resonance with the excitonic transition of a TMDs material, both the E_{2g} and the A_{1g} mode can be helicity conserved ($H > 0$) [68, 69].

D.5.3. BASE TRANSFORMATION

Still, the theory above does not adequately describe the measured helicity-resolved Raman of the WS_2 nanoflowers exhibits. Although the resonance condition explains why both Raman features exhibit the same helicity response, it does not explain the observed helicities between -0.20 and +0.20 for the A_{1g} mode, where a helicity of +1.0 would be expected. As mentioned in Chapter 7, the Raman polarizablity tensors are defined with respect to the crystal axes of flat TMDs layers, e.g., a frame of reference with the excitation light perpendicular to it. As the petals of the WS_2 flowers exhibit a variety of orientations with respect to the incident light, the Raman tensor needs to be defined in a different frame of reference (see [190–192]). Figure D.8a presents schematically a WS_2 flake in the horizontal x-y plane, excited by circularly polarized light propagating along z. Figure D.8b presents a wall-like WS_2 petal in the x-z plane. The WS_2 Raman tensor needs to be defined in this rotated coordinate system, where the base vectors transform to: $\hat{x}' = \hat{x}$, $\hat{y}' = -\hat{z}$ and $\hat{z}' = \hat{y}$. The Raman tensor of the A_{1g} mode will change to:

$$R'_A = \begin{bmatrix} a & 0 & 0 \\ 0 & -a & 0 \\ 0 & 0 & -b \end{bmatrix}. \tag{D.6}$$

If the incident and outgoing light have the same polarization handedness, the matrix element is zero: $\sigma_+^\dagger R'_A \sigma_+ = 0$. If the incident and the outgoing light have different polarization handedness, the matrix element is non zero: $\sigma_+^\dagger R'_A \sigma_- = 2a$. Note that now the A_{1g} mode is helicity reversed instead of helicity conserved: H=-1.0.

Applying the same base transformation to the tensors of the E_{2g} mode yields:

$$\begin{aligned} R'_{LO} &= \begin{bmatrix} a_F & 0 & -a_{DP} \\ 0 & a_F & 0 \\ -a_{DP} & 0 & a_F \end{bmatrix}, \\ R'_{TO} &= \begin{bmatrix} a_{DP} & 0 & 0 \\ 0 & 0 & 0 \\ 0 & 0 & -a_{DP} \end{bmatrix}. \end{aligned} \tag{D.7}$$

If the incident and outgoing light have the same polarization handedness, the matrix element are: $\sigma_+^\dagger R'_{LO} \sigma_+ = a_F$ and $\sigma_+^\dagger R'_{TO} \sigma_+ = \frac{1}{2} a_{DP}$. If the incident and outgoing light have different polarization handedness, the matrix elements are: $\sigma_+^\dagger R'_{LO} \sigma_- = 0$ and $\sigma_+^\dagger R'_{TO} \sigma_- = \frac{1}{2} a_{DP}$. Therefore the helicity again depends on the contribution of the DP and FI interactions [68]: $H = \frac{a_F^2}{a_F^2 + 1/2 a_{DP}^2}$.

D.5.4. HELICITY OF (FLAT) PYRAMIDS VS. FLOWERS

We observe that the Raman helicity of WS_2 petals is positive when they are oriented in the x-y plane, horizontally with respect to the surface, and the helicity is negative when

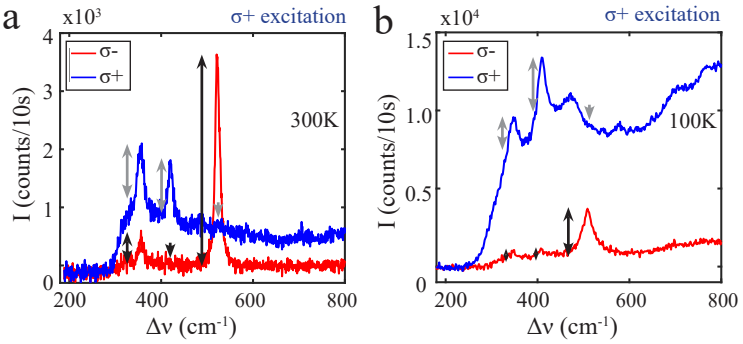

D

Figure D.9: Helicity of hollow WS_2 pyramid crater
a-b. Helicity-resolved spectra of a hollow WS_2 pyramid, where the pyramid is excited with σ_+ light, and the helicity is determined from the difference in σ_+ or σ_- emission. The spectra are taken at the flat crater of the hollow pyramids (see Chapter 6). Especially at 100 K, the spectra exhibit a large spectral background. Three Raman features can be distinguished: the two characteristic WS_2 features at 350 cm^{-1} and 417 cm^{-1}, and the Si mode at 520 cm^{-1}. The Si mode exhibits only σ_- emission (in red) and no σ_+ emission (in blue), and is therefore helicity-reversed. The second Raman feature, the A_{1g} mode, only exhibits σ_+ emission (in blue) and is therefore helicity-conserved. The first Raman feature, E_{2g},2LA(M), exhibits more σ_+ emission and is therefore more helicity-conserved. The helicity ranges from 0.50 at room temperature to almost 1.0 at 4 K.

they are wall-like, oriented vertically with respect to the surface. We conclude that the detected Raman helicity depends on the orientation of the WS_2 petals or flakes.

This is confirmed by the helicity-resolved spectra of hollow pyramids (see Chapter 6), depicted in Fig.D.9a,b. In contrast to the nanoflowers, both the crater in the middle of the hollow pyramids and the stair-like sides, exhibit WS_2 oriented horizontally with respect to the surface. For the spectra in Fig.D.9a-b, the pyramid is excited with σ_+ light and the helicity of the Raman features is determined from the difference in σ_+ (in blue) and σ_- (in red) emission. The spectra exhibit three Raman features: the two characteristic WS_2 features at 350 cm^{-1} and 417 cm^{-1}, and the Si mode at 520 cm^{-1}. Since the pyramid spectra exhibit a large spectral background, the intensity of the three Raman features with respect to the background is marked with arrows.

From the spectra at room temperature in Fig.D.9a, it becomes apparent that the Si mode exhibits only σ_- emission and is therefore helicity-reversed, which is in agreement with previous reports [68]. The second Raman feature, the the A_{1g} mode, only exhibits σ_+ emission (in blue) and is therefore helicity-conserved. The measured helicity of this mode is in agreement with the tensor in Eq.D.6, describing the Raman polarizability for horizontal WS_2. This confirms that the measured helicity H < 1.0 of the A_{1g} mode of the nanoflowers can be attributed to the vertical orientation of the flower petals.

The first Raman feature, E_{2g},2LA(M), exhibits more σ_+ emission and is therefore more helicity-conserved. The helicity ranges from 0.50 at room temperature to around 1.0 at 100 K. Note that in contrast to the nanoflowers, the helicity of the first Raman feature of the pyramid is always positive. There are two reasons why the helicity value of the first

Raman feature is not perfectly 1.0, that apply both to the randomly oriented nanoflower petals and to the horizontal pyramid layers. First of all, as we excite both WS_2 nanostructures in resonance with the excitonic transition, the relative contributions of the DP and FI interaction need to be taken into account, as described by the tensors in Eq.D.5. Second of all, note that the first Raman feature is a combination of the E_{2g} mode and a multiple of the longitudinal acoustic phonon. The interaction of the E_{2g} mode with polarized is described by the polarizability tensors mentioned above, but the polarization response of the longitudinal acoustic phonon will naturally also influence the measured Raman spectrum. The fact that both the influence of the excitonic resonance condition and the relative contribution of the 2LA(M) phonon can be temperature dependent [68], explains the temperature dependence of the helicity value of the first Raman feature of the pyramid spectra, ranging from 0.50 at room temperature to 1.0 at cryogenic temperatures.

BIBLIOGRAPHY

[1] Rienk Vermij. *Kleine geschiedenis van de wetenschap*. Uitgevery Nieuwezijds, Amsterdam, 01 2006.

[2] Clifford A. Pickover. *The Physics Book*. Sterling, New York, 01 2011.

[3] Eugene Hecht. *Optics*. Addison Wesley, San Francisco, 2002.

[4] T. H. Maiman. Stimulated optical radiation in ruby. *Nature*, 187(4736):493–494, 1960.

[5] K. S. Novoselov, D. Jiang, F. Schedin, T. J. Booth, V. V. Khotkevich, S. V. Morozov, and A. K. Geim. Two-dimensional atomic crystals. *Proceedings of the National Academy of Sciences*, 102(30):10451–10453, 2005.

[6] K. S. Novoselov, A. K. Geim, S. V. Morozov, D. Jiang, Y. Zhang, S. V. Dubonos, I. V. Grigorieva, and A. A. Firsov. Electric field effect in atomically thin carbon films. *Science*, 306(5696):666–669, 2004.

[7] Nikos Papadopoulos. *Mesoscopic transport in 2D materials and heterostructures*. PhD thesis, Delft University of Technology, 2019.

[8] Vera A.E.C. Janssen. *Electronic Properties of (Pseudo-) Two-Dimensional Materials*. PhD thesis, Delft University of Technology, 2020.

[9] Robin J. Dolleman, Dejan Davidovikj, Santiago J. Cartamil-Bueno, Herre S. J. van der Zant, and Peter G. Steeneken. Graphene squeeze-film pressure sensors. *Nano Lett.*, 16(1):568–571, January 2016.

[10] B. Radisavljevic, A. Radenovic, J. Brivio, V. Giacometti, and A. Kis. Single-layer mos2 transistors. *Nature Nanotechnology*, 6(3):147–150, 2011.

[11] Qing Hua Wang, Kourosh Kalantar-Zadeh, Andras Kis, Jonathan N. Coleman, and Michael S. Strano. Electronics and optoelectronics of two-dimensional transition metal dichalcogenides. *Nature Nanotechnology*, 7:699, November 2012.

[12] Kin Fai Mak, Changgu Lee, James Hone, Jie Shan, and Tony F. Heinz. Atomically thin mos2: A new direct-gap semiconductor. *PRL*, 105(13):136805, September 2010.

[13] Sabrya E. van Heijst, Masaki Mukai, Eiji Okunishi, Hiroki Hashiguchi, Laurien I. Roest, Louis Maduro, Juan Rojo, and Sonia Conesa-Boj. Illuminating the electronic properties of ws2 polytypism with electron microscopy. *ANNALEN DER PHYSIK*, 533:2000499, January 2021.

[14] Ruilong Yang, Shanghuai Feng, Xunyong Lei, Xiaoyu Mao, Anmin Nie, Bochong Wang, Kun Luo, Jianyong Xiang, Fusheng Wen, Congpu Mu, Zhisheng Zhao, Bo Xu, Hualing Zeng, Yongjun Tian, and Zhongyuan Liu. Effect of layer and stacking sequence in simultaneously grown 2h and 3r WS2 atomic layers. *Nanotechnology*, 30(34):345203, jun 2019.

[15] Yuan Huang, Eli Sutter, Norman N. Shi, Jiabao Zheng, Tianzhong Yang, Dirk Englund, Hong-Jun Gao, and Peter Sutter. Reliable exfoliation of large-area high-quality flakes of graphene and other two-dimensional materials. *ACS Nano*, 9(11): 10612–10620, 2015. PMID: 26336975.

[16] Andres Castellanos-Gomez, Michele Buscema, Rianda Molenaar, Vibhor Singh, Laurens Janssen, Herre S. J. van der Zant, and Gary A. Steele. Deterministic transfer of two-dimensional materials by all-dry viscoelastic stamping. *2D Materials*, 1 (1):011002, 2014.

[17] Jeong-Gyu Song, Jusang Park, Wonseon Lee, Taejin Choi, Hanearl Jung, Chang Wan Lee, Sung-Hwan Hwang, Jae Min Myoung, Jae-Hoon Jung, Soo-Hyun Kim, Clement Lansalot-Matras, and Hyungjun Kim. Layer-controlled, wafer-scale, and conformal synthesis of tungsten disulfide nanosheets using atomic layer deposition. *ACS Nano*, 7(12):11333–11340, December 2013.

[18] Yu Zhang, Yanfeng Zhang, Qingqing Ji, Jing Ju, Hongtao Yuan, Jianping Shi, Teng Gao, Donglin Ma, Mengxi Liu, Yubin Chen, Xiuju Song, Harold Y. Hwang, Yi Cui, and Zhongfan Liu. Controlled growth of high-quality monolayer ws2 layers on sapphire and imaging its grain boundary. *ACS Nano*, 7(10):8963–8971, October 2013.

[19] Chunxiao Cong, Jingzhi Shang, Xing Wu, Bingchen Cao, Namphung Peimyoo, Caiyu Qiu, Litao Sun, and Ting Yu. Synthesis and optical properties of large-area single-crystalline 2d semiconductor ws2 monolayer from chemical vapor deposition. *Advanced Optical Materials*, 2(2):131–136, February 2014.

[20] Carlo M. Orofeo, Satoru Suzuki, Yoshiaki Sekine, and Hiroki Hibino. Scalable synthesis of layer-controlled ws2 and mos2 sheets by sulfurization of thin metal films. *Appl. Phys. Lett.*, 105(8):083112, August 2014.

[21] Amutha Thangaraja, Sachin M. Shinde, Golap Kalita, and Masaki Tanemura. Effect of wo3 precursor and sulfurization process on ws2 crystals growth by atmospheric pressure cvd. *Materials Letters*, 156:156 – 160, 2015.

[22] Pengyu Liu, Tao Luo, Jie Xing, Hong Xu, Huiying Hao, Hao Liu, and Jingjing Dong. Large-area ws2 film with big single domains grown by chemical vapor deposition. *Nanoscale Research Letters*, 12(1):558, 2017.

[23] Irina Komen, Sabrya E. van Heijst, Sonia Conesa-Boj, and L. Kuipers. Morphology-induced spectral modification of self-assembled ws2 pyramids. *Nanoscale Adv.*, 3 (22):6427–6437, 2021.

[24] Mark Fox. *Optical Properties of Solids*. Oxford University Press, 2010.

[25] Mircea Dragoman Daniele Dragoman. *Optical Characterization of Solids*. Springer Berlin Heidelberg, 2002.

[26] Keliang He, Nardeep Kumar, Liang Zhao, Zefang Wang, Kin Fai Mak, Hui Zhao, and Jie Shan. Tightly bound excitons in monolayer wse_2. *Phys. Rev. Lett.*, 113:026803, Jul 2014.

[27] Alexey Chernikov, Timothy C. Berkelbach, Heather M. Hill, Albert Rigosi, Yilei Li, Ozgur Burak Aslan, David R. Reichman, Mark S. Hybertsen, and Tony F. Heinz. Exciton binding energy and nonhydrogenic rydberg series in monolayer ws_2. *Phys. Rev. Lett.*, 113:076802, Aug 2014.

[28] Bairen Zhu, Xi Chen, and Xiaodong Cui. Exciton binding energy of monolayer ws2. *Scientific Reports*, 5(1):9218, 2015.

[29] Jason S. Ross, Sanfeng Wu, Hongyi Yu, Nirmal J. Ghimire, Aaron M. Jones, Grant Aivazian, Jiaqiang Yan, David G. Mandrus, Di Xiao, Wang Yao, and Xiaodong Xu. Electrical control of neutral and charged excitons in a monolayer semiconductor. *Nature Communications*, 4(1):1474, 2013.

[30] G. Aivazian, Zhirui Gong, Aaron M. Jones, Rui-Lin Chu, J. Yan, D. G. Mandrus, Chuanwei Zhang, David Cobden, Wang Yao, and X. Xu. Magnetic control of valley pseudospin in monolayer wse2. *Nature Physics*, 11:148, January 2015.

[31] Weijie Zhao, Zohreh Ghorannevis, Leiqiang Chu, Minglin Toh, Christian Kloc, Ping-Heng Tan, and Goki Eda. Evolution of electronic structure in atomically thin sheets of ws2 and wse2. *ACS Nano*, 7(1):791–797, 2013. PMID: 23256505.

[32] Weijie Zhao, Zohreh Ghorannevis, Kiran Kumar Amara, Jing Ren Pang, Minglin Toh, Xin Zhang, Christian Kloc, Ping Heng Tan, and Goki Eda. Lattice dynamics in mono- and few-layer sheets of ws2 and wse2. *Nanoscale*, 5:9677–9683, 2013.

[33] Hualing Zeng, Gui-Bin Liu, Junfeng Dai, Yajun Yan, Bairen Zhu, Ruicong He, Lu Xie, Shijie Xu, Xianhui Chen, Wang Yao, and Xiaodong Cui. Optical signature of symmetry variations and spin-valley coupling in atomically thin tungsten dichalcogenides. *Scientific Reports*, 3(1):1608, 2013.

[34] A. A. Mitioglu, P. Plochocka, J. N. Jadczak, W. Escoffier, G. L. J. A. Rikken, L. Kulyuk, and D. K. Maude. Optical manipulation of the exciton charge state in single-layer tungsten disulfide. *PRB*, 88(24):245403, December 2013.

[35] Gerd Plechinger, Philipp Nagler, Julia Kraus, Nicola Paradiso, Christoph Strunk, Christian Schüller, and Tobias Korn. Identification of excitons, trions and biexcitons in single-layer ws2. *Phys. Status Solidi RRL*, 9(8):457–461, August 2015.

[36] M. Currie, A. T. Hanbicki, G. Kioseoglou, and B. T. Jonker. Optical control of charged exciton states in tungsten disulfide. *Appl. Phys. Lett.*, 106(20):201907, May 2015.

[37] Toshiaki Kato and Toshiro Kaneko. Transport dynamics of neutral excitons and trions in monolayer ws2. *ACS Nano*, 10(10):9687–9694, October 2016.

[38] Andrea Splendiani, Liang Sun, Yuanbo Zhang, Tianshu Li, Jonghwan Kim, Chi-Yung Chim, Giulia Galli, and Feng Wang. Emerging photoluminescence in monolayer mos2. *Nano Letters*, 10(4):1271–1275, 2010. PMID: 20229981.

[39] Maciej R. Molas, Karol Nogajewski, Artur O. Slobodeniuk, Johannes Binder, Miroslav Bartos, and Marek Potemski. The optical response of monolayer, few-layer and bulk tungsten disulfide. *Nanoscale*, 9(35):13128–13141, 2017.

[40] Su-Hyun Gong, Filippo Alpeggiani, Beniamino Sciacca, Erik C. Garnett, and L. Kuipers. Nanoscale chiral valley-photon interface through optical spin-orbit coupling. *Science*, 359(6374):443–447, 2018.

[41] V. M. Agranovich and O. A. Dubovskii. *Effect of Retarded Interaction on the Exciton Spectrum in One-Dimensional and Two-Dimensional Crystals*, pages 795–798. Springer US, Boston, MA, 1995. ISBN 978-1-4615-1963-8.

[42] Lucio Claudio Andreani and Franco Bassani. Exchange interaction and polariton effects in quantum-well excitons. *Phys. Rev. B*, 41:7536–7544, Apr 1990.

[43] Jacob B. Khurgin. Two-dimensional exciton-polariton-light guiding by transition metal dichalcogenide monolayers. *Optica*, 2(8):740–742, Aug 2015.

[44] Filippo Alpeggiani, Su-Hyun Gong, and L. Kuipers. Dispersion and decay rate of exciton-polaritons and radiative modes in transition metal dichalcogenide monolayers. *Phys. Rev. B*, 97:205436, May 2018.

[45] Tony Low, Andrey Chaves, Joshua D. Caldwell, Anshuman Kumar, Nicholas X. Fang, Phaedon Avouris, Tony F. Heinz, Francisco Guinea, Luis Martin-Moreno, and Frank Koppens. Polaritons in layered two-dimensional materials. *Nature Materials*, 16(2):182–194, 2017.

[46] D. N. Basov, M. M. Fogler, and F. J. García de Abajo. Polaritons in van der waals materials. *Science*, 354(6309), 2016.

[47] Sanfeng Wu, Sonia Buckley, John R. Schaibley, Liefeng Feng, Jiaqiang Yan, David G. Mandrus, Fariba Hatami, Wang Yao, Jelena Vučković, Arka Majumdar, and Xiaodong Xu. Monolayer semiconductor nanocavity lasers with ultralow thresholds. *Nature*, 520(7545):69–72, 2015.

[48] Damon B. Farmer, Phaedon Avouris, Yilei Li, Tony F. Heinz, and Shu-Jen Han. Ultrasensitive plasmonic detection of molecules with graphene. *ACS Photonics*, 3(4): 553–557, April 2016.

[49] Jon A. Schuller, Edward S. Barnard, Wenshan Cai, Young Chul Jun, Justin S. White, and Mark L. Brongersma. Plasmonics for extreme light concentration and manipulation. *Nature Materials*, 9(3):193–204, 2010.

[50] Peining Li, Martin Lewin, Andrey V. Kretinin, Joshua D. Caldwell, Kostya S. Novoselov, Takashi Taniguchi, Kenji Watanabe, Fabian Gaussmann, and Thomas Taubner. Hyperbolic phonon-polaritons in boron nitride for near-field optical imaging and focusing. *Nature Communications*, 6(1):7507, 2015.

[51] Thomas M. Devine and Fran Adar. *Raman Spectroscopy of Solids*, pages 1–38. American Cancer Society, 2012. ISBN 9780471266969.

[52] H.S.S.Ramakrishna Matte, A. Gomathi, Arun K. Manna, Dattatray J. Late, Ranjan Datta, Swapan K. Pati, and C.N.R. Rao. Mos2 and ws2 analogues of graphene. *Angewandte Chemie International Edition*, 49(24):4059–4062, 2010.

[53] Changgu Lee, Hugen Yan, Louis E. Brus, Tony F. Heinz, James Hone, and Sunmin Ryu. Anomalous lattice vibrations of single- and few-layer mos2. *ACS Nano*, 4(5): 2695–2700, May 2010.

[54] A. Molina-Sánchez and L. Wirtz. Phonons in single-layer and few-layer mos_2 and ws_2. *PRB*, 84(15):155413, October 2011.

[55] A. A. Mitioglu, P. Plochocka, G. Deligeorgis, S. Anghel, L. Kulyuk, and D. K. Maude. Second-order resonant raman scattering in single-layer tungsten disulfide ws_2. *PRB*, 89(24):245442, June 2014.

[56] Ayse Berkdemir, Humberto R. Gutiérrez, Andrés R. Botello-Méndez, Néstor Perea-López, Ana Laura Elías, Chen-Ing Chia, Bei Wang, Vincent H. Crespi, Florentino López-Urías, Jean-Christophe Charlier, Humberto Terrones, and Mauricio Terrones. Identification of individual and few layers of ws2 using raman spectroscopy. *Scientific Reports*, 3(1):1755, 2013.

[57] R. Saito, Y. Tatsumi, S. Huang, X. Ling, and M. S. Dresselhaus. Raman spectroscopy of transition metal dichalcogenides. *Journal of Physics: Condensed Matter*, 28(35): 353002, 2016.

[58] Sandro Mignuzzi, Andrew J. Pollard, Nicola Bonini, Barry Brennan, Ian S. Gilmore, Marcos A. Pimenta, David Richards, and Debdulal Roy. Effect of disorder on raman scattering of single-layer Mos_2. *PRB*, 91(19):195411, May 2015.

[59] William M. Parkin, Adrian Balan, Liangbo Liang, Paul Masih Das, Michael Lamparski, Carl H. Naylor, Julio A. Rodríguez-Manzo, A. T. Charlie Johnson, Vincent Meunier, and Marija Drndić. Raman shifts in electron-irradiated monolayer mos2. *ACS Nano*, 10(4):4134–4142, April 2016.

[60] C. Rice, R. J. Young, R. Zan, U. Bangert, D. Wolverson, T. Georgiou, R. Jalil, and K. S. Novoselov. Raman-scattering measurements and first-principles calculations of strain-induced phonon shifts in monolayer mos_2. *PRB*, 87(8):081307, February 2013.

[61] Lei Yang, Xudong Cui, Jingyu Zhang, Kan Wang, Meng Shen, Shuangshuang Zeng, Shadi A. Dayeh, Liang Feng, and Bin Xiang. Lattice strain effects on the optical properties of mos2 nanosheets. *Scientific Reports*, 4(1):5649, 2014.

[62] Namphung Peimyoo, Jingzhi Shang, Weihuang Yang, Yanlong Wang, Chunxiao Cong, and Ting Yu. Thermal conductivity determination of suspended mono- and bilayer ws2 by raman spectroscopy. *Nano Research*, 8(4):1210–1221, 2015.

[63] Anand P. S. Gaur, Satyaprakash Sahoo, J. F. Scott, and Ram S. Katiyar. Electron-phonon interaction and double-resonance raman studies in monolayer ws2. *J. Phys. Chem. C*, 119(9):5146–5151, March 2015.

[64] Xue Li, Jinhua Li, Kai Wang, Xiaohua Wang, Shuangpeng Wang, Xueying Chu, Mingze Xu, Xuan Fang, Zhipeng Wei, Yingjiao Zhai, and Bo Zou. Pressure and temperature-dependent raman spectra of mos2 film. *Appl. Phys. Lett.*, 109(24): 242101, December 2016.

[65] Jiake Li, Weitao Su, Fei Chen, Li Fu, Su Ding, Kaixin Song, Xiwei Huang, and Lijie Zhang. Atypical defect-mediated photoluminescence and resonance raman spectroscopy of monolayer ws2. *J. Phys. Chem. C*, 123(6):3900–3907, February 2019.

[66] Jia-He Fan, Po Gao, An-Min Zhang, Bai-Ren Zhu, Hua-Ling Zeng, Xiao-Dong Cui, Rui He, and Qing-Ming Zhang. Resonance raman scattering in bulk 2h-mx2 (m-mo,w, x-s,se) and monolayer mos2. *Journal of Applied Physics*, 115(5):053527, 2014.

[67] Shao-Yu Chen, Changxi Zheng, Michael S. Fuhrer, and Jun Yan. Helicity-resolved raman scattering of mos2, mose2, ws2, and wse2 atomic layers. *Nano Lett.*, 15(4): 2526–2532, April 2015.

[68] Yan Zhao, Shishu Zhang, Yuping Shi, Yanfeng Zhang, Riichiro Saito, Jin Zhang, and Lianming Tong. Characterization of excitonic nature in raman spectra using circularly polarized light. *ACS Nano*, 14(8):10527–10535, 2020. PMID: 32790282.

[69] Steven G. Drapcho, Jonghwan Kim, Xiaoping Hong, Chenhao Jin, Sufei Shi, Sefaattin Tongay, Junqiao Wu, and Feng Wang. Apparent breakdown of raman selection rule at valley exciton resonances in monolayer Mos_2. *Phys. Rev. B*, 95:165417, Apr 2017.

[70] J. E. Zucker, A. Pinczuk, D. S. Chemla, A. Gossard, and W. Wiegmann. Raman scattering resonant with quasi-two-dimensional excitons in semiconductor quantum wells. *Phys. Rev. Lett.*, 51:1293–1296, Oct 1983.

[71] Bruno R. Carvalho, Leandro M. Malard, Juliana M. Alves, Cristiano Fantini, and Marcos A. Pimenta. Symmetry-dependent exciton-phonon coupling in 2d and bulk mos_2 observed by resonance raman scattering. *Phys. Rev. Lett.*, 114:136403, Apr 2015.

[72] E. del Corro, A. Botello-Méndez, Y. Gillet, A. L. Elias, H. Terrones, S. Feng, C. Fantini, Daniel Rhodes, N. Pradhan, L. Balicas, X. Gonze, J.-C. Charlier, M. Terrones, and M. A. Pimenta. Atypical exciton–phonon interactions in ws2 and wse2 monolayers revealed by resonance raman spectroscopy. *Nano Letters*, 16(4):2363–2368, 2016. PMID: 26998817.

[73] Liam P. McDonnell, Chung-Che Huang, Qingsong Cui, Dan W. Hewak, and David C. Smith. Probing excitons, trions, and dark excitons in monolayer ws2 using resonance raman spectroscopy. *Nano Lett.*, 18(2):1428–1434, February 2018.

[74] K. Gołasa, M. Grzeszczyk, P. Leszczyński, C. Faugeras, A. A. L. Nicolet, A. Wysmołek, M. Potemski, and A. Babiński. Multiphonon resonant raman scattering in mos2. *Appl. Phys. Lett.*, 104(9):092106, March 2014.

[75] Weijie Zhao, R. M. Ribeiro, Minglin Toh, Alexandra Carvalho, Christian Kloc, A. H. Castro Neto, and Goki Eda. Origin of indirect optical transitions in few-layer mos2, ws2, and wse2. *Nano Lett.*, 13(11):5627–5634, November 2013.

[76] Di Xiao, Gui-Bin Liu, Wanxiang Feng, Xiaodong Xu, and Wang Yao. Coupled spin and valley physics in monolayers of mos_2 and other group-vi dichalcogenides. *Phys. Rev. Lett.*, 108:196802, May 2012.

[77] Bairen Zhu, Hualing Zeng, Junfeng Dai, Zhirui Gong, and Xiaodong Cui. Anomalously robust valley polarization and valley coherence in bilayer ws2. *Proceedings of the National Academy of Sciences*, 111(32):11606–11611, 2014.

[78] Kin Fai Mak, Di Xiao, and Jie Shan. Light-valley interactions in 2d semiconductors. *Nature Photonics*, 12(8):451–460, August 2018.

[79] Aaron M. Jones, Hongyi Yu, Nirmal J. Ghimire, Sanfeng Wu, Grant Aivazian, Jason S. Ross, Bo Zhao, Jiaqiang Yan, David G. Mandrus, Di Xiao, Wang Yao, and Xiaodong Xu. Optical generation of excitonic valley coherence in monolayer wse2. *Nature Nanotechnology*, 8:634, August 2013.

[80] Hualing Zeng, Junfeng Dai, Wang Yao, Di Xiao, and Xiaodong Cui. Valley polarization in mos2 monolayers by optical pumping. *Nature Nanotechnology*, 7:490, June 2012.

[81] Kin Fai Mak, Keliang He, Jie Shan, and Tony F. Heinz. Control of valley polarization in monolayer mos2 by optical helicity. *Nature Nanotechnology*, 7:494, June 2012.

[82] Ting Cao, Gang Wang, Wenpeng Han, Huiqi Ye, Chuanrui Zhu, Junren Shi, Qian Niu, Pingheng Tan, Enge Wang, Baoli Liu, and Ji Feng. Valley-selective circular dichroism of monolayer molybdenum disulphide. *Nature Communications*, 3: 887, June 2012.

[83] Pramoda K. Nayak, Fan-Cheng Lin, Chao-Hui Yeh, Jer-Shing Huang, and Po-Wen Chiu. Robust room temperature valley polarization in monolayer and bilayer ws2. *Nanoscale*, 8:6035–6042, 2016.

[84] Robert Schmidt, Gunnar Berghäuser, Robert Schneider, Malte Selig, Philipp Tonndorf, Ermin Malić, Andreas Knorr, Steffen Michaelis de Vasconcellos, and Rudolf Bratschitsch. Ultrafast coulomb-induced intervalley coupling in atomically thin ws2. *Nano Lett.*, 16(5):2945–2950, May 2016.

[85] Huimin Su, Chengrong Wei, Aiying Deng, Dongmei Deng, Chunlei Yang, and Jun-Feng Dai. Anomalous enhancement of valley polarization in multilayer ws2 at room temperature. *Nanoscale*, 9(16):5148–5154, 2017.

[86] G. Kioseoglou, A. T. Hanbicki, M. Currie, A. L. Friedman, D. Gunlycke, and B. T. Jonker. Valley polarization and intervalley scattering in monolayer mos2. *Applied Physics Letters*, 101(22):221907, 2012.

[87] Yanlong Wang, Chunxiao Cong, Jingzhi Shang, Mustafa Eginligil, Yuqi Jin, Gang Li, Yu Chen, Namphung Peimyoo, and Ting Yu. Unveiling exceptionally robust valley contrast in aa- and ab-stacked bilayer ws2. *Nanoscale Horiz.*, 4:396–403, 2019.

[88] Nourdine Zibouche, Pier Philipsen, Agnieszka Kuc, and Thomas Heine. Transition-metal dichalcogenide bilayers: Switching materials for spintronic and valleytronic applications. *Phys. Rev. B*, 90:125440, Sep 2014.

[89] Tao Jiang, Hengrui Liu, Di Huang, Shuai Zhang, Yingguo Li, Xingao Gong, Yuen-Ron Shen, Wei-Tao Liu, and Shiwei Wu. Valley and band structure engineering of folded mos2 bilayers. *Nature Nanotechnology*, 9(10):825–829, 2014.

[90] G. Wang, X. Marie, L. Bouet, M. Vidal, A. Balocchi, T. Amand, D. Lagarde, and B. Urbaszek. Exciton dynamics in wse2 bilayers. *Applied Physics Letters*, 105(18):182105, 2014.

[91] Sanfeng Wu, Jason S. Ross, Gui-Bin Liu, Grant Aivazian, Aaron Jones, Zaiyao Fei, Wenguang Zhu, Di Xiao, Wang Yao, David Cobden, and Xiaodong Xu. Electrical tuning of valley magnetic moment through symmetry control in bilayer mos2. *Nature Physics*, 9(3):149–153, 2013.

[92] Aaron M. Jones, Hongyi Yu, Jason S. Ross, Philip Klement, Nirmal J. Ghimire, Jiaqiang Yan, David G. Mandrus, Wang Yao, and Xiaodong Xu. Spin-layer locking effects in optical orientation of exciton spin in bilayer wse2. *Nature Physics*, 10: 130, January 2014.

[93] Su-Hyun Gong, Irina Komen, Filippo Alpeggiani, and L. Kuipers. Nanoscale optical addressing of valley pseudospins through transverse optical spin. *Nano Letters*, 20 (6):4410–4415, 2020. PMID: 32406694.

[94] Geoffrey Brooker and Alma Zook. Modern classical optics. *American Journal of Physics - AMER J PHYS*, 72:1531–1531, 12 2004.

[95] Lukas Novotny and Bert Hecht. *Principles of Nano-Optics*. Cambridge University Press, Cambridge, 2006.

[96] M. Andreas Lieb, James M. Zavislan, and Lukas Novotny. Single-molecule orientations determined by direct emission pattern imaging. *J. Opt. Soc. Am. B*, 21(6): 1210–1215, Jun 2004.

[97] Thomas Bauer. *Probe-based nano-interferometric reconstruction of tightly focused vectorial light fields*. PhD thesis, Friedrich-Alexander-Universität Erlangen-Nürnberg, 01 2017.

[98] Timo A. Nieminen, Alexander B. Stilgoe, Norman R. Heckenberg, and Halina Rubinsztein-Dunlop. Angular momentum of a strongly focused gaussian beam. *Journal of Optics A: Pure and Applied Optics*, 10(11):115005, 2008.

[99] Yiqiong Zhao, J. Scott Edgar, Gavin D. M. Jeffries, David McGloin, and Daniel T. Chiu. Spin-to-orbital angular momentum conversion in a strongly focused optical beam. *Phys. Rev. Lett.*, 99:073901, Aug 2007.

[100] K. F. Mak, K. L. McGill, J. Park, and P. L. McEuen. The valley hall effect in mos2 transistors. *Science*, 344(6191):1489–1492, 2014.

[101] Y. J. Zhang, T. Oka, R. Suzuki, J. T. Ye, and Y. Iwasa. Electrically switchable chiral light-emitting transistor. *Science*, 344(6185):725–728, 2014.

[102] John R. Schaibley, Hongyi Yu, Genevieve Clark, Pasqual Rivera, Jason S. Ross, Kyle L. Seyler, Wang Yao, and Xiaodong Xu. Valleytronics in 2d materials. *Nature Reviews Materials*, 1:16055, August 2016.

[103] Xiaodong Xu, Wang Yao, Di Xiao, and Tony F. Heinz. Spin and pseudospins in layered transition metal dichalcogenides. *Nature Physics*, 10:343, April 2014.

[104] Alexander Krasnok and Andrea Alù. Valley-selective response of nanostructures coupled to 2d transition-metal dichalcogenides. *Applied Sciences*, 8(7):1157, 2018.

[105] Thibault Chervy, Stefano Azzini, Etienne Lorchat, Shaojun Wang, Yuri Gorodetski, James A. Hutchison, Stéphane Berciaud, Thomas W. Ebbesen, and Cyriaque Genet. Room temperature chiral coupling of valley excitons with spin-momentum locked surface plasmons. *ACS Photonics*, 5(4):1281–1287, April 2018.

[106] Liuyang Sun, Chun-Yuan Wang, Alex Krasnok, Junho Choi, Jinwei Shi, Juan Sebastian Gomez-Diaz, André Zepeda, Shangjr Gwo, Chih-Kang Shih, Andrea Alù, and Xiaoqin Li. Separation of valley excitons in a mos2 monolayer using a subwavelength asymmetric groove array. *Nature Photonics*, 13(3):180–184, March 2019.

[107] Guangwei Hu, Xuanmiao Hong, Kai Wang, Jing Wu, He-Xiu Xu, Wenchao Zhao, Weiwei Liu, Shuang Zhang, Francisco Garcia-Vidal, Bing Wang, Peixiang Lu, and Cheng-Wei Qiu. Coherent steering of nonlinear chiral valley photons with a synthetic au-ws2 metasurface. *Nature Photonics*, 13:467—-472, April 2019.

[108] K. Y. Bliokh, F. J. Rodríguez-Fortuño, F. Nori, and A. V. Zayats. Spin-orbit interactions of light. *Nature Photonics*, 9:796, November 2015.

[109] Andrea Aiello, Peter Banzer, Martin Neugebauer, and Gerd Leuchs. From transverse angular momentum to photonic wheels. *Nature Photonics*, 9:789, November 2015.

[110] Peter Lodahl, Sahand Mahmoodian, Søren Stobbe, Arno Rauschenbeutel, Philipp Schneeweiss, Jürgen Volz, Hannes Pichler, and Peter Zoller. Chiral quantum optics. *Nature*, 541:473, January 2017.

[111] Francisco J. Rodríguez-Fortuño, Giuseppe Marino, Pavel Ginzburg, Daniel O'Connor, Alejandro Martínez, Gregory A. Wurtz, and Anatoly V. Zayats. Near-field interference for the unidirectional excitation of electromagnetic guided modes. *Science*, 340(6130):328, April 2013.

[112] Francisco J. Rodríguez-Fortuño, Isaac Barber-Sanz, Daniel Puerto, Amadeu Griol, and Alejandro Martínez. Resolving light handedness with an on-chip silicon microdisk. *ACS Photonics*, 1(9):762–767, 2014.

[113] D. O'Connor, P. Ginzburg, F. J. Rodríguez-Fortuño, G. A. Wurtz, and A. V. Zayats. Spin-orbit coupling in surface plasmon scattering by nanostructures. *Nature Communications*, 5:5327, November 2014.

[114] R. Mitsch, C. Sayrin, B. Albrecht, P. Schneeweiss, and A. Rauschenbeutel. Quantum state-controlled directional spontaneous emission of photons into a nanophotonic waveguide. *Nature Communications*, 5:5713, December 2014.

[115] Jan Petersen, Jürgen Volz, and Arno Rauschenbeutel. Chiral nanophotonic waveguide interface based on spin-orbit interaction of light. *Science*, 346(6205):67–71, 2014.

[116] R. J. Coles, D. M. Price, J. E. Dixon, B. Royall, E. Clarke, P. Kok, M. S. Skolnick, A. M. Fox, and M. N. Makhonin. Chirality of nanophotonic waveguide with embedded quantum emitter for unidirectional spin transfer. *Nature Communications*, 7:11183, March 2016.

[117] A. V. Akimov, A. Mukherjee, C. L. Yu, D. E. Chang, A. S. Zibrov, P. R. Hemmer, H. Park, and M. D. Lukin. Generation of single optical plasmons in metallic nanowires coupled to quantum dots. *Nature*, 450(7168):402–406, 2007.

[118] Beniamino Sciacca, Sander A. Mann, Frans D. Tichelaar, Henny W. Zandbergen, Marijn A. van Huis, and Erik C. Garnett. Solution-phase epitaxial growth of quasi-monocrystalline cuprous oxide on metal nanowires. *Nano Letters*, 14(10):5891–5898, 2014. PMID: 25233392.

[119] Ruoxue Yan, Daniel Gargas, and Peidong Yang. Nanowire photonics. *Nature Photonics*, 3:569, October 2009.

[120] Grzegorz Grzela, Djamila Hourlier, and Jaime Gómez Rivas. Polarization-dependent light extinction in ensembles of polydisperse vertical semiconductor nanowires: A mie scattering effective medium. *Phys. Rev. B*, 86:045305, Jul 2012.

[121] Tobias Voss, Geoffry T. Svacha, Eric Mazur, Sven Müller, Carsten Ronning, Denan Konjhodzic, and Frank Marlow. High-order waveguide modes in zno nanowires. *Nano Lett.*, 7(12):3675–3680, December 2007.

[122] Humberto R. Gutiérrez, Nestor Perea-López, Ana Laura Elías, Ayse Berkdemir, Bei Wang, Ruitao Lv, Florentino López-Urías, Vincent H. Crespi, Humberto Terrones, and Mauricio Terrones. Extraordinary room-temperature photoluminescence in triangular ws2 monolayers. *Nano Lett.*, 13(8):3447–3454, 2013. PMID: 23194096.

[123] Namphung Peimyoo, Jingzhi Shang, Chunxiao Cong, Xiaonan Shen, Xiangyang Wu, Edwin K. L. Yeow, and Ting Yu. Nonblinking, intense two-dimensional light emitter: Monolayer ws2 triangles. *ACS Nano*, 7(12):10985–10994, December 2013.

[124] Chunxiao Cong, Jingzhi Shang, Xing Wu, Bingchen Cao, Namphung Peimyoo, Caiyu Qiu, Litao Sun, and Ting Yu. Synthesis and optical properties of large-area single-crystalline 2d semiconductor ws2 monolayer from chemical vapor deposition. *Advanced Optical Materials*, 2(2):131–136, June 2020.

[125] Min Su Kim, Seok Joon Yun, Yongjun Lee, Changwon Seo, Gang Hee Han, Ki Kang Kim, Young Hee Lee, and Jeongyong Kim. Biexciton emission from edges and grain boundaries of triangular ws2 monolayers. *ACS Nano*, 10(2):2399–2405, 2016. PMID: 26758415.

[126] Hongwei Liu, Junpeng Lu, Kenneth Ho, Zhenliang Hu, Zhiya Dang, Alexandra Carvalho, Hui Ru Tan, Eng Soon Tok, and Chorng Haur Sow. Fluorescence concentric triangles: A case of chemical heterogeneity in ws2 atomic monolayer. *Nano Letters*, 16(9):5559–5567, 2016. PMID: 27479127.

[127] Shanghuai Feng, Ruilong Yang, Zhiyan Jia, Jianyong Xiang, Fusheng Wen, Congpu Mu, Anmin Nie, Zhisheng Zhao, Bo Xu, Chenggang Tao, Yongjun Tian, and Zhongyuan Liu. Strain release induced novel fluorescence variation in cvd-grown monolayer ws2 crystals. *ACS Applied Materials & Interfaces*, 9(39):34071–34077, 2017. PMID: 28902488.

[128] Kathleen M. McCreary, Marc Currie, Aubrey T. Hanbicki, Hsun-Jen Chuang, and Berend T. Jonker. Understanding variations in circularly polarized photoluminescence in monolayer transition metal dichalcogenides. *ACS Nano*, 11(8):7988–7994, 2017. PMID: 28763189.

[129] Matthew R. Rosenberger, Hsun-Jen Chuang, Kathleen M. McCreary, Connie H. Li, and Berend T. Jonker. Electrical characterization of discrete defects and impact of defect density on photoluminescence in monolayer ws2. *ACS Nano*, 12(2):1793–1800, 2018. PMID: 29320162.

[130] Christoph Kastl, Roland J. Koch, Christopher T. Chen, Johanna Eichhorn, Søren Ulstrup, Aaron Bostwick, Chris Jozwiak, Tevye R. Kuykendall, Nicholas J. Borys, Francesca M. Toma, Shaul Aloni, Alexander Weber-Bargioni, Eli Rotenberg, and Adam M. Schwartzberg. Effects of defects on band structure and excitons in ws2 revealed by nanoscale photoemission spectroscopy. *ACS Nano*, 13(2):1284–1291, 2019. PMID: 30645100.

[131] Pavel Kolesnichenko, Qianhui Zhang, Tinghe Yun, Changxi Zheng, Michael Fuhrer, and Jeffrey Davis. Disentangling the effects of doping, strain and disorder in monolayer ws2 by optical spectroscopy. *2D Materials*, 7, 12 2019.

[132] Andre Neumann, Jessica Lindlau, Léo Colombier, Manuel Nutz, Sina Najmaei, Jun Lou, Aditya D. Mohite, Hisato Yamaguchi, and Alexander Högele. Opto-valleytronic imaging of atomically thin semiconductors. *Nature Nanotechnology*, 12(4):329–334, 2017.

[133] G. Wang, X. Marie, B. L. Liu, T. Amand, C. Robert, F. Cadiz, P. Renucci, and B. Urbaszek. Control of exciton valley coherence in transition metal dichalcogenide monolayers. *Phys. Rev. Lett.*, 117:187401, Oct 2016.

[134] Robert Schmidt, Ashish Arora, Gerd Plechinger, Philipp Nagler, Andrés Granados del Águila, Mariana V. Ballottin, Peter C. M. Christianen, Steffen Michaelis de Vasconcellos, Christian Schüller, Tobias Korn, and Rudolf Bratschitsch. Magnetic-field-induced rotation of polarized light emission from monolayer ws_2. *Phys. Rev. Lett.*, 117:077402, Aug 2016.

[135] F. Cadiz, E. Courtade, C. Robert, G. Wang, Y. Shen, H. Cai, T. Taniguchi, K. Watanabe, H. Carrere, D. Lagarde, M. Manca, T. Amand, P. Renucci, S. Tongay, X. Marie, and B. Urbaszek. Excitonic linewidth approaching the homogeneous limit in mos_2-based van der waals heterostructures. *Phys. Rev. X*, 7:021026, May 2017.

[136] Tomasz Jakubczyk, Karol Nogajewski, Maciej Molas, Miroslav Bartos, Wolfgang Langbein, Marek Potemski, and J. Kasprzak. Impact of environment on dynamics of exciton complexes in a ws_2 monolayer. *2D Materials*, 5:031007, 09 2017.

[137] Kai Hao, Galan Moody, Fengcheng Wu, Chandriker Kavir Dass, Lixiang Xu, Chang-Hsiao Chen, Liuyang Sun, Ming-Yang Li, Lain-Jong Li, Allan H. MacDonald, and Xiaoqin Li. Direct measurement of exciton valley coherence in monolayer wse2. *Nature Physics*, 12(7):677–682, July 2016.

[138] Ziliang Ye, Dezheng Sun, and Tony F. Heinz. Optical manipulation of valley pseudospin. *Nature Physics*, 13(1):26–29, January 2017.

[139] Etienne Lorchat, Stefano Azzini, Thibault Chervy, Takashi Taniguchi, Kenji Watanabe, Thomas W. Ebbesen, Cyriaque Genet, and Stéphane Berciaud. Room-temperature valley polarization and coherence in transition metal dichalcogenide-graphene van der waals heterostructures. *ACS Photonics*, 5(12): 5047–5054, December 2018.

[140] Leonidas Mouchliadis, Sotiris Psilodimitrakopoulos, George Miltos Maragkakis, Ioanna Demeridou, George Kourmoulakis, Andreas Lemonis, George Kioseoglou, and Emmanuel Stratakis. Probing valley population imbalance in transition metal dichalcogenides via temperature-dependent second harmonic generation imaging. *npj 2D Materials and Applications*, 5(1):6, 2021.

[141] Yi Wei Ho, Henrique G. Rosa, Ivan Verzhbitskiy, Manuel J. L. F. Rodrigues, Takashi Taniguchi, Kenji Watanabe, Goki Eda, Vitor M. Pereira, and José C. Viana-Gomes. Measuring valley polarization in two-dimensional materials with second-harmonic spectroscopy. *ACS Photonics*, 7(4):925–931, 2020.

[142] I. Paradisanos, K. M. McCreary, D. Adinehloo, L. Mouchliadis, J. T. Robinson, Hsun-Jen Chuang, A. T. Hanbicki, V. Perebeinos, B. T. Jonker, E. Stratakis, and G. Kioseoglou. Prominent room temperature valley polarization in ws2/graphene heterostructures grown by chemical vapor deposition. *Applied Physics Letters*, 116 (20):203102, 2020.

[143] Wei-Hsiang Lin, Wei-Shiuan Tseng, Cora M. Went, Marcus L. Teague, George. R. Rossman, Harry A. Atwater, and Nai-Chang Yeh. Nearly 90% circularly polarized emission in monolayer ws2 single crystals by chemical vapor deposition. *ACS Nano*, 14(2):1350–1359, 2020. PMID: 31442375.

[144] Beth Schaefer, Edward Collett, Robert Smyth, Daniel Barrett, and Beth Fraher. Measuring the stokes polarization parameters. *American Journal of Physics*, 75 (2):163–168, 2007.

[145] Edward Collett. *Polarized light: fundamentals and applications*. Marcel Dekker, Inc, Measurements Concepts, New York, 1993.

[146] Edward Collett. *Field Guide to Polarization*. SPIE, John E. Greivenkamp, 2005.

[147] Tae-Young Jeong, Soungmin Bae, Seong-Yeon Lee, Suyong Jung, Yong-Hoon Kim, and Ki-Ju Yee. Valley depolarization in monolayer transition-metal dichalcogenides with zone-corner acoustic phonons. *Nanoscale*, 12(44):22487–22494, 2020.

[148] Lawson T. Lloyd, Ryan E. Wood, Fauzia Mujid, Siddhartha Sohoni, Karen L. Ji, Po-Chieh Ting, Jacob S. Higgins, Jiwoong Park, and Gregory S. Engel. Sub-10 fs intervalley exciton coupling in monolayer mos2 revealed by helicity-resolved two-dimensional electronic spectroscopy. *ACS Nano*, 15(6):10253–10263, 2021. PMID: 34096707.

[149] Shengnan Xu, Chen Si, Yang Li, Bing-Lin Gu, and Wenhui Duan. Valley depolarization dynamics in monolayer transition-metal dichalcogenides: Role of the satellite valley. *Nano Letters*, 21(4):1785–1791, 2021. PMID: 33586443.

[150] Fahad Mahmood, Zhanybek Alpichshev, Yi-Hsien Lee, Jing Kong, and Nuh Gedik. Observation of exciton–exciton interaction mediated valley depolarization in monolayer mose2. *Nano Letters*, 18(1):223–228, 2018. PMID: 29239177.

[151] Hiram J. Conley, Bin Wang, Jed I. Ziegler, Richard F. Haglund, Sokrates T. Pantelides, and Kirill I. Bolotin. Bandgap engineering of strained monolayer and bilayer mos2. *Nano Letters*, 13(8):3626–3630, 2013. PMID: 23819588.

[152] Tohid Farajollahpour and Arash Phirouznia. The role of the strain induced population imbalance in valley polarization of graphene: Berry curvature perspective. *Scientific Reports*, 7(1):17878, 2017.

[153] S. Dufferwiel, S. Schwarz, F. Withers, A. A. P. Trichet, F. Li, M. Sich, O. Del Pozo-Zamudio, C. Clark, A. Nalitov, D. D. Solnyshkov, G. Malpuech, K. S. Novoselov,

J. M. Smith, M. S. Skolnick, D. N. Krizhanovskii, and A. I. Tartakovskii. Exciton-polaritons in van der waals heterostructures embedded in tunable microcavities. *Nature Communications*, 6(1):8579, 2015.

[154] Yen-Jung Chen, Jeffrey D. Cain, Teodor K. Stanev, Vinayak P. Dravid, and Nathaniel P. Stern. Valley-polarized exciton-polaritons in a monolayer semiconductor. *Nature Photonics*, 11(7):431–435, 2017.

[155] Xiaoze Liu, Tal Galfsky, Zheng Sun, Fengnian Xia, Erh-chen Lin, Yi-Hsien Lee, Stéphane Kéna-Cohen, and Vinod M. Menon. Strong light-matter coupling in two-dimensional atomic crystals. *Nature Photonics*, 9(1):30–34, 2015.

[156] Itai Epstein, André J Chaves, Daniel A Rhodes, Bettina Frank, Kenji Watanabe, Takashi Taniguchi, Harald Giessen, James C Hone, Nuno M R Peres, and Frank H L Koppens. Highly confined in-plane propagating exciton-polaritons on monolayer semiconductors. *2D Materials*, 7(3):035031, jun 2020.

[157] Wenjing Liu, Zhurun Ji, Yuhui Wang, Gaurav Modi, Minsoo Hwang, Biyuan Zheng, Volker J. Sorger, Anlian Pan, and Ritesh Agarwal. Generation of helical topological exciton-polaritons. *Science*, 370(6516):600–604, 2020.

[158] Long Zhang, Rahul Gogna, Will Burg, Emanuel Tutuc, and Hui Deng. Photonic-crystal exciton-polaritons in monolayer semiconductors. *Nature Communications*, 9(1):713, 2018.

[159] F. Hu, Y. Luan, M. E. Scott, J. Yan, D. G. Mandrus, X. Xu, and Z. Fei. Imaging exciton-polariton transport in mose2 waveguides. *Nature Photonics*, 11(6):356–360, 2017.

[160] Z. Fei, M. E. Scott, D. J. Gosztola, J. J. Foley, J. Yan, D. G. Mandrus, H. Wen, P. Zhou, D. W. Zhang, Y. Sun, J. R. Guest, S. K. Gray, W. Bao, G. P. Wiederrecht, and X. Xu. Nano-optical imaging of ws2 waveguide modes revealing light-exciton interactions. *Phys. Rev. B*, 94:081402, Aug 2016.

[161] M. Mrejen, L. Yadgarov, A. Levanon, and H. Suchowski. Transient exciton-polariton dynamics in wse2 by ultrafast near-field imaging. *Science Advances*, 5 (2), 2019.

[162] C. Creatore and A. L. Ivanov. Strong and weak coupling limits in optics of quantum well excitons. *Phys. Rev. B*, 77:075324, Feb 2008.

[163] Xiaobo Yin, Ziliang Ye, Daniel A. Chenet, Yu Ye, Kevin O'Brien, James C. Hone, and Xiang Zhang. Edge nonlinear optics on a mos2 atomic monolayer. *Science*, 344 (6183):488–490, 2014.

[164] Jan Renger, Romain Quidant, Niek van Hulst, Stefano Palomba, and Lukas Novotny. Free-space excitation of propagating surface plasmon polaritons by nonlinear four-wave mixing. *Phys. Rev. Lett.*, 103:266802, Dec 2009.

[165] M. Kohl, D. Heitmann, P. Grambow, and K. Ploog. Luminescence of quantum-well exciton polaritons from microstructured $al_xga_{1-x}As-GaAs$ multiple quantum wells. *Phys. Rev. B*, 37:10927–10930, Jun 1988.

[166] Marko Spasenović, Thomas P. White, Sangwoo Ha, Andrey A. Sukhorukov, Tobias Kampfrath, Yuri S. Kivshar, C. Martijn de Sterke, Thomas F. Krauss, and L. (Kobus) Kuipers. Experimental observation of evanescent modes at the interface to slow-light photonic crystal waveguides. *Opt. Lett.*, 36(7):1170–1172, Apr 2011.

[167] Javier Hernandez-Rueda, Marc L. Noordam, Irina Komen, and L. Kuipers. Nonlinear optical response of a ws2 monolayer at room temperature upon multicolor laser excitation. *ACS Photonics*, January 2021.

[168] Liming Zhang, Kaihui Liu, Andrew Barnabas Wong, Jonghwan Kim, Xiaoping Hong, Chong Liu, Ting Cao, Steven G. Louie, Feng Wang, and Peidong Yang. Three-dimensional spirals of atomic layered mos2. *Nano Lett.*, 14(11):6418–6423, November 2014.

[169] Prasad V. Sarma, Prasanna D. Patil, Prahalad K. Barman, Rajeev N. Kini, and Manikoth M. Shaijumon. Controllable growth of few-layer spiral ws2. *RSC Adv.*, 6 (1):376–382, 2016.

[170] Abhay V. Agrawal, R. Kumar, Guang Yang, Jiming Bao, Mahesh Kumar, and Mukesh Kumar. Enhanced adsorption sites in monolayer mos2 pyramid structures for highly sensitive and fast hydrogen sensor. *International Journal of Hydrogen Energy*, 45(15):9268–9277, 2020.

[171] Pengfei Cheng, Qingwei Zhou, Xianbiao Hu, Shaoqiang Su, Xin Wang, Mingliang Jin, Lingling Shui, Xingsen Gao, Yanqing Guan, Richard Nözel, Guofu Zhou, Zhang Zhang, and Junming Liu. Transparent glass with the growth of pyramid-type mos2 for highly efficient water disinfection under visible-light irradiation. *ACS Appl. Mater. Interfaces*, 10(28):23444–23450, July 2018.

[172] Qingwei Zhou, Shaoqiang Su, Pengfei Cheng, Xianbao Hu, Min Zeng, Xingsen Gao, Zhang Zhang, and Jun-Ming Liu. Robust ferromagnetism in zigzag-edge rich mos2 pyramids. *Nanoscale*, 10(24):11578–11584, 2018.

[173] Jingying Zheng, Xingxu Yan, Zhixing Lu, Hailong Qiu, Guanchen Xu, Xu Zhou, Peng Wang, Xiaoqing Pan, Kaihui Liu, and Liying Jiao. High-mobility multilayered mos2 flakes with low contact resistance grown by chemical vapor deposition. *Adv. Mater.*, 29(13):1604540, April 2017.

[174] Liang Chen, Bilu Liu, Ahmad N. Abbas, Yuqiang Ma, Xin Fang, Yihang Liu, and Chongwu Zhou. Screw-dislocation-driven growth of two-dimensional few-layer and pyramid-like wse2 by sulfur-assisted chemical vapor deposition. *ACS Nano*, 8 (11):11543–11551, November 2014.

[175] Xiaopeng Fan, Ying Jiang, Xiujuan Zhuang, Hongjun Liu, Tao Xu, Weihao Zheng, Peng Fan, Honglai Li, Xueping Wu, Xiaoli Zhu, Qinglin Zhang, Hong Zhou, Wei

Hu, Xiao Wang, Litao Sun, Xiangfeng Duan, and Anlian Pan. Broken symmetry induced strong nonlinear optical effects in spiral ws2 nanosheets. *ACS Nano*, 11 (5):4892–4898, May 2017.

[176] Xianqing Lin, Yingying Liu, Kang Wang, Cong Wei, Wei Zhang, Yongli Yan, Yong Jun Li, Jiannian Yao, and Yong Sheng Zhao. Two-dimensional pyramid-like ws2 layered structures for highly efficient edge second-harmonic generation. *ACS Nano*, 12(1): 689–696, January 2018.

[177] Ruilong Yang, Shanghuai Feng, Xunyong Lei, Xiaoyu Mao, Anmin Nie, Bochong Wang, Kun Luo, Jianyong Xiang, Fusheng Wen, Congpu Mu, Zhisheng Zhao, Bo Xu, Hualing Zeng, Yongjun Tian, and Zhongyuan Liu. Effect of layer and stacking sequence in simultaneously grown 2h and 3r ws2 atomic layers. *Nanotechnology*, 30 (34):345203, 2019.

[178] Luojun Du, Qian Zhang, Tingting Zhang, Zhiyan Jia, Jing Liang, Gui-Bin Liu, Rong Yang, Dongxia Shi, Jianyong Xiang, Kaihui Liu, Zhipei Sun, Yugui Yao, Qingming Zhang, and Guangyu Zhang. Robust circular polarization of indirect q-k transitions in bilayer $3r - Ws_2$. *Phys. Rev. B*, 100:161404, Oct 2019.

[179] Maciej R. Molas, Karol Nogajewski, Marek Potemski, and Adam Babiński. Raman scattering excitation spectroscopy of monolayer ws2. *Scientific reports*, 7 (28698679):5036–5036, July 2017.

[180] M. Thripuranthaka, Ranjit V. Kashid, Chandra Sekhar Rout, and Dattatray J. Late. Temperature dependent raman spectroscopy of chemically derived few layer mos2 and ws2 nanosheets. *Appl. Phys. Lett.*, 104(8):081911, February 2014.

[181] J. H. Parker, D. W. Feldman, and M. Ashkin. Raman scattering by silicon and germanium. *PR*, 155(3):712–714, March 1967.

[182] Kunimitsu Uchinokura, Tomoyuki Sekine, and Etsuyuki Matsuura. Raman scattering by silicon. *Solid State Communications*, 11(1):47–49, 1972.

[183] B. A. Weinstein and Manuel Cardona. Two-phonon raman spectra of si and gap. *Solid State Communications*, 10(10):961–965, 1972.

[184] Dario Mastrippolito, Stefano Palleschi, Gianluca D'Olimpio, Antonio Politano, Michele Nardone, Paola Benassi, and Luca Ottaviano. Exciton-phonon coupling and power dependent room temperature photoluminescence of sulphur vacancy doped mos2via controlled thermal annealing. *Nanoscale*, 12(36):18899–18907, 2020.

[185] Yeonwoong Jung, Jie Shen, Yanhui Liu, John M. Woods, Yong Sun, and Judy J. Cha. Metal seed layer thickness-induced transition from vertical to horizontal growth of mos2 and ws2. *Nano Letters*, 14(12):6842–6849, 2014. PMID: 25406013.

[186] Y. B. Li, Y. Bando, and D. Golberg. Mos2 nanoflowers and their field-emission properties. *Applied Physics Letters*, 82(12):1962–1964, 2003.

[187] Xiao-Lin Li, Jian-Ping Ge, and Ya-Dong Li. Atmospheric pressure chemical vapor deposition: An alternative route to large-scale mos2 and ws2 inorganic fullerene-like nanostructures and nanoflowers. *Chemistry – A European Journal*, 10(23): 6163–6171, 2004.

[188] Arunvinay Prabakaran, Frank Dillon, Jodie Melbourne, Lewys Jones, Rebecca J. Nicholls, Phil Holdway, Jude Britton, Antal A. Koos, Alison Crossley, Peter D. Nellist, and Nicole Grobert. Ws2 2d nanosheets in 3d nanoflowers. *Chem. Commun.*, 50: 12360–12362, 2014.

[189] Xiuli Fu, Jingwen Qian, Xiaofen Qiao, Pingheng Tan, and Zhijian Peng. Nonlinear saturable absorption of vertically stood ws2 nanoplates. *Opt. Lett.*, 39(22):6450–6453, Nov 2014.

[190] Mingge Jin, Wei Zheng, Ying Ding, Yanming Zhu, Weiliang Wang, and Feng Huang. Raman tensor of van der waals mose2. *The Journal of Physical Chemistry Letters*, 11(11):4311–4316, 2020. PMID: 32393031.

[191] Ying Ding, Wei Zheng, Mingge Jin, Yanming Zhu, Ruinan Zhu, Zeguo Lin, and Feng Huang. Raman tensor of layered mos2. *Opt. Lett.*, 45(6):1313–1316, Mar 2020.

[192] Martin Hulman, Michaela Sojková, Karol Végsö, Nada Mrkyvkova, Jakub Hagara, Peter Hutár, Peter Kotrusz, Ján Hudec, Kamil Tokár, Eva Majkova, and Peter Siffalovic. Polarized raman reveals alignment of few-layer mos2 films. *The Journal of Physical Chemistry C*, 123(48):29468–29475, 2019.

[193] J. Krustok, R. Kaupmees, R. Jaaniso, V. Kiisk, I. Sildos, B. Li, and Y. Gong. Local strain-induced band gap fluctuations and exciton localization in aged ws2 monolayers. *AIP Advances*, 7(6):065005, June 2017.

[194] J. Jadczak, J. Kutrowska-Girzycka, P. Kapuściński, Y. S. Huang, A. Wójs, and L. Bryja. Probing of free and localized excitons and trions in atomically thin wse2, ws2, mose2 and mos2 in photoluminescence and reflectivity experiments. *Nanotechnology*, 28(39):395702, 2017.

[195] Zhengyu He, Xiaochen Wang, Wenshuo Xu, Yingqiu Zhou, Yuewen Sheng, Youmin Rong, Jason M. Smith, and Jamie H. Warner. Revealing defect-state photoluminescence in monolayer ws2 by cryogenic laser processing. *ACS Nano*, 10(6):5847–5855, June 2016.

[196] Jae-Ung Lee, Kangwon Kim, Songhee Han, Gyeong Hee Ryu, Zonghoon Lee, and Hyeonsik Cheong. Raman signatures of polytypism in molybdenum disulfide. *ACS Nano*, 10(2):1948–1953, February 2016.

[197] Jeremiah van Baren, Gaihua Ye, Jia-An Yan, Zhipeng Ye, Pouyan Rezaie, Peng Yu, Zheng Liu, Rui He, and Chun Hung Lui. Stacking-dependent interlayer phonons in 3r and 2h mos 2. *2D Materials*, 6(2):025022, 2019.

[198] Zhouxiaosong Zeng, Xingxia Sun, Danliang Zhang, Weihao Zheng, Xiaopeng Fan, Mai He, Tao Xu, Litao Sun, Xiao Wang, and Anlian Pan. Controlled vapor growth and nonlinear optical applications of large-area 3r phase ws2 and wse2 atomic layers. *Advanced Functional Materials*, 29(11):1806874, 2019.

ACKNOWLEDGEMENTS

Just like it takes a village to raise a child, it takes a good social network around you to complete a PhD project. Looking back, I see the fun I had playing with lasers in the lab, how much I enjoyed the international and challenging environment of the university, and how much I learned about physics and about myself. However, I also look back at a lot of stress, when project after project failed, and corona lockdowns created extra uncertainties. I am therefore thankful for all the scientific help that I received, and I feel blessed with all the moral support from colleagues, friends and family.

First of all, a PhD stands or falls with good supervision. **Kobus**, I enjoyed these years working with you in your group, although I know these were not the easiest years for you personally. I admit I wished sometimes that you were less busy, but luckily you have a talent for efficient meetings. You are not only a brilliant scientist, you also have an incredible talent for communicating a convincing and understandable message. I appreciate your sense of humor, your empathy and your people skills. I admire your ability to supervise and lead completely different kinds of people, to choose to be positive or critical appropriate to the person and situation. It is clear that I learned a lot from you, but more importantly, I also genuinely appreciated your company. **Sonia**, you were always in for a coffee and a chat, a listening ear and a dosage of optimism. Your enthusiasm in coming up with new plans, dreams, and ideas was encouraging, although some of them might not have been completely feasible. Your positive energy and the care that you display for all the people working here, surely makes this department a better place to be.

I really enjoyed my years in the Nano Optics group, with the nice atmosphere, the silly discussions on far-fetched topics, the strive for good communication and nice looking posters, and the overall habit of helping each other out where needed. I enjoyed our lunches and coffees, our group outings and our *Sinterklaas* celebrations. When I started, the group was growing fast, it contained many postdocs to ask for advice and learn from, and the level of craziness was high. Unfortunately, halfway my PhD the group shrank, and corona kicked in which reduced the number of social interactions. **Dolfine**, although the time we spent in the same group was short, you did make me feel welcome in my first few months. **Su-Hyun**, thanks for all the time and effort you put in training me to work in the cleanroom, to exfoliate 2D materials, to measure photoluminescence and valley polarization with the optical set-up and to rebuild it. I also enjoyed our chats in the corridor and online, I enjoyed meeting your super cute dog and I sincerely hope I never offended you too much with my Dutch directness. **Lorenzo**, I appreciate your infinite enthusiasm about physics, Disney movies and learning Dutch by reading *Jip en Janneke*. In a group of very self-conscious physicists, you would just sing out loud without feeling embarrassed. **Felipe**, thanks for introducing me to the world of Blender imaging and

animations, and for all the advice on style and layout. **Nikhil**, our paths did not cross very often, so I will always remember you as the guy that fell in the Delft canal three times. **Javi**, thanks for your advice on optical set-ups, and I hope to have inspired you with the thought that cleaning the lab is a good thing to do. **Aron**, you seem to have infinite knowledge on such a broad range of topics, and I learned a lot from you. You helped me building and rebuilding the optical set-up, processing scientific data, and made me aware of the many possibilities to join aluminium plates together to build a black box around the set-up. Thanks also for all the help with selecting and ordering the Montana cryostat options. Thanks also to you, **Martin**, for setting up the *Hyperion* python code to control lab hardware and assisting and teaching me to make the code for my experiment. None of the position-dependent optical measurements of this thesis would have been possible without the proper automization of my set-up. I enjoyed your company when corona lockdowns reduced lab attendance. **Thijs**, I enjoyed your company when we attended the summerschool in Italy together, although I fully understand it if you would never enter a car where I am the driver anymore, especially not around mountains. **Thomas**, you were always there across the hallway to answer any questions, ranging from optics to science to university related. My impatient personality may have collided with your thorough and detailed way of working, but I appreciate all your help and everything you taught me, and of course all the chocolate cakes you baked. **Marc**, I appreciate your optimism and your critical scientific questions, which made me rethink whatever I was claiming. I enjoyed our random coffee chats and *quatre mains* aligning lasers for our fancy dark project. **Sonakshi**, we have a lot more in common than just being female physicists. I learned a lot from your knowledge about 2D materials and their electronic properties, and I liked teaching you the basics of alligning and measuring with an optical set-up. I enjoyed hanging out with you, giving scientific advice and receiving life advice back. I even appreciated the times you persuaded me to go crazy and do sports.

Next to the group members, I would like to thank some of the people of the department of *Quantum Nanoscience*. **Sabrya**, thanks a lot for your interesting WS_2 samples that basically saved my PhD project. You were always available to answer another question or to take another SEM or AFM image of the sample. I enjoyed your company and that of **Rasa** and all my other office mates through the years. It's a pity we never did manage to get that female-only office. Thanks a lot **Nikos**, for all the training you gave me for exfoliating and stamping 2D materials. I enjoyed having lunch with the small core of QN people: **Luigi**, **Abel**, **Maarten**, and **Niccolo, Matthijs**, **Parsa**, **Nina**, **Bas**, **Rob**, (and everybody else I am forgetting) that challenged the threats of corona to come and work at the university. Thanks **Dima** and **Jorrit** for your advice on the Montana cryostat, and thanks **Allard** for your help when the cryostat broke down. Thanks **Michael, Brecht, Joris** for making me think with your questions about 2D materials and optics. **Tino**, thanks for always being available for some small talk or technical assistance or advice. **Heleen** and **Etty**, thanks for all the advice and support for our group. I enjoyed the times you guys joined us in our group outings.

Of course, there is more to life than work. I feel blessed with the abundance of friends I have, for all the moral support you gave me throughout these years, and for being able

to enjoy each others company. **Hanneke**, thanks for being the critical note in my life. We stayed connected even when you moved to far away countries, and kept sharing our daily lives. Although our PhDs are completely different, we found resemblence in our frustration. And it looks like we both made it, so we can start calling each other doctor now. **Kim**, you paved the way for me of moving from Leiden to Delft. Thanks for all the times you understood exactly my PhD related stress, and helped me to put it in perspective. I enjoyed the walks in the *Delftse Hout*, and of course all the liters of tea we drank together. **Sylvia**, I enjoyed being your neighbour both in Leiden and in Delft. You were always available for a chat and some distraction from PhD stress. **Rianne** and **Elsa**, I am happy that I could share the PhD experience with all its frustrations with people that understood. **Jiska**, thanks for the joy of your company, and of course for saving me from the gigantic spider. **Jacolien**, you understood the stress of having a first job, and the importance of relaxing with a cup of tea. **Jorien** and **Doreen**, thanks for all the times we could meet and hang out together.

I am not the first one in my family to do a PhD. **Papa**, you inspired me to follow in your footsteps, although I do not think you fully realized that when you brought me along to TU Delft when I was a baby. I enjoyed all your interest in my research and all the detailed questions. Although your in-depth knowledge of physics has gotten a little bit rusty, your experience in the world of science is very recent. You always made me feel confident that I could get through this PhD, just like you did twice. **Mama**, you are getting very experienced in supporting close family members during their PhD projects. You are very good in zooming out from the local stress and putting things in a general perspective. **Benjamin**, sorry for the disappointment I caused by demonstrating that you cannot, unfortunately, see a laser beam penetrating through the air like in movies. **Sharon**, we started as neighbours and, after your time of travelling, I am happy to welcome you back as a neighbour. **Ariël**, I enjoyed having you as a colleague for a summer. I really think the group profited from all the effort you put in programming lab software, and we will always be able to look back at your slightly peculiar git commits.

Doing a PhD project in the Nano Optics groups yielded more than a thesis, in-depth knowledge, friends and an interesting experience. **Filippo**, you were always happy to answer my stupid questions, and to waste your time in trying to squeeze exciton lifetimes out of my measured histograms. Although I valued you as a colleague, I am very happy with your promotion to boyfriend and fiancé. Thanks for letting me cry and for making me laugh, for all the times you put me on a bike to distract me from stress, and for being next to me. I am blessed with a person to count on, no matter what happens.

Finally I want to thank and acknowledge the One **God** that created both light and matter. I thank Him, who made nature interesting enough to challenge us to investigate it, and who put a deep curiosity and a yearning for knowledge in our hearts and minds.

CURRICULUM VITÆ

Irina KOMEN

15-03-1990 Born in Delft, the Netherlands.

EDUCATION

2002–2008 Highschool
ISG Arcus, Lelystad

2008–2009 EH-Basisjaar
Evangelische Hogeschool, Amersfoort

2009–2012 Bachelor in Physics
Leiden University
Thesis: Quantum optics with DNA encapsulated silver clusters on nanotubes
Supervisor: Prof. dr. D. Bouwmeester

2012–2014 Master in Physics
Leiden University
Thesis: Superconducting single photon detectors, magnetic field and polarization
Supervisor: Prof. dr. M.P. van Exter
Thesis: Combining photothermal imaging of gold nanorods and molecule fluorescence enhancement with optical tweezers
Supervisor: Prof. dr. M. Orrit

2014–2017 Educational Master
Leiden University

2017–2021 PhD in Physics
Delft University of Technology
Thesis: The interaction of light with WS_2 nanostructures
Promotor: Prof. dr. L. Kuipers

AWARDS

2018 Best Poster (Near-Field Optics, Troyes, France)
2019 Best Poster (NNV AMO Lunteren)

LIST OF PUBLICATIONS

7. **I. Komen**, S.E.van Heijst, M. Caldarola , S. Conesa-Boj, L. Kuipers, *Revealing the geometry and orientation of WS_2 nanoflowers by polarization-resolved Raman spectroscopy*, in submission, arXiv:2110.14976 (2021)

6. **I. Komen**, S.E.van Heijst, T. Bauer , S. Conesa-Boj, L. Kuipers, *Position-dependence of valley polarization and valley coherence of WS_2 monolayer flakes*, in submission, arXiv:2106.03472 (2021).

5. **I. Komen**, S.E.van Heijst, S. Conesa-Boj, L. Kuipers, *Morphology-induced spectral modification of self-assembled WS_2 pyramids*, Nanoscale Advances **3**, 6427-6437 (2021).

4. J. Hernandez-Rueda, M. Noordam, **I. Komen**, L. Kuipers, *Nonlinear Optical Response of a WS_2 Monolayer at Room Temperature upon Multicolor Laser Excitation*, ACS Photonics **8**, 2 (2021).

3. S.H.Gong* , **I. Komen***, F. Alpeggiani, L. Kuipers, *Nanoscale optical adressing of valley pseudospins through transverse optical spin*, Nano Letters **20**, 6 (2020).

2. J.J.Renema, Q. Wang, R. Gaudio, **I. Komen**, K.P.M. op 't Hoog, D. Sahin, A. Schilling, M.P. van Exter, A. Fiore, A. Engel and M.J.A. de Dood, *Position-Dependent Local Detection Efficiency in a Nanowire Superconducting Single-Photon Detector*, Nano Letters **15**, 7 (2015).

1. J.J.Renema, R.J.Rengelink, **I. Komen**, Q. Wang, R. Gaudio, K.P.M.op 't Hoog, Z. Zhou, D. Sahin, A. Fiore, P. Kes, J. Aarts, M.P.van Exter, M.J.A.de Dood, and E.F.C.Driessen, *The effect of magnetic field on the intrinsic detection efficiency of superconducting single-photon detectors*, Applied Physics Letters **106**, 6 (2015).

* contributed equally to this work